



Towards improved correction
methodology for regulatory aircraft engine
nvPM measurement

By

Eliot Faustin Durand

Thesis submitted to Cardiff University for the degree of Doctor of Philosophy

School of Engineering

Cardiff University

2019

Abstract

Local air quality and environmental concerns over particulate matter (PM) emissions have recently been exposed. Aircraft gas turbine engines produce ultrafine PM (<100 nm), which is believed to be particularly harmful due to their small size. Regulatory sampling and measurement systems have been introduced by ICAO to mitigate the emission of non-volatile PM (nvPM). Whilst this is a significant development, still several sources of measurement and correction uncertainty exist. An SAE-31 system loss tool (SLT) has recently been proposed to predict system loss correction factors in order to predict engine exit plane concentrations from the regulatory measurements. However, the SLT requires several assumptions which lead to unknown levels of uncertainty. The aim of this thesis is to reduce the uncertainty associated with predictions of engine exit plane nvPM mass and number concentrations.

Various methods for aerosol generation were proposed and characterised, leading to the selection of an optimised system for the laboratory particle loss experimentation. Silica, salt and graphite were found to provide a suitable range of morphological and physical particle characteristics. Theoretical models proposed for particle loss mechanisms comprising thermophoresis, diffusion and 'bend loss' theory, typically found within an ICAO compliant sampling system, have been validated experimentally at conditions representative of aircraft exhaust sampling. The impact of particle morphology on transport through the main sections of the sampling system has been established. The current ICAO compliant sampling and measurement system was deployed across a range of Rolls-Royce engine types and conditions, covering the entire thrust range. This provided a broad range of PM data - with average particle effective densities ranging between 0.3-0.8 g/cm³ derived - from which new correlations have been proposed.

Uncertainties associated with the regulatory nvPM sampling and measurement methodology have been independently evaluated; they are estimated to be 66% for EI_{number} and 25% for EI_{mass} for the smallest particles (10 nm). Preliminary studies have highlighted additional uncertainties associated with line shedding, ambient effects and fuel properties, which are not currently included within regulation. Theory predicts that losses <90% (for number) occur in a compliant sampling system with only thermophoresis currently corrected in reported EI 's. System loss correction has the potential to predict engine exit plane concentrations using measured EI_{number} and EI_{mass} by correcting for particle loss. Current SLT assumptions regarding lognormality, GSD and particle density were empirically validated and found to generate associated uncertainties of 76% and 27% for the predicted number and mass system loss correction factors respectively. It is demonstrated that an additional particle size measurement improves the estimation of engine exit plane concentrations by removing the requirement for assumptions, hence significantly reducing overall uncertainty.

Declaration and Statements

STATEMENT 1

This thesis is being submitted in partial fulfilment of the requirements for the degree of PhD

Signed _____

Date _____

STATEMENT 2

This work has not been submitted in substance for any other degree or award at this or any other university or place of learning, nor is it being submitted concurrently for any other degree or award (outside of any formal collaboration agreement between the University and a partner organisation)

Signed _____

Date _____

STATEMENT 3

I hereby give consent for my thesis, if accepted, to be available in the University's Open Access repository (or, where approved, to be available in the University's library and for inter-library loan), and for the title and summary to be made available to outside organisations, subject to the expiry of a University-approved bar on access if applicable.

Signed _____

Date _____

DECLARATION

This thesis is the result of my own independent work, except where otherwise stated, and the views expressed are my own. Other sources are acknowledged by explicit references. The thesis has not been edited by a third party beyond what is permitted by Cardiff University's Use of Third-Party Editors by Research Degree Students Procedure.

Signed _____

Date _____

WORD COUNT _____ ~67,000 _____

(Excluding summary, acknowledgements, declarations, contents pages, appendices, tables, diagrams and figures, references, bibliography, footnotes and endnotes)

Acknowledgements

I would like to thank Phil Bowen and Andrew Crayford for giving me the opportunity to do this PhD, and particularly to Andrew for his guidance, support and encouragement during the four years of my PhD and without whom I would not have been able to succeed.

I would also like to acknowledge Yura Sevenco who carefully taught me how to run the EASA nvPM reference system and with whom I attended many test campaigns.

Many thanks to Mark Johnson whose inputs were greatly appreciated and to Rolls-Royce for permitting me to use data measured on their engines and allowing many of the experiments presented in this thesis to be conducted.

Special thanks to the National Research Network in Advanced Engineering and Materials and to Cardiff university who funded my PhD.

To the European Aviation Safety Agency which allowed me to use instrumentation at multiple facilities and funded many test campaigns.

To all the staff and researchers at the Gas Turbine Research Centre and those sharing my office.

Finally, I would like to express my deepest gratitude to all my family and friends, and particularly to my partner Meg for her endless support and belief in me.

Published and Presented Work

- **Combustion Aerosol Conference 2019 (Cambridge Particle Meeting):**

Presentation - “Assessment of nvPM System Loss Prediction with Size Measurement towards Aviation Engine Regulation” ([Eliot Durand](#), Andrew Crayford, Mark Johnson).

- **SAE E-31 Annual Meeting 17-21/06/19:**

Presentation – “Appraisal of Additional Size Measurement for System Loss Correction” ([Eliot Durand](#), Andrew Crayford, Mark Johnson).

- **Forum-AE non-CO2 workshop 9/03/2017:**

Presentation - “nvPM Engine Measurement Results at a Safran Aircraft Engine Facility” ; Safran Aircraft Engines and Cardiff University (Nadine Harivel, [Delphine Lottin](#), Yura Sevcenco, [Eliot Durand](#), Hieu Pham, Olivier Penanhoat, Yoann Mery).

- **National Research Network Postgraduate conference 2017:**

Poster - “Accurate sampling & capture of Aircraft generated PM”.

- **National Research Network Postgraduate conference 2016:**

Poster - “ Accurate quantification of combustion generated ultrafine particulates and their health effects”.

Table of Contents

1	Introduction.....	1
1.1	Overview of gas turbine engines emissions.....	1
1.2	Particulate Matter.....	3
1.3	Soot formation in a gas turbine engine	5
1.4	Health and environmental impact of aircraft PM.....	6
1.4.1	Health	6
1.4.2	Environment.....	8
1.5	Aircraft PM regulation	10
1.6	Research motivations and thesis structure	14
2	Aircraft PM – Properties, Measurement and Sampling	16
2.1	Particle size and size distribution statistic	16
2.1.1	Particle size.....	16
2.1.2	Size distribution and lognormal statistic	18
2.2	Particle effective density.....	20
2.3	Nanoparticle loss mechanisms.....	24
2.4	Aircraft nvPM system loss correction methodology (SLT).....	34
2.4.1	Penetration efficiency prediction (UTRC model).....	36
2.4.2	Correction factor predictions in the SLT.....	37
2.5	Measurement uncertainty and error propagation	39
2.6	Reporting of large-scale aircraft engine nvPM emissions.....	40
2.7	Chapter Summary	42
3	Experimental Facilities and PM Instrumentation	43
3.1	Aircraft engine exhaust PM measurements	43
3.1.1	ICAO compliant nvPM sampling and measurement system	43
3.1.2	Cleanliness and Background checks	51
3.1.3	Particle size measurement	51
3.1.4	Measurement of nanoparticles in a liquid	55
3.2	Aerosol generation and conditioning techniques.....	58
3.2.1	Nebuliser.....	59
3.2.2	Centrifugation of suspensions	60
3.2.3	Graphite Aerosol Generator	61
3.2.4	Aerodynamic aerosol classification	62
3.2.5	Diffusion screens	63
3.3	Large-scale certification level engine testing.....	64
3.4	Other engines and experimental Rigs.....	65

3.5	Chapter Summary	66
4	Aerosol Generation and Characterisation	67
4.1	Aerosolization of solutions/suspensions for particle generation	68
4.1.1	Experimental characterisation of collision nebulisers.....	69
4.1.2	Characterisation of aerosolised suspensions and solutions.....	76
4.1.3	Characterisation and removal of Non-Volatile Residue (NVR).....	86
4.2	Classified aerosol size distributions for laboratory experiments.....	94
4.3	PM capture and characterisation in a liquid	98
4.3.1	Particle capture from gas to liquid	100
4.3.2	Characterisation of collected nanoparticle suspensions.....	108
4.4	Chapter summary.....	113
5	Particle Loss Experimentation and Quantification	115
5.1	Thermophoretic experiment.....	116
5.1.1	Experimental setup.....	118
5.1.2	Calculation of penetration efficiency	120
5.1.3	Heating/Cooling length estimation	121
5.1.4	Theoretical sensitivity analysis	123
5.1.5	Gas temperature calibration	125
5.1.6	Results	127
5.2	25 m Sample line experiment	133
5.2.1	Experimental set-up	133
5.2.2	Theoretical sensitivity analysis	134
5.2.3	Results	135
5.3	VPR experiment	139
5.3.1	Experimental set-up	140
5.3.2	Results	141
5.4	Chapter summary.....	142
6	Large-Scale Civil Aviation Engine PM measurements	144
6.1	Measured nvPM Correlations and Properties	144
6.1.1	Correlation of Measured nvPM to Relative Thrust	144
6.1.2	nvPM Size Measurements	147
6.1.3	Average particle effective density	153
6.2	Uncertainties associated with nvPM sampling & measurement.....	158
6.2.1	Number measurement uncertainty.....	158
6.2.2	Mass measurement uncertainty.....	165
6.2.3	Particle size distribution measurement uncertainty	169
6.2.4	Sampling system uncertainties.....	173

6.2.5	Total uncertainty from nvPM sampling & measurement.....	183
6.3	Uncertainty associated with soot source.....	185
6.3.1	Effect of humidity on nvPM emissions.....	185
6.3.2	Effect of fuel properties on nvPM emissions.....	186
6.4	Chapter summary.....	188
7	System Loss Correction of Regulatory nvPM Measurements.....	191
7.1	System loss tool inputs.....	192
7.1.1	Sampling system dimensions & locations.....	193
7.1.2	Prediction of GMD & GSD using measured size distribution.....	197
7.2	SLT lognormality assumption at Engine Exit Plane.....	201
7.2.1	Assessment of lognormality using assumed lognormal distribution at exit plane.....	201
7.2.2	Assessment of lognormality using predicted size distributions at the EEP.....	203
7.2.3	Correction factor uncertainty associated with lognormality assumptions.....	204
7.3	SLT GSD and particle density assumptions.....	205
7.3.1	Effect of assumed density and GSD on SLT predictions.....	206
7.3.2	Comparison of GMD predicted by SLT and size measurement.....	207
7.4	Chapter Summary.....	218
8	Conclusions.....	221
8.1	Aerosol Generation and Characterisation.....	221
8.2	Particle Loss Characterisation.....	221
8.3	Large-scale Engine PM Emission Measurements.....	222
8.4	System Loss Correction Methodology for Regulatory nvPM Measurements.....	223
8.5	Future Work.....	224
9	References.....	225
10	Appendices.....	235
10.1	Calibration certificates PM measurement.....	235
10.2	Other calibration certificates.....	242
10.3	Suspension/solution certificates.....	245

List of Figures

Figure 1-1: Simplified Schematic of an aircraft turbofan engine with the division of the combustion products [7].....	2
Figure 1-2: Illustration of the typical temperature and pollutant formation rates resulting from changes in AFR for gas turbine combustors [8]	3
Figure 1-3: Illustration of PM size in comparison to human air (a) and visual representation of major particle sizes use for classification of PM (b) [8].....	4
Figure 1-4: Diagram of the particle formation process in a gas turbine combustor	5
Figure 1-5: Simplified diagram of the exhaust products from a gas turbine engines with the environmental effects and human health effects of emitted compounds [7]	6
Figure 1-6: Predicted deposition efficiency of inhaled particles in different regions of the respiratory system [25].....	7
Figure 1-7: Annual mean of the atmosphere radiative forces from anthropogenic aerosol radiations interactions for the 1750-2010 period (<i>whiskers represent results from the AeroCom II model and solid coloured boxed present AR5 model estimates – BB stands for Biomass Burning aerosol while POA and SOA respectively stand for primary and secondary organic aerosols</i>) [37]	8
Figure 1-8: Radiative forcing components from global aviation from pre-industrial times until 2005 [43].....	9
Figure 1-9: LTO cycle with time and power setting for each mode.....	11
Figure 2-1: TEM image of 15 nm ((a) and (b)) and 50 nm (c) mobility-selected soot aggregates emitted from a CFM56-5B4-2P aircraft engine [20].....	17
Figure 2-2: Example of typical measured aircraft PM particle size distribution as a function of engine thrust [61]	18
Figure 2-3: Example lognormal particle distribution both number- and mass-weighted with a GMD of 40 nm, GSD of 1.7 and total number concentration of 10^7 particles/cm ³	20
Figure 2-4: Particle effective density distributions ($\rho_{eff2}(dp)$) determined for various thrust ranges and average effective density ($\rho_{eff2}(avg)$) as a function of engine thrust and volume median diameter from multiple aircraft engines [63]	22
Figure 2-5: Diagram of main nanoparticle deposition mechanisms in a tube (inspired from [74]) ...	24
Figure 2-6: Diagram of main nanoparticle transformation mechanisms in a tube (inspired from [74])	25
Figure 2-7: Illustration of a particle immersed in a gas with a temperature gradient [81].....	30
Figure 2-8: Cross-sectional view of an impactor [60]	32
Figure 2-9: Block diagram of the SLT correction methodology [57]	35
Figure 2-10: Example of nanoparticle penetration efficiency in a typical ICAO compliant sampling system estimated using the UTRC model	36

Figure 2-11: Example of nanoparticle penetration efficiency in an ICAO compliant cyclone, VPR and CPC using the SLT	37
Figure 2-12: Diagram of the SLT system loss correction factor methodology (Note that k_{thermo} and DF_1 cancel out and hence have no impact on the calculations) [57]	38
Figure 2-13: Illustration of a normal distribution with confidence bands representing the standard deviation (GSD) around the mean	39
Figure 2-14: SaM146 Turbofan Engine average normalised nvPM number (a) and mass (b) emission indices for different regimes [61]	41
Figure 2-15: nvPM number- (a) and mass-based (b) emission indices as a function of engine operating conditions for three engines [51]	41
Figure 2-16: Comparison of mass emission indices from Black Carbon measurement (MSS, LII) and Total Particle measurements (DMS-500, SMPS, FMPS) at different engine thrusts [63]	42
Figure 3-1: Overview schematic of an nvPM sampling and measurement system [59]	44
Figure 3-2: schematic of AVL Particle counter [47]	46
Figure 3-3: Diagram of the measuring principle of the AVL MSS [102]	47
Figure 3-4: Simplified operating principle of the Artium LII-300 [104]	48
Figure 3-5: Ejector diluter losses of diesel exhaust particles measured with various instruments [105] (a) and ejector diluter's penetration efficiencies unheated and heated at 150°C [106] (b)	48
Figure 3-6: Diagram of the ICAO compliant Dekati DI-1000 ejector [19]	49
Figure 3-7: Heated line used in the EASA mobile system (where Carbon loaded PTFE is coating the inner walls) [109]	50
Figure 3-8: Illustration of the DMS-500 sampling system with the two dilution stages and the 5m heated line [8]	52
Figure 3-9: DMS-500 sensitivity limits at different measurement rates with no dilution [110]	52
Figure 3-10: Diagram of the DMS-500 classifier column [111]	53
Figure 3-11: Screenshot of the DMS-500 user interface displaying the measurement of a bi-modal size distribution [112]	54
Figure 3-12: particles of different densities or size observed to sediment at different rates [135] ..	60
Figure 3-13: Diagram of the mechanical arrangement of the electrode unit inside a PALAS GFG 1000 [136]	61
Figure 3-14: Particle Size distributions generated PALAS graphite aerosol generator at different settings and measured by a DMS-500 (SC=Spark Frequency)	62
Figure 3-15: Diagram of the principle of operation of the Cambustion Aerodynamic Aerosol Classifier [77]	63
Figure 3-16: Theoretical penetration efficiency through the PSS using 5, 11 and 23 wire-mesh screens [144]	63
Figure 3-17: Simplified diagram of an ICAO compliant sampling system used during large-scale engine testing	64

Figure 3-18: Photograph of the EU/EASA Mobile Reference System location next to SR Technics test cell [49].....	64
Figure 3-19: Simplified diagram of the sampling system used during PM measurement on multiple engines and combustion rigs	65
Figure 3-20: Photograph of a GNOME gas turbine rig with sample lines [19].....	66
Figure 4-1: Effect of producing smaller droplets on non-volatile residue particle nucleation and coating [147]	68
Figure 4-2: Particle size distribution of nebulised 300 nm PSL spheres used for the calibration of the DMS-500 with both reconstructed lognormal (blue) and full spectral outputs (red) [111]	69
Figure 4-3: Photograph of three ‘medical’ nebulisers in series producing gold (a) and typical NVR size distribution when atomising distilled water with a ‘medical nebuliser’ (b)	70
Figure 4-4: Particle size distribution produced from the nebulisation of distilled water using a medical nebuliser and a Topas ATM-226 and measured by a DMS-500.....	71
Figure 4-5: Non-Volatile-Residue (NVR) size distribution ((a) GMD, (b) N_{tot} , (c) GSD) generated from the nebulisation of water with a Topas ATM-226 at different inlet flowrate measured by DMS-500	72
Figure 4-6: Effect of Relative Humidity and a diffusion drier on the GMD of SiO ₂ suspensions and NaCl solutions nebulised using an ATM-226 and measured with a TSI SMPS (red arrows represent time)	74
Figure 4-7: Particle size distribution on a log-log scale of different solvents atomised by an ATM-226 and measured by a DMS-500.....	75
Figure 4-8: particle size distribution of different aqueous solvents on a log-log scale (a) and on a log-linear scale (b) atomised by an ATM-226 and measured by a DMS-500.....	76
Figure 4-9: Particle size distributions of multiple BBI solutions gold suspensions atomised with an ATM-226 and measured using a DMS-500	77
Figure 4-10: Particle size distribution of 60 nm (a) and 100 (b) centrifuged gold suspensions atomised with an ATM-226 and measured by a DMS-500 with and without AAC classification	78
Figure 4-11: Photographs of a vial after the nebulisation of a gold suspension using the ATM-226 showing gold plating onto the walls acting as an impactor.....	79
Figure 4-12: Particle size distribution of 100 nm Carboxyl Latex beads suspended in distilled water atomised with an ATM-226 and measured with the the DMS 500 (a) and photograph of agglomerated beads forming visible white clusters (b)	80
Figure 4-13: Particle size distribution of 100 nm Carboxyl Latex beads suspended in distilled water mixed with bicarbonate soda, atomised with an ATM-226 and measured with the the DMS 500 (y-axis linear scale (a) and log scale (b)).....	81
Figure 4-14: Particle size distribution of different silica suspensions suspended in distilled water atomised using an ATM-226 and measured by a DMS-500.....	82

Figure 4-15: Effect of increasing silica suspension volume/concentration on the GMD measured with a DMS-500 for suspensions atomised by an ATM-226 in a constant volume of distilled water (a) and size distributions of atomised 50 nm silica suspensions diluted in ultrapure water type 1 at different concentration (b)	83
Figure 4-16: Bimodal reconstruction of particle size distributions of liquid suspension and powder 100 nm SiO ₂ suspended in distilled water at different concentrations atomised by an ATM-226 and measured by a DMS-500.....	84
Figure 4-17: TEM image for nebuliser-generated NaCl particles [153]	86
Figure 4-18: Particle size distribution of a saline solution (0.9% NaCl w/v) atomised by an ATM-226 and measured by a DMS-500.....	86
Figure 4-19: Diagram of the typical experimental set-up when investigating NVR formation and removal	87
Figure 4-20: Effect of vial material and liquid height (i.e. volume of IPA) on NVR's number concentration (a) and GMD (b) from Isopropanol atomised with an ATM-226 and measured with a DMS-500	88
Figure 4-21: Effect of storage time on the NVR and Silica peaks of 100 nm (sample A) and 180 nm (sample B) SiO ₂ mixed in ultrapure water type 1 and stored in a glass atomised with an ATM-226 and measured with a DMS-500	88
Figure 4-22: Effect of silica suspension concentration on the NVR peak when atomised with an ATM-226 and measured with a DMS-500	89
Figure 4-23: Particle size distributions of 50 nm (a) and 180 nm (b) SiO ₂ suspensions nebulised by an ATM-226 and measured by a DMS-500 before and after a tube furnace	90
Figure 4-24: Particle size distributions of nebulised distilled water heated at different temperatures on different days (T _{max} =570°C (a); T _{max} =830°C (b)) and measured by the DMS-500 before and after a tube furnace.....	91
Figure 4-25: Particle size distribution of a 50 nm Silica suspension with and without diffusion screen at different flowrates, atomised by an ATM-226 and measured by a DMS-500.....	92
Figure 4-26: Particle size distribution of a 100 nm (a) and 180 nm (b) Silica suspensions before and after a 40 min centrifugation at 40K RCF and replacement with ultrapure water, atomised by an ATM-226 and measured by a DMS-500.....	93
Figure 4-27: Particle size distribution of a 50 nm (a), 100 nm (b) and 180 nm (c) Silica suspensions with the Cambustion Aerosol Aerodynamic Classifier (AAC) on and off, atomised by an ATM-226 and measured by a DMS-500.....	94
Figure 4-28: Particle size distributions of a saline suspension (a) and silica suspension (b) classified by an AAC at different Rs and d _a settings, atomised with an ATM-226 and measured with a DMS-500.....	95
Figure 4-29: Particle size distributions of salt (a) and silica (b) suspensions atomised with an ATM-226 and graphite (c) classified with an AAC at different settings producing different GMDs and measured with a DMS-500.....	96

Figure 4-30: TEM picture of soot emitted by a diesel engine – (a) recovered from filters and suspended into water – (b) directly captured from the diluted exhaust gas [160].....	99
Figure 4-31: Diagram of particles being transfer from gas to liquid in a bubbler	100
Figure 4-32: Visualisation of bubbles under different column operating conditions: (A) 20 cm of liquid; (B) 10 cm of 1.5mm diameter glass beads in 20 cm of liquid; (C) 10c m of 2.75 mm diameter glass beads in 20 cm of liquid; (D) 10 cm of 1 mm diameter metal beads in 20 cm of liquid [159]	101
Figure 4-33: Photographs of the various bubblers used to capture nanoparticles in a liquid including a midget impinger (a), a conical flask (b), glass cylinder bubblers (c) and a stainless-steel bubbler in parts (d).....	102
Figure 4-34: diagram of the experimental set-up of the nozzle’s characterisation experiment.....	104
Figure 4-35: Graphite nanoparticles loss (a) and GMD variation (b) inside different nozzles measured by a DMS-500.....	105
Figure 4-36: Transfer efficiency from gas to liquid (a) and GMD variation (b) of soot-like nanoparticles in a bubbler containing different volumes of water and measured by a DMS-500	106
Figure 4-37: Diagram of the experimental set-up for the stainless-steel bubbler characterisation	107
Figure 4-38: Effect of liquid height and gas flowrate on the particle transfer efficiency of a Stainless Steel bubbler with soot-like particles generated by a PALAS graphite generator and measured with a DMS-500	108
Figure 4-39: Screenshots of sample 1 containing particles captured by the Nanosight LM10 camera	110
Figure 4-40: Size distribution of sample 1 measured by a Malvern Zetasizer and plotted against intensity (a), volume (b) and number (c).....	111
Figure 4-41: Individually normalised particle size distributions measured in the gas (DMS-500) and in the liquid (Zetasizer and Nanosight) of sample 1 (a) and sample 2 (b)	112
Figure 5-1: Simplified diagram of the experimental setup for thermophoretic, sample line and bends loss laboratory experiments	118
Figure 5-2: Diagram of the thermophoretic experiment test section	119
Figure 5-3: Photographs of thermophoretic experiment set-up.....	119
Figure 5-4: Example of measured number concentrations over time at different test points with salt (a), graphite (b) and silica (c) nanoaprticles using an AVL APC a Cambustion DMS-500.....	120
Figure 5-5: Theoretical penetration efficiencies of the thermophoretic test section at 20°C with varying sample flows (a) and at 1000°C with varying particle thermal conductivities (b)	125
Figure 5-6: Recorded hot (a) and cold (b) temperatures at different furnace temperature in the thermophoretic set-up.....	126
Figure 5-7: Photograph of the calibrated 6mm thick insulated thermocouple and the 3mm thick thermocouple	127

Figure 5-8: Measured (APC and DMS-500) and predicted (UTRC model) penetration efficiencies for different particle types (NaCl, SiO ₂ , graphite) in the thermophoretic test section at ambient temperature and flowrates of 8-24 Lpm	128
Figure 5-9: Penetration efficiencies of different nanoparticle types (graphite 'Δ', silica '*', salt 'o') and sizes measured in the thermophoretic set-up with the furnace on at different temperatures, measured with the DMS-500 and the APC at 8-24 Lpm	129
Figure 5-10: Penetration efficiencies of Graphite, silica and salt (NaCl) against gas temperature gradient averaged over size and measured with an APC (a) and a DMS-500 (b).	131
Figure 5-11: Power fit of penetration efficiencies of Graphite and silica and salt (NaCl) measured by an APC (a) and a DMS-500 (b) combined averaged over size and compared with theoretical predictions	132
Figure 5-12: Difference in GMD measured before and after the thermophoretic test section for salt (NaCl) nanoparticles (a) and difference in the measured penetration efficiency when using air or nitrogen (N ₂) as a carrier gas (b)	132
Figure 5-13: Photographs of the 25 m sample line experiment with the line 'straight' (a) & (b) and 'coiled' (c)	134
Figure 5-14: UTRC model penetration efficiency predictions in the coiled (3960°) 25 m sample line with different particles densities at 25°C (a) and difference between the coiled and straight (720°) (b) at different gas flowrates.....	135
Figure 5-15: Theoretical (UTRC model) and experimental (NaCl, Graphite & SiO ₂) diffusional penetration efficiencies measured with an APC and a DMS-500 in a 'straight' 25 m sample line at Reynolds numbers of 1410 – 2431	136
Figure 5-16: Penetration efficiencies of NaCl, SiO ₂ and graphite nanoparticles in the 'straight and 'coiled' 25 m sample line with their exponential fits measured by an APC and a DMS-500 at Reynolds numbers of 1410 - 4231.....	138
Figure 5-17: Measured (APC and DMS-500) and estimated deposition efficiency caused by coiling the 25 m sample line (i.e. difference 'straight'/'coiled') at Reynolds numbers of 1410 - 4231	139
Figure 5-18: Diagram of the VPR characterisation experiment	140
Figure 5-19: Particle number concentration of salt (NaCl) nebulised with an ATM-226 and classified with a DMA between 10-50 nm measured by two CPCs	141
Figure 5-20: VPR penetration efficiency of Silica, salt (NaCl) and graphite measured (a) and CPC cross-calibration corrected (b) compared with mini-CAST from AVL calibration	142
Figure 6-1: Normalised EI_{number} (a) and EI_{mass} (b) of four engine types at thrust settings corresponding to the LTO cycle.....	145
Figure 6-2: Relationship between relative thrust and N/M ratio (a), GMD (b) and GSD (c) over an LTO cycle (7%, 30%, 85% and 100% F_{00}) for four aircraft engines during certification tests.....	146
Figure 6-3: Normalised Log-Linear Particle Size Distributions of four engines types at various engine power conditions	148

Figure 6-4: GSD (a) and GMD (b) measured by a DMS 500 on various engine types against N/M ratio with power fit.....	149
Figure 6-5: measured GMD against measured GSD on various engine types	149
Figure 6-6: Examples of PSDs displaying a secondary peak measured by a DMS-500 and converted VSDs with and without the tail-cutting method	150
Figure 6-7: Mode, Mean and Median in lognormal and skewed distributions [60]	151
Figure 6-8: Lognormality assessment at instrument by means of comparing GMD and CMD (a) and GSDPSD and GSDVSD(b)	152
Figure 6-9: Example of the conversion from a PSD to a VSD with the tail-cutting method and its limits	153
Figure 6-10: Example of a derived Volume Size Distribution (VSD) corrected with method (1), (2) and (3)	154
Figure 6-11: Difference between effective densities calculated with method (1) and (3) (a) and method (2) and (3) (b) for different engine types plotted against the volume derived from the DMS size distribution at the 1 st common	155
Figure 6-12: Average effective density ($\rho_{eff1}(avg)$) calculated for various engine types plotted against N/M ratio (a) and GMD (b)	157
Figure 6-13: Penetration efficiencies of CPC (a) and VPR (b) from yearly calibration and laboratory experiments with dashed red line representing minimum regulatory requirements.....	159
Figure 6-14: Example of a measured and corrected particle size distribution (left axis) and the associated penetration efficiencies for APC and DMS (right axis) to the 1 st common point.....	163
Figure 6-15: Total DMS PM concentration Vs APC nvPM concentration measured with the EASA kit for different aircraft engines corrected to 1 st common point with 1 to 1 line and $\pm 24.5\%$ uncertainty lines.....	164
Figure 6-16: Difference between DMS Total PM concentration and APC nvPM concentration for different aircraft engines corrected to 1 st common point with 1 to 1 line and $\pm 24.5\%$ uncertainty lines - (NAPC – NDMSNAPC) Vs GMD.....	164
Figure 6-17: Coefficient of Variation (i.e. standard deviation/average) of MSS and LII nvPM mass measurements obtained on four aircraft engine types against mass (a) and GMD (b)	167
Figure 6-18: Comparison of measured MSS and LII-300 nvPM mass concentrations on various engine types.....	168
Figure 6-19: Example particle size distributions measured by a DMS and a SMPS at the exhaust of a GNOME engine (a) and RQL burner (b)	171
Figure 6-20: Comparison of size (a) and Number (b) measurements performed by a DMS-500 and SMPS on aircraft exhaust aerosols.....	172
Figure 6-21: Best and Worst penetration efficiencies of an ICAO compliant long sample line (left-axis) with their difference (right-axis).....	174
Figure 6-22: Diagram of the ejector diluter experimental set-up	176

Figure 6-23: Example particle size distributions of soot measured at the inlet and outlet (Particle Number Dilution Factor corrected) of an ejector diluter using a DMS-500 (a) and an SMPS (b).....	177
Figure 6-24: Difference in soot GMD (a) and GSD (b) when passing through and ejector diluter heated at different temperatures measured using a DMS-500 and an SMPS.....	178
Figure 6-25: Best and Worst penetration efficiencies of an ICAO compliant collection section with their difference	180
Figure 6-26: Typical Zero/Cleanliness (a) and Background/Ambient (b) checks measured by a DMS-500 prior and after three engine types emission test	181
Figure 6-27: Maximum Number & Mass size distribution measured by the DMS-500 during.....	182
Figure 6-28: Diagram of the uncertainties associated with ICAO compliant nvPM number concentration measurement	183
Figure 6-29: Diagram of the uncertainties associated with ICAO compliant nvPM mass concentration measurement.....	184
Figure 6-30: Reduction of Number (a), Mass (b) and Size (c) when injecting steam in the primary air for multiple fuels at primary diffusion flame Air-Fuel-Ratios of 6.2.....	186
Figure 6-31: Effect of blends of alternative and conventional fuel on EI_{number} plotted against primary ARF (a) and Hydrogen/Carbon ratio (b).....	187
Figure 6-32: Effect of blends of alternative and conventional fuel on EI_{number} (a), EI_{mass} (b) and GMD (c) at three power conditions plotted against hydrogen/carbon ratio	188
Figure 7-1: Typical Number, Mass and Size penetration efficiencies calculated using the UTRC model for a compliant aircraft engine emission sampling system (excluding collection section)	194
Figure 7-2: Diagram of an ICAO compliant sampling system with key locations for comparison of SLT	196
Figure 7-3: Example of a PSD measured by the DMS-500 at end of compliant sampling system, corrected for losses to various location of the sampling system	197
Figure 7-4: Examples of artefacts appearing when correcting some measured PSD down to the EEP	198
Figure 7-5: GMD Vs N/M ratio at multiple locations of the sampling system with power fits	199
Figure 7-6: GSD Vs N/M ratio at multiple locations of the sampling system (a) with power fits (b).....	199
Figure 7-7: Engine Exit Plane (EEP) corrected GMD against EEP GSD on various engine types	200
Figure 7-8: Measured GMD of four combined engine types against GMD predicted at the Engine Exit Plane (EEP) with linear trends.....	201
Figure 7-9: Lognormal distribution at the Engine Exit Plan and the estimated distribution at the instrument after applying typical non-thermophoretic size-dependent sampling system loss (Dilution omitted)	202
Figure 7-10: Lognormality assessment at the Engine Exit Plane by means of comparing GMD and CMD (a) and GSDPSD and GSDVSD(b).....	204

Figure 7-11: Difference in number (a) and mass (b) correction factors for four engine types estimated using the DMS-500 predicted size distributions and a lognormal distribution generated from the PSD's GMD and GSD.....	205
Figure 7-12: Measured-derived GMD against SLT-predicted GMD using default density and GSD assumptions for different engine types at various locations of the sampling system	208
Figure 7-13: Number (a) and Mass (b) correction factors against SLT GMD using default density and GSD assumptions at different locations of the sampling system for four Rolls-Royce Engine Types	209
Figure 7-14: Measured-derived GMD against SLT-predicted GMD using measured-derived GSD and density assumptions for different engine types at various locations of the sampling system	210
Figure 7-15: Differences in number (a) and mass (b) correction factors estimated from the System Loss Tool using the combined data of four engine types with different density and GSD assumptions	211
Figure 7-16: Measured-derived GMD against SLT-predicted GMD using empirically derived GSD and density assumptions for different engine types at the EEP.....	214
Figure 7-17: Measured-derived GMD against SLT-predicted GMD using a GSD fit and $\rho_{eff} = 0.62 \text{ g/cm}^3$ assumptions for different engine types at the Engine Exit Plane (EEP)	215
Figure 7-18: Measured-derived GMD against SLT-predicted GMD using GSD=1.8 (a) or GSD from fit at the EEP (b) and a size-dependent effective density derived from the literature for different engine types at the EEP	216
Figure 7-19: Measured-derived GMD against SLT-predicted GMD using default assumptions and the input APC nvPM number (a) or the DMS-500 total number (b) for different engine types at the EEP	217
Figure 7-20: Measured-derived GMD against SLT-predicted GMD using measured-derived assumptions and the input APC nvPM number (a) or the DMS-500 total number (b) for different engine types at the EEP.....	218

List of Tables

Table 1-1: Particle classification according to their size	3
Table 2-1: List of aircraft PM effective densities and mass-mobility exponents reported in the literature along with the instruments used for measurement.....	23
Table 3-1: Minimum allowed counting fractions of the VPR and CPC for nvPM number measurement	45
Table 3-2: Minimum requirements for particle penetration efficiency in the primary diluter of an ICAO compliant sampling system [14]	49
Table 3-3: Literature using Collision nebuliser to generate nanoparticles for loss experiments	58
Table 4-1: Fluid Properties of DEHS and water and comparative predicted droplet size	71
Table 4-2: Percentage difference of measured (DMS-500) to predicted silica nanoparticles concentration from atomisation of suspensions at different concentrations and silica GMDs.....	83
Table 4-3: Range of GMDs and GSDs measured by the DMS-500 using typical AAC parameters at different settings (small, medium and large GMD) during laboratory particle loss experiments (with the AAC sample flow Q_a fixed at 1.5 Lpm)	97
Table 4-4: Silica suspensions diameters measured in suspension (TEM) and after being atomised (AAC, DMS-500)	98
Table 4-5: Estimated particle number concentration in water captured with the Stainless-steel bubbler.....	109
Table 4-6: Summary of Zetasizer and Nanosight measurements on sample 1 and 2	111
Table 5-1: Summary of nanoparticle thermophoretic experiments available in the literature	117
Table 5-2: Estimations of heating and cooling length of a 8 mm ID tube at a furnace temperature of 1000°C and a cold heat exchanger temperature of 25°C	122
Table 5-3: Effect of changing particle and gaseous variables on losses in the thermophoretic experiment setup using the UTRC model	124
Table 5-4: Thermophoretic test section penetration efficiencies at ambient temperature averaged over particle type measured with an APC and a DMS-500, and predicted by the UTRC model (± 1 standard deviation).....	129
Table 6-1: Summary of the potential combinations to asses lognormality	152
Table 6-2: Minimum and maximum penetration efficiency reported during the calibration of the EASA and EMPA APCs between 2012 and 2018, and resulting difference in total number concentration at 10, 20 and 40 nm	161
Table 6-3: Typical dimensions and gas properties encountered in the collection section of a compliant sampling system.....	180
Table 6-4: Total mass measured by the DMS-500 during cleanliness checks assuming different effective densities	183

Table 7-1: Inputs used in the UTRC particle transport model to calculate typical penetration efficiencies from each instrument to the inlet of the collection section (i.e. splitter 1).....	194
Table 7-2: Inputs used in the UTRC particle transport model to calculate typical penetration efficiencies in the collection section.....	195
Table 7-3 : Examples of the predicted GMD, CMD and GSDs from PSD and VSD at the instrument when assuming a lognormal distribution at the EEP and accounting for losses in the sampling system	203
Table 7-4: Average absolute difference between predicted and measured corrected GMDs at different locations of the sampling system for four engine types combined (Mass>LOQ).....	208
Table 7-5: Maximum difference of SLT number and mass correction factors using different density and GSD assumptions at multiple locations of the sampling system using combined data of four engine types.....	212
Table 7-6: Summary of the average difference between SLT-predicted GMD and measured-derived GMD at the EEP using different GSD and density assumptions	219

List of Equations

Equation number and title	Page
Equation (1.1): Ideal complete combustion in gas turbine engine	2
Equation (1.2): nvPM emission indices general calculation	12
Equation (1.3): Simplified nvPM number emission index	12
Equation (1.4): Simplified nvPM mass emission index	12
Equation (1.5): Thermophoretic correction factor	13
Equation (1.6): Regulatory reporting of nvPM mass concentration	13
Equation (2.1): Conversion mobility to aerodynamic diameter	17
Equation (2.2): GMD calculation from particle size distribution	19
Equation (2.3): Total number concentration calculation from particle size distribution	19
Equation (2.4): GSD calculation from particle size distribution	19
Equation (2.5): Lognormal size distribution	19
Equation (2.6): Relationship between particle number, volume and mass	20
Equation (2.7): Particle effective density definition	21
Equation (2.8): Gas mean free path	25
Equation (2.9): Gas viscosity	26
Equation (2.10): Gas density	26
Equation (2.11): Reynolds number	26
Equation (2.12): Knudsen number	26
Equation (2.13): Stokes number	27
Equation (2.14): Cunningham correction factor	27
Equation (2.15): Particle diffusion coefficient	27
Equation (2.16): Particle relaxation time	28
Equation (2.17): Schmidt number	28
Equation (2.18): Dean number	28
Equation (2.19): Diffusional penetration efficiency	29
Equation (2.20): Diffusional deposition velocity	29
Equation (2.21-2.22): Inertial deposition velocity	29
Equation (2.23): Thermophoretic deposition velocity	30
Equation (2.24): Thermophoretic penetration efficiency	30
Equation (2.25): Thermophoretic correction factor	31

Equation (2.26): Electrostatic penetration efficiency	31
Equation (2.27): Diameter at which 50% of the particles are impacted onto a body	32
Equation (2.28): Bend penetration efficiency in laminar regime	32
Equation (2.29): Bend penetration efficiency in turbulent regime	32
Equation (2.30): Number concentration with coagulation	33
Equation (2.31): Size of particles with coagulation	33
Equation (2.32): Average coagulation coefficient	33
Equation (2.33): Chi-square minimisation to predict GMD in SLT	37
Equation (2.34): Geometric standard deviation and coefficient of variation	39
Equation (2.35): Propagated uncertainty of number emission index	40
Equation (2.36): Propagated uncertainty of measured penetration efficiency	40
Equation (3.1): Electrical mobility	53
Equation (3.2): Hydrodynamic diameter	57
Equation (3.3): Sedimentation velocity	60
Equation (3.4): RCF to RPM conversion	60
Equation (4.1): Concentration of Silica in aerosol from nebulisation of suspension	82
Equation (4.2): Mean and standard deviation of a lognormal distribution	85
Equation (4.3): Geometric standard deviation of a lognormal distribution	85
Equation (4.4): NVR concentration estimation in ppm	85
Equation (4.5): Predicted particle number concentration in liquid	109
Equation (5.1): Heat transfer heating/Cooling length	122
Equation (5.2): Nusselt number	122
Equation (5.3): Rate of heat transfer	122
Equation (5.4): LMTD	123
Equation (5.5): Heat transfer entrance effect length	123
Equation (5.6): Power fit correlating the number concentration between two CPCs	141
Equation (6.1): N/M ratio	146
Equation (6.2): Coefficient of variation of nvPM mass instruments	166
Equation (6.3): Particle residence time in sample tube	179
Equation (7.1): System loss correction factor (k_{SL})	204
Equation (7.2): Proposed GSD fit	213
Equation (7.3): Proposed average particle effective density fit	213
Equation (7.4): Size-dependent particle effective density derived from the literature	215

List of Notations

Symbol	Units	Description
C_p	J/K	Specific heat capacity
C_c	-	Cunningham slip correction factor
CMD	nm	Centre mean diameter
D	m^2/s	Diffusion coefficient
D_{tube}	M	Tube diameter
d_a	nm	Aerodynamic diameter
d_m	nm	Electrical mobility diameter
d_h	nm	Hydrodynamic diameter
d_p	Nm	Particle diameter
d_{50}	nm	Particle size at which an instrument has 50% counting efficiency
d_{90}	nm	Particle size at which an instrument has 90% counting efficiency
De	-	Dean's number
D_m	-	Mass-mobility exponent
F_{00}	%	Relative thrust
f	-	fanning friction factor
GMD	nm	Geometric mean diameter
GSD	-	Geometric standard deviation
h	$W/(m^2.K)$	Heat transfer coefficient
Kn	-	Knudsen number
k_x	$W/(m.K)$	Thermal conductivity
k_{thermo}	-	Thermophoretic correction factor
k_{SL}	$/cm^3$	System loss correction factor
K	-	Coagulation coefficient
k_B	J/K	Boltzmann constant
K_{th}	-	Thermophoretic coefficient
L_{tube}	m	Tube length
N	$\#/cm^3$	Particle number concentration
N_{EP}	$\#/cm^3$	Particle number concentration at the engine exit plane
Nu	-	Nusselt number
M	$\mu g/m^3$	Particle mass concentration

Q	m^3/s	Volumetric flowrate
Q_a	Lpm	Sample flowrate
Q_{sh}	Lpm	Sheath flowrate
q_c	C	Particle charge
q	J/s	Rate of heat transfer
P	Pa	Pressure
Pr	-	Prandtl Number
R	J/K/mol	Gas constant
R^2	-	Coefficient of determination
Re	-	Reynolds number
R_o	-	Curvature Ratio
Sc	-	Schmidt number
Stk	-	Stokes number
T	K	Temperature
V	m^3	Volume
V_t	m^2/s	Settling velocity
V_{avg}	m/s	Average velocity
Z_p	$\text{m}^2/\text{V/s}$	Electrical mobility
λ	m	Mean free path
ρ	g/cm^3	Density
ρ_{eff}	g/cm^3	Particle effective density
ν	m^2/s	Kinematic viscosity
σ_{STD}	-	Standard deviation
τ	s	Relaxation time
ϵ_0	$\text{C}^2 \cdot \text{s}^2/\text{g}/\text{cm}^3$	Permittivity of air
θ	$^\circ$ or rad	Angle of bend
η_{pen}	%	Particle penetration efficiency
η_g	Pa.s	Dynamic viscosity
$f_{\text{lognormal}}$	-	Lognormal function
f_{loss}	-	Loss penetration function
μ_{avg}	-	Average
M_x	u	Atomic mass

List of Abbreviations

AAC	Aerodynamic Aerosol Classifier	EEP	Engine Exit Plane
AIR	Aerospace Information Report	ELPI	Electrical Low-Pressure Impactor
AFR	Air to Fuel Ratio	EPA	Environmental Protection Agency
APC	Advanced Particle Counter	ET	Evaporation Tube
APU	Auxiliary Power Unit	FOA	First Order Approximation
ARP	Aerospace Recommended Practice	GMD	Geometric Mean Diameter
Au	Gold	GSD	Geometric Standard Deviation
BC	Black Carbon	GTL	Gas To Liquid
CAEP	Committee on Aviation Environmental Protection	H₂O	Water
CH₄	Methane	HC	Hydrocarbon
CO	Carbon monoxide	H/C	Hydrogen to Carbon ratio
CO₂	Carbon dioxide	HEFA	Hydro-processed Esters and Fatty Acids
CPC	Condensation Particle Counter	HEPA	High Efficiency Particulate Air
CV	Coefficient of Variation	ICAO	International Civil Aviation Organization
DEHS	Di-Ethyl-Hexyl-Sebacat	ID	Inner Diameter
DF	Dilution Factor	IARC	International Agency for Research on Cancer
DMA	Differential Mobility Analyser	ISA	International Standard Atmosphere
DMS	Differential Mobility Spectrometer	ITAKA	Initiative Towards sustAinable Kerosene for Aviation
EASA	European Aviation Safety Agency	LII	Laser Induced Incandescence
EC	Elemental Carbon	LMTD	Log Mean Temperature Difference
EI	Emission index	LOSU	Level Of Scientific Understanding
EGT	Exhaust Gas Temperature	Lpm	Litre per minute

LTO	Landing-Take-Off Cycle	RPM	Revolution Per Minute
MSS	Micro Soot Sensor	SAMPLE	Studying, sAmpling and Measuring of aircraft ParticuLate Emissions
NTP	Normal Temperature and pressure	SAE	Society of Automotive Engineers
NaCl	Salt	SiO₂	Silica
NO_x	Oxides of Nitrogen	SLT	System Loss Tool
nvPM	Non-volatile Particulate Matter	SMPS	Scanning Mobility Particle Sizer
NVR	Non-Volatile Residual	SN	Smoke Number
OC	Organic carbon	STD	Standard Deviation
OD	Outer Diameter	STP	Standard Temperature and Pressure
OH	Hydroxyl radical	SS	Stainless Steel
OEM	Original Equipment Manufacturer	TOT	Thermal Optical Transmittance
OPC	Optical Particle Counter	UN	United Nations
PAH	Polycyclic Aromatic Hydrocarbon	UTRC	United Technologies Research Centre
PM	Particulate Matter	VPR	Volatile Particle Remover
PM₁₀	Particulate matter with an aerodynamic diameter $\leq 10\mu\text{m}$	WHO	World Health Organization
PM_{2.5}	Particulate matter with an aerodynamic diameter $\leq 2.5\mu\text{m}$	WHX	Water Heat eXchanger
PMP	Particle Measurement Programme		
PTFE	Polytetrafluoroethylene		
PSL	Polystyrene latex bead		
PSS	Particle Size Selector		
RCF	Relative Centrifugal Force		
RF	Radiative Forcing		
RH	Relative Humidity		
RQL	Rich Quench Lean		

1 Introduction

Aviation is an essential mode of transportation in the modern world, connecting nations, economies and permitting the transportation of goods. The aircraft transport industry has been estimated to provide about twelve million skilled jobs and contribute over 700 billion euros to Europe's economy [1], with a global average annual growth rate of 2% forecast between 2017 and 2040 [2]. The aviation sector is the fastest-growing source of greenhouse gas emissions and accounts for over 2% of global carbon emissions [3] and the International Civil Aviation Organization (ICAO) forecasts that by 2050, they are projected to grow by 300-700% when compared with 2005 [4].

In a globalised world facing growing awareness about climate change, air pollution and increased scarcity of resources, the continuous growth of aviation has led to extensive research and development towards better performance, sustainability and security to reduce its impact on humans and the environment. In 2011, a European commission published the 'Flightpath 2050' report setting out challenging objectives for the aviation industry to achieve by 2050. These include [5]:

- A reduction of 75% in CO₂, 90% in NO_x and 65% in noise per passenger kilometre relative to the year 2000.
- 90% of travellers in Europe able to complete their journey within 4 hours.
- An air traffic management system capable of handling 25 million flights per year.

In addition to the emission of greenhouse gas pollutants from combustion processes, Particulate Matter (PM) has recently become a major concern, both health and environmentally wise.

This chapter aims at providing the reader with an introduction to some fundamental aspects of aircraft PM, including their formation in a gas turbine engine, a discussion on the harmful effects PM on local air quality and the environment, the regulation in place to mitigate aircraft PM emissions and to present the research motivations, aims and objectives of this thesis.

1.1 Overview of gas turbine engines emissions

Like all activities involving combustion, gas turbine engines powering aircrafts emit pollutants into the atmosphere. Pollutants arise from the incomplete combustion of fuel, lubrication oils and the conversion of fuel Sulphur compounds [6]. Modern efficient gas turbines predominantly produce CO₂ and H₂O by burning fuel mixed with air as shown in equation (1.1) representing ideal combustion. Because of the diffusion combustion technology employed, reactions during combustion are locally 'rich' and lead to incomplete combustion. The localised rich zone results in the formation of harmful

gaseous pollutants such as NO_x and CO coupled with unburnt hydrocarbon exiting the primary combustion zone resulting in the formation of other pollutants including PM (predominantly soot), as highlighted in **Figure 1-1**. Gas turbine PM exhaust is a polydisperse mixture of volatiles and non-volatile, liquid and solid particles in a hot and highly turbulent flow.

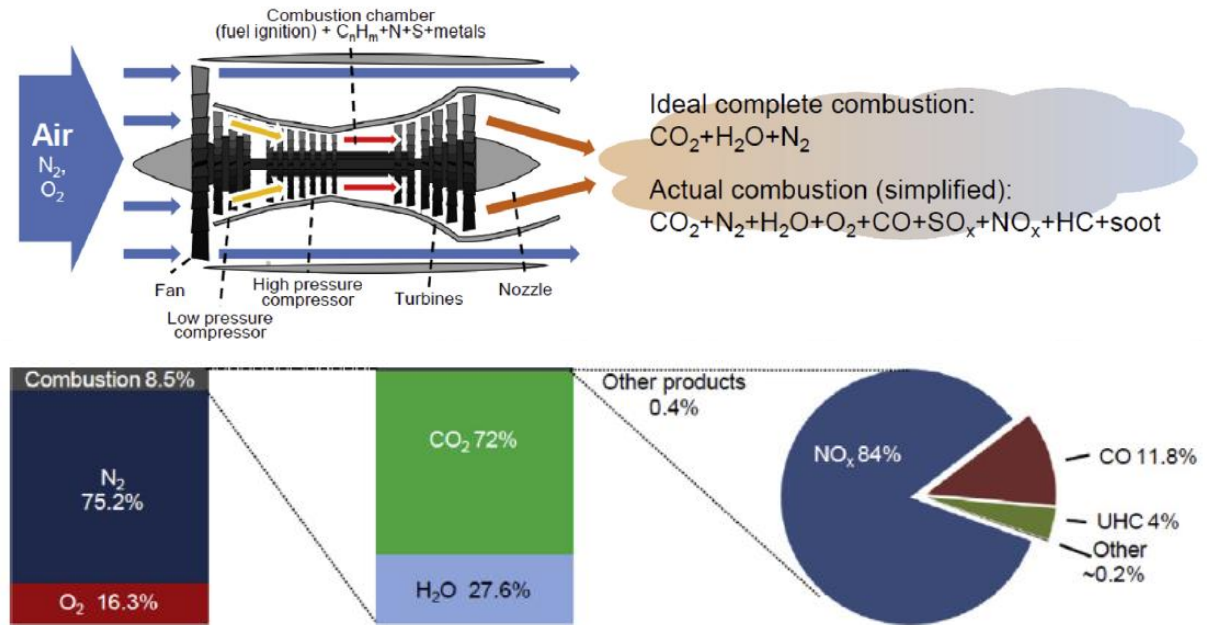
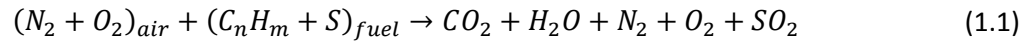


Figure 1-1: Simplified Schematic of an aircraft turbofan engine with the division of the combustion products [7]

Harmful engine emissions vary with the type of combustion governed by the Air-to-Fuel Ratio (AFR), as highlighted in **Figure 1-2**. When the AFR is low, **rich combustion** occurs leading to the production of solid carbon and emissions of unburnt hydrocarbons, CO and soot. **Stoichiometric combustion** happens when just enough air is provided to burn all the fuel, generating high quantities of NO_x. **Lean combustion** occurs when a large quantity of air is mixed with the fuel (high AFR).

It is noted that most of the current commercial aircraft fleet is composed of gas turbine engines that use Rich-Quench-Lean combustor technology due to its potential to go from rich burning to lean burning without producing a lot of NO_x.

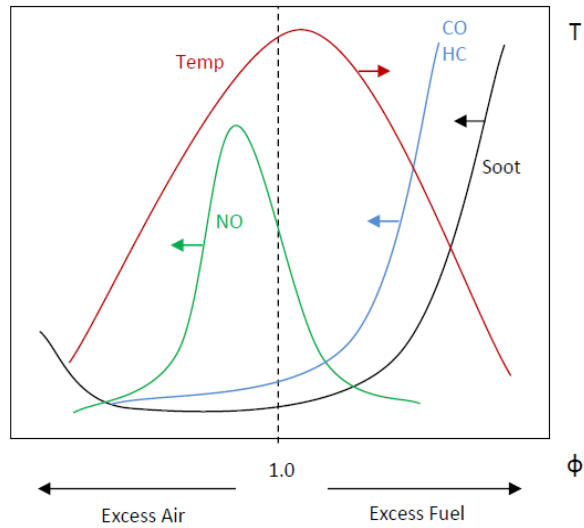


Figure 1-2: Illustration of the typical temperature and pollutant formation rates resulting from changes in AFR for gas turbine combustors [8]

1.2 Particulate Matter

Particulate Matter (PM) is the name given to a mixture of solid and liquid particles (i.e. extremely small constituents of matter) which are held in suspension in a gas (i.e. aerosol). The term aerosol refers to a suspension of solid or liquid in a gaseous medium. Particles are found everywhere in our atmosphere in the form of dust, salt, pollen, smoke, soot, etc. PM size can vary from a few nanometres in diameter to about 100 micrometres, and is generally classified into different categories according to their size as presented on **Table 1-1** and illustrated in **Figure 1-3**.

Table 1-1: Particle classification according to their size

Particle Type	Aerodynamic diameter	Equivalent size
Coarse Particles	> 10 μm	Hair, fine beach sand
PM ₁₀	2.5 μm – 10 μm	Bacteria
PM _{2.5}	1 nm - 2.5 μm	Viruses, Tabaco smoke
Ultrafine Particles	< 100 nm	Combustion soot

PM can be created naturally (e.g. salt crystals) developing by the sea or volcanic eruptions and forest fires producing fine ash particulate). It can also be produced in combustion processes like in aircraft gas turbine engines, with aircraft PM sizes typically below 100 nm [9]. Although typically referred as to soot, aircraft PM is a poly-disperse mixture of highly concentrated particles, whose properties and concentrations mostly depend on engine technology, power setting and fuel [10].

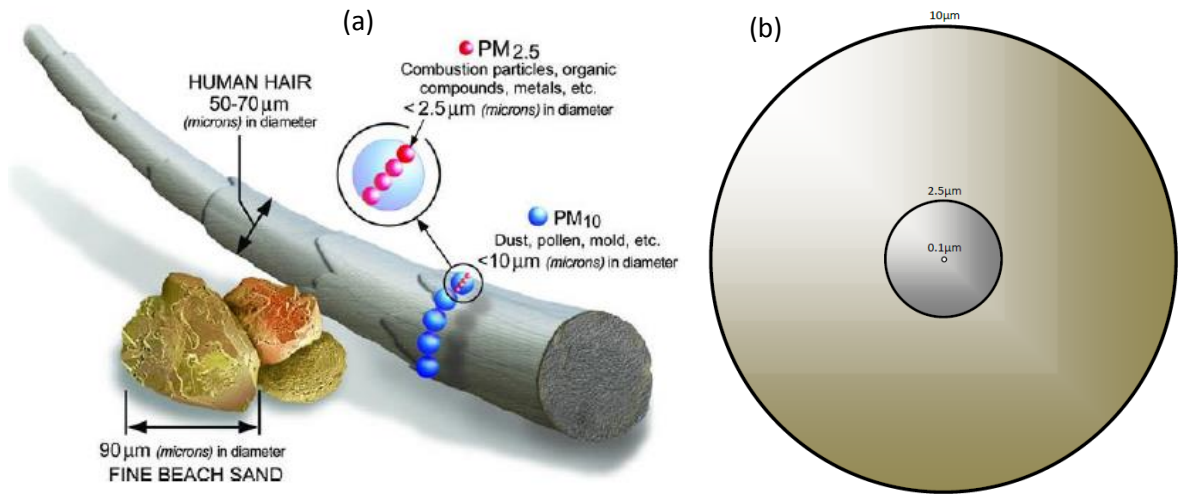


Figure 1-3: Illustration of PM size in comparison to human air (a) and visual representation of major particle sizes used for classification of PM (b) [8]

PM is generally comprised of a mixture of elements that can be complex to define. In the literature, PM component classification and terminology varies depending on the particle property (physical, optical, chemical) being measured [11]. Typical aircraft PM components are:

- **Solid carbonaceous matter (soot, BC, EC):** Carbonaceous particles that are produced during high temperature combustion and generally make up the largest fraction of total aircraft PM emitted [12]. Usually referred to as soot, they can differ in names and definitions and are discussed in the literature [11], [13]. Black Carbon (**BC**) refers to a measure of airborne soot-like carbon using light absorbing refractory methods. It is produced by incomplete combustion and has a graphitic-like microstructure. Elemental Carbon (**EC**) refers to a measure of soot-like carbon determined by thermo-optical methods that is not removed from a filter sample heated to 870°C in an inert atmosphere [14].
- **Organic Carbonaceous matter (OC):** Carbon in the form of organic matter that has chemically combined with hydrogen and other elements [11]. Organic Carbon (**OC**) refers to a measure of oxidised carbon determined by thermo-optical methods when heated on a quartz fibre filter sample at 870°C in Helium gas [14].
- **Non-carbonaceous volatile matter:** Defined as particles that remain in a gas phase when exiting the engine (350°C). They are typically made of Nitrates, Sulphates and Ammonia formed by the oxidation of NO_x and SO₂ in the fuel. They also include unburnt hydrocarbons (HC) caused by the incomplete combustion of the fuel and lubrication oils [6], [15]. Due to their low volatility, volatile matter can condense onto solid particles when the aerosol is cooled in the atmosphere, contributing to particle growth. They can also directly condense to form new nuclei.

- **Trace metals:** Formed by impurities or additives found in fuels. Metals are also formed by mechanical abrasion processes.

For regulatory purposes, combustion particles are normally divided in two categories namely non-volatile PM (nvPM) and total PM. NvPM is defined by ICAO civil aviation regulation [14] as particles exiting a gas turbine exhaust and that do not volatilise when heated to a temperature of 350°C and consisting essentially of soot. Total PM refers to all emitted particles including nvPM and volatile PM.

1.3 Soot formation in a gas turbine engine

Soot (i.e. Non-volatile carbonaceous PM) formation in combustion engines involves very complex and stochastic processes [16], [17]. In the flame of a gas turbine combustor, organic compounds within the fuel are broken down to molecular level, forming PAH/Hydrocarbons precursors (pyrolysis) [18]. The precursors then undergo transformation via dehydrogenation and aggregation leading to the formation of a solid nuclei (inception/nucleation). The highly concentrated solid nuclei grow by colliding with each other to form larger aggregates and with supersaturated vapours condensing onto the solid nuclei (surface growth/agglomeration). Downstream of the flame, soot aggregates are consumed by oxidation (mainly by OH radicals) while hydrocarbons are converted into gases (CO, CO₂, H₂O, etc) as added air is mixed with the fuel increasing the AFR. The rate of soot formation depends on several factors including the AFR, combustion temperature, fuel type, pressure, fuel atomisation, ambient conditions and combustor design [19], [20].

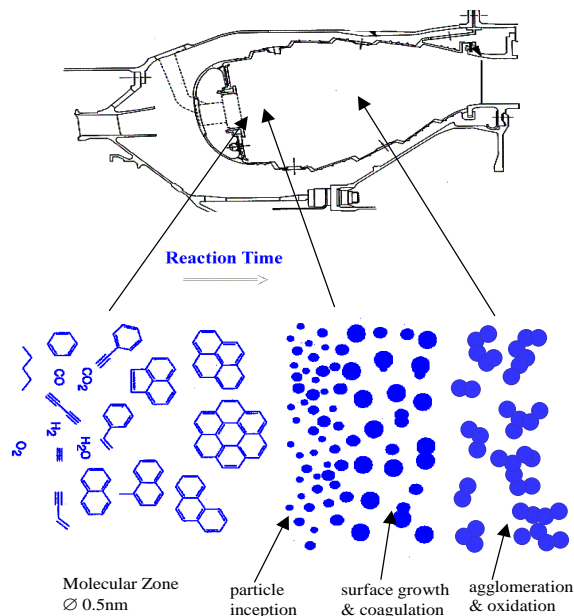


Figure 1-4: Diagram of the particle formation process in a gas turbine combustor

1.4 Health and environmental impact of aircraft PM

PM emissions from aircraft engines have a significant impact on both local and global air pollution and are a growing source of concern on health and the environment. The aircraft industry is the only anthropogenic source of emissions in the upper atmosphere at cruising altitudes and is linked to the deterioration of air quality and health hazards with large concentration of nanoparticles < 100 nm [21] in the vicinity of airports. PM in the lower atmosphere can also degrade visibility. A summary diagram of the impact of aircraft exhaust products on human health and the environment is displayed in **Figure 1-5** with a more detailed discussion found below.

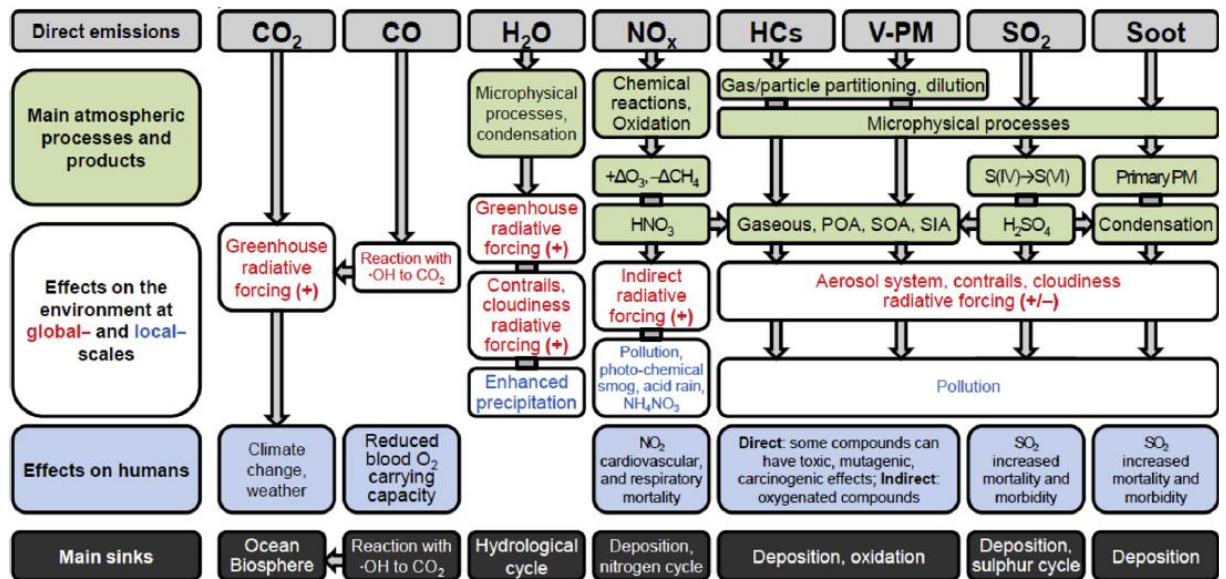


Figure 1-5: Simplified diagram of the exhaust products from a gas turbine engines with the environmental effects and human health effects of emitted compounds [7]

1.4.1 Health

The human body is constantly exposed to particles which are inhaled and can deposited in the body. The determination of aerosol deposition in the airways and removal in the body are essential mechanisms to assess the extent of consequent harmful effects. As highlighted in **Figure 1-6**, particles between 10-100 nm (typical of aircraft PM) mostly deposit into the Alveolar region of the lungs where gas exchanges with the blood take place [22]. Inhaled particles of different sizes tend to deposit in higher regions of the respiratory system either via inertial deposition (>100 nm) or by diffusion (<10 nm) in the small airways as discussed in section 2.3. Deposited ultrafine particles can induce oxidative stress leading to inflammation [23]. Particle toxicity effects not only depend on the mass deposited but also on the morphology and composition of the particle [24].

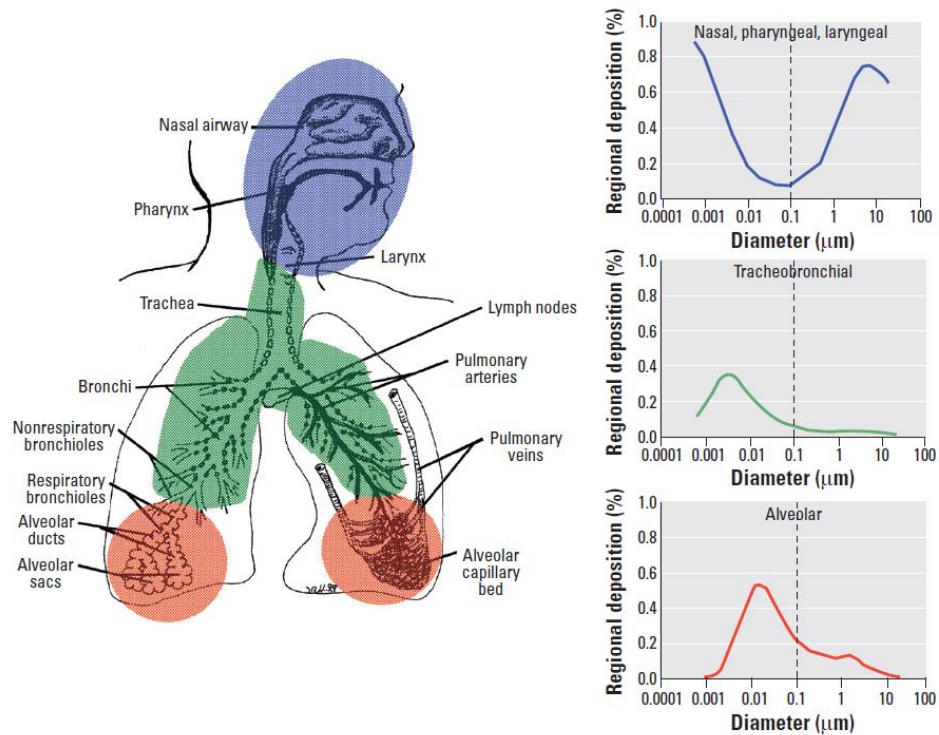


Figure 1-6: Predicted deposition efficiency of inhaled particles in different regions of the respiratory system [25]

PM_{2.5} has been associated with cardiovascular and respiratory disease as well as increased rate of lung cancer, with higher risks for susceptible groups such as children, elderly people and those with pre-existing lung or heart disease [26]–[29]. The World Health Organisation (WHO) estimated global premature deaths associated with air pollution to be 4.2 million per year in 2016, with mortality directly linked to small Particulate Matter (PM_{2.5}) [30]. Amongst those, aviation emissions were estimated to cause around 16,000 premature deaths per year and cost \$21 billion per year [26]. The International Agency for Research on Cancer (IARC) and WHO designated airborne particulates a Group 1 carcinogen. The WHO also estimated PM to be responsible for approximately 3% of cardiopulmonary and 5% of lung cancer deaths globally [27].

Although a large body of literature can be found on combustion generated aerosol from automotive engines linked to adverse health effect, the impact of newly regulated aircraft nvPM metrics (section 1.5) on health has not been clearly established yet [31]. Aircraft PM is generally smaller than PM observed in road traffic exhaust and hence supposedly more toxic as they penetrate through the respiratory tract more efficiently and have a larger surface area [25]. In one of the first studies directly utilising aircraft PM emissions, Jonsdottir et al. [31] showed that exposure to aircraft nvPM impaired bronchial epithelial cells and emissions at ground-idle conditions were the most hazardous due to higher nvPM reactivity. Also, carbonaceous nano-particles can enhance the formation of clots in the blood, provoking strokes and heart attacks [32]–[34]. In addition to the regulated nvPM, aircraft engines produce carcinogenic PAHs (Polycyclic Aromatic Compounds) [35].

As of 2015, the European Union imposed maximum yearly average exposure concentration obligations of $25 \mu\text{g}/\text{m}^3$ for $\text{PM}_{2.5}$. [36]. Similarly, The World Health Organization set guidelines of $10 \mu\text{g}/\text{m}^3$ for the annual average and $25 \mu\text{g}/\text{m}^3$ for the 24-hour mean in 2005 based on evidence of the adverse health effect [27].

1.4.2 Environment

The global effect of aerosols on climate change is still ambiguous with different anthropogenic aerosols shown to have positive and negative effects on the radiative balance as highlighted in **Figure 1-7**. The term Radiative Forcing (RF) is used to describe the environmental impact of exhaust constituent by either a warming (positive forcing) and cooling (negative forcing) effect. Aerosol particles interact with solar radiation through absorption and scattering and, to a lesser extent with terrestrial radiation through absorption, scattering and emission with some contributing to warming and other to cooling the atmosphere. Black Carbon (BC) found in soot produced by gas turbine engines is a positive contributor to global warming and is the main concern with the emission of PM from aircraft in the upper atmosphere. They can also serve as cloud condensation nuclei (CCN) and ice nuclei (IN) upon which cloud droplets and ice crystals form.

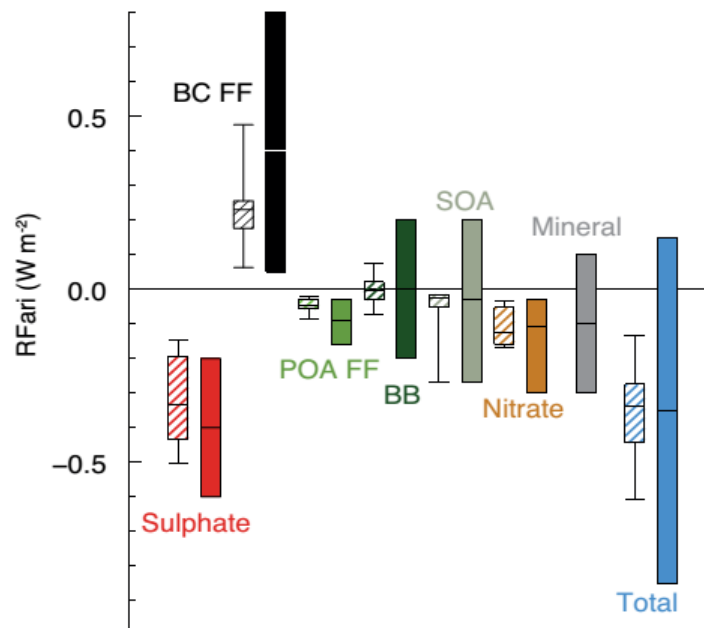


Figure 1-7: Annual mean of the atmosphere radiative forces from anthropogenic aerosol radiations interactions for the 1750-2010 period (*whiskers represent results from the AeroCom II model and solid coloured boxes present AR5 model estimates – BB stands for Biomass Burning aerosol while POA and SOA respectively stand for primary and secondary organic aerosols*) [37]

Specific exhaust emissions from aircraft engines affect the atmosphere in many ways as presented in **Figure 1-8**, with the net total contribution of aviation Radiative forcing estimated at +50

mW/m^2 . These include the direct emission in the atmosphere of CO_2 contributing to the greenhouse effect, NO_x adding to the ozone depletion and sulphur causing acid rains. In addition to gases, aircraft engines emit PM which can both scatter and absorb incoming solar radiation and indirectly interacting with radiation and cloud formation [38]. It is illustrated that PM has a relatively low impact when compared with other influencing factors like carbon dioxide. However, the potential impact of PM induced cirrus cloudiness is relatively high although the currently low level of scientific understanding (LOSU) makes the predictions highly uncertain. It was demonstrated that by reducing soot number emission, initial ice crystal numbers are reduced, leading to a reduction in the contrail cirrus lifetimes and coverage, hence reducing the contribution of aviation towards climate change [39], [40]. It is noted that the aerosol-cloud interaction is complex and remains poorly understood [41].

The composition and morphology of the exhaust aerosol can determine its impact in the upper atmosphere. Freshly generated soot mostly consists of hydrophobic spherical primary carbonaceous particles forming fractal aggregates (defined in section 2.1). However, when ageing in the atmosphere, volatile matter can condense onto the soot, increasing their hygroscopicity and, consequently, their ability to act as a cloud condensation nucleus [42]. Exposure to high humidity was also found to increase light scattering and absorption of soot particles [42].

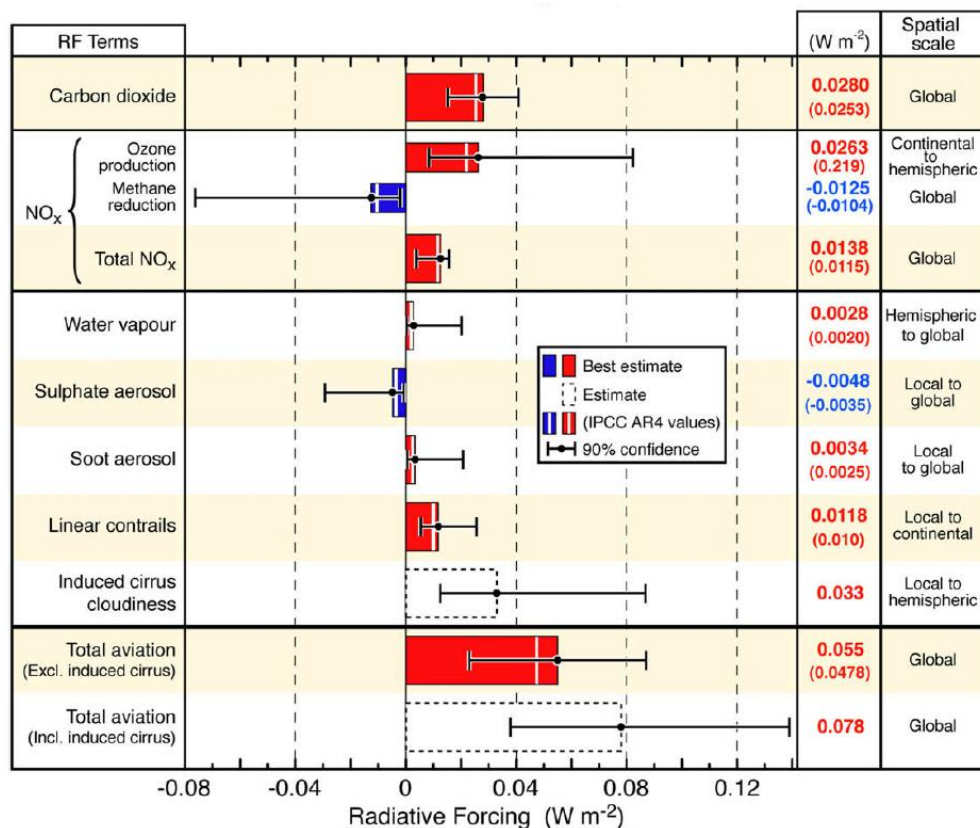


Figure 1-8: Radiative forcing components from global aviation from pre-industrial times until 2005

[43]

1.5 Aircraft PM regulation

The International Civil Aviation Organization (ICAO) is a UN specialized agency comprising 193 member states and is responsible for establishing aircraft emission regulations. It aims to achieve maximum compatibility between the development of civil aviation and human welfare by accounting for the adverse environmental and health impacts related to aircraft activity [44]. A technical committee known as the Committee on Aviation Environmental Protection (CAEP) was established by ICAO to develop International Standards and new policies for aircraft engine emissions and improving the outdated First Order Approximation (FOA) methodology to regulate PM emissions. CAEP requested that the SAE E-31 committee, a broad consortium including academics, aircraft engine manufacturers and government agencies, lead with the development of a new sampling and measurement methodology for nvPM. The development of this new methodology was constructed using results of multiple aircraft engine testing and experimental work available in the SAMPLE reports [45]–[50] and other North American (EPA) and Swiss (A-PRIDE [51]) funded programmes. The current legislation and recommended practices for aircraft smoke and gaseous emissions can be found in Volume II of Annex 16 (Environmental protection) to the Convention on International Civil Aviation [14]. Aerospace information reports (AIR 6241 [52]) and recommended practises (ARP 6320 [53]) describing methodologies for the measurement of nvPM emissions sampled at the exit plane of aircraft gas turbine engines are also available.

Since its creation in 1981, several amendments were made to Annex 16 increasing stringency on harmful emissions limits and improving smoke and gaseous emissions (CO_x , HC, CO, NO_x) certification procedures. The exhaust of a gas turbine engine is a hostile environment making aircraft PM measurement difficult. The exhaust aerosol must be diluted, cooled and conditioned before being transported and analysed by instruments. The required sampling system coupled with the small GMD of nvPM witnessed from gas turbines results in significant particle loss before measurement at the calibrated analysers, making it necessary to standardise the sampling system as far as practically possible to permit reporting of aircraft nvPM.

Until recently, standardised sampling techniques to measure aircraft nvPM did not exist. Instead, a FOA methodology was used determining the level of smoke from an engine exhaust based on the measurement of the decrease in reflectance of a paper filter following exposure to the exhaust PM [54], [55]. However, the smoke technique adopted in ICAO regulation in 1981 gives little or no indication of PM size, number or mass, and modern engines emit particle so small they are barely visible on a filter. Therefore, the Smoke Number (SN) is due to be retired in 2023 and replaced by a new PM metric sensitive to particle size which is thought to be a major factor in PM health effect.

After the tenth meeting of CAEP in 2016, nvPM sampling and measurement standards were first introduced for all turbofan and turbojet engines (subsonic propulsion) with rated thrust greater

than 26.7 kN and manufactured from 1 January 2020 [14], [56]. The standardised sampling system for the transport, acquisition and analysis of representative turbine engine nvPM exhaust is described in Appendix 7 of Annex 16 [14]. The current legislation for aircraft engine emission reporting requires that nvPM Emission Indices (EI's) are obtained from measured nvPM number and mass concentrations for each LTO operating mode (i.e. thrust) using a certified sampling system following ICAO guidelines as discussed below. It is noted that only nvPM is regulated due to the complexity of volatile particles evolution when being sampled and the difficulty to repeatably measure them.

1.5.1.1 LTO cycle

ICAO recommends the Landing-Take-Off (LTO) cycle to report harmful gaseous and particulate emissions of aircraft engines. The LTO cycle consists of different operating modes representative of aircraft activity near airports as described in **Figure 1-9**. It does not account for emission beyond and altitude of 3000 feet (914 metres) due to the sampling difficulty associated with taking in-flight samples. The LTO cycle is solely based on engine performance and does not take into account any of the airframe factors. Engine are tested at multiple thrust settings based on the rated thrust (F_{00}), which is defined as the maximum take-off thrust approved by the certifying authority for use under normal operating conditions at International Standard atmospheric (ISA) sea level conditions, and without the use of water injection [14]. As illustrated in **Figure 1-9**, thrust settings are varied from 7% F_{00} representing taxiing, 30% F_{00} for landing approach, 85% F_{00} for climb out to 100% F_{00} for take-off.

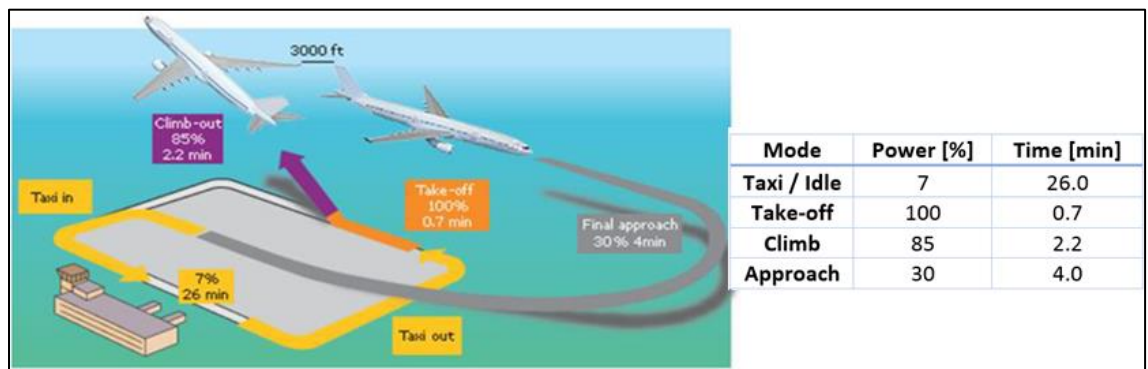


Figure 1-9: LTO cycle with time and power setting for each mode

1.5.1.2 Emission indices calculations (EIs)

Particulate Emission Indices (EI) as defined in ICAO annex 16 [14], represent the number and mass of aircraft engine exhaust particles per unit of hydrocarbon fuel mass used. It is a metric designed to compare engine emission performance independently of the engine and is defined as:

$$EI_{nvPM} = \frac{nvPM \text{ in exhaust}}{\text{Mass of fuel used}} = \frac{nvPM_{num/mass}}{([\text{CO}_2] + [\text{CO}] - T + x[\text{C}_x\text{H}_y] - U)(M_c + \alpha M_H)} \times \frac{0.082T}{P} \quad (1.2)$$

with the nvPM number or mass, 0.082 the gas constant in [L.atm.K⁻¹.mol⁻¹], T and P the temperature and pressure at which the nvPM measurements were made, $([X])$ the molar quantities of combustion exhaust gas, $M_c=12.011$ [u] and $M_H=1.008$ [u] the atomic mass of carbon and hydrogen, and α the Hydrogen-to-Carbon (H/C) ratio in the fuel. It is noted that engine performance should be reported at ISA reference atmospheric conditions at sea level and that the reference absolute humidity shall be 0.00634 kg_{water}/kg_{dry air}.

To predict EIs values independently of the engine exit plane temperature, nvPM EIs are required to be corrected for dilution in the sampling system and thermophoretic loss in the collection section (**Figure 3-1**). It is noted that although EIs are corrected for thermophoretic losses, other losses in the sampling and measurement system are not included in the correction and hence EIs are not currently reported at the engine exit plane.

The simplified EIs expressions used in this thesis and presented below with equations **(1.3)** and **(1.4)** use the following assumptions (note that a more detailed explanation of EI calculations and simplifications is available in the AIR 6241 [52]):

- All the fuel's carbon is converted to CO₂. Indeed, given the combustion efficiency of modern aircraft engines is >95% [14], $[\text{CO}_2] \approx ([\text{CO}_2] + [\text{CO}] - T + x[\text{C}_x\text{H}_y] - U)$.
- The CO₂ at the engine exit plane is expressed as $[\text{CO}_2] = [\text{CO}_{2\text{dil}}] \times DF_1$ with $[\text{CO}_{2\text{dil}}]$ the CO₂ measured after the first dilution stage of the sampling system and DF_1 the primary dilution.
- EIs are expressed at Standard Temperature and Pressure (STP) of 0°C and 101.325 kPa, respectively. Correcting nvPM emissions to STP is critical as nvPM concentrations are measured per volume, hence the volume needs to be defined at the same temperature and pressure.

The final simplified emission indices equations for nvPM number and mass emissions are:

$$EI_{num} = \frac{22.4 \times (nvPM_{num-STP} \times DF_2 \times 10^6)}{[\text{CO}_{2\text{dil}}](12.011 + \alpha \times 1.008)} \times k_{thermo} \quad [\#/kg_{fuel}] \quad (1.3)$$

$$EI_{mass} = \frac{22.4 \times (nvPM_{mass-STP})}{[\text{CO}_{2\text{dil}}](12.011 + \alpha \times 1.008)} \times k_{thermo} \quad [mg/kg_{fuel}] \quad (1.4)$$

with $nvPM_{num-STP} \times DF_2$ the STP corrected measured nvPM number concentration in [particles/cm³], $nvPM_{mass-STP}$ the STP corrected measured nvPM mass concentration [mg/m³], CO_{2dil} the CO₂ measured after the first dilution stage in [ppm], 22.4 the gas constant combined with the standard temperature (i.e. $0.082 \times 273.15 = 22.4$), α the H/C ratio in the fuel, and k_{thermo} the empirically derived thermophoretic loss correction factor in the collection section defined in equation (1.5) below and discussed in more details in section 2.3.1.4:

$$k_{thermo} = \left(\frac{T_1 + 273.15}{T_{EGT} + 273.15} \right)^{-0.38} \quad (1.5)$$

with T_1 the temperature at the outlet of the collection section and T_{EGT} the temperature at the engine exit plane entering the sample probe [14].

1.5.1.3 PM reporting

Currently, aircraft gas turbine engines are regulated for gaseous emissions and particulate via SN measurements. Engine certification data for gaseous and smoke emissions can be found in the ICAO emission databank but does not include nvPM data. While nvPM number and mass emissions are not regulated for current engines, their reporting is required for inventory and modelling purposes to help with future regulation, with number and mass nvPM emission indices (EIs) required to be reported at each thrust setting of the LTO cycle. First nvPM regulatory limits will apply to engines manufactured after 2020 which shall not exceed a nvPM mass concentration of $10^{(3+2.9F_{oo}^{-0.274})}$ with F_{oo} the rated thrust and the maximum nvPM mass concentration being defined as:

$$nvPM_{mass} = DF_1 \times nvPM_{Mass-STP} \times k_{thermo} \quad (1.6)$$

with $nvPM_{mass-STP}$ the measured mass concentration in [$\mu\text{g}/\text{m}^3$] corrected at STP conditions, DF_1 the primary dilution factor and k_{thermo} the thermophoretic correction factor defined in equation (1.5).

During CAEP 11 in February 2019, new standards for nvPM number and mass were agreed and are expected to replace the existing SN requirement by 2023. The standardised sampling system and loss correction methodology will lead to better estimations of aircraft nvPM emission and will permit a better assessment of nvPM impact on local air quality and the environment by correcting measured nvPM emissions for losses in the standardised sampling system as described in Appendix 8 of Annex 16 [14].

It is noted that due to aircraft nvPM having a complex morphology as discussed in section 2.1 and there currently being no traceable aerosol at sizes and morphologies typical of aircraft

engines as well as issues with particle size instrument data inversion robustness and time response, only nvPM number and mass are currently anticipated to be measured and regulated. Nevertheless, as discussed in this thesis, size information is required to determine losses in the sampling system [52], hence a mean diameter is currently estimated from nvPM number and mass information as prescribed in appendix 8 of Annex 16 [14].

1.6 Research motivations and thesis structure

Aircraft PM emissions have been demonstrated in the scientific literature to generally negatively contribute to human health and global climate change. New ICAO regulations introduced the use of a standardised sampling and measurement methodology to determine nvPM number and mass concentrations. However, across the typical particle size range of civil aviation gas turbines, losses have been anticipated to be as high as 90% for number and 50% for mass in a standard sampling system [14], [57] and EI's are currently not reported at engine exit plane. A System Loss Tool (SLT) has recently been proposed by the SAE E-31 committee to correct for losses in the sampling and measurement system.

The main motivation for this research is to quantify uncertainties and identify potential improvements to the ICAO prescribed methodology for sampling, measuring and reporting of aircraft nvPM to permit the accurate reporting of nvPM concentrations at the engine exit plane for modelling and regulatory purposes. More specifically, it was aimed to assess the theory and assumptions currently used in the ICAO and system loss correction methodology and demonstrate the potential advantages of an additional size measurement for future regulation. Experimental characterisation of particle loss occurring during the transport in a compliant sampling system was undertaken. These objectives were achieved by experimentally characterising particle loss in the main sections of the sampling and measurement system and analysing PM emission data taken with an ICAO compliant sampling system during several certification level large-scale engine tests. Results gained from this thesis will help further the development of improved aircraft nvPM sampling, measurement and corrections methodologies.

The EU/EASA mobile reference system, referred in this thesis as the EASA reference system, designed in compliance with ICAO Annex 16 appendix 7 was used during multiple aircraft engine certification testing to report on gaseous and nvPM emissions. Furthermore, specific components of the EASA reference system were experimentally investigated including the 25 m sample line, diluter, volatile particle remover (VPR) and nvPM analysers.

In order to achieve the previously described aims, this thesis was structured in eight chapters, with Chapter 2 introducing some fundamentals of aircraft PM, particle deposition mechanisms and the nvPM loss correction methodology. Chapter 3 describes the instrumentation used to measure

PM including a list of all the facilities and PM sources used. Chapter 4-7 discuss the main results of this research, namely:

- Chapter 4 investigates various particle generation, characterisation techniques and capture processes for different particle types to select an optimised system for the laboratory particle loss experimentation.
- Chapter 5 experimentally assesses in laboratory particle loss experiments theory, assumptions and particle deposition mechanisms prescribed in aircraft nvPM sampling, measurement and loss correction methodology.
- Chapter 6 investigates large-scale engine PM emission data to derive new trends and determine the uncertainty associated with the current nvPM sampling and measurement methodology. It presents PM emissions from multiple Rolls-Royce aircraft gas turbine engine types taken during certification level testing. An allowed performance uncertainty analysis is also performed on the currently prescribed ICAO compliant nvPM sampling and measurement system, along with a discussion on the effect of fuel type and ambient conditions on nvPM emissions.
- Chapter 7 assesses the additional uncertainty associated with the new system loss tool correction methodology by evaluating the currently required lognormal, geometric standard deviation (GSD) and particle density assumptions. The advantages of additional particle size measurement for system loss correction is also reviewed.
- Chapter 8 discusses the main findings from this research, including recommendations for the reduction of uncertainties associated with aircraft nvPM reporting and proposed future works.

2 Aircraft PM – Properties, Measurement and Sampling

Aircraft nvPM can be expressed in terms of number, mass and size. As discussed previously, only nvPM number and mass are prescribed in the current ICAO regulation and are measured after a long sampling system which cools, dilutes and conditions the exhaust aerosol. To report emitted nvPM, losses within the sampling system need to be accounted-for. However, because of the size-dependent nature of some loss mechanisms (section 2.3), the correction of nvPM number and mass concentration is problematic without a specific measurement of size and the knowledge of the particle morphology. To resolve this issue without a size measurement, a ‘System Loss Tool’ (SLT) was designed by the SAE E-31 committee to determine system loss correction factor from measured nvPM number and mass concentration only.

This chapter provides the reader with fundamentals of aircraft nvPM properties discussed throughout this thesis and necessary for understanding the challenges associated with aircraft nvPM sampling and measurement. They include particle size, effective density and deposition mechanisms when being sampled. The SLT model determining the nvPM sampling and measurement system loss correction factors as per ICAO annex 16 appendix 8 guidelines is also introduced and discussed. A review of the available literature that has reported on aircraft engine nvPM emission is also presented.

2.1 Particle size and size distribution statistic

2.1.1 Particle size

Particle size is a crucial parameter that determines the particle’s behaviour in an aerosol and hence how likely it is to deposit in a sampling system or in the respiratory system. Size is generally described with the particle diameter (d_p). Due to the challenges with measuring the physical diameter of nanoparticles, an equivalent diameter is usually measured. An equivalent diameter is defined as the diameter of a sphere having the same value of a specific physical property as the particle in consideration. Many equivalent diameters exist, amongst which the aerodynamic equivalent diameter, the hydrodynamic diameter and the electrical mobility diameter are used in the scope of this thesis and defined below:

- Aerodynamic diameter (d_a): Diameter of a standard-density sphere (i.e. 1 g/cm³) having the same terminal velocity when settling under gravity as the investigated particle.

- Electrical mobility diameter(d_m): Often called mobility diameter, it is the diameter of a spherical particle having the same electrical mobility when an electrical field is applied as the investigated particle.
- Hydrodynamic diameter(d_h): Diameter of a hard sphere that diffuses at the same speed as the particle being measured.

Particle diameter is unambiguous for spherical particles but is more challenging to define for non-spherical particles like aircraft nvPM which are composed of multiple small particles clustered together producing irregular shapes as highlighted in **Figure 2-1**. Aircraft nvPM particles are generally described as fractal aggregates which refers to a group of particles with a similar structure over a finite range of length scales, with the particles composing the aggregate referred as primary particles [58]. The diameter of soot nanoparticles may strongly differ when reported in different equivalent diameters and particles of the same equivalent diameter may look completely different.

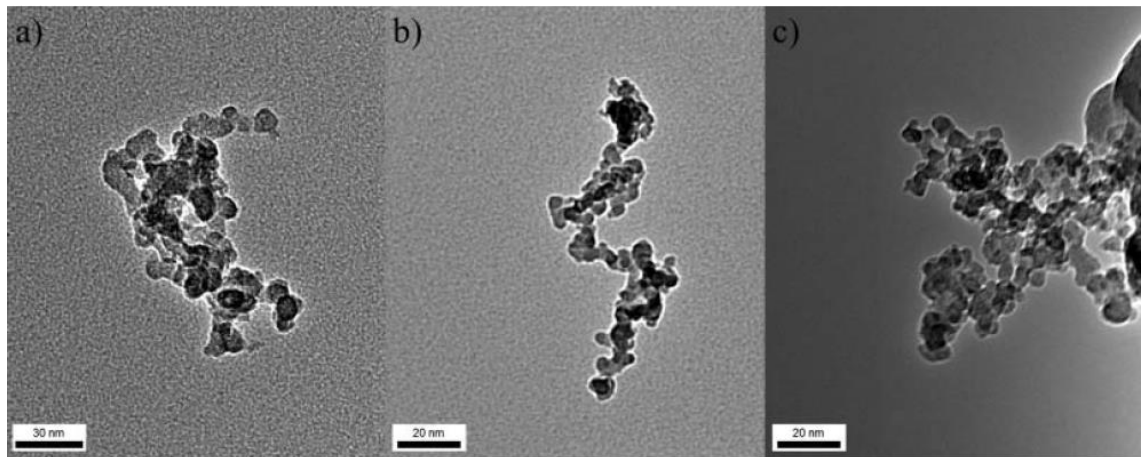


Figure 2-1: TEM image of 15 nm ((a) and (b)) and 50 nm (c) mobility-selected soot aggregates emitted from a CFM56-5B4-2P aircraft engine [20]

For example, a 15 nm mobility diameter particle may be 100 nm long and 5 nm wide, equating to a different aerodynamic diameter. Similarly, two 15 nm mobility diameter particles can have different morphologies (**Figure 2-1 (a) and (b)**). The fractal nature of aircraft nvPM and the lack of traceability currently make particle size regulation impossible and expose that it is critical to compare particle size using the same metric.

When attempting to compare equivalent diameters, it is necessary to correct them appropriately and generally requires the assumption of particle sphericity. For example, assuming sphericity, the mobility diameter is related to the aerodynamic diameter by the following expression:

$$\rho_p \times d_m^2 \times Cc(d_m) = \rho_o \times d_a^2 \times Cc(d_a) \quad (2.1)$$

where C_c is the Cunningham slip correction factor (equation (2.14)), ρ_0 is the unit density (1 g/cm^3) and ρ_p is the particle density.

2.1.2 Size distribution and lognormal statistic

Most aerosols in nature are polydisperse and have particle sizes that range over two or more orders of magnitude. This has been regularly observed for aircraft engine nvPM emissions with distributions with a finite width in the nanometre range [59]. In fact, most particle formation mechanisms like gas turbine combustion are stochastic processes generating skewed distributions with long tails to the larger sizes, that are generally described with a lognormal distribution [60, p. 90]. Although no fundamental reasons were found as for why particle size distributions should approximate the lognormal distribution, it has been found to apply to most single-source aerosols and its mathematical form is convenient to describe aerosols.

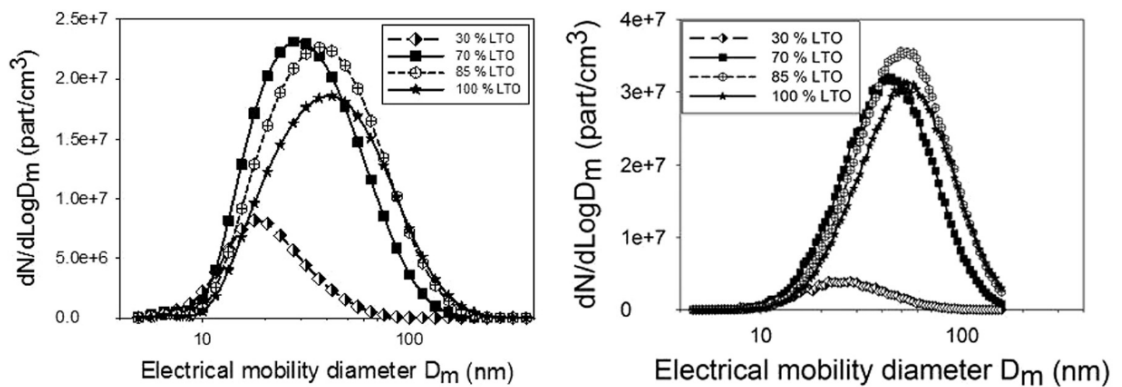


Figure 2-2: Example of typical measured aircraft PM particle size distribution as a function of engine thrust [61]

Given the importance of size in predicting particle loss in the sampling system, it is necessary to characterise particle size distributions by statistical means. This section describes lognormal distribution statistics and equations defined by Hinds [60] and Baron et al. [62] used throughout this thesis to characterise nanoparticle size distributions.

Commonly used quantities for defining the location of a distribution are the mean, mode, and median:

- The **mean**, or arithmetic average is simply the sum of all the particle sizes divided by the number of particles ($\bar{d}_p = (\sum n_i \times d_i) / \sum n_i$).
- The **median (CMD)** is the diameter for which one-half the total number of particles are smaller and one-half are larger, also referred to as CMD (count median diameter). It is also the diameter that divides the frequency distribution curve into equal areas, and the diameter corresponding to a cumulative fraction of 0.5.

- The **mode** is the size which has the highest number concentration.

For normal or symmetrical distributions like the lognormal distribution, the mean, median and mode will have the same value but for a skewed distribution, their values differ. Because in a lognormal distribution, the logarithm of d_p is normally distributed, the arithmetic mean, and standard deviation are defined with their logarithmic counterpart.

In a lognormal distribution, the mean is called **geometric mean (GMD)** with $GMD = (\sum n_i \times \log(d_i)) / \sum n_i$ and is the N^{th} root of the product of N values. The size axis is logarithmically spaced and therefore the concentration size spectrum is expressed in $dN/d\log Dp$. The GMD can be calculated as followed:

$$GMD = 10^{\left[\frac{\int [\log d_p \cdot dN/d\log d_p] d\log d_p}{N} \right]} \quad (2.2)$$

with d_p the particle diameter and N the total number of particles defined as the area under the distribution graph and is calculated as followed:

$$N = \int_{\log d_{p_{min}}}^{\log d_{p_{max}}} \left[\frac{dN}{d\log d_p} \right] d\log d_p \quad (2.3)$$

Furthermore, the geometric standard deviation (GSD), a dimensionless quantity representing the width of the distribution, can be derived from N and the GMD as followed:

$$GSD = \left(\frac{d_{84\%}}{d_{16\%}} \right)^{\frac{1}{2}} = 10^{\left[\frac{\int [(\log d_p)^2 \cdot dN/d\log d_p] d\log d_p - (\log GMD)^2}{N} \right]} \quad (2.4)$$

Therefore, the size distribution of a lognormal particle size distribution at the exhaust of an aircraft engine can be expressed as:

$$\frac{\Delta N(d_p)}{\Delta \ln(d_p)} = \frac{N_{EP}}{\sqrt{2\pi} \ln(GSD)} \times e^{-\frac{1}{2} \left(\frac{\ln(d_p) - \ln(GMD)}{\ln(GSD)} \right)^2} = N_{EP} \times f_{\lognormal}(d_p) \quad (2.5)$$

with N_{EP} the particle number concentration at the engine exit plane and f_{\lognormal} the lognormal function.

A size distribution can have different weighting (number, mass, volume) all giving a different insight of the investigated particles. Assuming an effective density and sphericity, particle number (N) can easily be converted into particle mass (M) using the following equation:

$$M(d_p) = N(d_p) \times V(d_p) \times \rho_{eff}(d_p) = N(d_p) \times \frac{\pi \rho_{eff}(d_p) d_p^3}{6} \quad (\text{a}) \quad (2.6)$$

$$M_{total} = N_{total} \times V_{total} \times \rho_{eff}(avg) \quad (\text{b})$$

with ρ_{eff} the particle effective density defined in section 2.2 and V the particle volume. Equation (2.6) can be used for a single particle or at a specific size d_p using a size-dependent particle effective density ((2.6) (a)). It can also be used to with total concentrations using an average particle effective density ((2.6) (b)).

When plotting a lognormal particle size distribution using different weighting (i.e. Number, Volume or Mass), distributions are shown to shift but remain lognormal and have the same GSD, as highlighted in Figure 2-3 where a Number-size distribution was converted into a Mass-size distribution using equation (2.6).

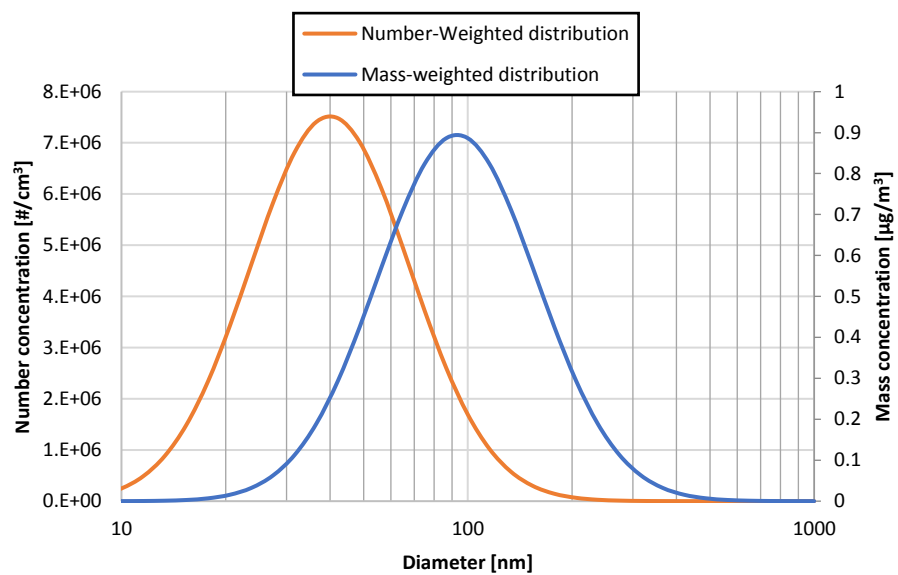


Figure 2-3: Example lognormal particle distribution both number- and mass-weighted with a GMD of 40 nm, GSD of 1.7 and total number concentration of 10^7 particles/cm³

It is noted that aircraft exhaust PM size distributions are generally measured according to their mobility diameter given the current technology available to directly measure nanoparticles size (section 3.1.3) [20], [51], [63].

2.2 Particle effective density

Exhaust aerosols from gas turbine engines consist mainly of solid spherical primary particles (i.e. soot) that coagulate and form larger non-spherical fractal aggregate (Figure 2-1). The fractal particles contain voids making their density lower than that of the constituent material and more complicated to characterise [63], [64]. Particle effective density is a fundamental property that provides a description of fractal-like aggregates, combining the particle material density with its

complex morphology. For a given size, particle effective density influences several factors such as the particles transport behaviour, radiative properties and health impact and hence its knowledge is critical and also impacts particle diameter measurements [64]–[66]. Density can be used to determine mass concentrations from measured number concentrations (equation (2.6)) and links mobility with aerodynamic diameter (equation (2.1)).

The effective density of fractal aggregates is defined as the mass divided by the volume of a spherical particle with a diameter equal to the measured mobility diameter and is described using a power-law relationship [67]:

$$\rho_{\text{eff}} = \frac{M}{\left(\frac{\pi}{6}\right) d_m^3} = C \times d_m^{D_m-3} \quad (2.7)$$

with M the particle mass, d_m the particle mobility diameter, D_m the mass-mobility exponent ranging from 1 for long chains to 3 for spheres, and C a scaling constant sometimes called the density-mobility pre-factor.

Multiple definitions exist for particle effective density which depend on the measurement technique used. Densities measured from different techniques are not necessarily comparable. Furthermore, particle effective density can be reported at different sizes (size-dependent), or as an average over the aerosol size distribution (average). A comprehensive review of particle effective density definitions is given by DeCarlo et al. [64], with the definitions used in this thesis introduced below:

- $\rho_{\text{eff}}^1 = \frac{M}{V}$ (*average*) is the ratio of the total particle mass (M) to the total particle volume (V) calculated assuming sphericity. It can be derived using a mass instrument (e.g. MSS, MAAP, LII-300) and a size instrument (e.g. DMS-500, SMPS) from which the volume can be derived from the number-weighted particle size distribution [63], [68].
- ρ_{eff}^2 (*average or size-dependent*) is determined by classifying and measuring particles according to their mass and mobility. Using this technique, particle effective density can be measured at individual sizes. An average effective density $\rho_{\text{eff}}^2(\text{avg})$ can be estimated by combining the size-dependent effective density with the particle size distribution [51], [63], [69].
- ρ_{eff}^3 (*average or size-dependent*) is determined by comparing the mobility and aerodynamic diameters [10], [21], [70].

Aircraft PM effective density has been substantially investigated in several studies as presented in **Table 2-1**. Particle density was shown to vary with fuel composition, engine power, engine technology and particle size. It was reported to vary between 0.22–2 g/cm³ with the mass-mobility exponent ranging between 2.3–2.82 and a soot material/bulk density reported between 1.8–2 g/cm³ [21], [63], [65], [69]. As can be seen in **Figure 2-4(a)**, particle effective density is size-dependent and decreases with increasing particle diameter due to larger particles corresponding to larger aggregates and hence containing more internal voids. Density also increases with engine thrust as primary particles are reported larger with increasing thrust, thus particles contain fewer less dense voids. When averaging the size-dependent particle effective density over the measured size distribution, the average particle effective density was shown to remain fairly constant as highlighted in **Figure 2-4(b)** where the density of exhaust PM from a CFM56 aircraft engine averages at ~1 g/cm³. It was also reported that soot effective density increased with increasing volatile fraction in the aerosol as some volatile material, having a larger density than the voids, condensed onto the soot particles and filled the internal voids of the aggregates [10]. The high variability of aircraft PM particle effective density demonstrates that no single expression can be used to estimate aircraft PM density.

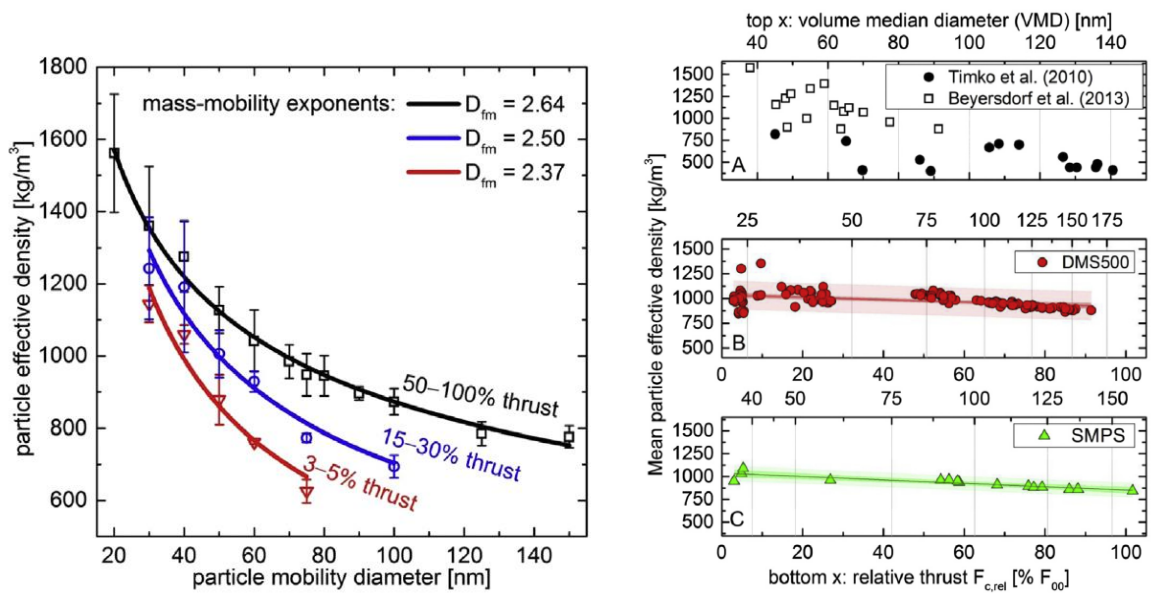


Figure 2-4: Particle effective density distributions ($\rho_{eff}^2(d_p)$) determined for various thrust ranges and average effective density ($\rho_{eff}^2(avg)$) as a function of engine thrust and volume median diameter from multiple aircraft engines [63]

Table 2-1: List of aircraft PM effective densities and mass-mobility exponents reported in the literature along with the instruments used for measurement

Authors	Measuring instrument	Engine Type	D_f mass-mobility exponent	ρ_{eff} [g/cm ³] with d_m [m] (except Olfert et al. where d_m [nm])	Comments & Additional properties
Timko et al. [21]	MAAP - SMPS AMS - SMPS	PW308	-	$\rho_{\text{eff}}^1(\text{avg}) = 0.4 - 0.82$ $\rho_{\text{eff}}^3(\text{avg}) = 0.71 - 0.84$	Fuel tested: JP-8 & FT $d_m = 45 - 140$ nm $\rho_{\text{bulk}} = 1.8$ g/cm ³
Williams et al. [10]	DMS - AMS	APU	2.53-2.54	$\rho_{\text{eff}}^3(\text{avg}) = 1.3 - 2.5$	$d_m = 20-90$ nm
Beyersdorf et al. [68]	MAAP - EEPS	CFM-56-2C1	-	$\rho_{\text{eff}}^1(\text{avg}) = 0.9 - 1.6$	Fuel tested: JP-8 & FT
Durdina et al. [63]	DMA - CPMA - CPC	CFM56-7B26/3	2.37-2.64	$\rho_{\text{eff}}^1(\text{avg}) = 0.9 - 1.1$ $\rho_{\text{eff}50-100\%}^2(d_p) = 2.44 * d_m^{2.635-3}$ $\rho_{\text{eff}15-30\%}^2(d_p) = 0.2 * d_m^{2.5-3}$ $\rho_{\text{eff}3-5\%}^2(d_p) = 0.02 * d_m^{2.37-3}$	Fuel tested: Jet-A $d_m=20-150$ nm
Abegglen et al. [65]	DMA - CPMA - CPC	CFM56-7B26/3	2.54 - 2.79 ($F_{oo} > 30\%$) 1.86 - 2.32 ($F_{oo} < 30\%$)	$\rho_{\text{eff}67-105\%}^2(d_p) \sim 3.544 * d_m^{2.68-3}$ $\rho_{\text{eff}22-33\%}^2(d_p) \sim 0.0753 * d_m^{2.35-3}$	Fuel tested: JP-8 $d_m = 20 - 150$ nm
Johnson et al. [69]	CPMA - DMS	CFM56-5B4/2P CFM56-7B26/3 PW4000-100	2.68 - 2.82	$\rho_{\text{eff}dil+CS}^2(d_p) = 11.92 * d_m^{2.76-3}$ $\rho_{\text{eff}dil}^2(d_p) = 13.88 * d_m^{2.76-3}$ $\rho_{\text{eff}raw+CS}^2(d_p) = 35.83 * d_m^{2.82-3}$ $\rho_{\text{eff}raw}^2(d_p) = 44.64 * d_m^{2.82-3}$	$d_m = 20 - 100$ nm
Boies et al. [20]	DMS	CFM56-5B4/2P	-	$\rho_{\text{eff}}^2(\text{avg}) = 0.72 - 0.9$	-
Lobo et al. [71]	DMA-CPMA-CPC DMS	CFM56-5B4/2P	2.57	$\rho_{\text{eff}}^1(\text{avg}) = 0.85$ $\rho_{\text{eff}}^2(d_p) = 0.606 * d_m^{2.57-3}$ $\rho_{\text{eff}}^3(\text{avg}) = 0.89 - 0.97$	Fuel tested: Jet-A $d_m = 20 - 50$ nm
Olfert et al. [72]	DMA-CPMA-CPC	GNOME	2.44 - 2.61	$\rho_{\text{eff}13K}^2(d_p) = 6556 * d_m^{2.44-3}$ $\rho_{\text{eff}13K+CS}^2(d_p) = 6665 * d_m^{2.395-3}$ $\rho_{\text{eff}22K}^2(d_p) = 3046 * d_m^{2.612-3}$ $\rho_{\text{eff}22K+CS}^2(d_p) = 3172 * d_m^{2.621-3}$	Fuel tested: Jet-A $d_m = 20 - 250$ nm
Ubogu et al. [73]	DMA-CPMA-CPC	APU	2.3 - 2.42	$\rho_{\text{eff}NL}^2(d_p) = 0.0210 * d_m^{2.36-3}$ $\rho_{\text{eff}BL}^2(d_p) = 0.0078 * d_m^{2.30-3}$	Fuel tested: Jet-A, Diesel, NP 1014 $d_m = 20 - 300$ nm

2.3 Nanoparticle loss mechanisms

Given the force required for a nanoparticle to adhere to a surface is generally smaller than that necessary to bounce or detach, nanoparticles attach firmly to any solid surface they enter into contact with, whether it is another particle (i.e. agglomeration) or the inner walls of a sampling line [60]. At the nanoscale, the main adhesive forces are the London-Van Der Waals force and the electrostatic force. Still, particle adhesion is a very complex problem and it remains poorly understood [62].

When sampling an aerosol, numerous mechanisms affect particles and force them to deviate from the carrier gas trajectory, causing them to deposit onto the inner walls of the transport system. Therefore, it is critical to grasp a good understanding of those mechanisms to accurately characterise losses in a sampling system and determine PM concentration at the inlet of the sampling system. This is particularly true with aircraft PM sampling as long sampling systems are required to transport the hot and highly concentrated exhaust aerosol to the analysers.

The main nanoparticle deposition mechanisms are diffusion, inertia, thermophoresis, bending and electrostatic loss, as highlighted in **Figure 2-5**. Each of those mechanisms depend differently on particle and carrier gas properties.

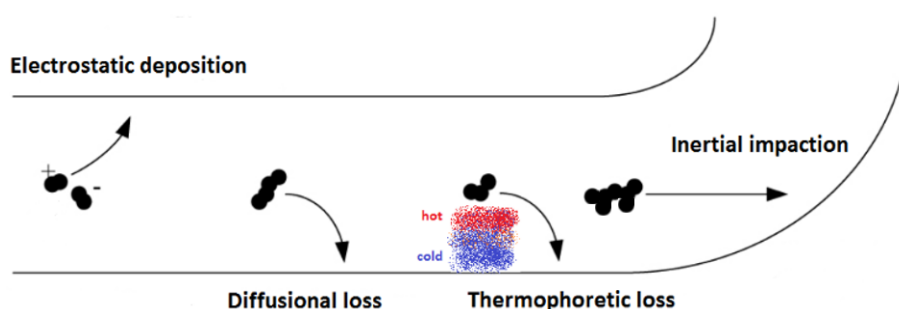


Figure 2-5: Diagram of main nanoparticle deposition mechanisms in a tube (inspired from [74])

As well as depositing onto the walls, particles can agglomerate in regions of high concentrations, resulting in a loss of particle number and an increase in particle size while the mass is conserved. If the gas carrier is saturated, vapor molecules may condense onto particles causing them to grow, or even cause spontaneous nucleation generating new particles. While these phenomena do not directly affect sampled particle number concentration, they can indirectly affect number concentration measurements by modifying the particle size and, consequently, the deposition efficiency in the sampling system.

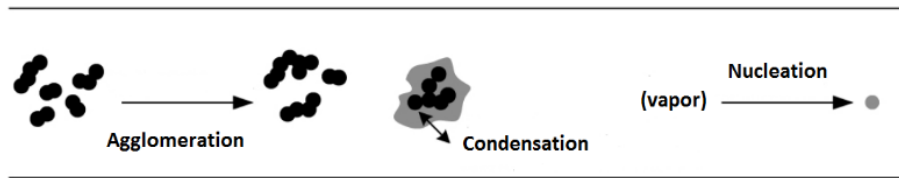


Figure 2-6: Diagram of main nanoparticle transformation mechanisms in a tube (inspired from [74])

When a wall surface is saturated with particles after long period of sampling, the adhered particles can detach and be re-entrained in the sampled aerosol. This re-entrainment phenomenon is usually referred to as line shedding.

In this section, the theory of nanoparticle deposition mechanisms and re-entrainment necessary for the characterisation of loss in a sampling system are discussed along with fundamental gas and particle properties.

2.3.1.1 Carrier gas properties

The carrier gas used to transport nanoparticles in a sampling system is usually dry (i.e. low relative humidity) particle-free air. Gas properties affect some particle deposition mechanisms and hence need to be assessed. Important gas properties used in this research are listed below with temperature and pressure dependent properties are generally calculated from the corresponding values at Normal Temperature and Pressure (NTP) at $T_0 = 293.15$ K and $P_0 = 101.325$ kPa. It is noted that important gas properties including the gas mean velocity (V_{avg}), volumetric flowrate (Q), thermal conductivity (k_g) and specific heat capacity (C_p) and useful dimensionless number namely the Prandtl number (Pr), and the fanning friction factor (f) are not listed below but are defined in [60], [62].

- **Gas Mean free path:**

The gas mean free path is the average distance between collisions for a gas molecule. It is calculated for any given temperature using the formula presented by Kulkarni et Al. [62] with $\lambda_0 = 67.3$ nm [75] and the Sutherland constant $C = 110.4$ [62].

$$\lambda = \lambda_0 \times \left(\frac{T_i}{T_0}\right) \times \left(\frac{P_0}{P_i}\right) \times \left(\frac{1 + C/T_0}{1 + C/T_i}\right) [\text{m}] \quad (2.8)$$

with T_i the input temperature and P_i the input pressure.

- **Gas viscosity :**

Viscosity refers to the resistance of a fluid to a change in shape or movement, opposing itself to the flow. The gas viscosity (i.e. dynamic viscosity) is calculated for any given temperature using

Sutherland's formula with $C = 110.4$ and the reference viscosity $\mu_0 = 1.83245 \times 10^{-5} \text{ kg} \cdot \text{m}^{-1} \cdot \text{s}^{-1}$ for air [62]:

$$\mu = \mu_0 \times \left(\frac{T_i}{T_0}\right)^{3/2} \times \left(\frac{T_0 + C}{T_i + C}\right) [\text{Pa} \cdot \text{s}] \equiv [\text{kg} \cdot \text{m}^{-1} \cdot \text{s}^{-1}] \quad (2.9)$$

with T_i the input temperature.

- **Gas density:**

The density of an ideal gas is given by:

$$\rho = \frac{M_m \times P_i}{R \times T_i} = \frac{M_m \times P_i}{8314 \times T_i} [\text{kg} \cdot \text{m}^{-3}] \quad (2.10)$$

with M_m the molar mass of the gas ($M_{m_{air}} \sim 29 \text{ g} \cdot \text{mol}^{-1}$), R the gas constant, T_i the input temperature and P_i the input pressure.

- **Reynolds number:**

The Reynolds number is the ratio of inertial forces to viscous forces and describes the flow regime in a system. The turbulent regime is generally assumed when $Re > 2300$ while the flow condition is laminar when $Re < 2300$ [62], [76]. It is defined as:

$$Re = \frac{\rho V_{avg} D_{tube}}{\eta_g} \quad (2.11)$$

with ρ the fluid density, V_{avg} the fluid average velocity, D_{tube} the tube diameter and η_g the fluid viscosity.

2.3.1.2 Particles properties

Essential particle properties used for characterisation and the determination of particle loss during transport of an aerosol are listed below.

- **Knudsen number:**

Knudsen number is the ratio of the carrier gas mean free path (λ) to the particle diameter (d_p) and is defined as [62, p. 19]:

$$Kn = \frac{2 \times \lambda}{d_p} \quad (2.12)$$

The Knudsen number is an indicator of the regime in which the particle is; when $Kn \gg 1$, particles are in the free molecular flow and when $Kn \ll 1$, they are in the continuum flow. When $Kn \sim 1$, particles are in the transition regime.

- **Stokes number:**

Stokes number is a dimensionless parameter representing the ratio of particle response time to a characteristic time of the fluid flow. It governs particle impaction when a flow suddenly changes and is defined as [62, p. 25]:

$$Stk = \frac{\tau \times V_{avg}}{D_{tube}} = \frac{\rho_p \times C_c \times d_p^2 \times V_{avg}}{18 \times \mu \times D_{tube}} \quad (2.13)$$

with τ the particle relaxation time, V_{avg} the average gas velocity, D_{tube} the tube diameter, ρ_p the particle density, C_c the slip correction factor, d_p the particle size, μ the gas viscosity.

- **Slip correction factor (i.e. Cunningham correction factor):**

The slip correction factor is used to determine particle drag for particle sizes near that of the gas mean free path ($Kn \geq 1$). In this regime, particles can slip between the molecules before colliding with any obstacle on their path leading to increased velocity and reduced drag force to that predicted by Stokes' law. The slip correction factor can be expressed as followed [62]:

$$C_c = 1 + Kn(A + B \times \exp(-C/Kn)) \quad (2.14)$$

with A , B and C empirical values depending on the particle type and the sampling conditions and Kn the Knudsen number. The values $A = 1.165$, $B = 0.483$ and $C = -0.997$ are recommended for use in the *ISO15900:2009* standard for electrical mobility measurements, as verified by Kim et al. [75] for solid particles in the nanometre range (i.e. $0.5 < Kn < 83$).

- **Particle diffusion coefficient:**

The particle diffusion coefficient is used to characterise diffusive transport and losses under Brownian motion. It is defined as [60, p. 152]:

$$D = \frac{kTC_c}{3\pi\mu d_p} \quad (2.15)$$

with k the Boltzmann constant, C_c the slip correction factor, μ the gas viscosity and d_p the particle diameter.

- **Particle relaxation time:**

The particle relaxation time is the time taken to adjust to a new external force acting upon it. It is defined mathematically as the product of the particle 's mass (M) and mobility (B) and can be expressed as followed [62], [77]:

$$\tau = M \times B = \frac{\rho_p d_p^2 C_c}{18\mu} \text{ [s]} \quad (2.16)$$

with ρ_p the particle density, d_p the particle diameter, C_c the slip correction factor and μ the gas viscosity. It is noted that the relaxation time is derived from the particle settling velocity: $V_T = \tau \times \frac{F}{m}$, with F the force acting on the particle.

- **Schmidt number:**

Schmidt number expresses the ratio of kinematic viscosity to diffusion coefficient and is used to describe convective mass transfer relative to Brownian diffusion of particles [62, p. 23]. It is defined as:

$$Sc = \frac{\eta_g}{\rho_g \times D} = \frac{\nu}{D} \quad (2.17)$$

with η_g the gas viscosity, ρ_g the gas density and D the diffusion coefficient.

- **Dean number:**

Dean number is the ratio of the square root of the product of inertial and centrifugal forces to the viscous force and is used to characterise flows through curved pipe [78]. It is defined as:

$$De = \frac{Re}{\sqrt{R_o}} = Re \times \sqrt{\frac{r_{tube}}{r_{curvature}}} \quad (2.18)$$

with Re the Reynolds number, R_o the curvature ratio, r_{tube} the tube radius and $r_{curvature}$ the curvature radius.

2.3.1.3 Diffusional and inertial losses

Diffusion of particles is caused by a concentration gradient, where a force is generated from the region of higher concentration towards the region of lower concentration. Brownian motion, resulting from particle colliding with the molecules in the gas, is the main contributor to particle diffusion. Accordingly, diffusion mostly affect smaller particles which are more strongly affected by gas molecules. For particles in an ICAO compliant sampling system where the flowrate is generally turbulent ($Re > 4000$ in long sample lines), two diffusive regimes of deposition are considered: turbulent eddy diffusion, and turbulent inertial diffusion.

For Eddy diffusion, the walls of a sampling system act as a sink for the particles which diffuse towards the inner walls and deposit on it. Particle loss in a tube caused by turbulent diffusion (i.e. eddy diffusion), based on the mass conservation principle, is defined as [62]:

$$\eta_{diffusion} = \exp \left[-\frac{\pi \cdot D_{tube} \cdot L_{tube} \cdot V_{diff}}{Q} \right] \quad (2.19)$$

with D_{tube} the tube diameter, L_{tube} the tube length, Q the gas volumetric flowrate and V_{diff} the diffusional deposition velocity. V_{diff} may be estimated using the equation proposed by Friedlander et al. [62, p. 90] in a turbulent flow:

$$V_{diff,eddy} = \frac{0.0118 \times Re^{\frac{7}{8}} \times Sc^{\frac{1}{3}} \times D}{D_{tube}} \quad (2.20)$$

with D_{tube} the tube diameter, Re the Reynolds number, Sc the Schmidt number and D the diffusion coefficient. In laminar flow regimes, the formulation of Gormley and Kennedy [62, p. 90] may also be used to estimate diffusional loss.

In addition to eddy diffusion, which mostly affects the smallest particles ($<0.1 \mu\text{m}$), larger particles can be projected onto the wall due to inertial diffusive forces because of slow fluid flow near the tube walls. The penetration efficiency from inertia can be estimated using equation (2.19) and replacing the diffusional deposition velocity by the inertial deposition velocity defined as [79] :

$$V_{inertia} = V_{di} \times U \quad (2.21)$$

$$V_{di} = 27.13 \times \left(\frac{\rho_p}{\rho_g} \right)^{0.249} \times \left(\frac{d_p}{D_{tube}} \right)^{2.223} \times Re^{0.73} \quad \text{and} \quad U = V_{avg} \cdot \sqrt{\frac{f}{2}} \quad [80] \quad (2.22)$$

with ρ_p and ρ_g respectively the particle and gas density, d_p the particle diameter, D_{tube} the tube diameter, Re the Reynolds number, V_{avg} the average gas velocity and f a friction factor.

2.3.1.4 Thermophoretic loss

When a temperature gradient is established in an aerosol, the hotter gas molecules have more kinetic energy and can push suspended nanoparticles towards the cooler region. This phenomenon as depicted in **Figure 2-7** is called thermophoresis. For example, during the sampling of a hot aerosol, particles are pushed towards the colder walls and are consequently lost by thermophoretic deposition.

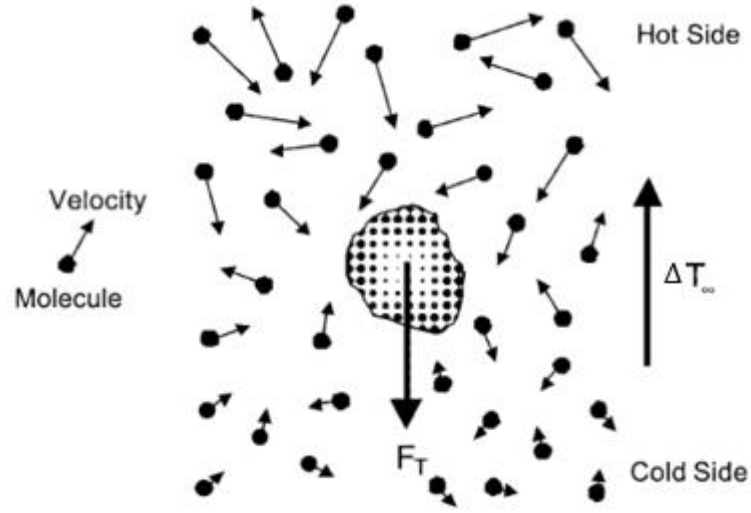


Figure 2-7: Illustration of a particle immersed in a gas with a temperature gradient [81]

The thermal force applied to particles is generally expressed in term of thermophoretic velocity V_{th} . For particles whose diameter is close to that of the gas mean free path (i.e. < 100 nm with air), the thermophoretic velocity depends on the thermophoretic coefficient K_{th} and the temperature gradient as express in equation (2.23) presented by Talbot et al. [82]. It is noted that K_{th} is generally approximated to 0.55 for particles in the free molecular or transition regime [83]–[85].

$$V_{th} = K_{th} \times \frac{\Delta T}{T} \text{ with } K_{th} = \frac{2C_s C_c}{1 + 3C_m Kn} \left(\frac{\frac{k_g}{k_p} + C_t Kn}{1 + \frac{2k_g}{k_p} + 2C_t Kn} \right) \quad (2.23)$$

with Kn the Knudsen number, k_g and k_p respectively gas and particle thermal conductivities, C_s (=1.17), C_t (=2.18), C_m (=1.14) [82] and C_c respectively the slip, thermal, momentum, and the Cunningham correction factor. For soot particles, the thermal conductivity k_p is generally assumed to be 0.2 W/(m.K) [83].

The determination of thermophoretic deposition in a sample line can be challenging due to changing temperature gradients and because the particle thermal conductivity not necessarily the same as the particle material thermal conductivity (voids in fractal particles) [62]. The thermophoretic deposition efficiency in a turbulent flow may be estimated using Romay et al. [86] theoretical expression:

$$\eta_{thermophoresis} = \left(\frac{T_{wall} + (T_{gas} - T_{wall}) \exp\left(\frac{-\pi \cdot D_{tube} \cdot h \cdot L}{\rho_p \cdot Q \cdot C_p}\right)}{T_{gas}} \right)^{Pr \cdot K_{th}} \quad (2.24)$$

with T_{wall} the wall temperature, T_{gas} the aerosol temperature, D_{tube} the tube internal diameter, h the heat transfer coefficient, L the tube length, ρ_p the particle density, Q the standard flowrate, C_p the specific heat capacity of the gas, Pr the Prandtl number and K_{th} the thermophoretic coefficient.

Assuming a long enough sampling tube for the initially hot aerosol to reach the cooler wall temperature ($T_{gas} > T_{wall}$), the above expression for thermophoretic deposition may be empirically simplified to the expression k_{thermo} [53], [74], as introduced in section 1.5:

$$k_{thermo} \approx \eta_{thermophoresis} = \left(\frac{T_{wall}}{T_{gas}} \right)^{Pr \cdot K_{th}} \approx \left(\frac{T_{wall} + 273.15}{T_{gas} + 273.15} \right)^{0.38} \quad (2.25)$$

Because K_{th} is assumed constant in the size regime of aircraft exhaust particles, the product of K_{th} and Pr is evaluated to 0.38 [74].

2.3.1.5 Electrostatic loss

When sampling an aerosol, charged particles can deposit onto walls via electrostatic forces. Particle charging generally occurs from diffusion of ions, which are constantly produced in our environment by cosmic radiation, to the particles or by the process that generates particles [62]. Thus, even in an aerosol that is, on average, electrostatically neutral, some particles are charged. The sampling system material may also induce electrostatic loss if not conductive or earthed as building up of electric charges in the wall can produce an electrical field and cause particle deposition by Coulombic attraction [87]. Giechaskiel et al. [74] demonstrated that tubing material is important as non-conductive tubes were shown to display higher losses when compared with conductive tubes. Particles can be charged to a predictable level using a unipolar or bipolar charger [88].

Electrostatic penetration efficiency in a sampling line, assuming singly charged particles, can be calculated using the following equation [59]:

$$\eta_{electrostatic} = 1 - \left(\frac{(q_c^2 \cdot L_{tube} \cdot C_c)}{\pi \cdot \epsilon_0 \cdot d_p \cdot D_{tube} \cdot Q} \right)^{\frac{1}{3}} \quad (2.26)$$

with q_c the charge on the particle and ϵ_0 the permittivity of air. Note that electrostatic losses are minimised, when no electric field exists in the sampling line [62]. This can be done by using electrically conductive and grounded lines.

2.3.1.6 Bend loss (impaction theory)

In a straight sampling line, particles travel along the same direction as the gas flow. However, when an aerosol flow bends or bypasses a body or plate, larger particles that have more inertia due to their higher mass deviate from the flow and may impact onto the body/wall, as highlighted in **Figure 2-8**. Losses in bends and impactors are governed by the Stokes number. In the case of impactor and cyclones, impaction losses are best described with d_{50} corresponding to the particle diameter at which 50% of particles are lost (i.e. cut-off size), defined as [60, p. 122]:

$$d_{50} = \sqrt{\frac{18 \times \eta_g \times D_{body} \times (Stk_{50})}{\rho_p \times V_{avg} \times C_c}} \quad (2.27)$$

with η_g the gas viscosity, D_{body} the impaction body diameter, Stk_{50} the Stokes number at d_{50} , ρ_p the particle density, V_{avg} the gas average velocity and C_c the slip correction factor.

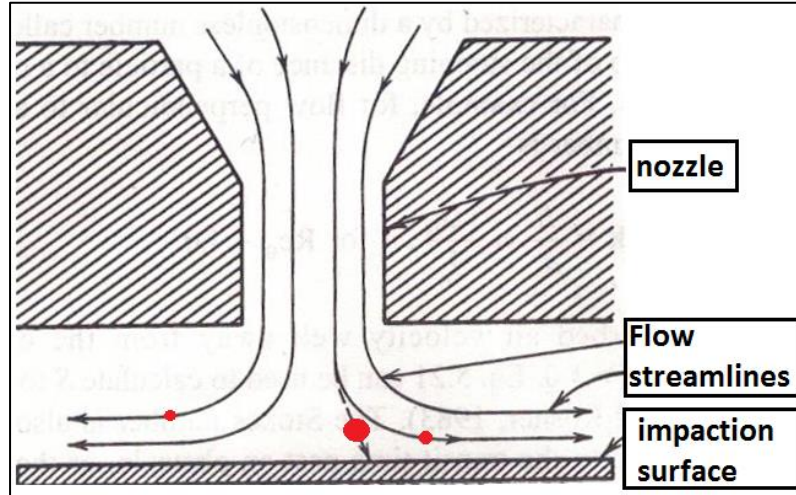


Figure 2-8: Cross-sectional view of an impactor [60]

The deposition efficiency of nanoparticles caused by bends can be estimated using the following equations proposed by Crane and Evans [89] and Pui et al. [90]:

$$\eta_{bend} = 1 - Stk \times \theta \text{ for } Re < 5000 \quad (2.28)$$

$$\eta_{bend} = \exp[-2.823 \cdot Stk \cdot \theta] \text{ for } Re > 5000 \quad (2.29)$$

with θ the angle of bend in radians and Stk the Stokes number.

Wang et Al. [91] showed that the bends and elbows could increase diffusional loss of monodisperse 5-15 nm diameter particles to up 44% when compared with a straight tube with the same length. For $Re < 150$, the particle loss depends on the geometry of the sampling line whereas for $Re > 150$, it is insensitive to the flow geometry. The results also suggested that having a larger inner radius reduces the losses through the bends. ICAO regulation recommends that any necessary bends should have a radius greater than ten times the inside diameter of the lines [14].

2.3.1.7 Agglomeration

Agglomeration, also called coagulation, is a process occurring in an aerosol in regions of high concentrations wherein nanoparticles subject to Brownian motion collide with one another and adhere to form larger particles. This leads to a decrease in particle concentration coupled with an

increase in average particle size. Because coagulation is governed by the rate of diffusion of particles to the surface of each other, it affects more strongly smaller particles that have a higher diffusion coefficient. The theory defined below describes how particle number concentration and size change as a function of time for typical combustion exhaust nanoparticles.

When investigating coagulation, the number concentration at any given time can be solved with [62, pp. 38–39]:

$$N(t) = \frac{N_0}{1 + N_0 K t} \quad (2.30)$$

with N_0 the number concentration at time zero, $N(t)$ the number concentration at time t and K the coagulation coefficient. Assuming particle sphericity, number concentration and average size are related with mass concentration as shown in equation (2.6). As the mass remains constant during coagulation, the change in particle size caused by coagulation over a period t can also be predicted with

$$d(t) = d_0 (1 + N_0 K t)^{\frac{1}{3}} \quad (2.31)$$

with d_0 the particle diameter at time zero.

For a polydisperse aerosol with particles <100 nm, the main difficulty with describing agglomeration resides in estimating K as no explicit solution exists. Each individual particle size distribution has a different K value that must be numerically solved. For the case of coagulation of an aerosol with a lognormal distribution with a known CMD and GSD, Lee and Chen (1984) have derived an equation for the average coagulation coefficient \bar{K} :

$$\bar{K} = \frac{2kT}{3\eta} \times \left[1 + \exp(\ln^2 GSD) + \left(\frac{2.49\lambda}{CMD} \right) \times [\exp(0.5 \ln^2 GSD) + \exp(2.5 \ln^2 GSD)] \right] \quad (2.32)$$

where k is the Boltzmann constant, T is the gas temperature, η is the gas viscosity, λ is the gas mean free path, and CMD and GSD are the centre mean diameter and geometric standard deviation of the particle size distribution, respectively. This value of \bar{K} can be used with equations (2.30) and (2.31) for which there only is a modest change in CMD.

2.3.1.8 Re-entrainment

After extensive aerosol transport in sample lines, their inner walls can become saturated over time with particles that have deposited. Clusters of particles on the inner walls can be detached and resuspended in the sampled aerosol as a result of air jets, mechanical forces, the impaction of other particles, or electrostatic forces [58, p. 99], and is generally referred to as line shedding. The rate of

re-entrainment depends on the nature of the flow, the particle-surface adhesive forces, and the particle-particle collisions rate.

Re-entrainment is a stochastic process that is not well characterised and is very hard to reliably predict. Because adhesion forces are proportional to d_p and removal forces are proportional to d_p^2 or d_p^3 , the larger the particle and the greater the air velocity, the greater the probability of re-entrainment [60, p. 145]. Typically, steady flows and stable conditions will not produce much re-entrainment. In an unsteady turbulent flow, the boundary layer at the surface of walls generally protects from re-entrainment except for the occasional bursts of turbulent eddies penetrating through the boundary layer detaching particles.

2.4 Aircraft nvPM system loss correction methodology (SLT)

The hostile environment and high particle concentrations at the exhaust of an aircraft engine make the use of a sampling system compulsory for the measurement of the exhaust aerosol. To appropriately regulate aircraft nvPM and evaluate its impact on health and the environment, it is necessary to correct the measured nvPM concentration at the engine exit where the aerosol enters the atmosphere. As previously discussed, size measurement is not prescribed although it is required to determine size-dependent losses in the sampling system.

In line with the introduction of a standardised aircraft nvPM sampling system in the latest ICAO regulation in Annex 16 (appendix 7), a procedure for estimating nvPM system loss correction factors for number ($k_{SL_{num}}$) and mass ($k_{SL_{mass}}$) concentrations is also provided (appendix 8) [14]. The correction methodology is referred to as the System Loss Tool (SLT) and was designed to provide nvPM number and mass correction factors for losses in the sampling system by only using the measured nvPM number and mass concentrations. To do so, a GMD is iteratively estimated at the exit plane until losses yield the measured nvPM number and mass concentrations. Then, a lognormal size distribution is generated using the predicted GMD and other assumptions from which nvPM system loss factors are determined. The SLT is available with the purchase of the SAE information report AIR 6504 [59] and the recommended practice ARP 6481 [57]. It is noted that the correction methodology discussed in this section does not include the significant thermophoretic loss in the Collection Part as those are separately estimated using k_{thermo} discussed in section **2.3.1.4**.

The SLT uses several assumptions for the predictions of correction factors which are generally accepted as being representative of aircraft nvPM, namely:

- An assumed average particle effective density of 1 g/cm³ (partly derived from the work of Durdina et al. [63]).

- A lognormal size distribution at the Engine Exit Plane (EEP) as generally witnessed for aircraft exhaust aerosol and is mathematically advantageous [59].
- An assumed GSD of 1.8 at the EEP derived from a large number of measurements during aircraft engine testing [59] and reported by Lobo et al. [9].
- No losses in the primary ejector diluter.
- No agglomeration occurs in the sampling system as the rapid dilution supposedly prevent particle agglomeration. To confirm this assumption, is it recommended to verify that the nvPM number concentration corrected for losses is $<10^8$ particles/cm³ [57].
- Estimated penetration efficiencies reported at electrical mobility particle diameters (d_m).
- An assumed nvPM particle thermal conductivity of 0.2 [W/(m.K)].

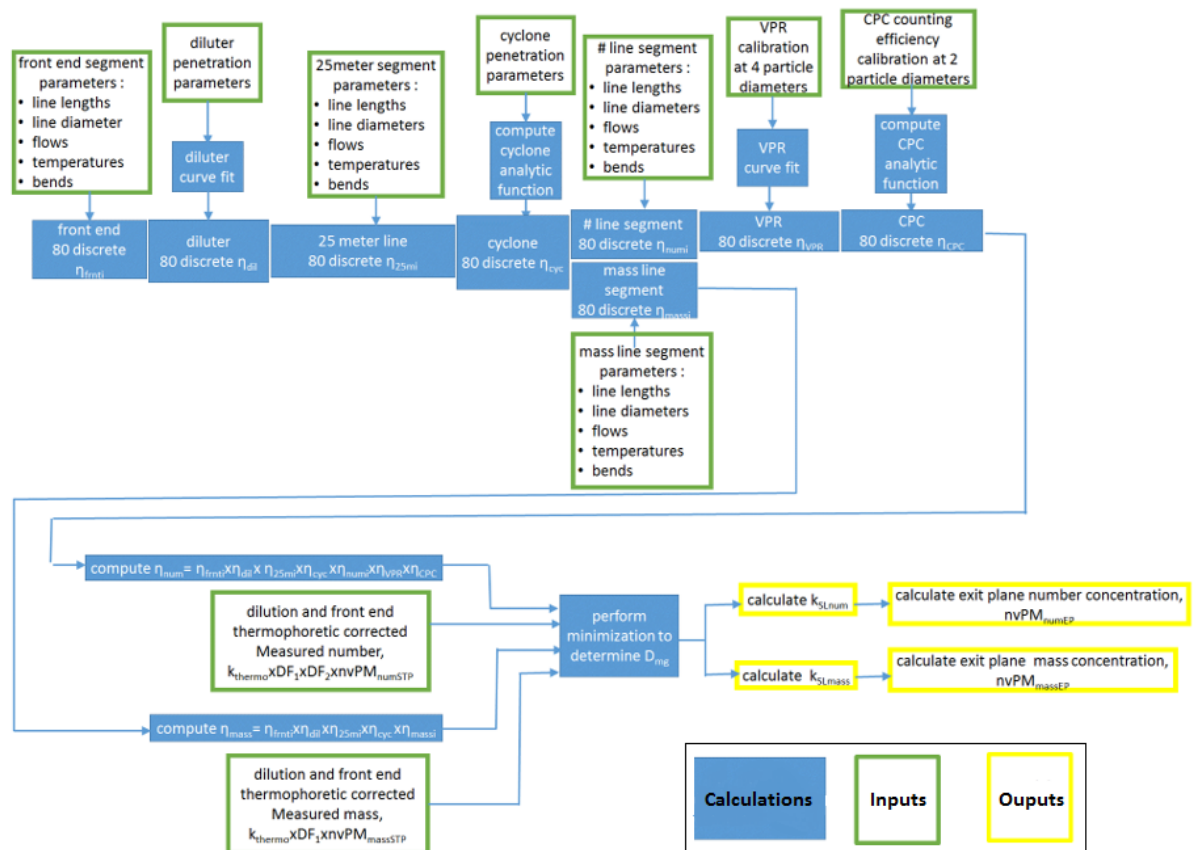


Figure 2-9: Block diagram of the SLT correction methodology [57]

In the SLT, the number correction factor ($k_{SL_{num}}$) is only calculated for $d_p > 10$ nm due to the very high uncertainties associated with small (< 10 nm) particles. Also, assuming a constant GSD in the SLT for all engine types and thrust conditions can be problematic. When the predicted GMD at the Engine Exit Plane (EEP) is small (i.e. < 20 nm) with a GSD as large as 1.8, the generated lognormal distribution at the EEP has non-zero value for number concentrations at a size of 0 nm which is impossible. Moreover, a SAMPLE reports [50] stated that raw distributions showed little evidence of

particles below 10 nm. The impact of this enforced size cut-off means the particle loss correction factor will be underestimated when the predicted GMD at the EEP is <20 nm.

An overview of the SLT is displayed in **Figure 2-9** with the specific operation of penetration efficiency calculation (UTRC model) and number and mass correction factors predictions discussed below. To operate, the SLT requires multiple inputs, namely:

- the measured nvPM number and mass concentrations corrected for dilution.
- the VPR, CPC and cyclone penetration functions derived from annual calibration.
- The dimensions, flowrates, pressures and temperatures of the different segments making the sampling system.

2.4.1 Penetration efficiency prediction (UTRC model)

An important task of the SLT consists in estimating the size-dependent penetration efficiency of the entire sampling system by accounting for all loss mechanisms discussed in section 2.3. Particle transport efficiency in the sampling lines are calculated using the UTRC (United Technologies Research Centre) particle transport model published with the AIR 6241 [52].

The UTRC model, available as an excel- or MATLAB-based tool, assumes steady state flow and calculates particle losses in different sampling system segments using standard equations discussed in section 2.3 and combining the effect of the five major deposition mechanisms (i.e. diffusion, thermophoresis, electrostatic loss, inertial loss and bend loss) by coupling flow characteristics to gas and particle properties.

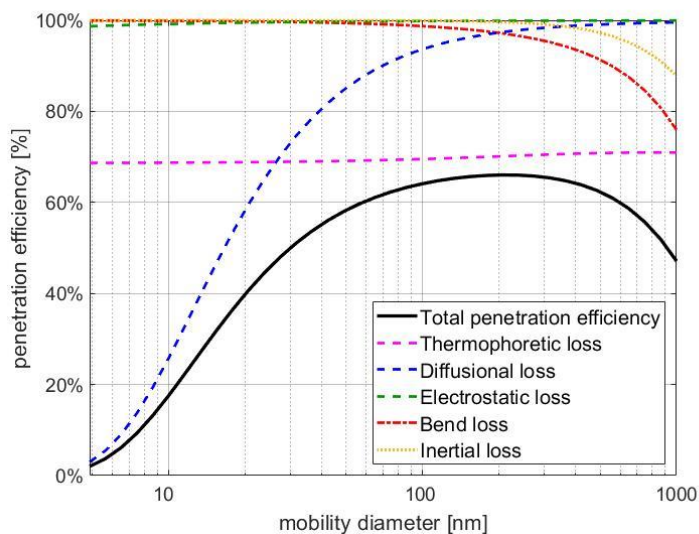


Figure 2-10: Example of nanoparticle penetration efficiency in a typical ICAO compliant sampling system estimated using the UTRC model

The UTRC model only requires the input of the dimensions of the sampling system and the aerosol properties (flowrate, temperature, pressure) and can predict transport efficiency for particles over a range of sizes, as shown in **Figure 2-10**.

In addition to particle deposition in the sampling system, the SLT accounts for losses in cyclones, the VPR and the CPC (section **3.1.1.1**). Such losses are highlighted in **Figure 2-11**.

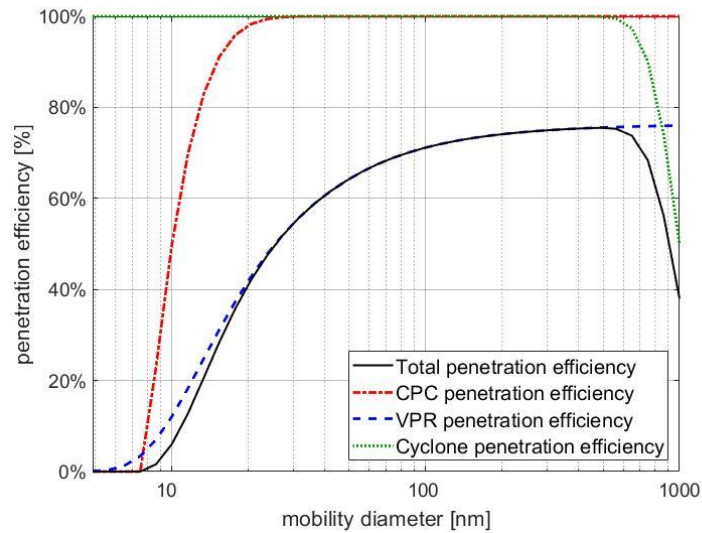


Figure 2-11: Example of nanoparticle penetration efficiency in an ICAO compliant cyclone, VPR and CPC using the SLT

2.4.2 Correction factor predictions in the SLT

Once the inputs are computed in the solver, the approach of the SLT for the estimation of correction factors can be separated into six steps:

- **1)** Given the dimensions of the sampling system and properties of the gas flow, particles penetration efficiency in the sampling system and instruments are calculated using the UTRC model and the calibrated VPR, CPC and cyclone penetration functions.
- **2)** Using the input nvPM number and mass concentrations, an assumed density of 1 g/cm³ and the penetration efficiency calculated in 1), the only remaining unknowns are the exit plane number concentration and the GMD. A chi-square minimisation of the fractions errors is used by adjusting the GMD at the EEP, as represented by the simplified equation:

$$\delta = \left(1 - \frac{nvPM_{numrEEP}(GMD, f_{log}, \eta_{mass}, GSD) / (nvPM_{massEEP}(GMD, f_{log}, GSD, \eta_{num}, \rho_{eff}))}{nvPM_{numrSTP} / (nvPM_{massSTP})} \right)^2 \quad (2.33)$$

with GMD the iterative Geometric Mean Diameter at the EEP, $nvPM_{xSTP}$ the measured nvPM number and mass concentrations, $nvPM_{xEEP}$ the predicted nvPM number and mass at the EEP,

GMD, f_{log} the generated lognormal distribution at the EEP, $\eta_{num/mass}$ the number and mass penetration efficiencies from the UTRC model, and ρ_{eff} the particle average effective density.

- **3)** Once the best ‘GMD’ has been predicted from the Chi-square minimisation above, it is used with an assumed GSD of 1.8 to produce a lognormal distribution using equation (2.5).
- **4)** The number correction factor $k_{SL_{num}}$ is predicted by dividing the sum of the modelled distribution at the EEP with the sum of the same distribution multiplied by the sampling system penetration efficiency previously calculated.
- **5)** The mass correction factor $k_{SL_{mass}}$ is predicted similarly to $k_{SL_{num}}$ by converting the number weighted size distribution at the EEP into a mass-weighted size distribution using equation (2.6) and the assumed particle density.
- **6)** Iterations 2) to 5) are repeated until the solver has found the minimum value of the square of the fractional errors, that is until line losses yield the reported downstream nvPM number and mass concentrations. $k_{SL_{mass}}$, $k_{SL_{num}}$ and the GMD are outputted.

A summary diagram in **Figure 2-12** visually represents the steps to estimate the number and mass correction factors in the SLT with D_{mg} corresponding to the GMD, σ_g corresponding to the GSD, DF_1 referring to the primary dilution (see section 3.1.1.3) and DF_2 referring to the secondary dilution occurring in a compliant nvPM number instrument (see section 3.1.1.1).

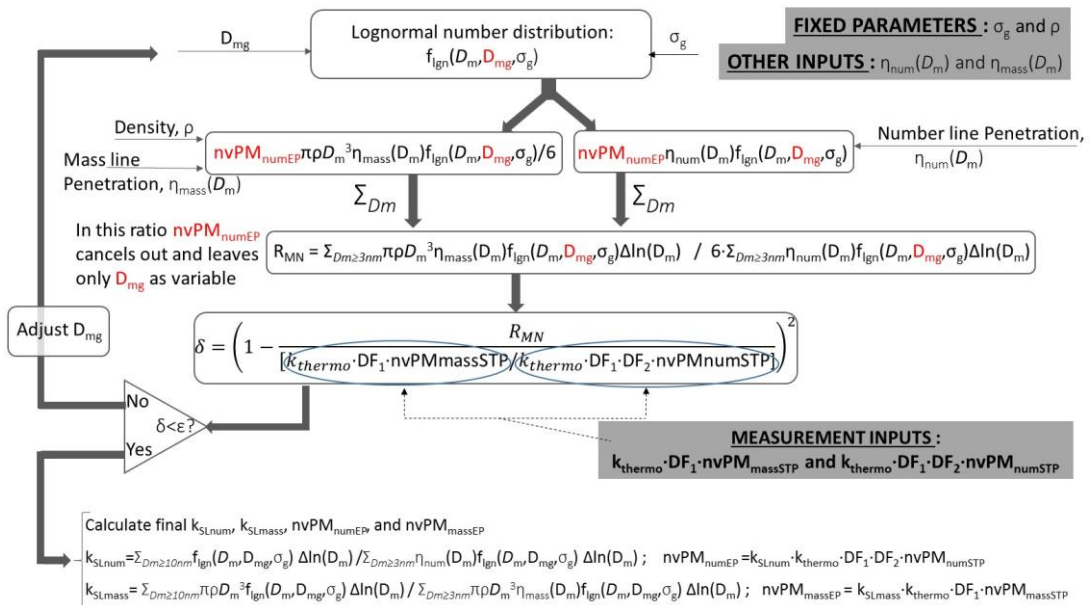


Figure 2-12: Diagram of the SLT system loss correction factor methodology (Note that k_{thermo} and DF_1 cancel out and hence have no impact on the calculations) [57]

2.5 Measurement uncertainty and error propagation

Measurement of nanoparticles is challenging and can lead to significant uncertainties. This section briefly describes some fundamentals of uncertainty analysis that were considered in this work.

Nanoparticle measurement uncertainties can be separated in two categories: Systematic errors which are usually the result of inaccurate calibration, with the measurement value always larger (or smaller) than the 'true' value. Random errors that refer to the variation in the measurement of a single quantity which can be dealt with in a statistical manner and represented with error bars.

Nanoparticle measurements are generally reported as an average of a characteristic repeatedly measured over time (e.g. number/mass concentration). For example, during aircraft exhaust emission certification testing, nvPM are usually characterised over a period of 30 seconds for each tested condition. The standard deviation (σ_{STD}) as defined in equation (2.34) and represented in **Figure 2-13** can be used to represent the scatter around the reported average and is a measure of the precision of the result. The coefficient of variation (CV) corresponds to the standard deviation divided by the mean.

$$\sigma_{STD} = \sqrt{\frac{1}{N} \sum_{i=1}^N (x_i - \text{mean})^2} \rightarrow CV = \frac{\sigma_{STD}}{\text{mean}} \quad (2.34)$$

with N the number of repeats, x_i the value at the repeat 'i'.

To represent the scatter around reported nvPM data, error bars corresponding to ± 2 standard deviations from the average may be plotted as they represent a 95% confidence interval ($\pm 1 \sigma_{STD}=68\%$ and $\pm 3 \sigma_{STD}=99\%$ confidence).

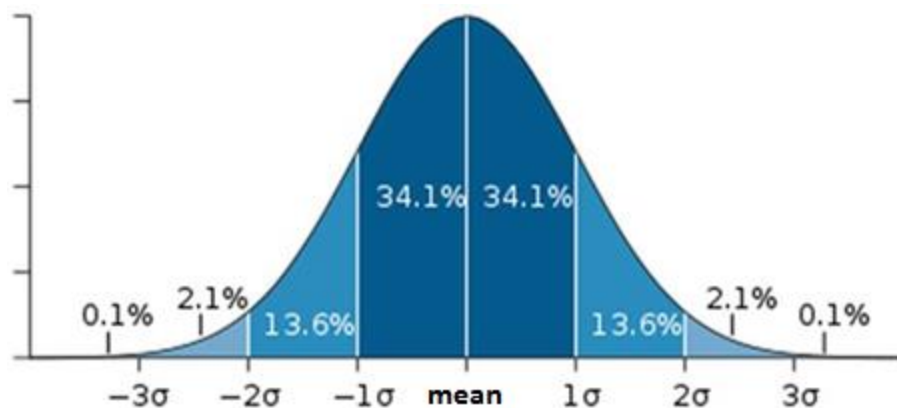


Figure 2-13: Illustration of a normal distribution with confidence bands representing the standard deviation (GSD) around the mean

When repeating a measurement without making any changes and hence expecting the same value, the variation around the mean may be represented by the standard error defined as the standard deviation divided by the square-root of the number of repeats ($SE = \sigma_{STD}/\sqrt{n}$).

Propagation of uncertainty:

When estimating a parameter from a combination of measured values, each associated with individual uncertainties, the resultant uncertainty may be determined using error propagation. Depending on the mathematical operation, error propagation is estimated as followed:

- Addition/subtraction: $z = x \pm y$ gives $\Delta z = \sqrt{\Delta x^2 + \Delta y^2}$
- Multiplication/Division : $z = x \frac{x}{y}$ gives $\Delta z = z \times \sqrt{\left(\frac{\Delta x}{x}\right)^2 + \left(\frac{\Delta y}{y}\right)^2}$

For example, the propagated uncertainty of EI_{number} (section 1.5.1.2) using particle number concentration (N) and diluted CO_2 measurements is:

$$\sigma_{EI_{\text{Number}}} = EI_N \times \sqrt{\left(\frac{\sigma_N}{N}\right)^2 + \left(\frac{\sigma_{\text{CO}_2 \text{dil}}}{\text{CO}_2 \text{dil}}\right)^2} = EI_N \times \sqrt{(CV_N)^2 + (CV_{\text{CO}_2})^2} \quad (2.35)$$

with σ representing the standard deviation of the individual measurements.

Another example is the propagated uncertainty of the repeated estimation of particle penetration efficiency (standard error) as used in chapter 5:

$$\sigma_{\text{Penetration efficiency}} = \sqrt{n^{\circ} \text{ repeats}} \times \left(\frac{N_{\text{outlet}}}{N_{\text{inlet}}}\right) \times \sqrt{\left(\frac{\sigma_{N_{\text{outlet}}}}{N_{\text{outlet}}}\right)^2 + \left(\frac{\sigma_{N_{\text{inlet}}}}{N_{\text{inlet}}}\right)^2} \quad (2.36)$$

with $N_{\text{outlet/inlet}}$ the particle number concentration measured at the inlet/outlet of the test section.

2.6 Reporting of large-scale aircraft engine nvPM emissions

When investigating aircraft engine particulate emissions, nvPM number and mass concentrations per volume of gas (i.e. / cm^3) are generally measured. Several studies available in the literature have reported PM emissions from aircraft exhaust over the last decade [9], [20], [51], [61], [63], [92], [93]. In addition to the investigation of aircraft exhaust aerosol properties (including density, morphology and volatility) towards better understanding of aircraft PM, most studies reported nvPM Emission indices (EIs) derived from measured number and mass concentrations as prescribed by current ICAO guidelines (section 1.5).

Examples of reported nvPM emission indices found in the literature are presented in **Figure 2-14**, **Figure 2-15** and **Figure 2-16** where nvPM number and mass emission indices (EI) are plotted

against relative thrust (F_{00}) for different engine types. Indeed, aircraft PM emissions are generally presented against thrust relative to the rated thrust F_{00} (section 1.5). However, rated thrust is calculated at International Standard Atmospheric (ISA) sea level conditions [14] and any variations in temperature and pressure during engine testing can cause the rated thrust to vary for a similar engine power. For example, for the same power settings, the relative thrust estimated at an engine testing in a hot and moist location can vary by several percent when compared with an engine testing in a cold and dry location.

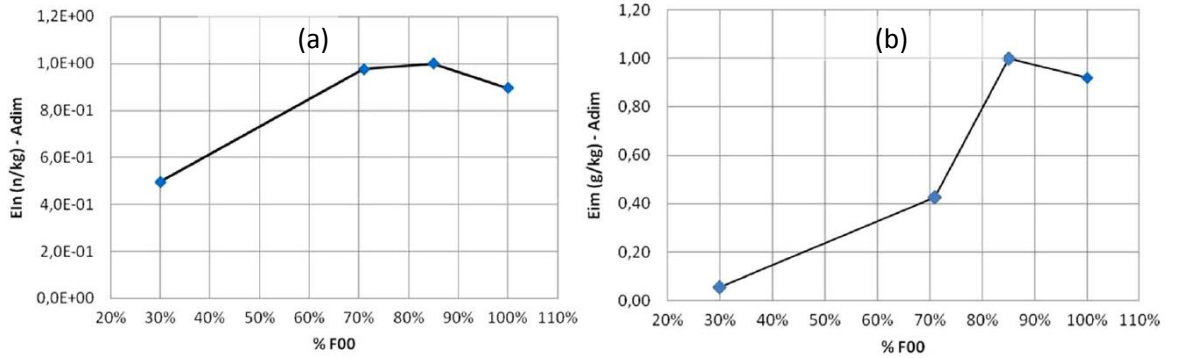


Figure 2-14: SaM146 Turbofan Engine average normalised nvPM number (a) and mass (b) emission indices for different regimes [61]

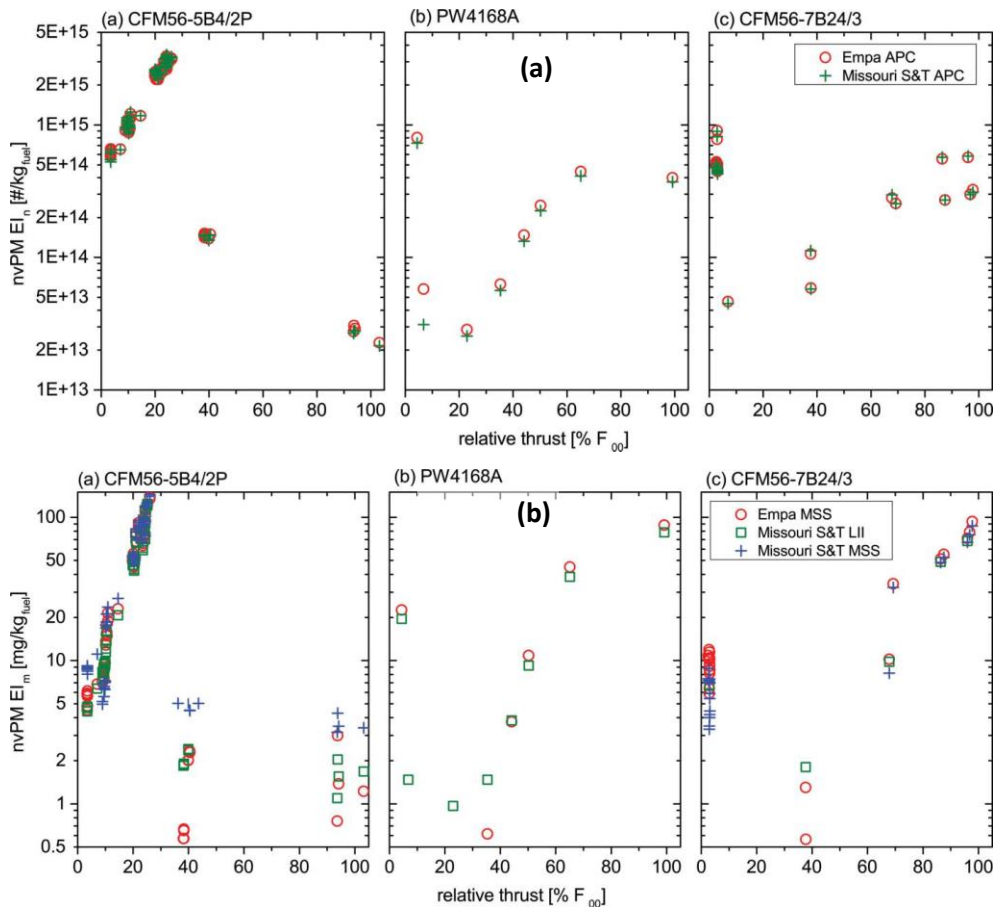


Figure 2-15: nvPM number- (a) and mass-based (b) emission indices as a function of engine operating conditions for three engines [51]

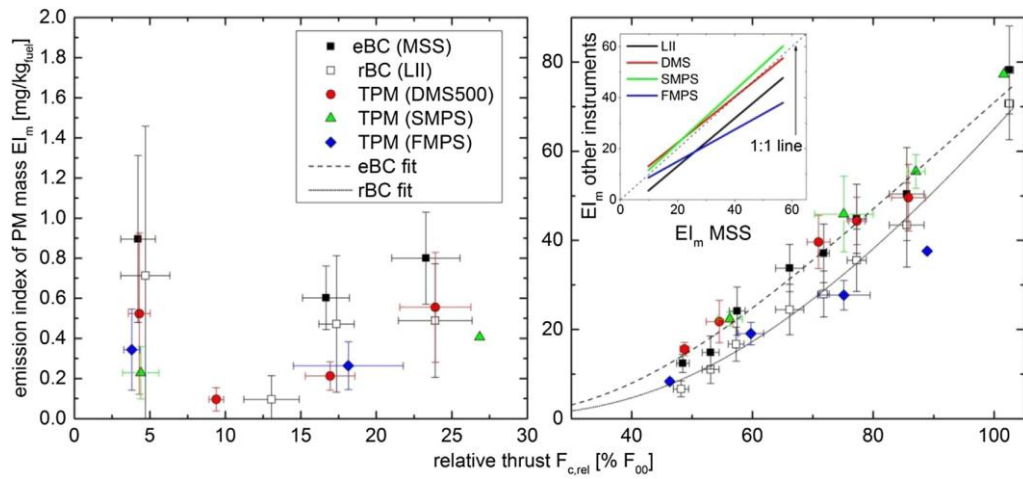


Figure 2-16: Comparison of mass emission indices from Black Carbon measurement (MSS, LII) and Total Particle measurements (DMS-500, SMPS, FMPS) at different engine thrusts [63]

It is observed from **Figure 2-14**, **Figure 2-15** and **Figure 2-16** that EIs correlations with thrust are engine specific and that the highest thrust doesn't necessarily correspond to the higher EI. In the literature, nvPM EIs quoted for aircraft engines vary by several orders of magnitude for both EI number and mass as highlighted by the figures below. This large difference can be explained by factors such as engine technology, age and efficiency, fuel type, atmospheric condition and sampling system which all impact on nvPM emissions and measurement.

2.7 Chapter Summary

The harmful effects of Particulate Matter (PM) produced by aircraft gas turbine on health and the environment are a growing concern. ICAO has recently implemented new guidelines for the sampling and measurement of aircraft nvPM for reporting purpose as a baseline for future regulation. This chapter has presented fundamental properties of aircraft PM, defining the concept of particle size, size distribution statistics, particle effective density and particle loss mechanisms occurring when being sampled. The methodology for system loss correction including the UTRC model and the SLT as prescribed by ICAO regulation were also discussed, along with uncertainty analysis basics used in this thesis and typical aircraft PM emissions reported in the literature.

3 Experimental Facilities and PM Instrumentation

Within the work presented in this thesis, several industrial and research-based facilities were used to perform experimental testing. These sites provided the opportunity for extensive PM characterisation on numerous aerosols sources, spanning from large-scale civil aviation aircraft engines to combustor rigs and laboratory aerosol generators. Various sampling systems and PM measuring analysers were employed.

This chapter discusses the instrumentation and sampling systems used most prominently to produce the results which are presented in later result chapters and briefly summarises the facilities of interest.

3.1 Aircraft engine exhaust PM measurements

Over the course of this thesis, multiple large-scale aircraft engine certification level emission testing has been attended. PM emissions were generally characterised using the ICAO compliant EASA/EU nvPM mobile reference system, also called 'EASA reference system'. This section discusses the different segments composing the EASA reference system and additional instrumentation employed to characterise aircraft PM.

3.1.1 ICAO compliant nvPM sampling and measurement system

As previously discussed, a nvPM sampling and measurement methodology has been standardised to permit the accurate reporting and comparison of nvPM emissions from aircraft engines [14]. The EASA reference system was designed in accordance with those standards and can be divided into five sections as represented in **Figure 3-1**. The 1st common point, primary diluter inlet and EEP are highlighted as they are important locations in the scope of this work. Section 1 represents the collection section including the sampling probe and short sampling lines (<8 m) where consequent aerosol cooling occurs. Sections 2 to 4 correspond to the remainder of the sampling system including the primary diluter and the 25 m sample line where the aerosol is further cooled and diluted. Section 5 refers to the various instruments measuring nvPM and gases (CO₂). A detailed overview of the compliant EASA system along with calibration and maintenance discussions is available in SAMPLE reports [50]. Example calibration certificates of instruments measuring PM are available in the Appendix (**10.1**).

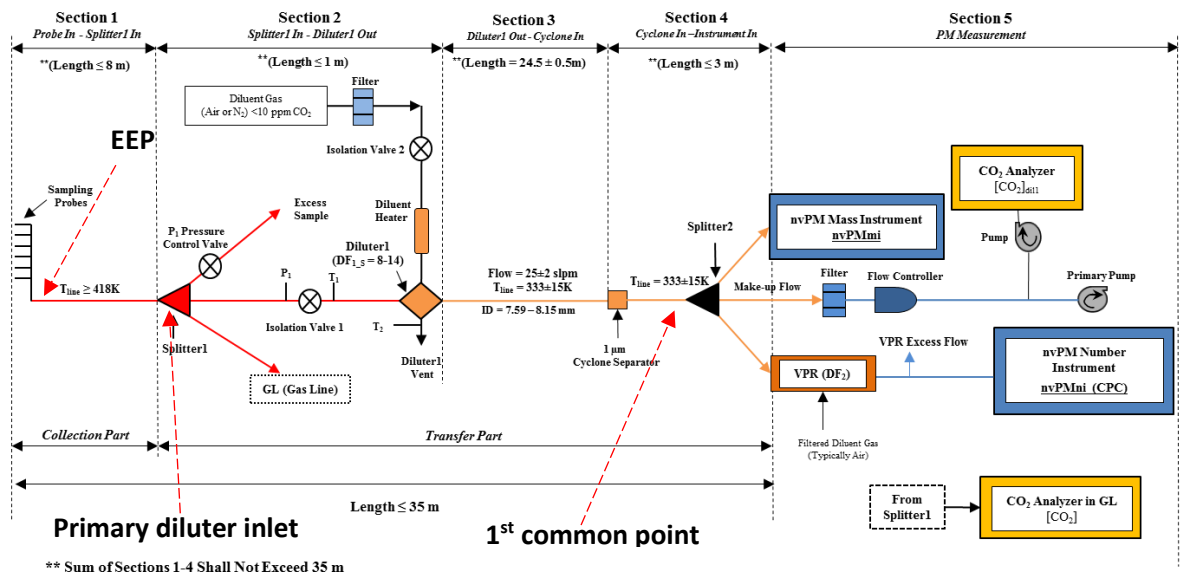


Figure 3-1: Overview schematic of an nvPM sampling and measurement system [59]

It is noted that although ICAO proposed regulation for compliant nvPM sampling systems was designed to standardise the sampling and measurement methodology, small variations are tolerated in sample line temperature, gas flow, pressure, dilution and dimensions [14] that can all result in additional nvPM measurement uncertainties. Lobo et al. [51] compared two ICAO compliant sampling systems as part of A-PRIDE 4 campaign and reported agreement within 6% for nvPM number and within 15% for nvPM mass. Inter-comparison between three ICAO compliant sampling systems was also performed during SAMPLE campaigns [50] which established that variability for nvPM number and mass emission indices was respectively $\pm 6\%$ and $\pm 9\%$.

3.1.1.1 nvPM Number measurement

ICAO regulation requires aircraft nvPM number concentration measurement to be determined using a system consisting of a volatile particle remover (VPR) and a n-butanol condensation particle counter (CPC) in series. The VPR shall be maintained at $350^{\circ} \pm 15^{\circ}\text{C}$ to evaporate volatile species and must include a dilution system (DF_2) to maintain particle number concentration within CPC single count mode and to reduce sample temperature to between 10°C and 35°C at the CPC inlet. Also, the VPR shall have a volatile removal efficiency so that more than 99.5% of tetracontane ($\text{CH}_3(\text{CH}_2)_{38}\text{CH}_3$) particles with an inlet concentration >10000 particles/ cm^3 at 30 nm electrical mobility diameter are removed.

Deposition of nanoparticles in the nvPM number measuring instrument is relatively high and size-dependent (Figure 2-11), thus requires regular calibration to ensure the accuracy of reported concentrations. The main mechanisms by which particles are lost are thermophoresis and diffusion in the VPR. Calibration is also required to verify volatile removal efficiency.

Table 3-1: Minimum allowed counting fractions of the VPR and CPC for nvPM number measurement

D_m [nm]	VPR _{15nm}	VPR _{30nm}	VPR _{50nm}	VPR _{100nm}	CPC _{10nm} (d_{50})	CPC _{15nm} (d_{90})
Minimum Penetration fraction [%]	30%	55%	65%	70%	50%	90%

Both the VPR and CPC are required to be calibrated annually to confirm each device meets the performance specifications prescribed by ICAO regulation, with the minimum penetration fractions listed in **Table 3-1**. The CPC counting efficiency must be determined with emery oil while the VPR is generally calibrated with a soot source (any solid particle can be used for VPR penetration efficiency calibration¹). It is noted that the ≤ 10 nm CPC 50% cut-off (d_{50}) was chosen based on measurements performed with different CPC's of cut points < 10 nm providing the same result when measuring aircraft exhaust PM using a compliant sampling system [12] and size distribution measurements showing that virtually no particles were observed < 10 nm downstream of the CS-VPR [48].

NvPM number measurement in the EASA reference system is performed using AVL Advanced Particle Counter (APC) in accordance with the regulation. It is hence composed of a CPC that counts particles and a VPR that cools, dilutes and denudes (i.e. remove volatiles) the sampled aerosol.

VPR:

The VPR consists of a primary heated dilution at 150°C (chopper diluter), an Evaporation Tube (ET) at 300-400°C including a Catalytic Stripper (CS), and a secondary cold dilution, as depicted in **Figure 3-2**. The primary heated dilution is necessary as it was shown that without thermal pre-treatment (i.e. hot dilution), some particle material could be modified in the evaporation tube of the APC, causing different losses to occur and hence inaccurate measurements [94].

It was also reported that PMP compliant VPRs, which don't include a CS didn't completely remove volatile peaks but instead reduced its GMD below < 23 nm [47], [95], [96]. Hence, the APC includes a CS assisting volatile removal via oxidation. It was proven that the addition of a CS downstream of a 350°C evaporation tube in a PMP compliant VPR allowed the efficient removal of volatile material ≤ 10 nm [47], [48], [97]. The secondary dilution is used to cool the aerosols within operation range of the CPC, prevent re-condensation and control the particle concentration. The APC

¹ if soot generated by a propane diffusion flame is used for particle generation, then a thermal pre-treatment device heated to 350°C may be needed to deliver only nvPM to the VPR

has numerous set points to control the dilution ratio (DF_2) from 100 to 2500:1 which enables continuous CPC measurement at the required more accurate single count mode [47].

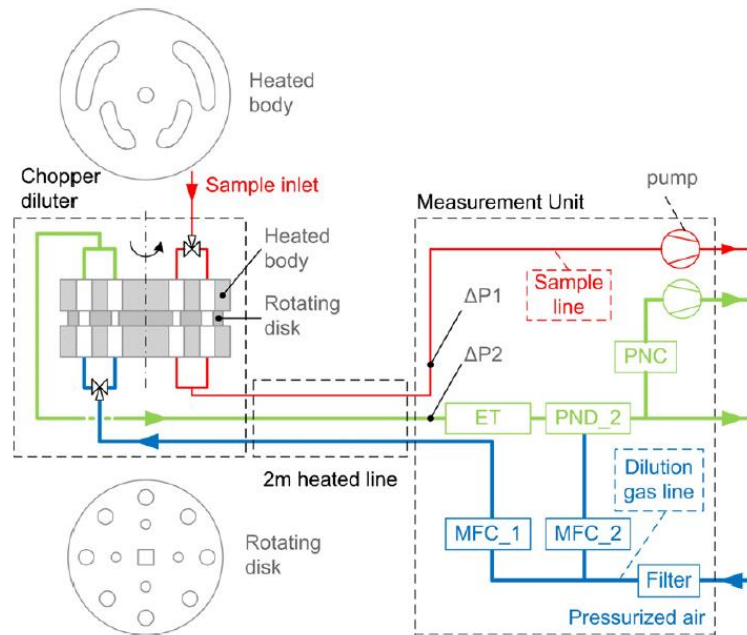


Figure 3-2: schematic of AVL Particle counter [47]

CPC:

Traditionally, aerosol particle number was measured using an Optical Particle Counter (OPC) which is comprised of photo-sensitive detectors analysing the scattering of a light source as particles are sampled through the analyser. The operating range of an OPC is typically in the micron range (>300 nm [98]) and hence is insensitive to typical aircraft PM. To address this issue, Condensation Particle Counters CPC were designed to enlarge nanoparticles to a detectable size through condensation techniques consisting in exposing the sampled particles to a super-saturated gas. The TSI CPC 3790E part of the EASA reference system uses butanol as its working fluid due to its high ratio thermal diffusivity to vapour diffusivity characteristics [99] and has a 50% cut-off diameter (d_{50}) of 10 nm and a 90% cut-off diameter (d_{90}) of 15 nm.

Uncertainty:

ICAO regulation requires the VPR dilution factor DF_2 at any time to be less than or equal to $\pm 10\%$ of the calibrated values and a CPC counting accuracy of $\pm 10\%$ from 2000 particles/cm³ to the upper threshold of the single count mode [14]. The resulting estimated nvPM number measurement propagated uncertainty from current regulation guidelines may be calculated as $\sqrt{10\%^2(\text{CPC}) + 10\%^2(\text{DF}_2)} = 14.1\%$.

3.1.1.2 nvPM Mass measurement

ICAO regulation defines nvPM mass as equivalent to Elemental Carbon (EC) and lists multiple requirements that instruments must meet for aircraft nvPM mass measurement. Mass analysers must be annually calibrated with the Thermal Optical Transmittance (TOT) method (NIOSH 5040) and must achieve mass concentrations within $\pm 10\%$ of the target EC mass specified which itself has a $\pm 16.7\%$ stated accuracy [100]. They must be insensitive to volatile PM and have a range of 0-1000 $\mu\text{g}/\text{m}^3$ with a resolution of 1 $\mu\text{g}/\text{m}^3$ or better. The resulting propagated nvPM mass uncertainty is $\sqrt{10\%^2 + 16.7\%^2} = 19.5\%$.

The ARTIUM Laser-Induced Incandescence analyser (LII300) and AVL Micro Soot Sensor (MSS) are used in the EASA reference system to measure nvPM mass and they both meet the requirements listed above. The two instruments measure nvPM by perturbing the emissions aerosol with near-infrared radiation efficiently absorbed by black bodies (i.e. soot) and observing different physical responses.

MSS:

The MSS operating principle is based on the photoacoustic effect [101]. It measures the black carbon mass of an aerosol by exposing it to an intensity modulated laser beam that is preferentially absorbed by soot particles. This induces a modulated heating and cooling of the gas surrounding black absorbing heated particles which generates an acoustic wave that can be measured by a sensitive microphone. The recorded sound wave is proportional to the light absorption coefficient and mass of soot in the aerosol.

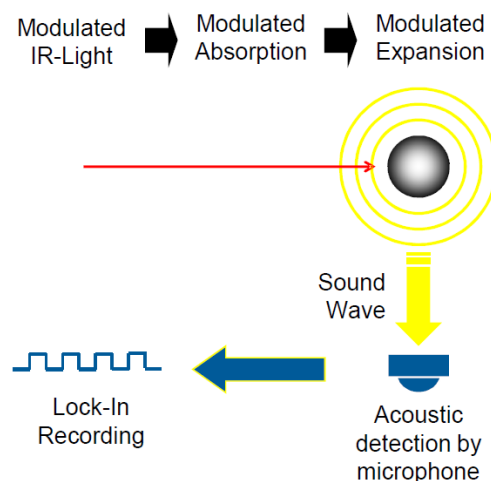


Figure 3-3: Diagram of the measuring principle of the AVL MSS [102]

LII300:

The LII300 uses a non-intrusive laser-induced incandescence method to measure black carbon mass [103]. Light absorbing particles (i.e. BC) are rapidly heated by a pulsed laser of high

energy causing them to heat to temperatures of up to 4500K, just below soot sublimation temperature. The thermal radiation (i.e. incandescence) emitted from the heated particles are detected by photodetectors. The recorded signals are converted to absolute intensities by calibration with a spectral radiance standard which are coupled with the temperature to obtain soot mass concentrations.

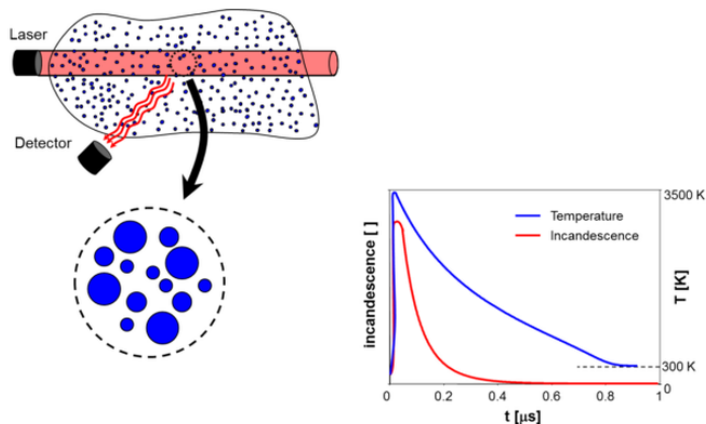


Figure 3-4: Simplified operating principle of the Artium LII-300 [104]

3.1.1.3 Dilution system

When sampling aircraft exhaust aerosols, dilution with dry filtered air is necessary for multiple reasons, namely: to prevent particle agglomeration by reducing the particle concentration per volume of gas, to cool the aerosol without additional thermophoretic losses, to dry the aerosol minimising risks of volatiles condensing onto the particles, to ensure mixing, and to draw exhaust samples without the need of a pump. ICAO regulation requires the use of an ejector-type diluter which are advantageous as they were proven to induce low additional nanoparticles losses, even when heated [105]–[108], as depicted in **Figure 3-5**.

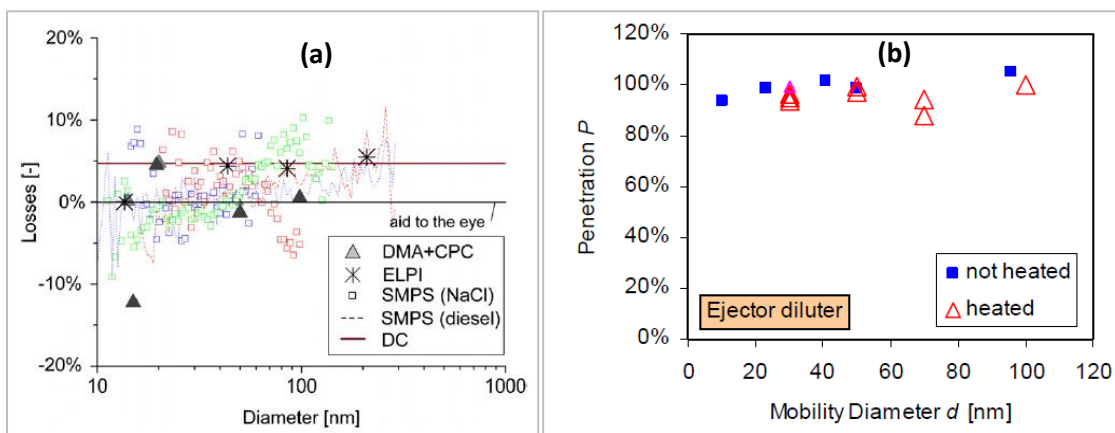


Figure 3-5: Ejector diluter losses of diesel exhaust particles measured with various instruments [105] (a) and ejector diluter's penetration efficiencies unheated and heated at 150°C [106] (b)

The minimum requirements for particle penetration fractions of an ICAO compliant ejector diluter are listed in **Table 3-2**. It is noted that CO₂ is generally used to measure the dilution factor of diluters as it is a stable gas and is relatively easy and accurate to measure.

Table 3-2: Minimum requirements for particle penetration efficiency in the primary diluter of an ICAO compliant sampling system [14]

Particle mobility diameter [nm]	15 nm	30 nm	50 nm	100 nm
Minimum particle penetration fraction	80%	90%	90%	90%

The diluter used in the EASA system is a DEKATI DI-1000 working on the ejection principle as illustrated in **Figure 3-6**. The sampled aerosol is drawn inside the diluter due to the pressure drop occurring at the nozzle where flow reaches high velocities.



Figure 3-6: Diagram of the ICAO compliant Dekati DI-1000 ejector [19]

3.1.1.4 Sampling lines

Sampling lines in an ICAO compliant sampling and measurement system are used to deliver the aerosol to the instruments and connect different parts of the sampling system. When sampling aircraft nvPM, the aerosol must be maintained above 60°C ($\pm 15^\circ\text{C}$) to prevent condensation and hence the sample lines are required to uniformly heat the transported gas. Also, to minimise electrostatic loss, the inner walls of the sample lines must meet the recommended anti-static resistance limits defined in ISO 8031:2009 [53]. Two wall materials are recommended for the heated sample lines:

- **Carbon loaded PTFE:** Carbon loaded PTFE (i.e. polytetrafluoroethylene) is one of the most suitable materials for sampling particles. In addition to being flexible and hydrophobic, it is an excellent dielectric, has a very low friction coefficient, and is non-reactive.

- **Stainless steel:** Stainless steel is an excellent alternative to Carbon loaded PTFE as it can support much higher temperatures and has a higher electrical conductivity. However, it is not as flexible and can be a significant inconvenience for mobile sampling systems.

The EASA reference system uses flexible Winkler WAKG heated lines with the inner wall made of carbon-loaded PTFE allowing sampling at temperatures up to 250°C. The active heating is provided via inductance through cables surrounding a layer of heat conductive stainless steel, as displayed in **Figure 3-7**. The lines are also electrically grounded to minimise any unwanted electrostatic behaviour.

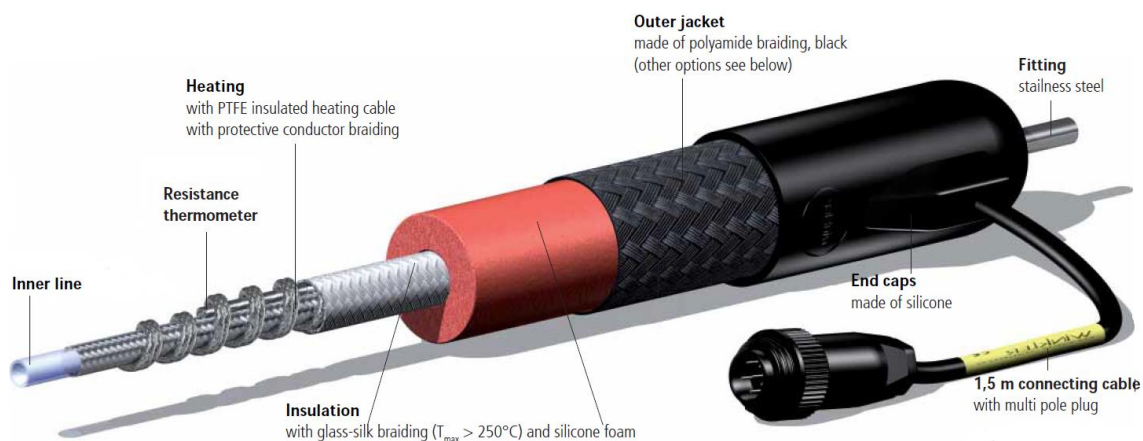


Figure 3-7: Heated line used in the EASA mobile system (where Carbon loaded PTFE is coating the inner walls) [109]

3.1.1.5 Cyclone

A cyclone is an inertial separator without moving parts using cyclonic separation to remove particulate from a gas or liquid stream through vortex separation. It is used in the EASA reference system near the analysers to remove the larger particles in an aerosol, preventing mass contamination from undesirable line shedding events. The cyclone prevents blockages of small orifices by eliminating particles larger than 1 μm (or 2.5 μm) entering the sampling tube and instruments. The two parameters of interest in a cyclone are:

- 50% Cut-off efficiency ($\eta_{50\%}$)
- Sharpness ($\eta_{84\%} / \eta_{16\%}$)

ICAO regulation requires a cyclone separator with a cut-off size of 1 μm and sharpness ≤ 1.25 is used at the outlet of 25 metres line.

3.1.2 Cleanliness and Background checks

Zero checks, also called cleanliness checks, are performed at the beginning and end of any aircraft exhaust measurement testing to ensure that the sampling system and measuring instruments are clean and leak-free. As described in ICAO regulation, a cleanliness check is performed by sampling HEPA (High Efficiency Particulate Air) filtered air via the primary dilution and measuring nvPM number and mass for 30 seconds. To pass the cleanliness check, the averaged nvPM mass and number concentrations shall respectively be less than $1 \mu\text{g}/\text{m}^3$ for the nvPM mass and $2 \text{ particles}/\text{cm}^3$ for nvPM number. It is noted that given the EASA reference system nvPM number analyser (AVL APC) runs an online dilution prior to the CPC (as is the case for any ICAO compliant system), a measured number concentration of $2 \text{ particles}/\text{cm}^3$ actually corresponds to a concentration of $\sim 130 \text{ particles}/\text{cm}^3$ at the inlet of the instrument given the lowest dilution factor setting is of the AVL APC ~ 67 .

Ambient/background nvPM measurements are also performed to characterise representative concentrations from the air entering the aircraft engine. Lobo et al. [9] showed that background PM could reach number concentrations above $10^6 \text{ particles}/\text{cm}^3$ on airport runways although it is noted that engine tests are generally performed in test beds where the background PM is much lower.

3.1.3 Particle size measurement

Particle size distribution measurements, while not currently prescribed by ICAO regulation, were regularly performed during aircraft exhaust aerosol measurements and on other laboratory experiments presented in this body of work. Size measurements were generally carried out using a Cambustion Ltd DMS-500 which is a fast response Differential Mobility Spectrometer permitting the measurement of nanoparticles in the 5-1000 nm range. In this section the features, operating principle, outputs and calibration of DMS-500 are described.

The DMS-500 is comprised of a $1 \mu\text{m}$ cyclone at its inlet preventing micron size particles from contaminating the readings. It includes an optional 5 metres heated arm with an annular type primary dilution and a secondary chopper diluter inside the main unit allowing sample dilution of up to 3000 and sampling of hot aerosol as presented in **Figure 3-8**, permitting aerosol measurements at concentrations between 10^3 and $10^{11} \text{ particles}/\text{cm}^3$.

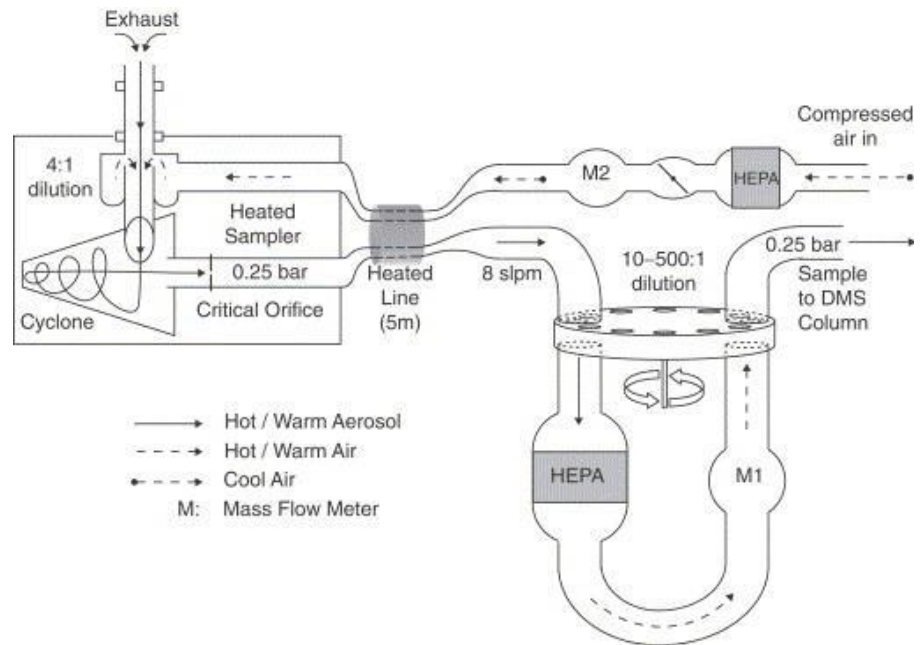


Figure 3-8: Illustration of the DMS-500 sampling system with the two dilution stages and the 5m heated line [8]

The analyser requires an inlet flowrate of 1.2-8 standard Lpm depending on the dilution ratio used. It also operates a 0.25 bar pressure, reducing losses within the unit by reducing residence time and isolating the instrument from fluctuating sample pressure. The sensitivity of the DMS-500 is dependent on the dilution used, the sampling frequency and the particle size as illustrated in **Figure 3-9**.

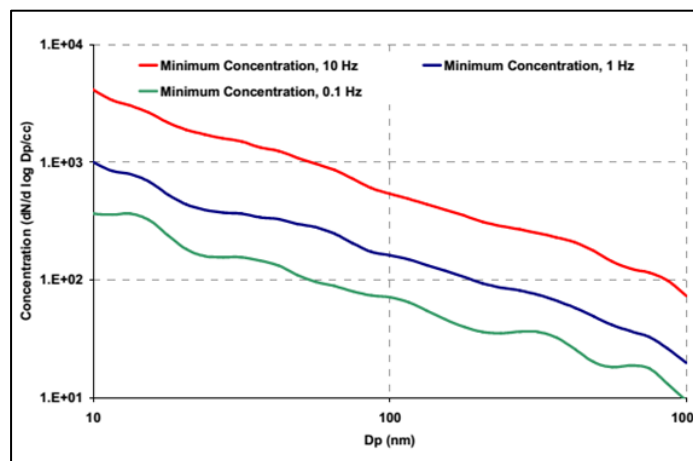


Figure 3-9: DMS-500 sensitivity limits at different measurement rates with no dilution [110]

3.1.3.1 Electrical classification theory

Particle size distributions are measured in the DMS-500 by charging the sampled aerosol using a unipolar diffusion charger (corona discharge) and measuring the current generated by particles deflecting onto electrometer rings in a classifier column when subjected to a strong

electrical field, as shown in **Figure 3-10**. A particle's trajectory in the classifier is a function of their charge to drag ratio (i.e. electrical mobility) and can be translated into particle number and size data. Indeed, when a charged particle suspended in a gas is placed in an electric field, the particle experiences a force which is dependent on its charge and the strength of the electric field. This force causes the particle to accelerate along the electric field lines. This acceleration is opposed by viscous forces within the fluid, which are dependent on fluid viscosity and particle size and increase with increasing particle velocity. Thus, a particle reaches its terminal velocity when electrical and viscous forces are balanced. Electrical mobility is described by the following equation derived from Stokes' law:

$$\text{Electrical mobility} = \frac{\text{Electrostatic force}}{\text{aerodynamic drag}} \rightarrow Z_p = \frac{n \cdot e \cdot C_c}{3 \cdot \eta_{vis} \cdot d_p} \quad (3.1)$$

where Z_p is the electrical mobility [$\text{m}^2/\text{V}/\text{s}$], n is the number of charges on the particle, e is the elementary charge [C], C_c is the slip correction factor, η_g is the dynamic viscosity of air and d_p is the particle diameter [m].

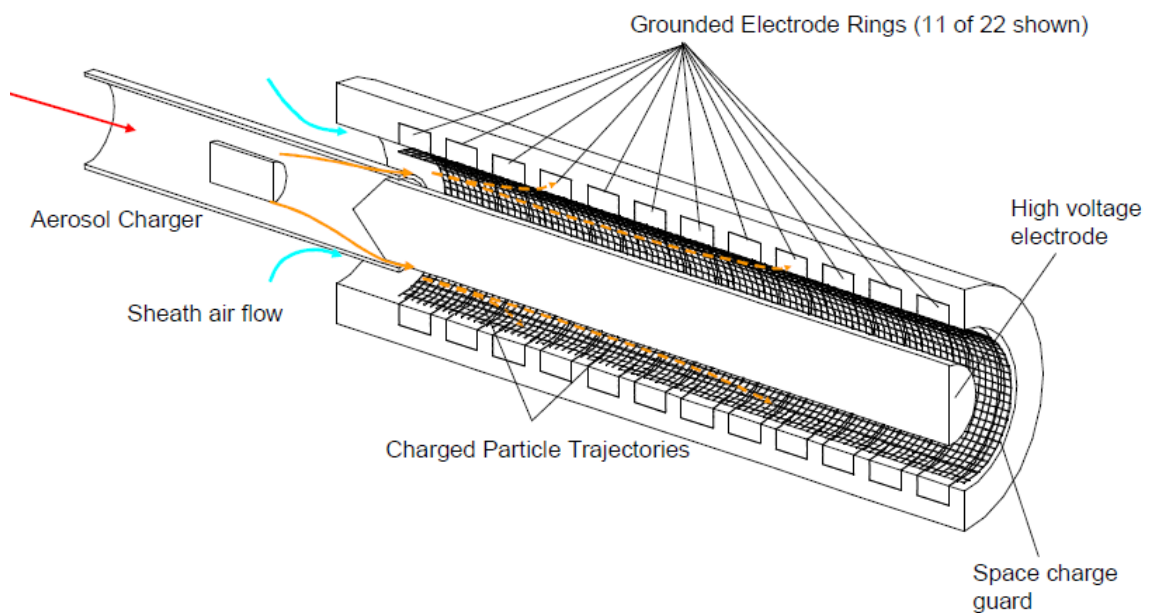


Figure 3-10: Diagram of the DMS-500 classifier column [111]

3.1.3.2 DMS-500 Outputs:

The DMS-500 measures the sampled aerosol size distribution and outputs the total number concentration, GMD and GSD which are derived from the discrete $dN/d\log d_p$ spectrum respectively using equations (2.3), (2.2) and (2.4) as previously discussed. The main outputs of the DMS-500 can be separated in two categories [112]:

- **Discrete spectrum data:** The spectral output by the DMS-500 is a ‘discrete’ approximation to the continuous spectrum made of triangular bins, with outputted aerosol statistics of the discrete spectrum (total number concentration, GMD, GSD and CMD).
- **Aerosol mode data:** In parallel with the discrete spectrum data inversion, the DMS-500 outputs summary information of the main peak lognormal mode (aerosol mode number concentration, CMD, GSD) corresponding to a lognormal function which would best give the measured ring current. Its accuracy depends upon whether the aerosol mode is truly lognormal.

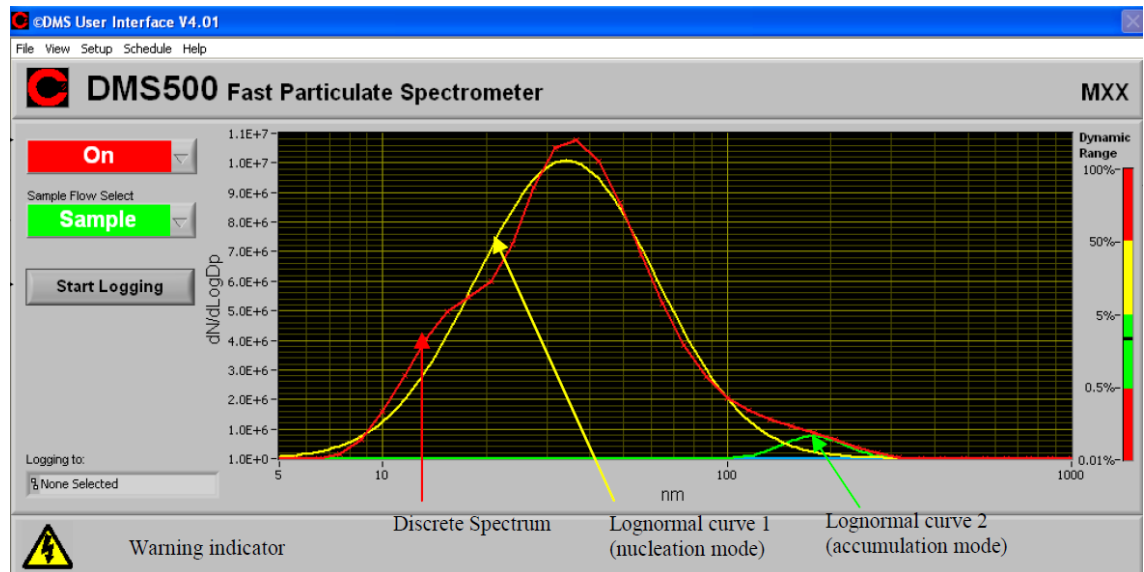


Figure 3-11: Screenshot of the DMS-500 user interface displaying the measurement of a bimodal size distribution [112]

3.1.3.3 DMS-500 Calibration:

Given particle size is relative to its morphology and the means by which it is measured, the DMS-500 requires to be calibrated to provide accurate particle size measurements. Several calibration inversion matrices are made available by the manufacturer, each specific to a particle type or analysis methodology. To calibrate the DMS-500 for particle size and number, a transfer function mapping particle size to ring currents is modelled using aerosol properties, sheath flows, unipolar diffusion charger characteristics, and classifier column voltage, pressure, temperature and geometry [111]. After the DMS has been checked for correct operation, the transfer function is empirically adjusted with real aerosols. The DMS calibration procedure is similar to the calibration procedure generally used for CPC [113], with particle size selected using a DMA and counted with a standard electrometer. An electrometer is used instead of a CPC because of the minimal practical concentration for particle measurement generally being too high for most CPCs to operate in

photometric mode ($> 10^4$ particles/cm³). It is noted that particle losses occurring in the heated line and chopper diluter when used are not corrected for in the calibration.

The DMS-500 is calibrated for spheres and fractal particles in the nanometre range using a variety of particle generation methods listed below (it is noted that fractal particles were shown to converge with spheres at mobility diameter below 80 nm) [111]:

- Nebulised & nucleated classified sulphuric acid (spherical calibration): 5-50nm (GMD~15 nm)
- Nebulised classified sodium chloride (spherical calibration): 50-300 nm (GMD~50 & 100 nm)
- NIST Traceable PSL spheres (spherical calibration): 300-1000 nm
- Classified soot from Jing Mini-CAST generator (fractal/soot calibration): 50-300 nm (GMD~50, 75, 100 & 200 nm)

The transfer functions generated from calibration for different particle types are listed below, with results derived from the discrete spectrum and the lognormal fit of the aerosol mode:

- Monomodal: spherical calibration for discrete spectrum and lognormal fit (unconstrained)
- Monomodal aggregates: soot calibration for discrete spectrum and lognormal fit
- Diesel: spherical calibration for discrete spectrum, constrained lognormal fit with sphere calibration between 10-35 nm (nucleation mode) and constrained lognormal fit with soot calibration for second peak (accumulation mode)
- GDI: spherical calibration for discrete spectrum, constrained lognormal fit with sphere calibration between 10-35 nm (nucleation mode) and constrained lognormal fit with sphere calibration for second peak (accumulation mode)

Bimodal calibration files are also available where the discrete spectrum remains unchanged but two lognormal peaks are fitted to the data.

3.1.4 Measurement of nanoparticles in a liquid

In the scope of this thesis, particles were sometimes characterised when suspended in a liquid. The Zetasizer Nano ZS and Nanosight LM10 from Malvern instruments were both utilised for this purpose. Both instruments use technologies that rely on Dynamic Light Scattering (DLS) theory as discussed below.

- **Zetasizer Nano ZS (DLS)** [114]:

The Malvern Zetasizer Nano ZS is an instrument with a 633 nm He-Ne laser that uses DLS to measure physical properties of nanoparticles in suspensions. It can measure particle hydrodynamic diameters down to 0.3 nm, particle size distributions, zeta potentials and other properties such as

the sample conductivity and mobility. Some important aspects of the instrument are described below:

- The original size distribution information is intensity weighted and obtained from a DLS measurement which requires the knowledge of the liquid viscosity and refractive index. To transform the intensity size distribution into a volume and number size distribution, the particle refractive index and absorption are needed, and the assumptions of sphericity and uniform density are made.
- The recommended concentration for particles ranging from 10 nm to 100 nm varies from 0.1mg/L up to 5% of the total suspension mass.

- **Nanosight LM10 (NTA)** [115]:

The Malvern NanoSight LM10 combines the properties of both light scattering and Brownian motion (DLS) in order to obtain the size distribution and concentration measurement of particles in liquid suspensions. A laser beam is passed through the sample chamber, and particles in the path of this beam scatter light in such a manner that they can easily be visualized via a magnification microscope onto which a camera is mounted. The camera tracks individual particles undergoing Brownian motion and calculates their hydrodynamic diameters using equation (3.2), with particle movements varying according to their size. It makes an absolute measurement method that doesn't require any calibration. This technique is called Nanoparticle Tracking Analysis (NTA) and can extract particle number concentration, size and polydispersity. Some important aspects of the instruments are described below:

- The particle concentration in the suspension should be: $\sim 10^6 < \text{sample} < \sim 10^9$ particles/cm³ which should correspond to 20-100 particle in the field of view of the camera.
- The sample should not be visibly too concentrated (it can be sonicated and filtered prior to analysis).
- Polydisperse and low concentration samples need to be captured for longer to generate more accurate data.

3.1.4.1 Dynamic Light Scattering theory

DLS, also known as Photon Correlation Spectroscopy (PCS) or Quasi-Elastic Light Scattering (QELS), is a non-destructive technique used to characterise nanoparticles dispersed in liquids. Unlike static light scattering, it can yield size information down to the tens of nanometres by measuring the

speed at which the particles are diffusing due to Brownian motion from scattered light fluctuations when illuminated [62, p. 281]. DLS relies on Rayleigh isotropic scattering theory for particle less than $1/10^{\text{th}}$ of the laser wavelength and Mie scattering theory for particles more than $1/10^{\text{th}}$ of the laser wavelength to convert measured scattered light intensity into particle size and volume data [116]. DLS measures the particle hydrodynamic diameter (d_h) that can be calculated using the following equation derived from the Stokes-Einstein relation:

$$d_h = \frac{kT}{3\pi\eta_{vis}D} \quad (3.2)$$

With d_h the hydrodynamic diameter defined as the diameter of a hard sphere that diffuses at the same speed as the particle being measured, D the diffusion coefficient, k Boltzmann constant, T the absolute temperature and η_{vis} the liquid dynamic viscosity.

Notable uncertainties arise from the measurement of d_h using DLS theory as discussed below:

- Given the intensity of scattered light is proportional to a sixth of the power of the particle diameter ($I \propto d_p^6$), DLS doesn't precisely resolve multi-modal and polydisperse sample because the scattered intensity of larger particles will strongly overlay that of smaller particles [117].
- The apparent size measured by DLS can be affected by the media conductivity, the particle surface structure and morphology [116]:
 - If the liquid medium has a low conductivity (i.e. low ionic concentration), an extended double layer of ions will be produced around particles, reducing the diffusion speed and resulting in a larger, apparent d_h .
 - If a layer of absorbed polymers coats the surface of particles, the diffusion speed and in turn the apparent size can be changed by several nanometres.
 - The d_h of a non-spherical particle is the diameter of a sphere that has the same translational diffusion speed as the particle. If the shape of a particle changes in a way that affects the diffusion speed, then the d_h will change. For example, small changes in the length of a rod-shaped particle may directly affect the size, whereas changes in the rod's diameter, which will hardly affect the diffusion speed, can be more difficult to detect.
- DLS tends to overestimate the width of the peaks in the intensity-weighted distributions and this can be magnified when transforming the weight of the distributions to volume and number. Thus, the volume and number size distributions should only be used for estimating the relative amounts of material in separate peaks as the means and particularly the widths are less reliable.

3.1.4.2 Zeta potential

Zeta potential is a physical property referring to the electric potential difference between the dispersion medium and the stationary layer of fluid attached to the dispersed particle [118]. It is derived from electrophoretic mobility measurement and the Henry equation and used to describe the stability, or state of agglomeration, of solid particles in a liquid solution. The higher the absolute value of the zeta potential, the more they repulse each other and the more stable the suspension. When measuring a zeta potential between -30 and +30 mV, the suspension is assumed unstable and particles are expected to agglomerate over time.

3.2 Aerosol generation and conditioning techniques

As an alternative to aircraft PM generated from a gas turbine engine which is expensive and logistically difficult to operate, a significant body of work in this thesis used alternative aerosol generation (nebuliser, graphite generator) and conditioning techniques (centrifugation, diffusion screen, aerodynamic classification) for experimental work, as discussed in this section.

Table 3-3: Literature using Collision nebuliser to generate nanoparticles for loss experiments

Author	Particle generated	Deposition mechanism investigated
Romay et al. [86]	NaCl & PSL (100-700 nm)	Thermophoresis
Tsai et al. [119]	NaCl (40-500 nm)	Thermophoresis
Muñoz-Bueno et al. [84]	NiO (20-200 nm)	Thermophoresis
Brugiere et al. [85]	PSL (30-600 nm)	Thermophoresis
Lin et al. [120], Yin et al. [121]	Oil (8-550 nm)	Bend/inertial loss
Yin and Dai [122]	Oil (6-550 nm)	Diffusional loss
Kumar et al. [76]	NaCl (5-200 nm)	Diffusional loss
Tsai [123]	NaCl (10-100 nm)	Diffusional loss
Cheng et al. [108]	NaCl, DOP (20-400 nm)	Losses in an ejector diluter
Giechaskiel et al. [105]	NaCl (30-100 nm)	Losses in an ejector diluter

Comprehensive experimental works are found in the literature characterising nanoparticles behaviours. In these studies, the authors generated nanoparticles using numerous methods. The aerosol generation technique most commonly discussed is the nebulisation of a solution containing either suspended solid particles or a dissolved chemical solute in a particle-free solvent (**Table 3-3**). Nebulisation operates by generating very small droplets which are subsequently suspended in a 'dry' carrier gas. Upon evaporation of the solvent, solid particles consisting of either the suspended solid

or the solute are present in the gas flow. Another popular aerosol generation method is the evaporation-condensation technique, which consists of evaporating a solid material, generally in the form of powder, then quenching the vapour to produce nano-particles [78], [124]–[126].

Other aerosol generation processes used in the literature include spark discharge generators (section 3.2.3), blender feeders, heated wire and the direct sampling of combustion exhaust like Diesel engines or diffusion flames (e.g. Jing CAST [127]).

3.2.1 Nebuliser

Nebulisation of colloidal suspensions necessitate atomisation of a liquid solution containing solid nanoparticles, or soluble material. A nebuliser, also referred to as atomiser, produces small droplets containing particles which evaporate shortly after atomisation in a ‘dry’ carrier gas, resulting in particles transported in the gas flow. Droplet evaporation can be aided with a furnace, a membrane drier, or simply by ensuring the carrier gas is well below its saturation limit for the liquid used as the solvent. This methodology is commonly used in medicine research studies [128] (drug delivery, health impact of harmful nano-particles, etc) and to test particulate filter efficiency [129]. Advantages of liquid atomising techniques for nanoparticle generations are numerous, namely low cost, availability of a wide range of particle size, composition and morphology, and suspensions are generally already characterised by manufacturers using techniques such as SEM/TEM and DLS (section 3.1.4.1).

There are a number of nebuliser technologies commercially available discussed in the literature, with brief descriptions of their operation presented below:

- **Ultrasonic nebulisers** (i.e. ultrasonic spray pyrolysis [130]): High frequency ultrasound is propagated through the liquid suspension, forming small micro-droplets by impinging on the liquid-gas interface.
- **Electrospray**: An electric field is used to disperse the liquid suspension, producing a controllable monodisperse droplet distribution [131], [117]. Electrosprays have been demonstrated to produce mono-modal sub-micrometric droplets down to 100 nm. However, suspensions of specific electrical conductivity are required [132].
- **Collision Nebuliser** (i.e. Pneumatic, Air-blast): Compressed air is ejected through a small orifice nozzle, sucking a liquid into a small mixing chamber, the high velocity air jet subsequently atomising the liquid into droplets [62, p. 458], [133],[132]. The use of an impaction plate at the exit of the nebuliser orifice can prevent the escape of larger droplets, reducing the droplet size distribution [117], [132]. This form of nebuliser with impactor has

been shown to produce a stable stream of aerosolized particles and can be used with a wide variety of suspensions (**Table 3-3**).

In this thesis, a Topas ATM-226 atomiser aerosol generator [134] (collision type nebuliser) was used to generate nanoparticles as discussed in section 4.1. The calibration certificate of this nebuliser is available in the appendix (10.2).

3.2.2 Centrifugation of suspensions

When characterising liquid suspensions, centrifuges can be used for nanoparticle separation and conditioning. Subject to a centrifugal force, particles present in a suspension will sediment towards the centre of the centrifuge (i.e. bottom of the vial) at a rate depending on their density and size, as depicted in **Figure 3-12**. The larger and denser the particles, the faster it will sediment.

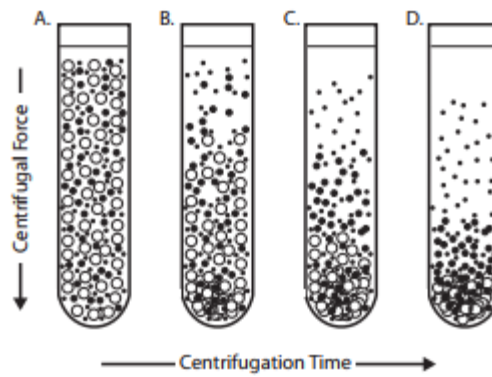


Figure 3-12: particles of different densities or size observed to sediment at different rates [135]

The sedimentation velocity in a centrifuge can be derived from Stokes' law using the centrifugal acceleration definition $a = r \cdot \omega^2$ with r the radius of rotation [m] and ω the speed of rotation (angular velocity) [rad/s]:

$$v_c = \frac{d_p^2 \times (\rho_{\text{particle}} - \rho_{\text{liquid}})}{18\eta_{\text{vis}}} \times r\omega^2 = \frac{d_p^2 * (\rho_{\text{particle}} - \rho_{\text{liquid}})}{18\eta_{\text{vis}}} \times r \frac{2\pi \cdot \text{RPM}}{60} \quad (3.3)$$

with v_c the sedimentation velocity in [m/s], d_p the particle diameter in [m], ρ_{particle} and ρ_{liquid} the densities of the particle and the liquid in [kg/m³] and η_{vis} the viscosity of the liquid in [kg/m/s].

The centrifugal force of a centrifuge is generally expressed in Relative Centrifugal Force (RCF) or Round Per Minute (RPM), with conversion from one to the other defined as followed:

$$\text{RCF} = 11.18 \times r[\text{mm}] \times \left(\frac{\text{RPM}}{1000}\right)^2 \quad (3.4)$$

3.2.3 Graphite Aerosol Generator

Carbonaceous nanoparticles can be generated in a laboratory setup using graphite generators. The PALAS Graphite Aerosol Generator GFG 1000 (i.e. spark discharge generator) is one of such, producing soot-like particles utilising spark discharge at a high voltage between two graphite electrodes, as presented in **Figure 3-13**. The electrodes are shielded in a non-reactive argon atmosphere to avoid carbon oxidation [136]. The carbon evaporated from the graphite electrodes condenses into very small primary particles ~ 5 nm [85], [137] with densities around 2 g/cm^3 [138] that subsequently coagulate into bigger agglomerates. This generator can be used as a surrogate for atmospheric and combustion soot and has been demonstrated to maintain constant operation over time periods of several hours [137], [138] and [136].

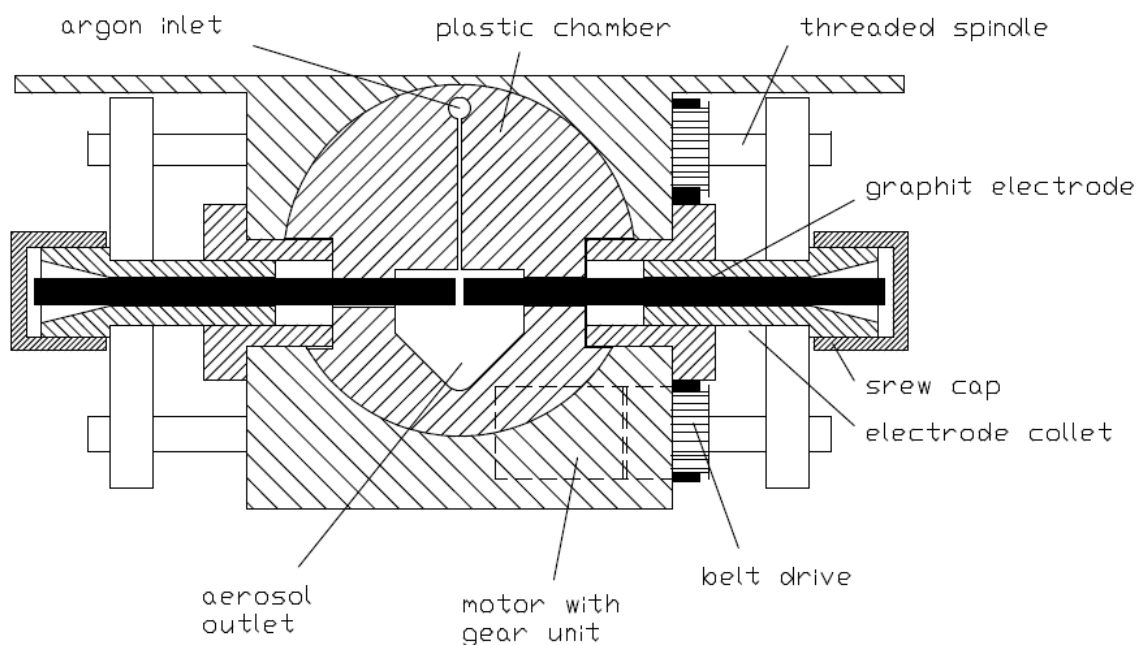


Figure 3-13: Diagram of the mechanical arrangement of the electrode unit inside a PALAS GFG 1000 [136]

The size and number concentration of the aerosol leaving PALAS generator is mostly controlled by the coagulation process of the primary particles into larger agglomerates which can be modified by adjusting the Argon flowrate, dilution air flowrate and storm current (spark frequency-SC). Characterisation of the PALAS generator was performed using a Cambustion DMS-500 (section 3.1.3). It was determined that the GFG-1000 could be used to produce stable aerosol with particle GMD ranging between 20 and 100 nm and associated GSD ranging from 1.4 to 2.2 at total number concentrations of 10^6 - 10^9 particles/cm³. Examples of particle size distributions produced by the PALAS generator for different settings can be found in **Figure 3-14**.

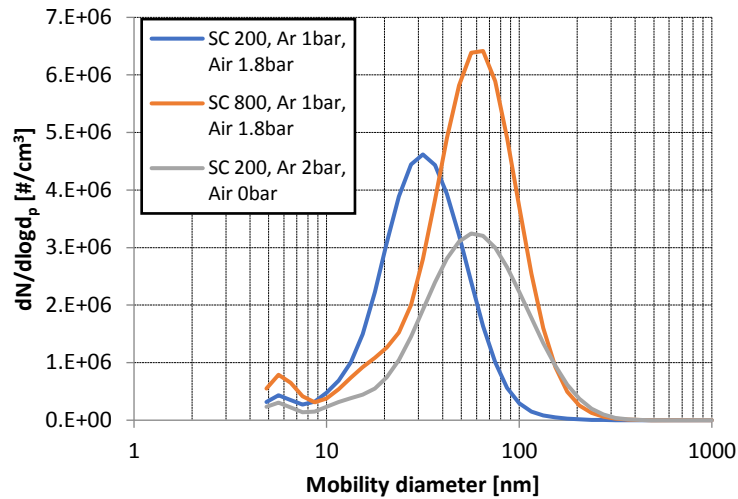


Figure 3-14: Particle Size distributions generated PALAS graphite aerosol generator at different settings and measured by a DMS-500 (SC=Spark Frequency)

3.2.4 Aerodynamic aerosol classification

Classification techniques were used in laboratory experiments to size-select aerosols. The Combustion Aerodynamic Aerosol Classifier (AAC) is a relatively novel instrument (released in 2016) using centrifugal force to classify particles of a polydisperse aerosol according to their aerodynamic diameter [139]. Combined with a particle counting instrument, the AAC can be used to determine an aerosol particle size distribution. Mass distribution, effective density and other properties of a polydisperse aerosol can also be determined when pairing and AAC with a DMA/CPMA [139].

In the AAC, the inlet aerosol is mixed with sheath air transporting the aerosol through the classifier and controlling particle's residence time, as highlighted in **Figure 3-15**. Centrifugal force applied to particles is controlled by the classifier rotational speed and compels particles to migrate differently depending on their aerodynamic diameter directly proportional to the particle relaxation time (equation (2.16)) [140]. Particles larger and smaller than the chosen set-point are lost to the walls and excess flow respectively while particles of the desired size exit the AAC as a 'truly monodisperse' aerosol.

Detailed studies on the theory of centrifugal classification and validation of the AAC with transfer function predictions were performed by Tavakoli and Olfert [140], [141] and by Johnson et al. [142].

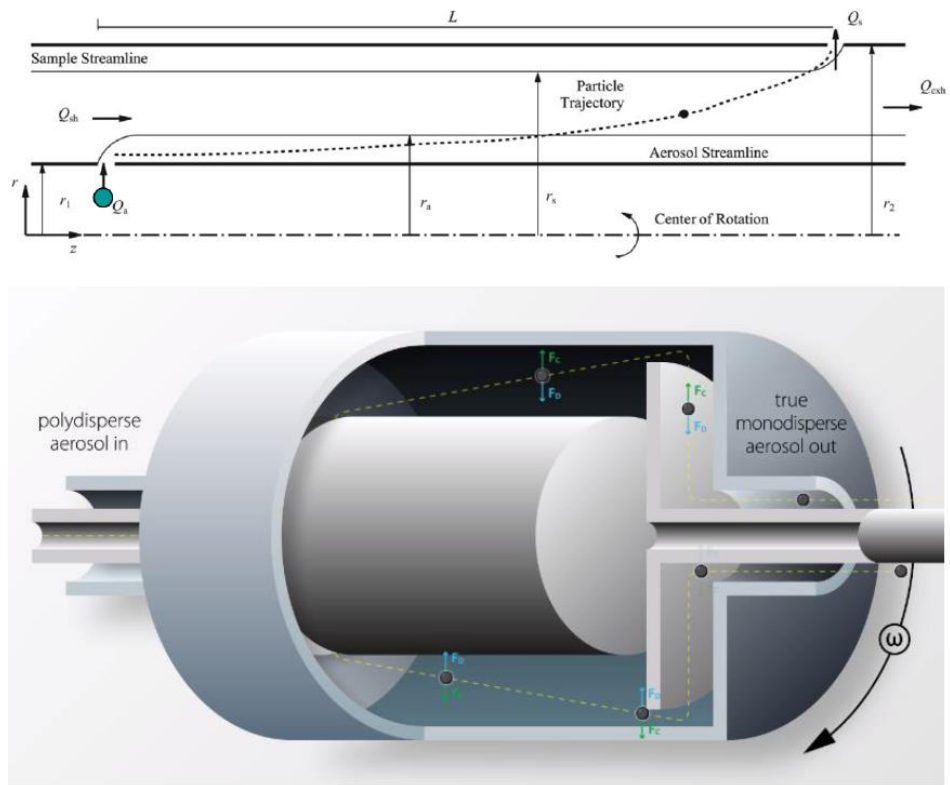


Figure 3-15: Diagram of the principle of operation of the Combustion Aerodynamic Aerosol Classifier [77]

3.2.5 Diffusion screens

Aerosol size distributions were also classified by using stacked diffusion screens inducing diffusional losses and hence removing the smaller portion of the aerosol distribution [143]. A TSI Particle Size Selector (PSS) 376060 was used consisting of a cone assembly capable of holding up to 23 diffusion screens. By knowing the mesh size, wire radius, number of screens and the flowrate, it is possible to predict the penetration efficiency through the stack of screens (**Figure 3-16**).

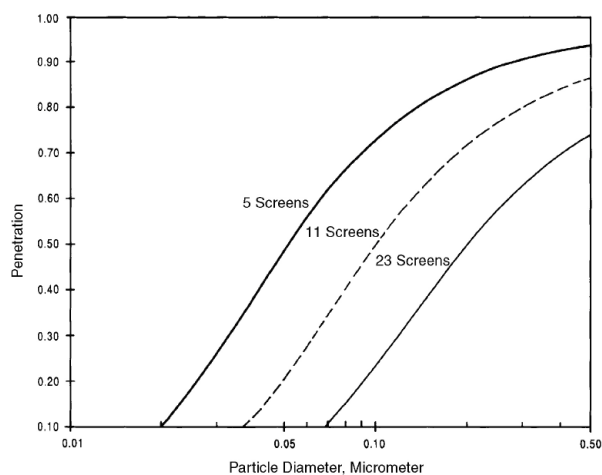


Figure 3-16: Theoretical penetration efficiency through the PSS using 5, 11 and 23 wire-mesh screens [144]

3.3 Large-scale certification level engine testing

Over the course of this work, multiple certification level emission measurements using a fully ICAO compliant sampling system (**Figure 3-1**) were performed on large-scale gas turbine engines from Rolls-Royce Derby, Rolls-Royce Deutschland and Safran. Due to proprietary reasons, only data from Rolls-Royce engines is considered in this thesis. The data, discussed in chapter 6 and 7, represent seven engines corresponding to four engine types with nvPM emissions measured using three different test beds and two ICAO compliant sampling probes. Additional particle size measurement was performed with a Cambustion DMS-500 within the EASA reference system.

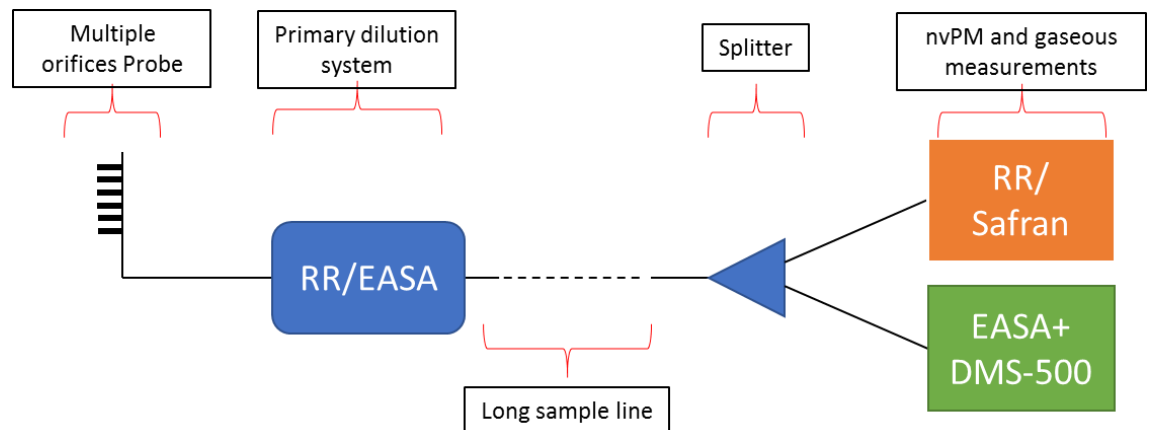


Figure 3-17: Simplified diagram of an ICAO compliant sampling system used during large-scale engine testing

These tests generally consisted of an aircraft engine suspended in a test bed (**Figure 3-18**) with a sampling probe positioned in the exhaust of the engine and the primary dilution located within the test bed facilities. A long sample line transported the sampled aerosol outside of the test bed to the nvPM measuring instrument as presented in **Figure 3-17**.

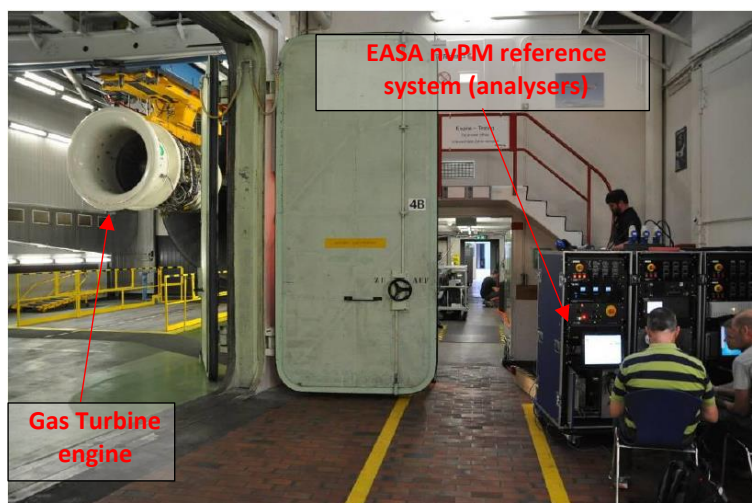


Figure 3-18: Photograph of the EU/EASA Mobile Reference System location next to SR Technics test cell [49]

3.4 Other engines and experimental Rigs

Additional PM measurements discussed in this work were performed on smaller engines and combustion rigs as discussed below, with **Figure 3-19** depicting the typical setup.

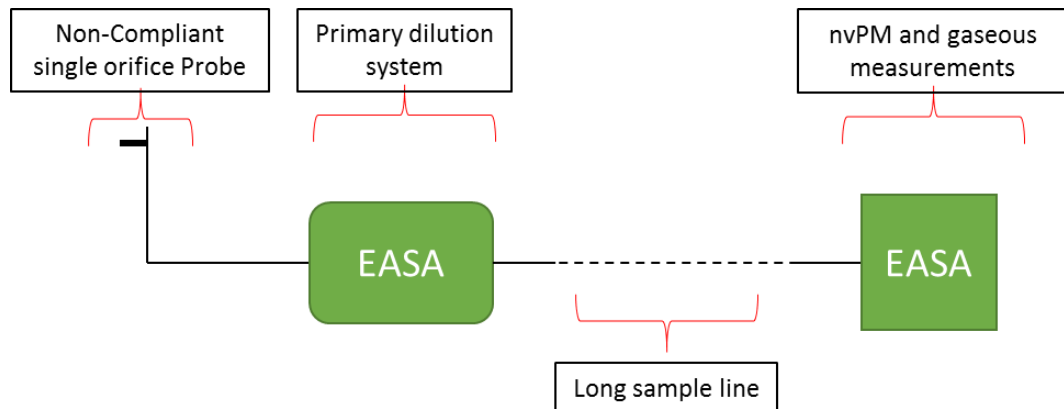


Figure 3-19: Simplified diagram of the sampling system used during PM measurement on multiple engines and combustion rigs

Gas Turbine Research Centre (GTRC) – Cardiff University:

The GTRC is an academic multi-purpose combustion facility for research and development of combustors located in Port Talbot, South Wales. The centre comprises an RQL combustion rig which allows the investigation of exhaust emissions at different combustors operating conditions (AFR, temperature, pressure) using different fuels and atomisation nozzles. The impact of alternative fuel and humidity on nvPM emission was investigated on the RQL at the GTRC.

GNOME engine – Rolls-Royce Derby:

Emission characterisation of large-scale aircraft gas turbine is expensive and rarely performed other than during engine certification. As a more affordable alternative, the Strategic Research Centre based at Rolls-Royce has built a real gas turbine experimental rig using a Rolls-Royce GNOME engine as shown in **Figure 3-20**, permitting the extensive study of gas turbine engine emissions. The GNOME single spool turboshaft helicopter engine is composed of an annular combustor and a ten stage all-axial compressor. Density and volatility of particles emitted by the Rolls-Royce GNOME engine have been extensively investigated [72].

In this thesis, work performed using this engine include nvPM mass, number and size comparison with different instruments and the calibration of nvPM mass analysers. It was generally operated using commercial aircraft kerosene (jet A) fuel and particulate emissions were varied by changing the engine power conditions from low to high (throttle settings from 11,000 revolutions per minute to 21,000 rpm).



Figure 3-20: Photograph of a GNOME gas turbine rig with sample lines [19]

Low Carbon Combustion Centre (LCCC) – Sheffield University:

The LCCC is an academic research facility targeting research experiments across different areas of combustion. Within this body of work, nvPM measurements performed on a small-scale aviation engine (APU) at the LCCC using blends of conventional and alternative fuels are discussed. Several studies characterising particulate emission of the LCCC APU are available in the literature [71], [73], [145].

An auxiliary power unit (APU) is a small gas turbine engine usually used in commercial aircrafts to produce electricity in the aircraft and assist with main engine starting. An APU can also be used to run hydraulic pump control and air conditioning. The particular APU used at the LCCC is a Garrett Honeywell GTCP85.

3.5 Chapter Summary

This chapter described the instrumentation and facilities used during aircraft engine certification level test campaigns and during laboratory experiments providing PM data reported and discussed in the following result chapters. A detailed discussion of the different segments of an ICAO compliant sampling and measurement system is provided along with the operating principle of the analysers used to characterise aircraft nvPM. Other particle generation and conditioning techniques used during laboratory experiments were also introduced.

4 Aerosol Generation and Characterisation

The transport and conditioning of Particulate Matter (PM) from the exhaust of a combustion source to the analysers can result in significant losses dependent on the sampling system and particle size [53]. Large-scale gas turbine engines are not a practical nor economically viable PM source when performing calibrations and nanoparticles experiments. Hence, cheaper, simpler and safer particle generation methods are desirable for laboratory experiments (section 3.2). To be representative of modern gas turbine PM, the aerosol generated by alternative methods should display a GMD between 10-100 nm [9], [20], [92].

Comprehensive laboratory experimental studies are found in the literature characterising loss mechanisms. In these studies, the authors generally produce nanoparticles from solutions/suspensions using a collision nebuliser/nebuliser (**Table 3-3**), or directly with a spark discharge generator [83] or a propane diffusion burner [85]. Given loss mechanisms of diffusion and inertia are size-dependent (section 2.3), it is necessary for loss analysis to be performed using aerosols of different sizes. To the author's knowledge, all particle generation processes produce polydisperse distributions, sometimes even multimodal, and hence generally need to be conditioned with a classification instrument (e.g. DMA [86], [105], [107], [108]).

The main objective of this chapter was to produce nanoparticles representative of aircraft PM (size and morphology) in a laboratory setting to permit the experimental investigation of some particle loss mechanisms occurring when sampling aircraft PM as presented in chapter 5. Given some losses mechanisms are size-dependent, it was aimed to produce monomodal and monodisperse aerosols at a range of sizes using aerodynamic classification. Generation of particles of different morphologies and properties (e.g. density) was also desirable to see how they could impact particle loss.

Aerosolization of nanoparticles with a collision nebuliser (section 3.2.1) classified with a Combustion Aerodynamic Aerosol Classifier (section 3.2.4) was undertaken with a Combustion DMS-500 used to determine the resultant size distribution. Non-volatile Residual (NVR) by-product particles generated from the atomisation of suspensions were also investigated in detail with the aim of reducing their contribution to the generated aerosol. This study facilitated particle generation processes required for the laboratory loss investigations discussed in chapter 5. The potential of capture and characterisation of aircraft PM in a liquid was also assessed for later use in calibration and health studies.

4.1 Aerosolization of solutions/suspensions for particle generation

Due to the simplicity of operation and wide variety of commercially available suspensions, a collision nebuliser was found to be a suitable generation technique for use in this research (section 3.2.1). However, nanoparticle generation by atomising a liquid suspension can have major drawbacks including concerns with residual particles and agglomeration [117], [129], [146].

When an intended particle-free nebulised droplet dries, Non-Volatile Residual (NVR) present in the liquid in the form of impurities can crystallise and form unrequired particles which are generally <100 nm [117], [146]. NVR's can form new particles, or they can coat suspended particles during the drying process when nebulised droplets evaporate (**Figure 4-1**). The size of NVR particles depends on the impurity levels and the liquid droplet size; for a given impurity level, a larger droplet will produce larger NVR particles or NVR coating given the concentration of impurity in the droplet increases with the droplet volume (i.e. size), as illustrated in **Figure 4-1**.

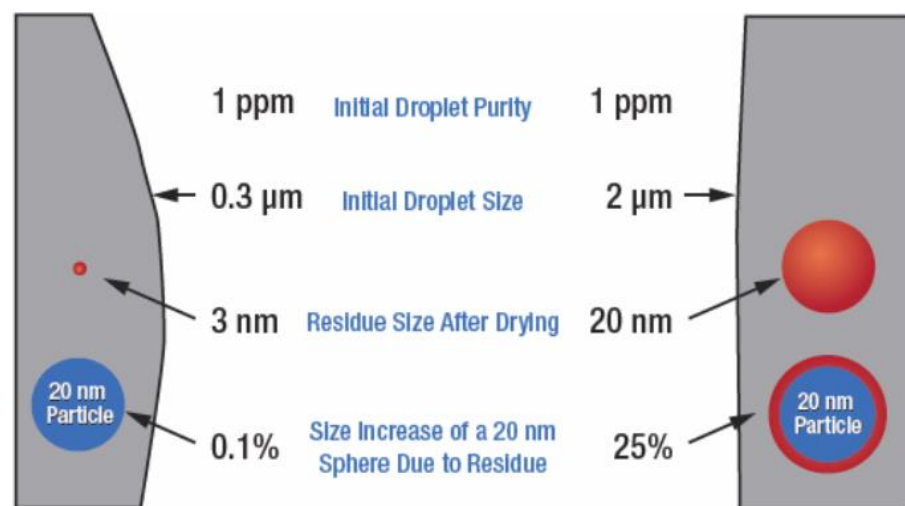


Figure 4-1: Effect of producing smaller droplets on non-volatile residue particle nucleation and coating [147]

Characterisation of NVR is very important as they can distort the intended nanoparticle size distribution and composition. The DMS-500's manufacturer Cambustion states that PSL suspensions used for calibration purpose are unsuitable below 100 nm due to the NVR mode distorting the PSL peak at those sizes [111], as illustrated in **Figure 4-2**.

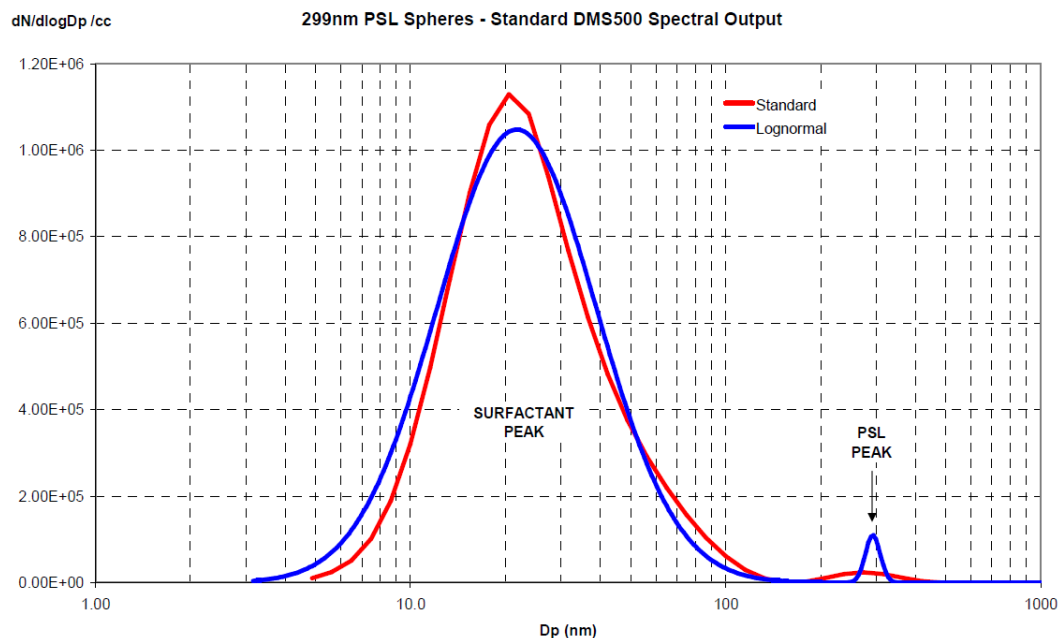


Figure 4-2: Particle size distribution of nebulised 300 nm PSL spheres used for the calibration of the DMS-500 with both reconstructed lognormal (blue) and full spectral outputs (red) [111]

When the concentration of suspended nanoparticles is too high in a solution, the nebulised aerosol is statistically likely to contain more than one particle per droplet, which may result in agglomeration during the drying process [62, p. 458]. It is suggested that agglomeration can hence be avoided by reducing the concentration of nanoparticles, either by diluting the suspension with impurity-free solvents or by generating sufficiently small droplets to ensure they are statistically likely to contain a maximum of one particle.

Collision nebulisers were operated using saline (NaCl) solutions, Silica (SiO₂) suspensions, gold (Au) suspensions and Polystyrene latex bead (PSL) suspensions to both characterise the different nebuliser designs and investigate NVR contamination.

4.1.1 Experimental characterisation of collision nebulisers

4.1.1.1 Nebuliser performance comparison

Two nebulisers were investigated to produce nanoparticles from a suspension. Preliminary experiments were performed using a commercially available ‘medical nebuliser’ which was estimated to have a mean droplet size in the 1-10 μm region [60]. This nebuliser is a collision nebuliser (section 3.2.1) consisting of a plastic vial containing the solution and a cone with a small aperture from where compressed air is ejected at high velocity. It was demonstrated that both the droplet size distribution and concentration could be changed by varying the compressed air pressure and flowrate rate. **Figure 4-3(a)** shows a pictorial representation of three ‘medical nebulisers’ plumbed in series to generate sufficiently high concentrations of gold nanoparticle from suspension

(gold suspensions - 4.1.2.1). As seen in **Figure 4-3(b)**, it was observed that the relatively larger droplet size distribution experienced with this nebuliser resulted in a larger non-volatile residual (NVR) particle peak (dashed blue line) naturally occurring from impurities present in the distilled water which overlapped the intended nanoparticle peak (vertical lines represent theoretical atomised gold concentration), resulting in a poorly defined aerosol.

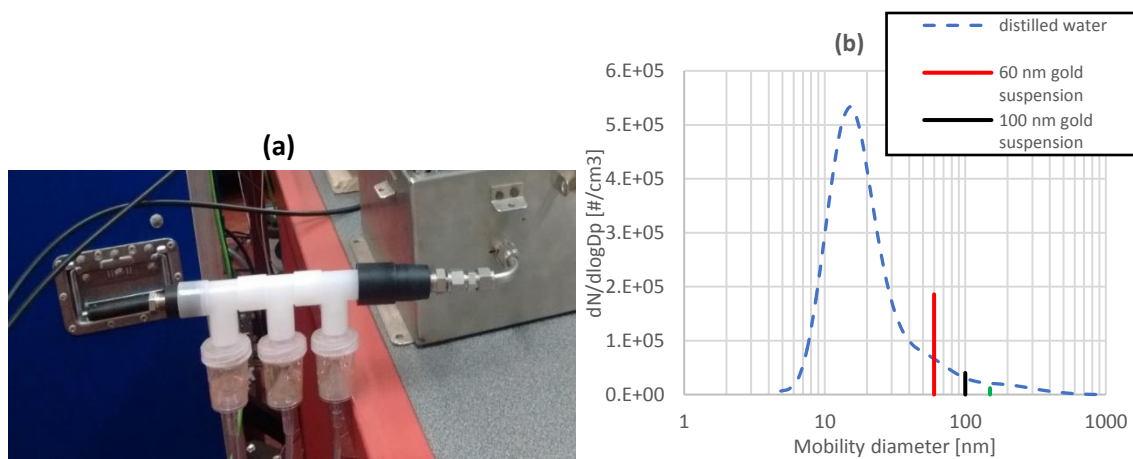


Figure 4-3: Photograph of three 'medical' nebulisers in series producing gold (a) and typical NVR size distribution when atomising distilled water with a 'medical nebuliser' (b)

In an effort to minimise this NVR interference, a Topas ATM-226 aerosol generator specifically designed for nanoparticle preparation was purchased (section 3.2.1). The ATM-226 is similar to models employed by Jeon et al. [132] (Kanomax Nanoparticle Nebulizer Model 9110), Fissan et al. [117] (TSI Inc., prototype model 3485), and Park et al. [146] (Nebuliser TSI 3075) whom atomised and measured nanoparticle suspensions from 5-1000 nm.

It was proposed that in line with the theory discussed above (**Figure 4-1**), the relatively smaller droplets produced by the ATM-226, of approximate GMD 200 nm [134] would result in fewer smaller NVR particles. This theory was experimentally validated by nebulising in-house distilled water (type 3 water [148]) with both the ATM-226 and a medical nebuliser and measuring the NVR size distribution from impurities naturally present in the nebulised droplets, as presented in **Figure 4-4**. It can be seen that the medical nebuliser has a significantly larger and wider NVR particle peak. Conversely, the ATM-226 produced relatively fewer and smaller NVR particles ranging between 5 and 30 nm, making it conducive to nebulising suspensions of nanoparticles for use in laboratory experimentation.

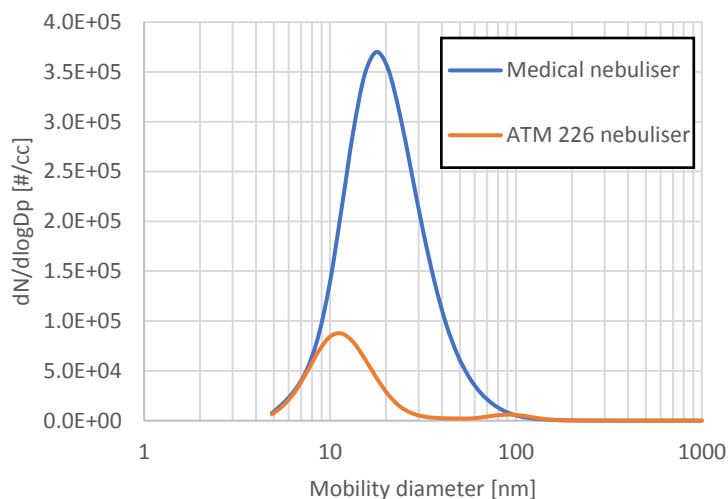


Figure 4-4: Particle size distribution produced from the nebulisation of distilled water using a medical nebuliser and a Topas ATM-226 and measured by a DMS-500

4.1.1.2 Characterisation of the Topas ATM-226

In this section, droplet formation and evaporation, size distribution, air flow and atomisation rate were investigated for the Topas ATM-226 nebuliser using a Cambustion DMS-500 (section 3.1.3) to characterise generated particles.

Droplet size distribution:

The droplet size distribution produced by the ATM-226 using DEHS (Di-Ethyl-Hexyl-Sebacat) oil is provided in the manufacturer’s calibration certificate (appendix 10.2). DEHS is convenient for droplet size distribution characterisation as droplets have a long lifetime due to the low vapour pressure. The solvents used in these laboratory experiments were different grades of water (section 4.1.3.1), thus an analysis was performed to estimate water droplet size distribution from calibrated DEHS size distribution.

When generating droplets from a spray, at least three fluids properties have a significant impact on the droplet size distribution: the specific gravity, the viscosity and the surface tension [149]. Using basic droplet theory [149], differences between DEHS and water droplet size were calculated using the relative fluid properties detailed in **Table 4-1**.

Table 4-1: Fluid Properties of DEHS and water and comparative predicted droplet size

(at 20°C)	Water	DEHS
Density [g/cm ³]	1	0.912
Dynamic Viscosity [cP]	1	23
Surface Tension [Dynes/cm]	73	32

Considering density, dynamic viscosity and surface tension, it was estimated that the size of the water droplets would be approximately 17% smaller than that of DEHS droplets. Hence, given the GMD for DEHS from calibration is ~ 200 nm, it can be assumed the ATM-226 produces a water droplet size distribution with a $GMD \approx 165$ nm, making it suitable to minimise NVR influence on nebulised nanoparticles as discussed previously. It is also specified in the calibration certificate that the total droplet number concentration is $> 10^8$ particles/cm³.

Flow and atomisation rates:

The ATM-226 flowrate rate is controlled by a flow restriction valve. As an exact flowrate measurement was required, the ATM-226 pump was isolated and particle-free dry compressed air, controlled by a flowrate controller, was directly connected to the nebuliser’s nozzle to nebulise distilled water. To determine an optimal flowrate for this nebuliser, the dependency between air flowrate and NVR size distribution was investigated. Results are presented in **Figure 4-5** displaying the measured GMD **(a)**, number concentration **(b)**, and GSD **(c)** of the atomised NVR peak at different flows.

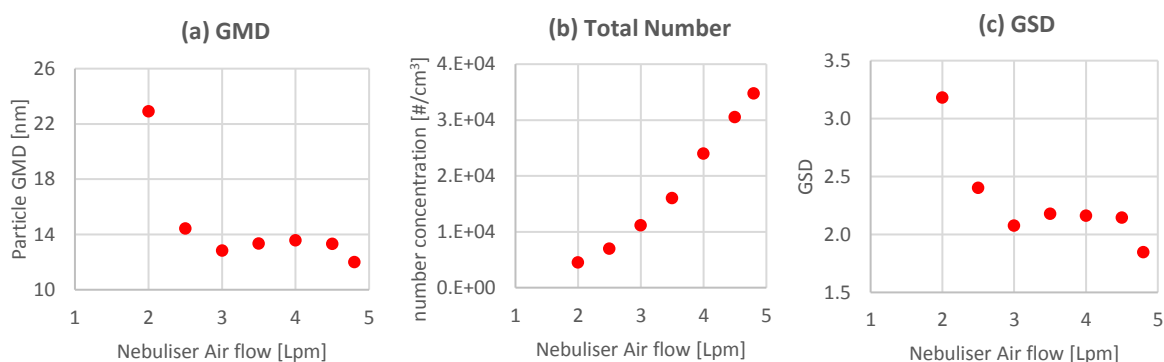


Figure 4-5: Non-Volatile-Residue (NVR) size distribution ((a) GMD, (b) N_{tot} , (c) GSD) generated from the nebulisation of water with a Topas ATM-226 at different inlet flowrate measured by DMS-500

It is seen that an increase in the nebuliser’s inlet air flowrate produces a higher NVR number concentration and a smaller GMD and GSD. This is indicative of the atomisation rate increasing with the flow, rendering the atomisation more efficient and generating more smaller droplets [18, p. 265]. Also, as the flow increases, the cut-off diameter impaction plate of the ATM-226 is reduced (section 2.3.1.6), removing more larger droplets and hence reducing the NVR peak’s GMD.

An ‘optimal’ flowrate for the ATM-226 was estimated at **4.8 Lpm** as it was the largest sustainable flow and produced the smallest NVR GMD and GSD hence was used for all subsequent laboratory experiments. It is noted that the measured number concentrations and GMDs were near the limit of detection of the DMS-500, hence there is a large uncertainty associated with the data displayed in **Figure 4-5**.

The atomisation rate of the ATM-226 was estimated at the 'optimal' flowrate of 4.8 Lpm by mass measurement using a precision balance (± 0.01 g). Water mass loss was characterised at 20-minute intervals over a period of two hours, with the average atomisation rate determined as **0.08 ± 0.01 ml/min.**

Droplet lifetime and effect of humidity (drier):

When the ambient partial pressure of vapor is less than that of the saturated pressure, droplets evaporate. At 15°C and ambient pressure with dry air, the expected evaporation time of a 1 μm droplet is ~ 1 ms and reduces with droplet size [60]. However, atomisation of suspensions increases the Relative Humidity (RH) of the produced aerosol, thus decreases the saturated pressure and if RH exceeds 100%, droplets won't evaporate. In the literature, when atomising suspensions/solutions, a drier is typically combined with a DMA to maintain a low RH ensuring the sampled flow is of a similar RH to that of the sheath flow to prevent particle size from changing during classification [84], [86], [108], [119]. High aerosol RH shouldn't be problematic when using a DMS-500 as it operates at 60°C and a reduced pressure of 250 mbar(a) which significantly increases the saturated pressure. However, high humidity within a test section may prevent droplets from evaporating entirely.

The particle generation setup used for line-loss experimentation (i.e. atomisation with the ATM-226 [4.8 Lpm airflow and 0.08 ml/min solution] and diluted with dry air [5 Lpm airflow] at 15°C and ambient pressure) was estimated [150] to have a RH of 96% prior to the dilution (48% post-dilution). At this humidity, the evaporation time of a 200 nm water droplets was calculated to be ≤ 173 ms (≤ 1 ms post-dilution) using the theory described by Hinds [60, pp. 278–303] which considers Fuchs effect and temperature depression corrections. The delivery pipework from the nebuliser to the diluter was designed to have a residence time > 173 ms (> 0.5 m $3/8''$ ID tube) facilitating full evaporation before the dilution stage which ensured that re-condensation could not occur. Hence, nano-droplets generated by the ATM-226 were deemed not to require a drier.

To confirm that particle size wouldn't vary at $\text{RH} \leq 50\%$, an experiment was performed using a TSI SMPS and an aerosol diffusion drier supplied by Manchester university. SiO_2 suspensions and a saline solution (0.9% NaCl w/v) were nebulised and an SMPS was used to monitor size distribution and aerosol RH. The RH was varied by continuously sampling nebulised aerosols with or without a drier.

As presented in **Figure 4-6**, it was observed that varying the RH from 10 to 50% did not affect the GMD of solid SiO_2 particles. A small GMD increase over time (represented by red arrows) was observed for NaCl particles but was not attributed to RH as it continuously increased from ~ 50 nm to 80 nm independently of RH fluctuation. Instead, it was conjectured that continuous atomisation

of the NaCl solution caused the nebuliser's nozzle to be increasingly obstructed by NaCl particles, causing the GMD to slowly shift over time ($\sim +0.33$ nm/min). To prevent this from being an issue in future experiments, the ATM-226 was regularly cleaned. It is noted that the larger GMD observed for NaCl and SiO₂ particles with a drier was due to additional diffusional loss inside the drier causing more smaller particles to be lost.

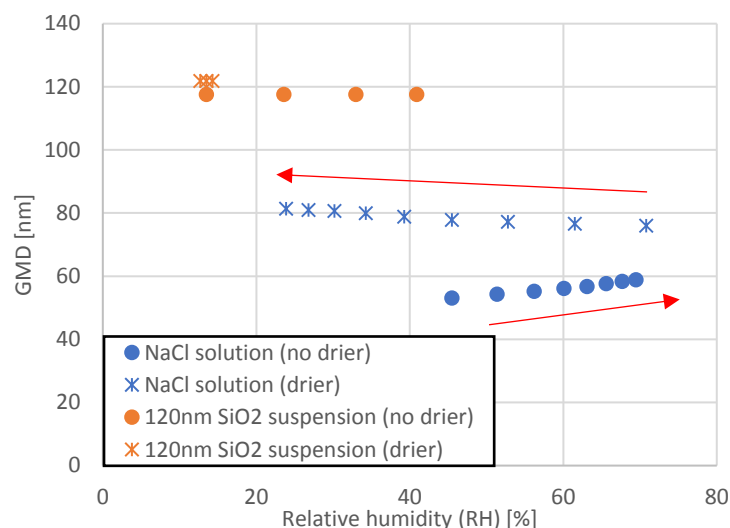


Figure 4-6: Effect of Relative Humidity and a diffusion drier on the GMD of SiO₂ suspensions and NaCl solutions nebulised using an ATM-226 and measured with a TSI SMPS (red arrows represent time)

As it was anticipated that low RH (<50%) were suitable for use in a DMS-500 and it was shown that a drier wasn't required to successfully produce dry aerosols from suspensions/solutions, laboratory experiments in this thesis were not performed with a drier. This decision also negated the additional diffusional loss (**Figure 4-6**) witnessed in driers facilitating higher concentrations of nanoparticles.

4.1.1.3 Solvent characterisation with the Topas ATM-226

As discussed previously and highlighted in **Figure 4-2**, atomisation of suspensions results in the production of unwanted residual particles from dissolved impurities. Although nanoparticles are generally suspended in aqueous solutions [84]–[86], both aqueous solvents and organic solvents were trialled in an attempt to limit NVR particles. Various solvents were atomised with an ATM-226, and the NVR size distribution measured with a DMS-500.

High purity (>99.8%) Acetone, Ethanol & propanol were initially investigated in addition to numerous grades of distilled water, with the resultant NVR size distributions presented in **Figure 4-7**. As seen the three organic solvents produced large concentrations of NVR particles ($>10^7$ particles/cm³) at sizes ranging from 10 to 300 nm, which is notably higher than concentrations observed for standard distilled water (type 3 [148]) ($\leq 10^5$ particles/cm³). Therefore, it was concluded

that organic solvents of this purity were not suitable suspensions used in this work. It was deduced that the higher NVR concentrations produced by the atomisation of organic solvents originated from a higher level of impurities present in organic solvents (ppm range) when compared with that of ultrapure water (ppb range). This is in agreement with the work of Jeon et al. [132] whom also measured a significant increase to the NVR peak when adding organic solvents to ultrapure water suspensions for pH control.

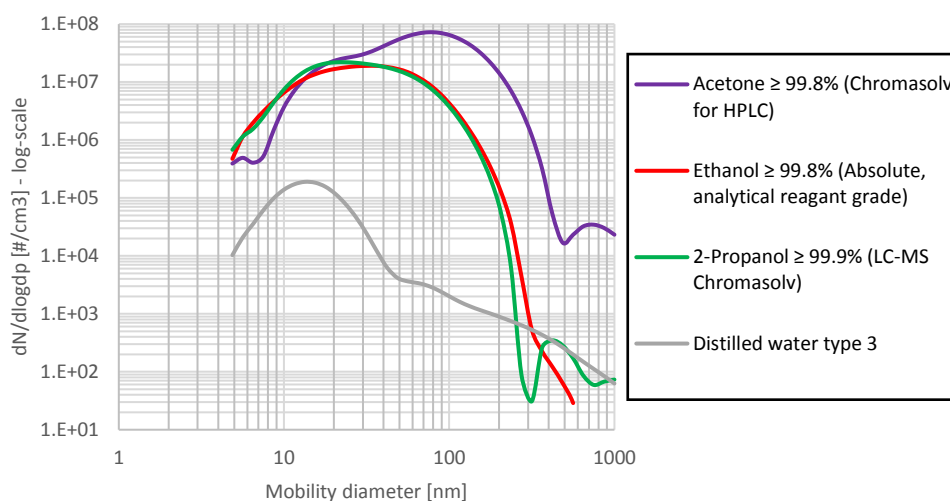


Figure 4-7: Particle size distribution on a log-log scale of different solvents atomised by an ATM-226 and measured by a DMS-500

The particle size distributions generated from the nebulisation of aqueous solvents of different purities were also investigated, as presented in **Figure 4-8**. It is observed in **Figure 4-8 (a)** that tap water produces the largest NVR peak and that ultrapure water type 1 [148] generates the smallest NVR peak with a GMD around 10 nm and a total number concentration $\sim 10^4$ particles/cm³. UHPLC (High Performance Liquid Chromatography) water from Sigma-Aldrich was investigated with the ambition to further reduce NVR production but it was seen to produce a larger NVR peak than the in-house produced ultrapure water type 1, suggesting that it contained more impurities (see impurity level in specification sheet in appendix **10.3**). The size distribution in **Figure 4-8 (b)** reveals that ultrapure water type 1 only produces detectable NVR particles up to 20 nm, hence demonstrating it as the most suitable solvent for nanoparticle suspensions. Similarly, Gomez et al. [129] and Park et al. [146] reported NVR total concentration in the order of magnitude of 10^3 - 10^5 particles/cm³ when atomising different types of ultrapure water using a similar nebuliser technology.

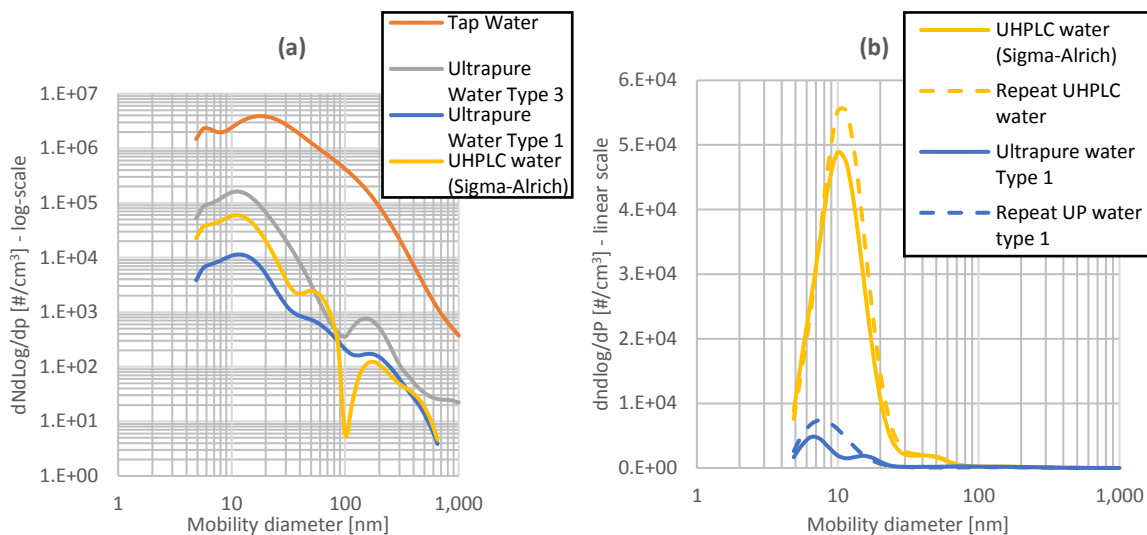


Figure 4-8: particle size distribution of different aqueous solvents on a log-log scale (a) and on a log-linear scale (b) atomised by an ATM-226 and measured by a DMS-500

4.1.2 Characterisation of aerosolised suspensions and solutions

In this study, three nanoparticles suspensions and a saline solution were assessed for laboratory experiments namely:

- 60-150 nm suspended Gold nanoparticles from BBI Solutions [151]. They are spherical, have a high melting point (1063°C) and a large material density (19.3 g/cm³).
- 100 nm suspended carboxyl charge-stabilized hydrophobic polystyrene beads (i.e. PSL) from ThermoFisher Scientific. Commonly used in the literature [85], [86], PSL are spherical and have a material density (1.055g/cm³ at 20°C) near that of nvPM soot [57].
- 50-180 nm Silica (SiO₂) nanoparticles from Nanocomposix, purchased both suspended and in powder form. Silica particles are spherical, have a high melting point (~ 1700°C) and a material density of 2.165 g/cm³.
- 10-300 nm Salt (NaCl) nanoparticles from a saline solution (material density ~2.2 kg/m³). This technique is commonly used in the literature [76], [105], [119].

They were atomised using the aforementioned ATM-226 and characterised using a DMS-500. The particles were chosen to investigate the effects of morphology and density on particle losses to validate the theory used in the UTRC model discussed in chapter 5.

4.1.2.1 Gold nanoparticles

The atomisation of different sized gold nanoparticles suspended in distilled water (BBI Solutions) was trialled with the ATM-226 but was unsuccessful. It was observed that 60, 100 or 150

nm gold suspensions only produced a measured GMD between 10 and 30 nm with no distinguishable gold nanoparticle peak as presented in **Figure 4-9**. To confirm that gold nanoparticles were present in the purchased suspensions, they were first measured in solution using a Malvern Nano-sight (section **3.1.4**) which successfully detected gold at the expected size and concentration specified by the manufacturer.

Given the measured peaks in **Figure 4-9** had a higher number concentration than that of distilled water alone (**Figure 4-4**), it was conjectured that the measured particles were NVR present in the gold suspension originating from the manufacturing process, as stated in the product datasheets [151]. It was witnessed that the generated particle peak from the 60 nm gold suspension is about three times higher than that of 100 and 150 nm gold. This may be due to the larger concentration of particles in the suspensionⁱⁱ resulting in more residual chemical left from manufacture.

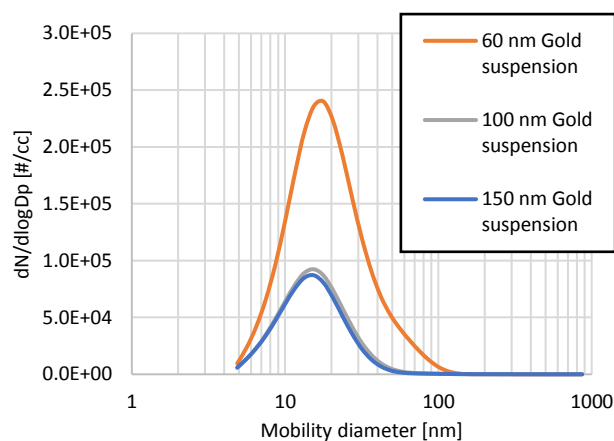


Figure 4-9: Particle size distributions of multiple BBI solutions gold suspensions atomised with an ATM-226 and measured using a DMS-500

Separation of dissolved impurities and the relatively dense (19.3 g/cm^3) gold nanoparticles was attempted using centrifugation (**3.2.2**). After centrifugation, the gold-free solution (at the top of the vials) was decanted and replaced with ultrapure water type 1 [148]. In addition to centrifugation, aerodynamic classification of the atomised suspensions was attempted with a Cambustion AAC (section **3.2.4**). The AAC relies on the principle of centrifugal force to size-select particles. Given gold has a relatively high density (19.3 g/cm^3) and NVR are likely to have a lower density, the AAC should in theory be capable of separating atomised gold from NVR, that is if a gold peak is present within the NVR peak. Measured size distributions from the atomisation of centrifuged gold suspensions with and without the AAC classification are presented in **Figure 4-10**.

ⁱⁱ 2.6×10^{10} particles/ml for 60 nm suspension Vs 5.6×10^9 particles/ml for 100 nm suspension and 1.66×10^9 particles/ml for 150 nm suspension as quoted by the manufacturer

It was observed for the 60 nm gold suspension (**Figure 4-10(a)**) that a small peak is present near 60 nm, indicating centrifugation was partially successful although the gold peak could not be separated from the 15 nm peak (NVR) by the DMS-500. On the other hand, centrifugation did not improve the 100 nm gold suspension (**Figure 4-10(b)**). As for aerodynamic classification, even with the AAC setup for equivalent aerodynamic diameters corresponding to the quoted gold size (orange plots), no changes in the measured size distribution were observed. It was concluded that the NVR peak originating from BBI Solutions gold suspensions must have a similar density to that of gold or isn't sensitive to centrifugal classification. It is noted that the reduction in total number concentration (difference between orange and grey lines) was caused by losses and dilution occurring in the AAC as discussed in section 4.2.

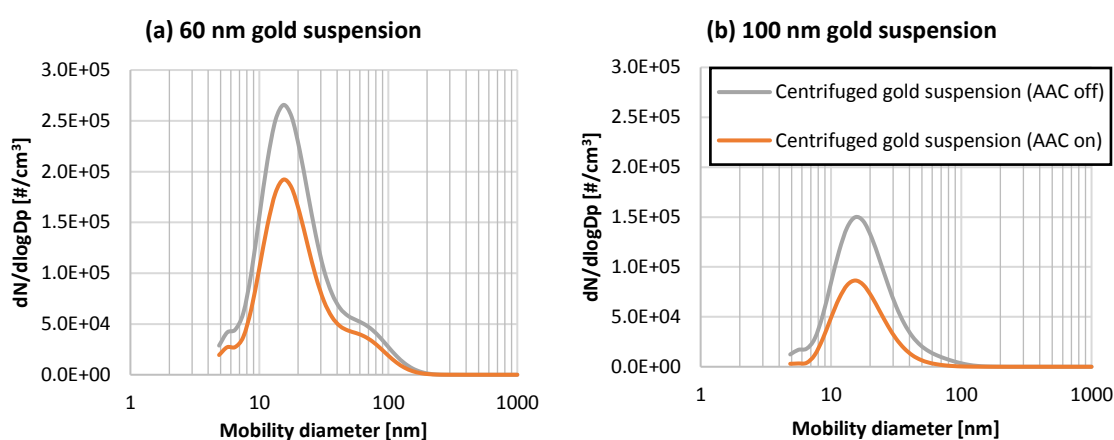


Figure 4-10: Particle size distribution of 60 nm (a) and 100 nm (b) centrifuged gold suspensions atomised with an ATM-226 and measured by a DMS-500 with and without AAC classification

Different hypotheses were investigated to understand what was preventing the gold suspensions from being measured after being atomised, namely:

- **Gold Concentration in the solvent too low:**

The theoretical concentrations of the BBI solution gold suspensions when purchased was 2.6×10^{10} particles/ml for 60 nm suspension, 5.6×10^9 particles/ml for 100 nm suspension and 1.66×10^9 particles/ml as provided in the product datasheet. Those concentration were also increased by removing some solvent after centrifugation. In general, gold particles concentration in the suspensions was similar to that of SiO₂ suspensions from Nanocomposix which were successfully atomised (**Figure 4-14**) using the same nebuliser. This proves that the concentration of gold in the suspension should be high enough to produce an aerosol peak detectable by the DMS-500.

- **Gold not efficiently classifying in DMS-500 Corona discharge:**

It was hypothesised that gold couldn't be detected by the DMS-500 because of charging or classification issue in the measurement analyser. However, it was confirmed that Tungsten, which has a similar density and electrical conductivity to gold, has previously been measured by a DMS-500 [private conversation J. Symonds – Cambustion 12/10/2017]. Furthermore, many studies have measured gold nanoparticles using a SMPS which relies on the same principle than the DMS-500 [117], [132] as discussed in section 6.2.3.1.

- **Gold trapped in DMS-500 cyclone or Nebuliser's impactor:**

Because of its relatively high density, gold may be trapped in the 1 μm cyclone at the inlet of the DMS-500 or on the ATM-226 vial wall which acts as an impaction plate to remove larger droplets. Using the inertial impaction theory (section 2.3.1.6), it was estimated that the cyclone 50% cut-off (d_{50}) for dense gold particles was 227.6 nm, indicating that at least 50% of gold particles ≤ 227.6 nm should penetrate the DMS-500's cyclone.

As for the ATM-226 impactor, as shown in **Figure 4-11**, it was observed that the vial wall acting as an impaction plates had some red colouring indicative of plated gold particles, suggesting that gold particles could be lost in the nebuliser's impactor. This hypothesis was supported by the fact that the ATM-226 only atomises droplets ≤ 300 nm (see appendix in 10.3) suggesting the nebuliser has a 50% cut-off (d_{50}) of ≤ 68 nm for droplets as dense as gold. It is noted that this explanation does not contradict the successful atomisation of gold nanoparticles with a similar nebuliser in the literature as only gold < 30 nm was investigated [117], [132].



Figure 4-11: Photographs of a vial after the nebulisation of a gold suspension using the ATM-226 showing gold plating onto the walls acting as an impactor

In conclusion, the generation of gold nanoparticles wasn't successfully achieved in this particular experimental setup. It is thought that nebulised gold particles are impacting on the ATM-226 vial walls, preventing them from being measured. To validate these findings, further experiments could be performed using gold suspensions with a GMD smaller than 60 nm, a larger nebuliser vial and a different measuring analyser.

4.1.2.2 Polystyrene Latex nanoparticles (PSL)

Due to their sphericity and density being close to unity, PSL spheres are often used for calibration of size instruments [111] and have been used in nanoparticle loss studies [85], [86]. However, it is noted that surfactant is often present in PSL suspensions to avoid agglomeration, causing a significant NVR peak to be produced in the sub 100 nm region. For this reason, 100 nm Carboxyl Latex beads (4% w/v), part of the IDC-Surfactant-free Latex Beads range offered by ThermoFisher Scientific, was trialled. Example specification sheet of the Carboxyl latex beads (appendix 10.3) specifies that the beads are negatively charged polystyrene microspheres with carboxyl functional groups on the surface, and that they are stable at neutral to high pH.

Initial atomisation of the Carboxyl latex beads suspended in distilled water (ultrapure water type 1 [148]) with the ATM-226 was unsuccessful, as seen in **Figure 4-12 (a)** displaying the measured particle size distributions at different PSL number concentrations. It can be seen that NVR peaks were observed with the main peak's GMD around 30 nm at concentrations well above that of the of pure water (blue line) and the NVR total number concentration increasing with the PSL concentration. It was later deduced that the 100 nm latex beads were not measured because they had agglomerated in the solution, as seen in **Figure 4-12 (b)**. A 30 minute ultrasonication was attempted to de-cluster the beads but made no difference as illustrated by the dotted size distribution in **Figure 4-12 (a)**.

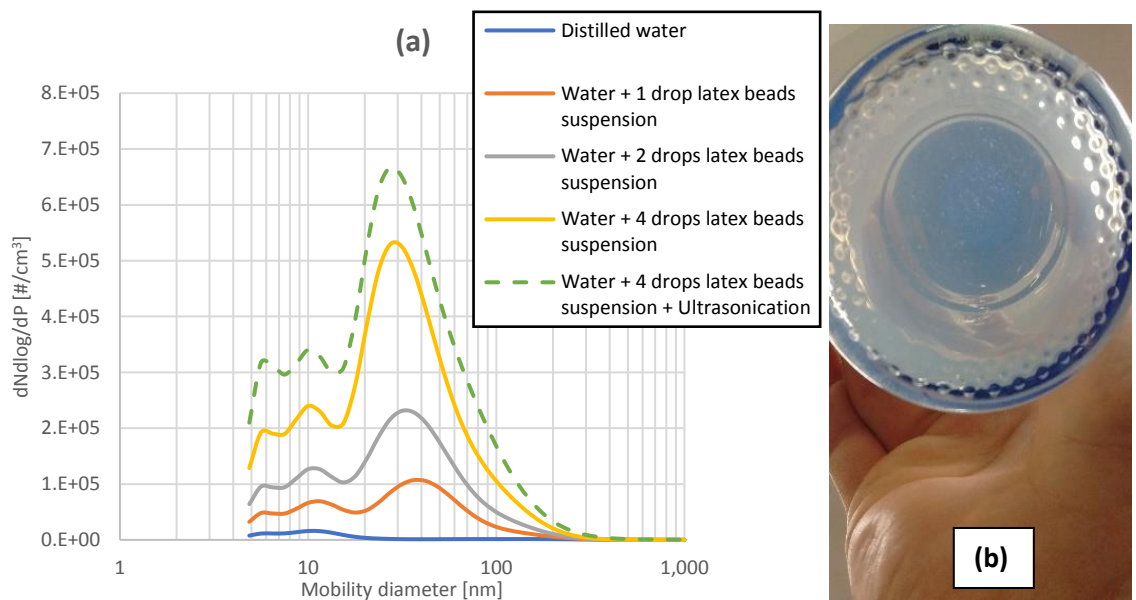


Figure 4-12: Particle size distribution of 100 nm Carboxyl Latex beads suspended in distilled water atomised with an ATM-226 and measured with the the DMS 500 (a) and photograph of agglomerated beads forming visible white clusters (b)

As it was stated in the specification sheet that the beads were only stable at neutral to high pH, it was investigated whether the pH of the solution was the cause of PSL agglomeration. It was

found that the pH of the water solution containing the beads had a pH of 6 (lower than neutral), hence it may have caused the latex to agglomerate. To confirm this hypothesis, the pH of the solution was increased by adding a small quantity of bicarbonate soda (<0.05 g) to the solution, increasing its pH to 8.3. As can be seen in **Figure 4-13** presenting the bimodal size distribution of the higher pH solution, the 100 nm carboxyl latex beads were now detected by the DMS-500, although the addition of bicarbonate soda lead to the production of a major NVR peak < 100 nm.

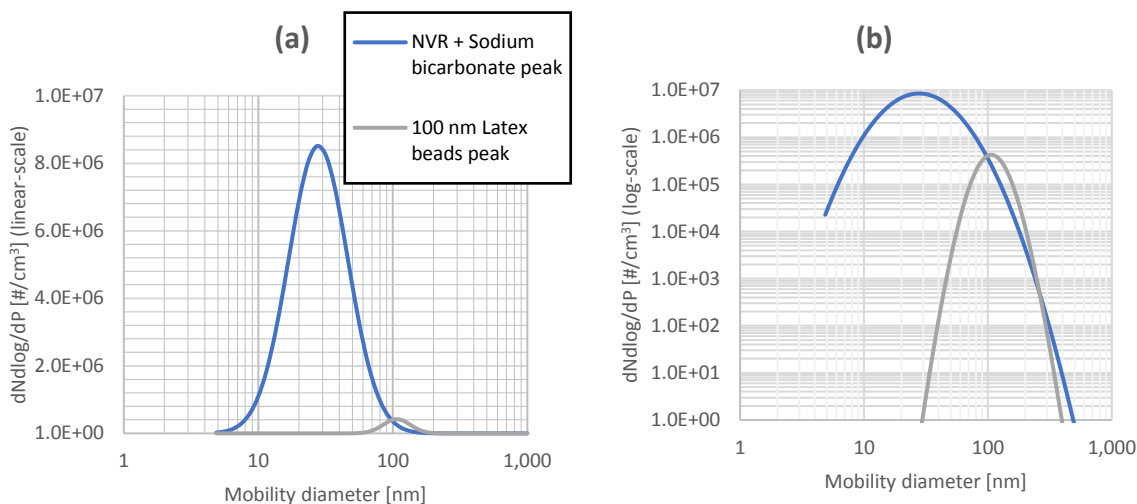


Figure 4-13: Particle size distribution of 100 nm Carboxyl Latex beads suspended in distilled water mixed with bicarbonate soda, atomised with an ATM-226 and measured with the the DMS 500 (y-axis linear scale (a) and log scale (b))

Therefore, the so-called 'surfactant-free' carboxyl latex beads (<100 nm) were deemed unsuitable for particle generation and use in future laboratory experiments as the PSL peak couldn't be isolated. To the author's knowledge, no other surfactant-free PSL suspensions stable at low pH are commercially available.

4.1.2.3 Silica nanoparticles (SiO₂)

Nanocomposix Silica suspensions ranging between 50-180 nm suspended in distilled water were successfully atomised and measured, as shown in **Figure 4-14** where both NVR peaks (GMD 10-20 nm) and SiO₂ peaks can be clearly differentiated. It is noted that the NVR peak number concentration, GMD and GSD increases with increasing SiO₂ GMD. This may be indicative of NVR concentration in the suspensions being proportional to the surface area of the SiO₂ particles.

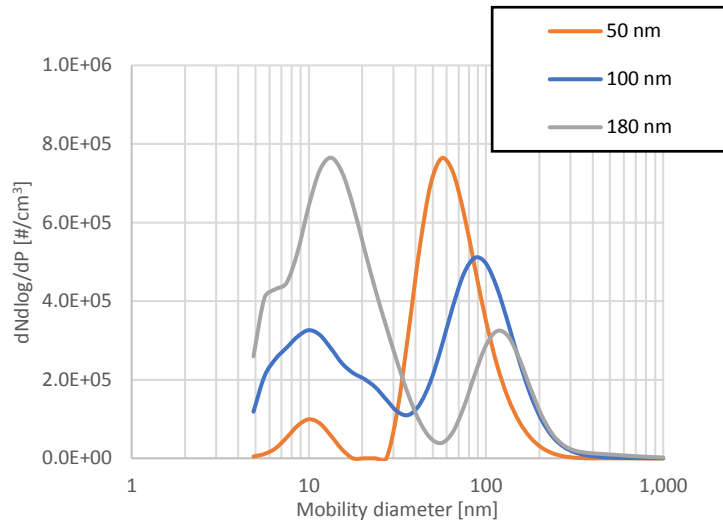


Figure 4-14: Particle size distribution of different silica suspensions suspended in distilled water atomised using an ATM-226 and measured by a DMS-500

A detailed analysis was performed on SiO₂ generated from the Nanocomposix suspensions to attempt to maximise the SiO₂ concentration and better understand the atomisation process.

- **Number Concentration and GMD of SiO₂ particles:**

With different sizes and concentrations of SiO₂ purchased, it was possible to compare the total number concentrations derived from size measurement with theoretical predictions. Theoretical SiO₂ concentrations within the gas phase were calculated using the following equation with the SiO₂ suspension concentration given in the specification sheet (appendix 10.3) and an atomisation rate of 0.08 ml/min (section 4.1.1.2):

$$\text{SiO}_2_{\text{predicted}} (\text{aerosol}) [\#/\text{cm}^3] = \text{SiO}_2 \text{ suspension } [\#/\text{ml}] \times \frac{\text{volume suspension} [\text{ml}]}{\text{volume water } [\text{ml}]} \times \frac{\text{Atomisation rate } [\text{ml}/\text{min}]}{\text{gas flow } [\text{cm}^3/\text{min}]} \quad (4.1)$$

The measured aerosolised SiO₂ concentrations were derived by performing a log-normal reconstruction of the 2nd peak of the size distribution and ranged from 10⁴ - 10⁷ particles/cm³. The measured concentration was always found to be < 20% of the predicted concentration (equation (4.1)) with the ratio measured/predicted decreasing with decreasing SiO₂ GMD (Table 4-2). Different hypotheses are listed below:

- Some SiO₂ particles are lost in the sampling lines connecting the nebuliser to the DMS-500.
- The uncertainty associated with the DMS-500 total number concentration is 20% [111].
- The suspended SiO₂ concentration [# / ml] is a theoretical value given by Nanocomposix and may be inaccurate for specific batches.

- Some SiO₂ particles may have agglomerated during atomisation if two or more particles are present in the same droplet. This is however unlikely as the range of measured SiO₂ concentrations (10⁴ – 10⁸ particles/cm³) is well below the droplet production rate of the ATM-226 (>10⁸ droplets/cm³).

Table 4-2: Percentage difference of measured (DMS-500) to predicted silica nanoparticles concentration from atomisation of suspensions at different concentrations and silica GMDs

GMD SiO ₂ suspension	measured/predicted				
	50 nm	80 nm	100 nm	120 nm	180 nm
0.4 ml suspension/ 40 ml water	6.2%	9.5%	9.6%	14.2%	12.6%
0.8 ml suspension/ 40 ml water	6.2%	9.2%	10.2%	15.4%	18.6%
1.2 ml suspension/ 40 ml water	5.9%	9.0%	8.2%	16.2%	19.7%
1.6 ml suspension/ 40 ml water		7.3%	12.2%	10.6%	18.7%
2 ml suspension/ 40 ml water		-	11.8%	10.8%	18.7%
2 ml suspension/ 40 ml water (repeat)		-	12.6%	-	21.7%
average	6.1%	8.8%	10.7%	13.5%	18.3%

Furthermore, results presented in **Figure 4-15(a)** show that for a given SiO₂ suspension, the measured GMD of the SiO₂ increases with the suspension concentration. The increase in GMD combined with the wider distributions witnessed in **Figure 4-15(b)** may be caused by a higher impurity concentration with a constant droplet size distribution causing more NVR to coat the SiO₂ during the atomisation process as previously discussed with **Figure 4-1**. This may also be due to a change in the suspensions characteristics which would affect the atomisation efficiency and ultimately the concentration and GMD as stated by Gomez et al. [129].

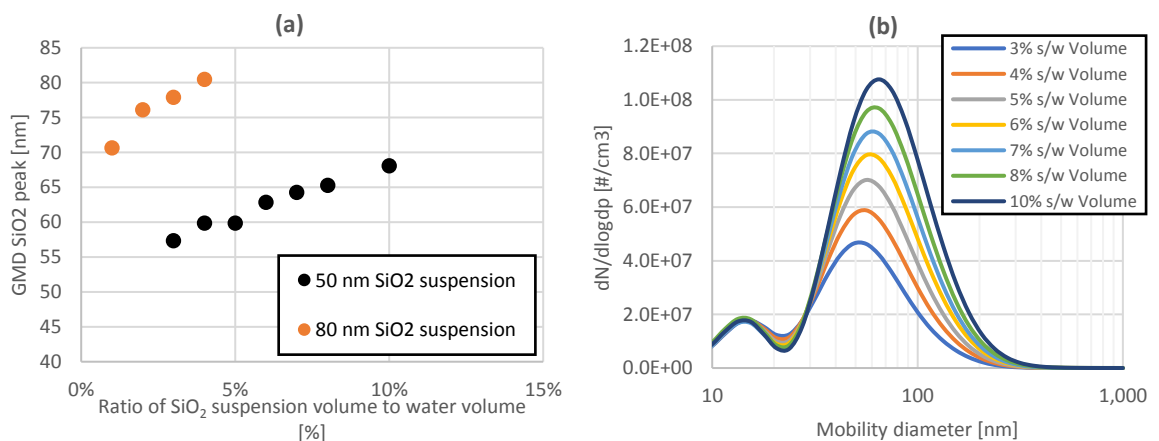


Figure 4-15: Effect of increasing silica suspension volume/concentration on the GMD measured with a DMS-500 for suspensions atomised by an ATM-226 in a constant volume of distilled water (a) and size distributions of atomised 50 nm silica suspensions diluted in ultrapure water type 1 at different concentration (b)

- **Dried SiO₂ Vs. suspended SiO₂:**

In addition to silica liquid suspensions (10 ml), SiO₂ was also purchased in the form of a power (10 mg) at a stated size of 100 nm. The powder was mixed in distilled water and dispersed using an ultrasonic bath. The lognormal reconstruction of the measured size distributions for the powder (dashed line) and liquid suspension (full line) at similar SiO₂ concentrations is presented in **Figure 4-16**. As can be seen, both powder and suspension produced a measurable 100 nm SiO₂ peak, with the powder generally producing a lower NVR peak and narrower SiO₂ peak. It is possible the distilled water used for the suspension of the powder (ultrapure water type 1 [148]) was cleaner than that of the SiO₂ liquid suspension, hence generating less NVR. This highlights the importance of the purity of the solvent for NVR contamination.

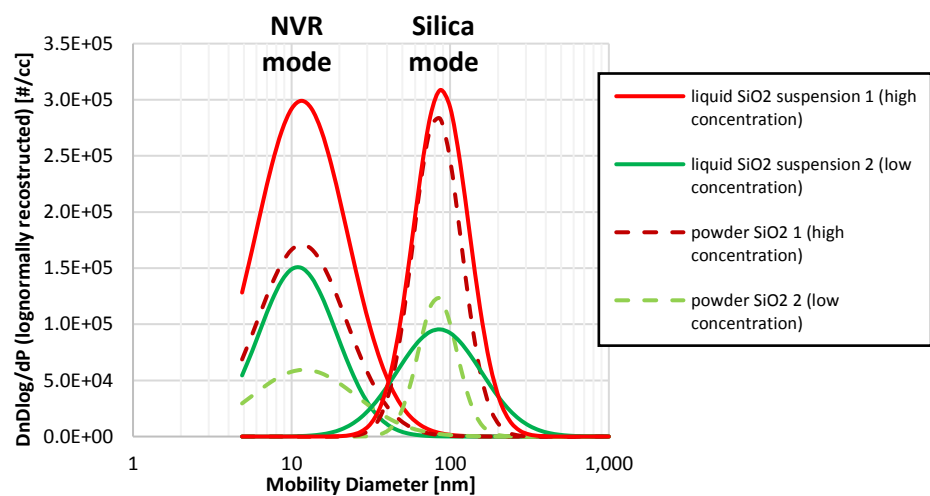


Figure 4-16: Bimodal reconstruction of particle size distributions of liquid suspension and powder 100 nm SiO₂ suspended in distilled water at different concentrations atomised by an ATM-226 and measured by a DMS-500

- **SiO₂ peak width (i.e. GSD):**

An advantage of atomising solid suspensions for nanoparticle generation is the supposedly narrow size distribution of the atomised particles when compared with the generally polydisperse nature of other particle generation methods (section 3.2). In this section, the GSD of SiO₂ suspensions prescribed in the specification sheet (appendix 10.3) was compared to that measured by a DMS-500 after atomisation.

The GSD of atomised SiO₂ suspensions of different sizes was found to range between 1.3 to 1.8, However, the Coefficient of variation (CV) for the same SiO₂ suspensions in liquid was quoted as 4 -10%. Converting the CV into a GSD resulted in a value of <1.1 using the calculation method presented below. The larger GSD of the atomised SiO₂ suspensions may be explained by NVR contamination and coating. Indeed, Fissan et al. [117] reported similar GSDs ranging between 1.12

and 1.22 when measuring atomised gold and silver nanoparticles suspensions with SEM and an SMPS when no NVR contamination was occurring. It is noted that the DMS-500 was demonstrated to be capable of measuring a GSD as low as 1.07 [152], hence it should not be the source of this difference.

GSD Calculation from the Coefficient of Variation (CV):

A lognormal distribution has two parameters μ_{avg} and σ_{STD} , respectively the average and standard deviation of the distribution.

$$\mu_{\text{avg}}(\ln(d_p)) = \ln\left(\frac{\mu_{\text{avg}}(d_p)}{\sqrt{\left(1 + \frac{\sigma_{\text{STD}}^2(d_p)}{\mu_{\text{avg}}^2(d_p)}\right)}}\right) \quad \& \quad \sigma_{\text{STD}}^2(\ln(d_p)) = \ln\left(\left(1 + \frac{\sigma_{\text{STD}}^2(d_p)}{\mu_{\text{avg}}^2(d_p)}\right)\right) \quad (4.2)$$

Furthermore, the Geometric Standard Deviation (GSD) is defined as:

$$\text{GSD} = \exp(\sigma_{\text{STD}}(\ln(d_p))) \quad (4.3)$$

The GSD can be estimated using the two equations above and the Coefficient of Variation (CV) defined as the standard deviation divided by the mean. For example, with a mean diameter of 97 nm and a CV of 9%:

$$\mu_{\text{avg}} = 97 \text{ nm}; \quad \sigma_{\text{STD}} = CV \times \mu_{\text{avg}} = 9.1\% \times 97 = 9 \text{ nm}$$

$$\mu_{\text{avg}}(\ln(d_p)) = \ln\left(\frac{97}{\sqrt{\left(1 + \frac{9^2}{97^2}\right)}}\right) = 4.57 \quad \& \quad \sigma_{\text{STD}}(\ln(d_p)) = \sqrt{\ln\left(\left(1 + \frac{9^2}{97^2}\right)\right)} = 0.0926$$

$$\text{GSD} = \exp(0.0926) = \mathbf{1.097}$$

4.1.2.4 Salt nanoparticles (NaCl)

Unlike suspensions of solid particles, NaCl particles are generated from the atomisation of a saline solution containing dissolved salt (0.9% NaCl w/v). As the atomised droplets evaporate, the dissolved NaCl present in those droplets saturates and crystallises to form cubic nanoparticles [153], [154], as seen in **Figure 4-17**.

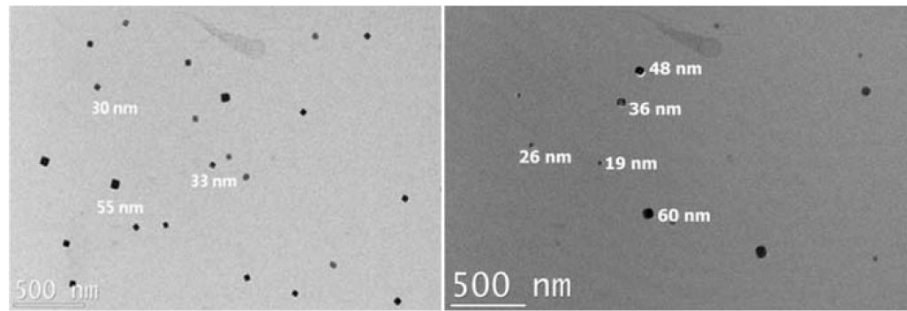


Figure 4-17: TEM image for nebuliser-generated NaCl particles [153]

A size distribution of NaCl atomised with the ATM-226 is presented in **Figure 4-18**. It was found that the concentration of dissolved salt in the solution and the nebuliser droplet size distribution both affected the produced aerosol.

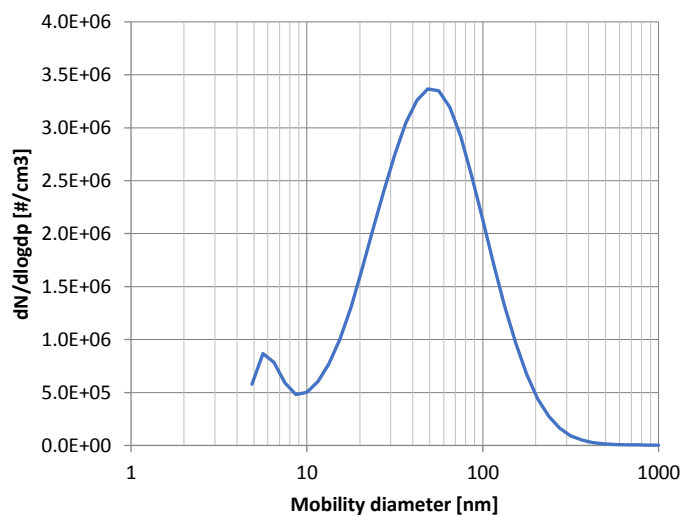


Figure 4-18: Particle size distribution of a saline solution (0.9% NaCl w/v) atomised by an ATM-226 and measured by a DMS-500

4.1.3 Characterisation and removal of Non-Volatile Residue (NVR)

Laboratory experiments were designed to determine parameters affecting NVR formation and to minimise its impact on nebulised aerosol size distributions. The experiments assessing NVR formation consisted in trailing different solvents and vials and investigating the effect of liquid height and aging on NVR peak production. They were performed using a Topas ATM-226 nebuliser (section **3.2.1**), an ejector diluter (Palas VKL 10E) to condition the aerosol, conductive tubing (Carbon-loaded PTFE) and a DMS-500 (without the 5m heated dilution line – section **3.1.3**) sampling at 8 Lpm. A schematic representation of the experimental set-up is displayed in **Figure 4-19**. A small furnace and diffusion screens (**3.2.5**) were utilised in an attempt to remove NVR peaks.

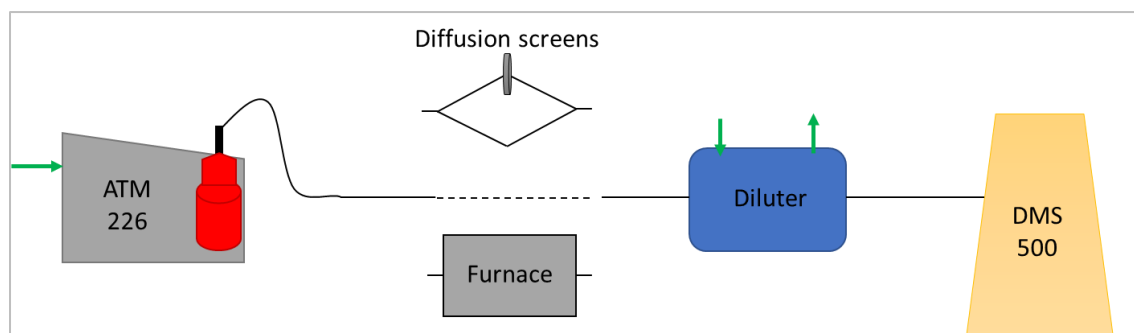


Figure 4-19: Diagram of the typical experimental set-up when investigating NVR formation and removal

For the data presented in this section, the NVR peak and nanoparticle peak properties were again derived from the DMS-500 size distribution fitted with a bi-modal inversion matrix (section 3.1.3) and generally lognormally reconstructed (aerosol mode). It is noted that prior to all experiments, the vials from which the suspensions were atomised were thoroughly rinsed with ultrapure water type 1. Zero (empty vial) and ‘clean water’ (ultrapure water type 1) checks were performed using the DMS-500 to verify that there were no leaks or contamination in the set-up.

4.1.3.1 Parameters affecting NVR formation

As discussed in section 4.1.1.3, the solvent containing suspended particles strongly impacts the NVR concentration and size distribution. It was determined that in-house ultrapure water type 1 produced the least NVR.

Liquid height and vial material impact on the atomisation efficiency and NVR production were investigated by varying the liquid height between 15 mm (25 ml) and 55 mm (125 ml) in laboratory glass vials (Duran GLS 80) and polystyrene vials (Plastic - Corning Costar Inc). In this study, isopropanol was used as a solvent as it produced high concentrations of NVR and hence any variation could be better detected by the DMS-500. Differences of 27% for total number concentration (**Figure 4-20(a)**) and 13% for GMD (**Figure 4-20(b)**) were observed when comparing plastic and glass vials. Similarly, differences of 39% for total number concentration and 16% for GMD were noticed when increasing the liquid height.

The results indicate that less NVR are generated when liquid height is increased, possibly because of a better atomisation efficiency. Due to the large uncertainty of the total number concentration measurement ($\geq 20\%$ [113]) and the high sensitivity of NVR production to any contamination, it was concluded from this study that the effect of material leaching was negligible. Nevertheless, LaFranchi et al. [155] reported that distilled water filled Pyrex (glass) containers produced more than double residual particles of HDPE (polystyrene) containers.

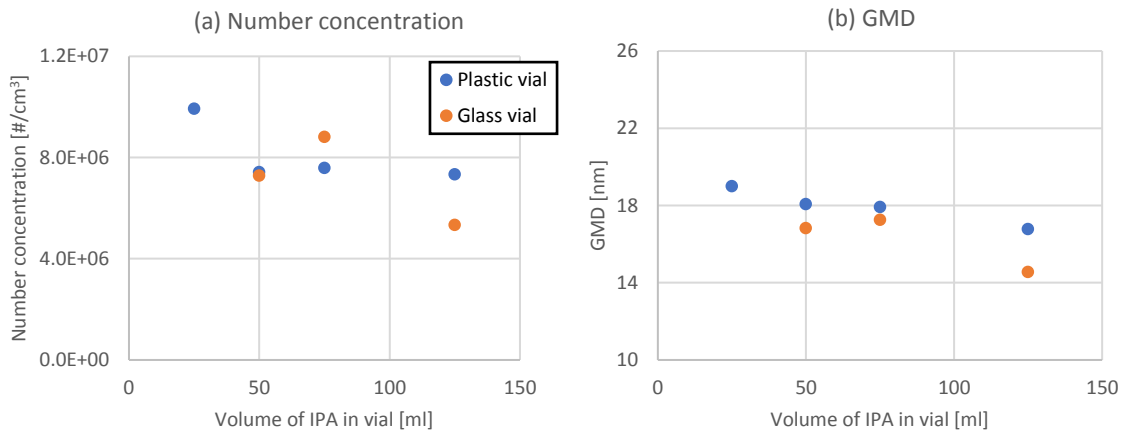


Figure 4-20: Effect of vial material and liquid height (i.e. volume of IPA) on NVR's number concentration (a) and GMD (b) from Isopropanol atomised with an ATM-226 and measured with a DMS-500

The effect of vial wall leaching and suspension ageing on NVR production were further studied by re-atomising silica suspensions mixed in ultrapure water type 1 stored in a glass vial over a period of nineteen days. It was hypothesised by LaFranchi et al. [155] that leaching from the container walls may increase the concentration of dissolved impurities with time. In this study, no significant contamination from storage in a Glass vial was measured over the three week period with both NVR and silica peaks remaining similar relative to the uncertainty (**Figure 4-21**). This indicated that the same suspension stored in a glass vial may be re-used over the course of several weeks. It is noted that the observed fluctuations over time may be attributed to the high noise signal present during the measurements, the DMS-500 being cleaned in between measurements, and the uncertainty associated with using the instrument's bi-modal fitting.

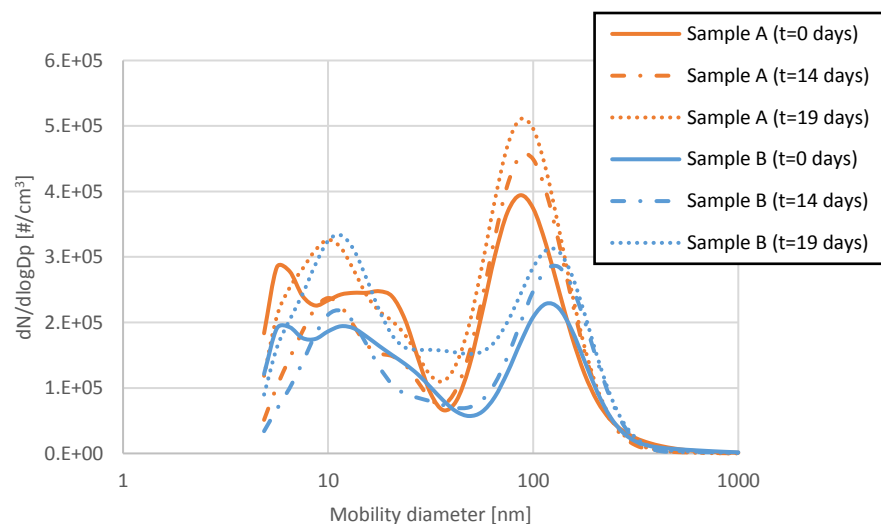


Figure 4-21: Effect of storage time on the NVR and Silica peaks of 100 nm (sample A) and 180 nm (sample B) SiO₂ mixed in ultrapure water type 1 and stored in a glass atomised with an ATM-226 and measured with a DMS-500

It is also seen in **Figure 4-21** that the NVR peak number concentration generated from the silica suspensions is higher ($<10^5$ particles/cm³) than that of ultrapure water type 1 as previously discussed with **Figure 4-8** ($\sim 10^4$ particles/cm³), suggesting that the majority of NVR originate from the purchased silica suspensions as discussed in more details below.

To assess the effect of nanoparticle suspension concentration on NVR production, the concentration of solid SiO₂ suspensions was varied by changing the volume of suspension in a constant volume of ultrapure water (type 1). The results presented in **Figure 4-22(a)** demonstrate that NVR number concentration increase linearly with increasing SiO₂ suspension concentration. This further proves that NVR mostly originates from soluble material present in the purchased suspensions (trace of surfactant, impurities, chemicals, etc, from the manufacturing process). Indeed, as the concentration of impurities increases in the atomised suspension, a given droplet will contain more impurities, causing more NVR to be produced. However, as can be seen in **Figure 4-22 (b)**, the NVR GMD remains fairly constant at any given concentrations (<20 nm), confirming that the NVR GMD strongly depends on the droplet size distribution produced by the nebuliser, as previously discussed in section **4.1.1.1**.

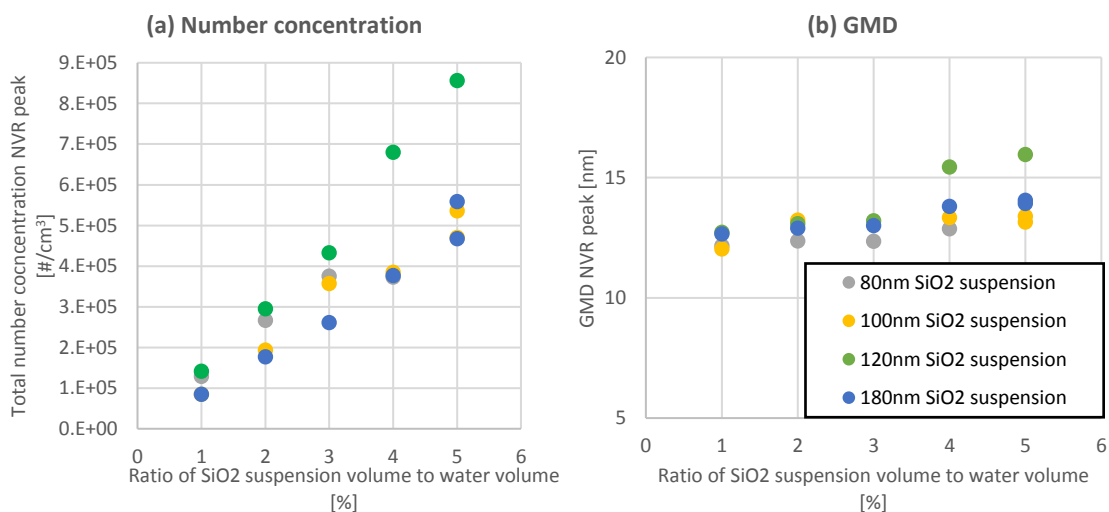


Figure 4-22: Effect of silica suspension concentration on the NVR peak when atomised with an ATM-226 and measured with a DMS-500

It is noted that on in **Figure 4-22**, the 50 nm SiO₂ suspension was not presented because the DMS-500 was not capable of differentiating the NVR peak from the 50 nm silica peak and hence the GMD and number concentration of the NVR peak could only be visually deduced.

4.1.3.2 NVR peak reduction

It was previously discussed that the atomisation of nanoparticle suspensions produced NVR which interfered with the solid nanoparticle size distribution. An investigation to remove or minimise the NVR peak generated from the atomisation of silica suspensions was performed by means of

aerosol heating, centrifugation and classification using both TSI PPS 376060 diffusion screens (section 3.2.5) and a Cambustion Aerodynamic Aerosol Classifier (section 3.2.4). It is noted that NVR interference could also be reduced by using purer water and/or generating smaller droplets. Fissan et al. [117] reported gold and silver nanoparticles down to 22 nm by synthesizing the particles themselves (modified Turkevich method) and using online dilution with ultrapure water (water NVR concentration $< 2 \times 10^3$ particles/cm³) with a nebuliser producing a droplet size distribution similar to the ATM-226. Jeon et al. [132] measured Nanocomposix gold nanoparticles ranging from 5 - 30 nm using online dilution with ultrapure water (impurity levels below 1 ppb by volume) and an nebuliser generating a droplet size distribution with a GMD estimated at 100 nm.

Temperature:

The effect of temperature on the NVR was investigated in conjunction with the thermophoretic experiment (section 5.1) to assess if the residual particles could be evaporated. Nebulised SiO₂ suspensions (50 and 180 nm) were heated at a temperature of up to 910°C in a tube furnace and then cooled (diagram in Figure 5-2) with size distributions measured before and after the furnace, as presented in Figure 4-23. It can be observed that heating the aerosol to those temperatures didn't remove the NVR peak, suggesting that the evaporation temperature of the NVR peak for SiO₂ suspensions is higher than 910°C, or that the residual particles have re-condensed to similar sizes during the cooling which is unlikely. It is noted that the reduction in both NVR and SiO₂ peaks was caused by thermophoretic and diffusional losses, as discussed in chapter 5.

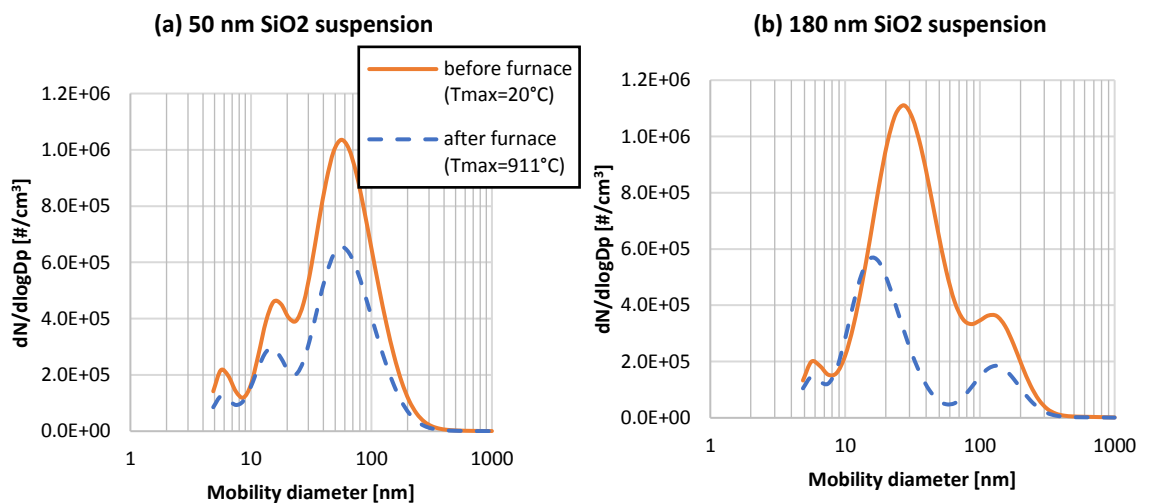


Figure 4-23: Particle size distributions of 50 nm (a) and 180 nm (b) SiO₂ suspensions nebulised by an ATM-226 and measured by a DMS-500 before and after a tube furnace

The effect of high temperatures on residual particles was also assessed with NVR produced from the atomisation of distilled water (type 3 [148]), as presented in Figure 4-24. Differently to atomised SiO₂ suspensions, the NVR peak from atomised water has disappeared after heating the

aerosol to 830°C. Given the NVR peak is still measured after heating at 570°C (**Figure 4-24 (a)**), it can be assumed that NVR produced from distilled water evaporates between 570 and 830°C.

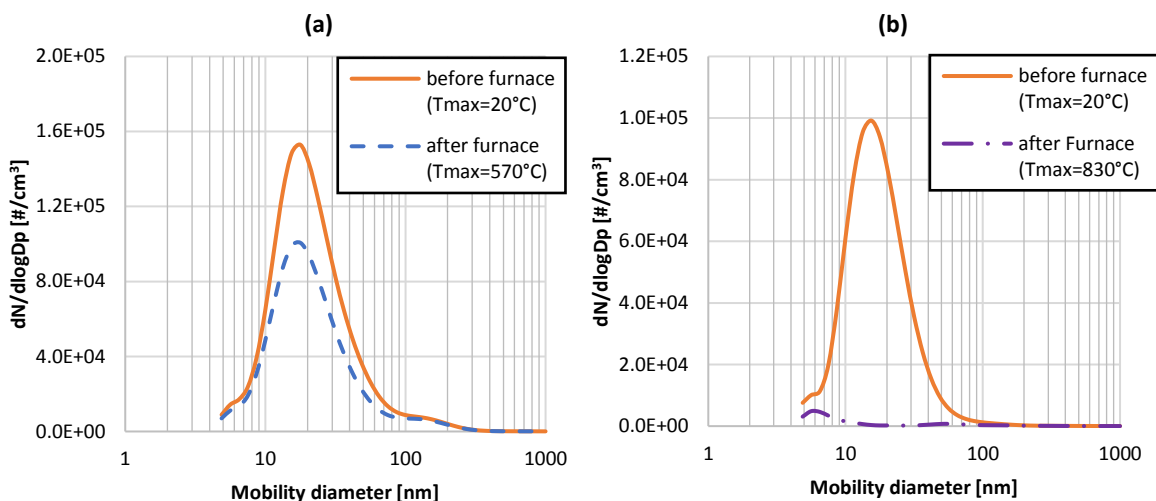


Figure 4-24: Particle size distributions of nebulised distilled water heated at different temperatures on different days ($T_{\max}=570^{\circ}\text{C}$ (a); $T_{\max}=830^{\circ}\text{C}$ (b)) and measured by the DMS-500 before and after a tube furnace

The observed different evaporation temperatures with NVR source highlights that NVR properties and composition must depend on the atomised suspension (i.e. manufacturing process).

Diffusion screens:

As discussed in previously, the smaller particles of an aerosol can be lost via diffusion by transporting it through finely meshed screens. For nebulised nanoparticle suspensions discussed in this chapter, the NVR peak usually ranged between 10-30 nm and is always smaller than the suspended nanoparticles of interest. Thus, the use of three stacked diffusion screens (TSI Particle size selector 376060) was investigated to eliminate NVR contamination.

The size distribution of nebulised 50 nm SiO_2 suspension was measured with and without diffusions screen (setup **Figure 4-19**) at different flowrates corresponding to different penetration efficiency functions, as presented in **Figure 4-25**. It is observed that the NVR peak is reduced by 50% (4.8 Lpm) up to 86% (0.5 Lpm) when using diffusions screens. When comparing with theoretical predictions [144] displayed as grey dotted lines, the measured SiO_2 distribution with screen correlate well the predictions for the main peak although the NVR peak isn't reduced as much as predicted. This difference may be indicative of NVR particles not being spherical as the theory is assuming sphericity, or the diffusion screens are not as efficient as predicted at smaller sizes.

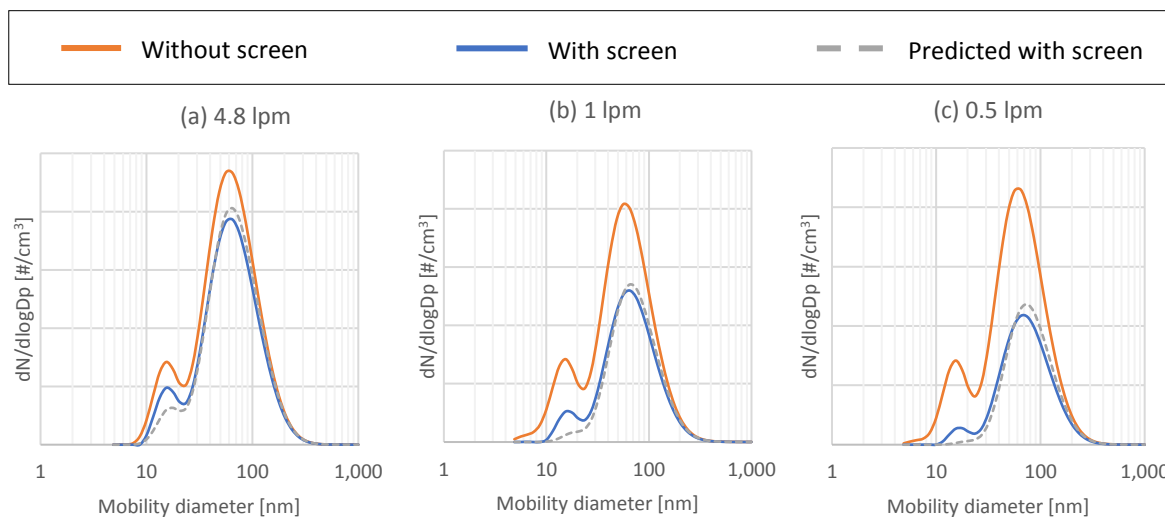


Figure 4-25: Particle size distribution of a 50 nm Silica suspension with and without diffusion screen at different flowrates, atomised by an ATM-226 and measured by a DMS-500

It is noted that as only three diffusion screens were available, sample flows as low as 0.5 Lpm needed to be reached to theoretically remove the NVR peak. However, at such low flows, the uncertainty associated with the measurement of the flow is relatively high and may explain in part the difference between the measured and predicted size distributions when the diffusion screens are used.

Centrifugation:

Centrifugation of nanoparticle suspensions was trialed to separate the suspended particles from NVR precursors present in the solution prior to atomisation. During centrifugation (section 3.2.2), solid nanoparticles sediment towards the bottom, while impurities remain dispersed in the solution. After centrifugation, the top half of the suspension was decanted and replaced with ultrapure water type 1, previously shown to produce minimal residual particles (Figure 4-8). The sedimented particles were then re-dispersed in the purer solution using an ultrasonic bath.

Particle size distributions of atomised silica suspensions (100 and 180 nm) were measured prior and after centrifuging for long periods of time (up to 40 minutes) at a speed of 40,000 RCF, as presented in Figure 4-26. The volume of the decanted water after centrifugation was also atomised and is referred to as 'residual' (grey dashed line). Results show that centrifugation was partly successful in separating the NVR peak from the SiO₂ peak, with the NVR peak reduced by a factor of ~5. However, the separation wasn't optimal as some NVR remained in the centrifuged suspensions and some SiO₂ particles transferred to the 'residual', particularly with the 100 nm Silica suspension (~50% lost - Figure 4-26 (a)). These outcomes were expected as only part of the original suspension was replaced with ultrapure water and the sedimented SiO₂ particles easily resuspend after centrifugation (i.e. particles were seen to re-disperse when replacing some of the suspension with water).

It is noted that centrifugation was originally attempted with a lower power centrifuge (4200 RCF) for longer periods of time (up to 3h) and similar results were observed. It was also found that the centrifuge breaking parameter was important as slowing down the centrifuge too fast resulted in solid nanoparticles re-dispersing while still in the centrifuge.

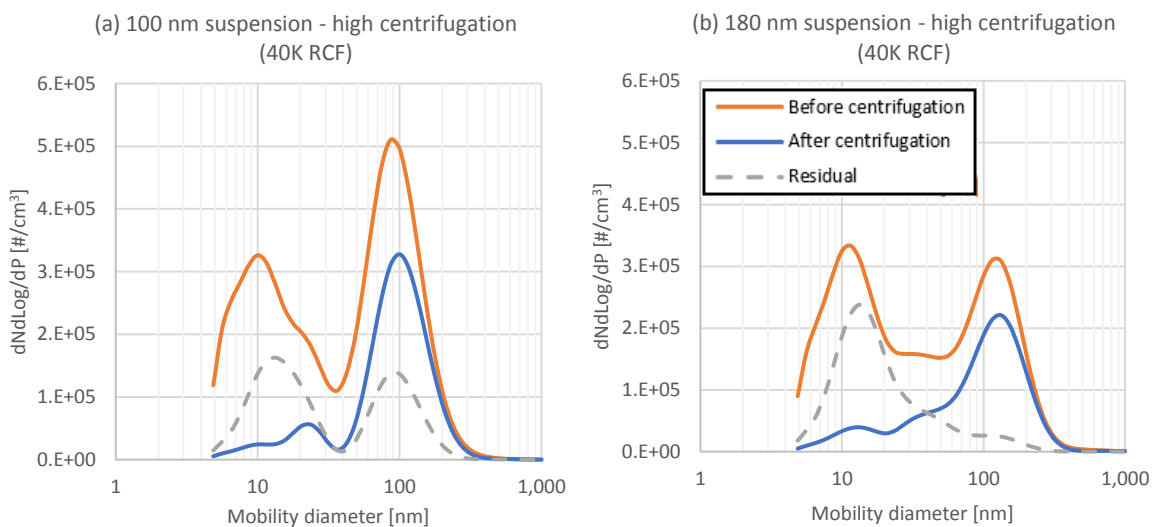


Figure 4-26: Particle size distribution of a 100 nm (a) and 180 nm (b) Silica suspensions before and after a 40 min centrifugation at 40K RCF and replacement with ultrapure water, atomised by an ATM-226 and measured by a DMS-500

It was also attempted to analyse the chemical composition of the NVR peak using an inductively Coupled Plasma Mass Spectrometry (ICP-MS – Optima 2100 DV) on the 180 nm SiO₂ suspension after centrifugation (grey dashed line **Figure 4-26 (b)**). IPC-MS can measure 28 chemical elements against calibration standards at 0.1, 1 and 10 mg/L (1 mg/L= 1 ppm).

It was first theoretically estimated whether the expected NVR concentration was above 0.1 ppm using equation (4.4) with a nebuliser flow of 4.8 Lpm and an atomisation rate of 0.08 ml/min (section 4.1.1.2). The NVR total mass concentration was determined at $3 \times 10^{-7} \mu\text{g}/\text{cm}^3$ using the NVR peak of the measured ‘residual’ size distribution (grey dashed line **Figure 4-26 (b)**) and converting it into a mass-weighted distribution using equation (2.6) while assuming a particle density of 1 g/cm³. It is noted that a dilution of 2 was included in the calculation as the sampled aerosol needed to be diluted to achieve a flow of 8 Lpm at the inlet of the DMS-500.

$$\frac{\text{NVR mass } [\mu\text{g}/\text{cm}^3] \times \text{atomiser flow } [\text{cm}^3/\text{s}]}{\text{atomisation rate atomiser } [\text{ml}/\text{s}]} = \text{NVR concentration } [\mu\text{g}/\text{mL} = \text{ppm}] \quad (4.4)$$

A NVR concentration of **0.036 ppm** was determined using the method described above, suggesting the NVR concentration was below the range of detection of the IPC-MS. In agreement with this finding, no elements were detected in the ultrapure water nor the ‘residual’ solution when

measured in the IPC-MS. To assess the NVR residual chemical composition in the future, an analyser with a resolution higher than 0.1 ppm should be used.

AAC classification:

A Cambustion Aerosol Aerodynamic Classification (AAC) was tested on nebulised silica suspensions in an attempt to isolate the silica peak from the NVR peak. Using the Silica density and mass-mobility exponent as inputs (i.e. 2.165 g/cm³ and spherical), the AAC should in theory classify SiO₂ particles. Size distributions of 50, 100 and 180 nm SiO₂ suspensions with the AAC on and off are presented in **Figure 4-27**. It can be seen the AAC is partly successfully at removing the NVR contamination with less than 10% of the original NVR peak being measured with the AAC on. Given the AAC classifies according to the particle's aerodynamic diameter, it is possible that a small fraction of the NVR has a similar aerodynamic diameter to the classified SiO₂ and hence passes through the classifier.

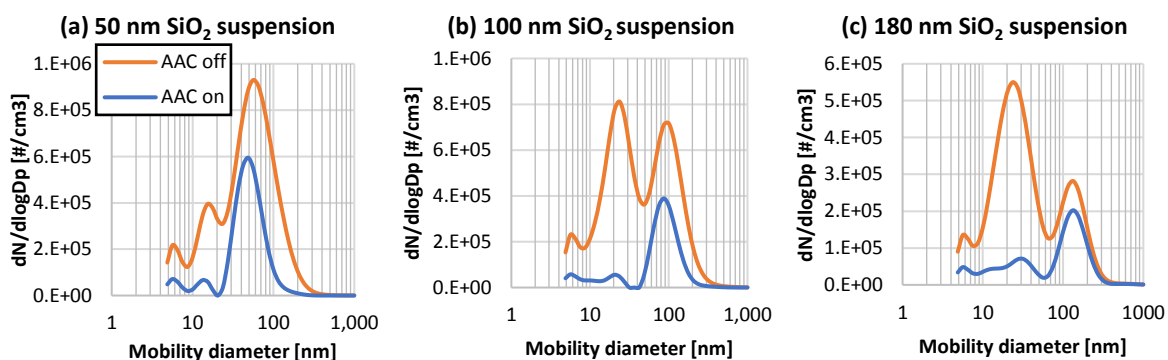


Figure 4-27: Particle size distribution of a 50 nm (a), 100 nm (b) and 180 nm (c) Silica suspensions with the Cambustion Aerosol Aerodynamic Classifier (AAC) on and off, atomised by an ATM-226 and measured by a DMS-500

4.2 Classified aerosol size distributions for laboratory experiments

As seen in section 4.1, the laboratory produced particle size distributions are generally not to monomodal nor monodisperse. In this section, particle classification was investigated to produce more monomodal size distributions at sizes representative of aircraft nvPM. As an alternative to the commonly used Differential Mobility Analyser (DMA), a Cambustion Aerodynamic Aerosol Classifier (AAC) was investigated to classify nanoparticles generated from the atomisation of suspensions (SiO₂), solutions (NaCl) and from a graphite generator (PALAS GFG-100 - section 3.2.2) according to their aerodynamic diameter.

The AAC relies on the centrifugal force and relaxation time to classify particles and hence has a better transmission efficiency, 2 to 5 times higher, than electrostatic classifiers like the DMA that have uncertainties associated with multiple-charging artefact [142]. Other instruments classifying

particles according to their aerodynamic diameters are commercially available such as the TSI APS (Aerodynamic Particle Sizer) and the Dekati ELPI (Electrical Low Pressure Impactor) [142]. Nevertheless, the AAC has a better resolution, a larger scan range (25 nm - 5 μm) and its recommended inlet sample flow ranges between 0.3 and 1.5 Lpm [139], making it the most suitable aerodynamic classifier for laboratory experiments performed in this thesis.

The investigated aerosols classified with the AAC were characterised by measuring their size distribution using a DMS-500. In the AAC user interface, two settings can be modified to change the classification range: the size (i.e. d_a or equivalently d_m using equation (2.1) for conversion) and the resolution parameter R_s defined as the ratio of sheath flow (Q_{sh}) to sample flow (Q_a). The variation of these parameters causes the rotational speed and sheath flow to change to permit classification at the specified size. Hence, the AAC capabilities were first assessed by varying the aerodynamic diameter (d_a) and the Resolution parameter (R_s) or the sheath flow (Q_{sh}) when the sample flow (Q_a) is kept constant.

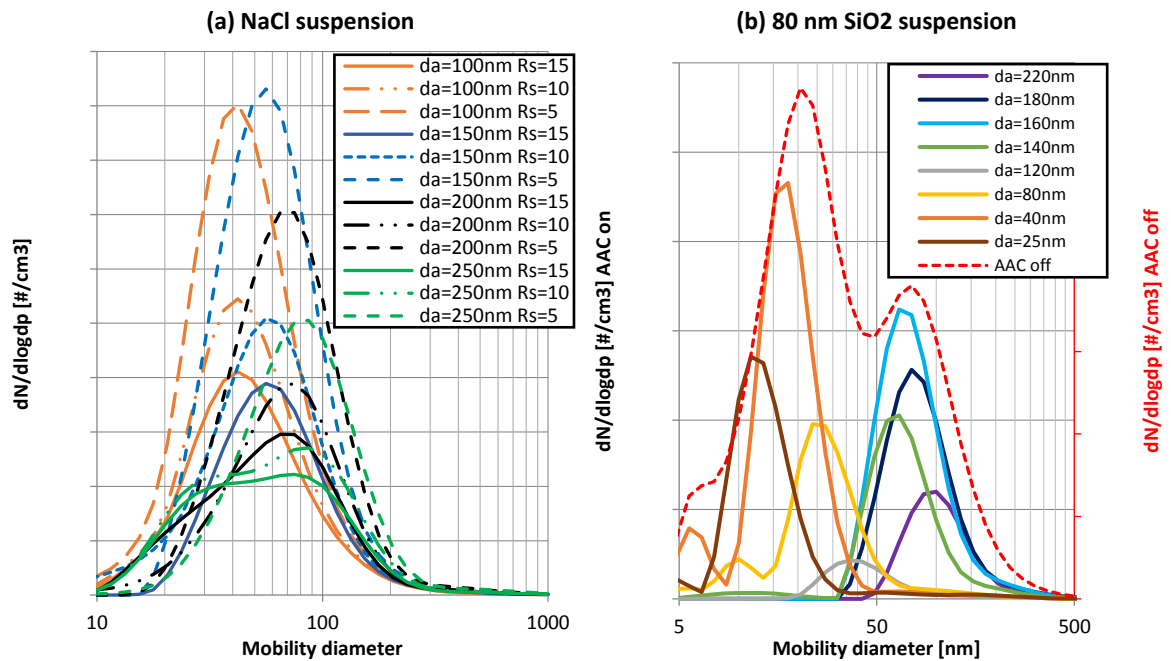


Figure 4-28: Particle size distributions of a saline suspension (a) and silica suspension (b) classified by an AAC at different R_s and d_a settings, atomised with an ATM-226 and measured with a DMS-500

The classification capabilities of the AAC were initially tested by varying d_a and R_s on a saline suspension (0.9% NaCl w/v) and a 80 nm silica suspension atomised by the ATM-226. As presented in **Figure 4-28**, it was observed for the saline suspension that varying the two parameters modified the measured size distribution (**Figure 4-28 (a)**). The largest R_s values ($R_s=15$) displayed the widest distributions and lowest number concentrations, due to the higher sheath flow to sample flow ratio. Reducing the aerodynamic diameter parameter (d_a) logically shifted the size distribution towards

smaller size. When keeping R_s constant, it can be seen for the silica suspension (**Figure 4-28 (b)**) that varying d_a reproduced a similar shape to that of the original size distribution without the AAC (red dashed line) and that the NVR and SiO_2 could be separated.

In preparation for laboratory particle loss experiments, R_s (i.e. Q_{sh}) and d_a AAC settings were varied to produce the highest concentration and narrowest particle peak (i.e. smallest GSD) for each particle type (SiO_2 , NaCl, graphite) at sizes representative of aircraft PM (10-200 nm). Three typical resultant size distributions for each particle type measured by the DMS-500 are presented in **Figure 4-29** along with the original size distributions generated without the AAC (red dashed line). As can generally be seen, AAC-classified size distributions appear monodisperse but are not perfectly monomodal according to their mobility diameters. Particle concentrations with the AAC turned on are lower when compared with the unclassified distributions due to losses (i.e. spectral broadening) in the instrument. Nevertheless, all concentrations remained $> 10^5$ particles/cm³ which is an ideal range for DMS-500 measurements.

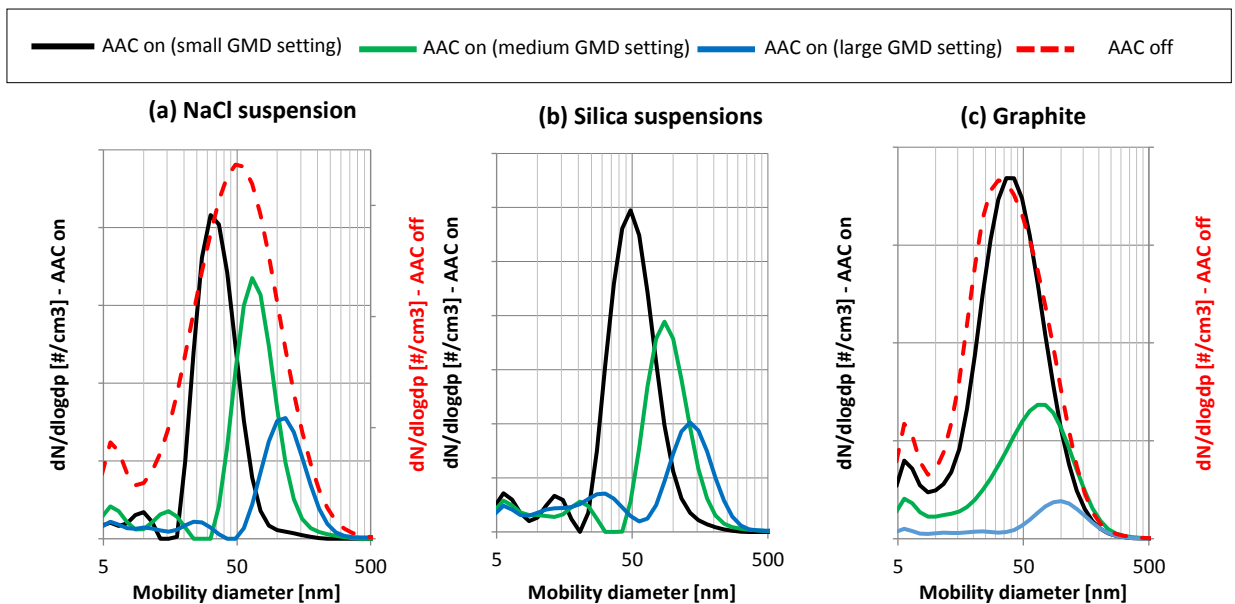


Figure 4-29: Particle size distributions of salt (a) and silica (b) suspensions atomised with an ATM-226 and graphite (c) classified with an AAC at different settings producing different GMDs and measured with a DMS-500

It is noted that small NVR peaks for the atomised suspensions and small secondary peaks for the graphite are generally still present after classification (**Figure 4-29**), highlighting that the AAC doesn't perfectly classify the nebulised silica and salt according to their mobility diameter. Therefore, the GMD, GSD and total number concentration of the classified particle size distributions were derived not from the discrete spectrum but from the DMS-500 main aerosol mode which only includes a lognormal fit to the main particle peak, hence disregarding the small secondary peaks at low sizes (section 3.1.3).

It is also noted that there is no “AAC off” distribution (red dashed line) in **Figure 4-29(b)** given that with silica, the AAC was solely used to minimise the NVR peak (section **4.1.3.2**), while for salt and graphite, the AAC was used to size-select particles from the originally wide distributions (GSD>2).

Given particle generation and classification were shown to fluctuate on a daily basis, the generated particle size distributions with the same AAC settings sometimes appeared different. Hence, specific GMD and GSD were targeted prior to any experimentation. The range of GMD and GSD of the generated size distributions with typical AAC settings (varying Q_{sh} and d_a with $Q_{sh}=1.5$ Lpm) observed during the laboratory experiments discussed in chapter **5** are presented in **Table 4-3**.

Table 4-3: Range of GMDs and GSDs measured by the DMS-500 using typical AAC parameters at different settings (small, medium and large GMD) during laboratory particle loss experiments (with the AAC sample flow Q_a fixed at 1.5 Lpm)

		Small GMD setting	Medium GMD setting	Large GMD setting
Silica	GMD range [nm]	48 - 53	84 - 94	119 - 142
	GSD range	1.36 - 1.50	1.32 - 1.55	1.32 - 1.51
	Typical AAC parameters	$d_a = 100$ nm $Q_{sh} = 4$ Lpm	$d_a = 180$ nm $Q_{sh} = 5$ Lpm	$d_a = 300$ nm $Q_{sh} = 3$ Lpm
Salt	GMD range [nm]	28 - 46	61 - 76	91 - 115
	GSD range	1.23 - 1.40	1.25 - 1.44	1.33 - 1.37
	Typical AAC parameters	$d_a = 100$ nm $Q_{sh} = 10$ Lpm	$d_a = 220$ nm $Q_{sh} = 10$ Lpm	$d_a = 350$ nm $Q_{sh} = 6$ Lpm
Graphite	GMD range [nm]	37 - 42	52 - 74	92 - 139
	GSD range	1.60 - 1.85	1.6 - 1.89	1.37 - 1.61
	Typical AAC parameters	$d_a = 22$ nm $Q_{sh} = 2$ Lpm	$d_a = 40$ nm $Q_{sh} = 4$ Lpm	$d_a = 50$ nm $Q_{sh} = 4$ Lpm

The targets for salt size distributions were GMDs around 40, 70 and 100 nm respectively and a GSD of ~ 1.3 , as displayed in **Figure 4-29(a)**. The targets for classified silica suspensions were GMDs of approximately 50, 95 and 135 nm and a GSD of ~ 1.35 , as shown in **Figure 4-29(b)**. The targets for classified graphite aerosol distributions were GMDs of 40, 60 and 95 nm respectively with a GSD varying between 1.6 -1.9, as represented in **Figure 4-29(c)**. As highlighted by the larger GSD, graphite aerodynamic classification was shown to be the least efficient, particularly at lower sizes. The spectral broadening in the AAC caused by diffusion and sheath flow disturbances is currently corrected with an empirical fit derived from measurements with oil droplets [77]. Hence, it may differ for non-spherical particles or aggregate, especially at lower sizes where diffusion losses are dominant [142]. This may explain why graphite wasn’t as efficiently classified and may be corrected in future studies by applying a spectral correction factor estimated using soot-like particles. It is noted that cubic salt particles (section **4.1.2.4**) were classified as well as spherical silica particles, demonstrating that the current spectral broadening correction is applicable to cubic particles.

To better understand the different definitions of particle diameter as introduced in section 2.1.1, the ‘optimal’ AAC aerodynamic diameter (d_a) was compared to the mobility (d_m) measured by the DMS-500 and the physical (TEM) diameter provided in the specification sheet for silica suspensions (appendix 10.3), as presented in Table 4-4. The AAC’s d_a was converted to d_m by numerically solving equation (2.1) as performed in the AAC software [77] assuming a silica particle density of 2.165 g/cm³ and sphericity.

Table 4-4: Silica suspensions diameters measured in suspension (TEM) and after being atomised (AAC, DMS-500)

	80 nm SiO ₂	100 nm SiO ₂
d_a AAC [nm]	160	190
d_m AAC (derived from d_a) [nm]	89	105
d_m DMS-500 (CMD aerosol mode) [nm]	73	91
d_{TEM} [nm]	82±5	97±9

The mobility diameters derived from the AAC and the DMS-500 and the physical diameter agree within 18% and 13% for the 80 nm and 100 nm SiO₂ suspension, respectively.

It was shown that the AAC was capable of classifying graphite, silica and salt nanoparticles permitting the generation of relatively monomodal aerosols at different GMDs. The size distributions presented in Figure 4-29 were hence used in laboratory experiments (chapter 5).

4.3 PM capture and characterisation in a liquid

As discussed previously health effects of PM from aircraft engines are still largely unquantified, since exposure at relevant conditions are challenging [31]. Aircraft engine combustion exhaust contain particles below 100nm [9] that, when inhaled, can penetrate through the respiratory system reaching the alveolocapillary membrane (i.e. blood-air barrier) and entering the blood stream [25]. It has been hypothesised [33], [34] that once in the blood, fractal soot nanoparticles may modify clot formation and generate abnormal clot structures that can be more difficult for the body to re-dissolve.

To perform in-vitro studies of inhaled soot nanoparticles in the blood, aircraft PM need first be captured in a solvent whilst preserving the size of the airborne PM. Ultrafine particles are generally collected for chemical and toxicological analysis by filtration, as it is practical and has a good collection efficiency [156], [157]. Nevertheless, this approach has drawbacks - a need for a dispersing agent (i.e. surfactant), poor particle recovery from the filter, and filter clogging can induce a pressure drop, increasing over time, requiring regular media cleaning or replacement [158],[159].

Also, when collected onto filters, nanoparticles adhere to each other and form large agglomerates that can't be re-separated back to their original size [160],[118]. Agglomeration during filter collection is highlighted in **Figure 4-30** comparing particles recovered from a filter **(a)** and directly captured in the exhaust **(b)**.

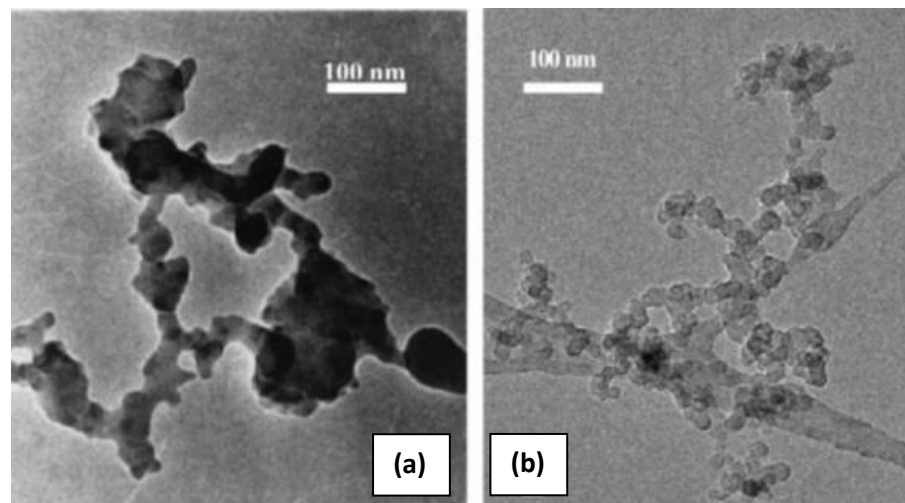


Figure 4-30: TEM picture of soot emitted by a diesel engine – (a) recovered from filters and suspended into water – (b) directly captured from the diluted exhaust gas [160]

An alternative to filter collection is particle capture by liquid impingement (i.e. bubbling), as commonly employed by industry for gas cleaning purposes [161]. The theory of absorption of particles from gas bubbles during their rise in a liquid was originally modelled by Fuch and revisited by Pich and Schutz [158], [159]. When a small bubble containing a particle travels through a liquid, particles contained in the bubble can reach the gas-liquid interface by diffusion and be transferred to the liquid, as highlighted in **Figure 4-31**. It was stated that the sticking probability of particles at the gas-liquid interface is one and is independent of particle structure and hydrophobicity [161].

Fresh soot being extremely hydrophobic [162], it can become unstable in an aqueous solution and coagulate. However, soot produced from combustion is also mixed with gaseous species like ozone and soluble inorganic compounds like H_2SO_4 that can chemically alter soot surface properties, making it more hydrophilic [162]. The presence of combustion product gaseous species can also affect a suspension's stability by turning the pH more acidic via the absorption of CO_2 and the formation of sulfuric and nitric acids (i.e. SO_3 and NO_2) [118].

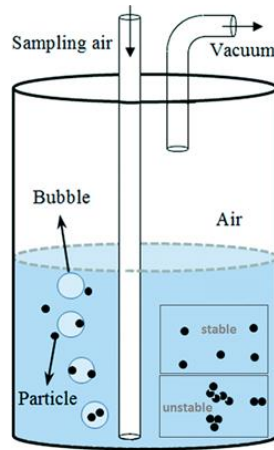


Figure 4-31: Diagram of particles being transfer from gas to liquid in a bubbler

Capture and preservation of combustion exhaust particles in suspensions may also be used for calibration, via atomisation and re-suspension of the soot in the gas phase. Anderlohr and Schaber [118] have proven experimentally with 60 nm silica nanoparticles that transfer to a liquid and re-atomisation had nearly no influence on the particle size distribution. Currently, nvPM instruments must be shipped to a certified calibration center once a year for calibration, which presents both a time constraint and a significant expense. Furthermore, there is no current method for testing these instruments for compliance in the field when being used for expensive and timely engine emissions testing. Unforeseen issues or complications with the test instrumentation could invalidate critical engine testing if not corrected. Such issues could be identified and corrected if a field-deployable system were available that provides operational validation or calibration of the measurement system in real time during a test.

In this section, capture of aircraft PM in a liquid was attempted by sampling exhaust aerosol using numerous bespoke bubblers to investigate the potential of liquid suspensions for particle generation as a validation and calibration method. Outside the scope of this study, collected samples were also provided to the Complex Fluids Research Group of Swansea University's College of Engineering to assess the impact of aircraft particulate materials on blood clot formation. At the time of submission of this thesis that work is incomplete and conclusions regarding pernicious modification of blood clot structure by particulate matter are yet to be drawn [private communication with Rebecca Hudson].

4.3.1 Particle capture from gas to liquid

There are several challenges with transferring nanoparticles < 100 nm to a liquid using a bubbler. The bubble residence time in the liquid needs to be long enough and the bubble's diameter small enough for particles in the bubble to travel via Brownian motion from its centre to the gas-liquid interface. The rising velocity of a bubble in a liquid is driven by buoyancy and drag force as

described by Stokes law, meaning that the smaller the bubble, the slower it is hence the longer it stays in the liquid [163]. Also, in smaller bubbles, the distance between the particles and the gas/liquid interface inside the bubble is smaller, hence increasing the transfer efficiency [164]. Discussed below are important parameters affecting bubble residence time and size and hence the particle transfer efficiency of a bubbler.

- Bubbler's nozzle: Bubbles are typically generated by flowing a gas through a nozzle. Using a fritted nozzle instead of a single hole nozzle can increase the number of bubbles per gas volume. Hence decreasing the size of holes/frits can reduce bubble size, increasing the transfer efficiency [165].
- Packing beads: The use of beads can potentially increase the transfer efficiency by preventing bubble coalescence, increasing the bubble residence time in the liquid and increasing the contact surface area between of the droplets in the liquid [159], [166]. However, the use of beads can also increase pressure drop and generate preferential path reducing the overall transfer efficiency if the density of the beads is too low, as shown in **Figure 4-32**. Indeed, glass beads were shown to be inefficient at generating smaller bubbles (**Figure 4-32(b)&(c)**), but 1 mm metals beads permitted the generation of smaller and more uniform bubbles (**Figure 4-32(d)**) when compared with no beads bubbles (**Figure 4-32(a)**).

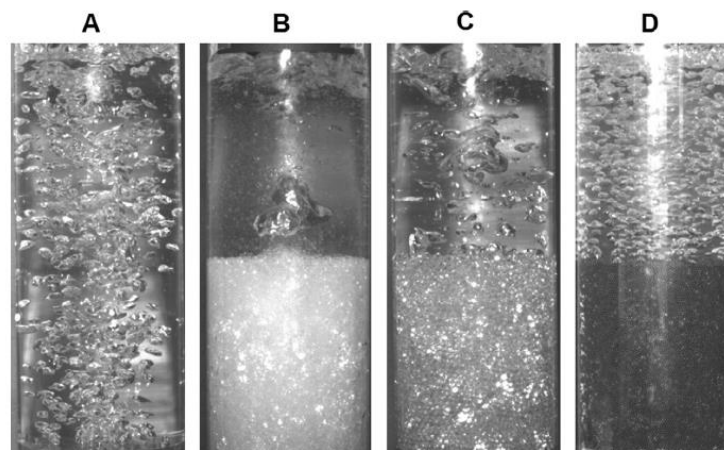


Figure 4-32: Visualisation of bubbles under different column operating conditions: (A) 20 cm of liquid; (B) 10 cm of 1.5mm diameter glass beads in 20 cm of liquid; (C) 10 cm of 2.75 mm diameter glass beads in 20 cm of liquid; (D) 10 cm of 1 mm diameter metal beads in 20 cm of liquid [159]

- Aerosol flow in the bubbler: Particle transfer efficiency may reduce with increasing aerosol flow in the laminar regime due to the shorter bubble residence time in the liquid. In contrast, transfer efficiency may increase with increasing flow in the turbulent regime thanks to the

formation of micro-bubbles turbulent diffusional force in the bubble increasing particles velocity [164], [166].

- Liquid height: Increasing the liquid height and hence the bubble residence time in the liquid can enhance the transfer efficiency of gas-born particles [158], [159], [161], [165], [166].
- Liquid solvent: Particles transfer efficiency can vary depending on the solvent [165]. When exposed to saturated vapor of organic solvent in bubbles, fractal particles can restructure to a more compact form and hence modify the captured particles [42]. Furthermore, particles may agglomerate if the suspension is unstable in the solvent (pH, ionic strength).
- Particle charging state: Higher transfer efficiencies can be achieved by charging the particles, inducing electrostatic forces that forces the particles to the air-liquid interface [158].
- Surfactant: The presence of surfactant in the solvent can help produce monodisperse and spherical bubbles, preventing bubble coalescence and lowering the surface tension at the gas-liquid interface, in turn increasing the transfer efficiency [161]. On the other hand, a small amount of surfactant can produce a large amount of foam during bubbling causing foam to enter the exhaust. Surfactant is also a source of NVR (section 4.1.3).

Multiple bubblers with different characteristics were investigated at capturing combustion exhaust nanoparticles, as shown in **Figure 4-33**.

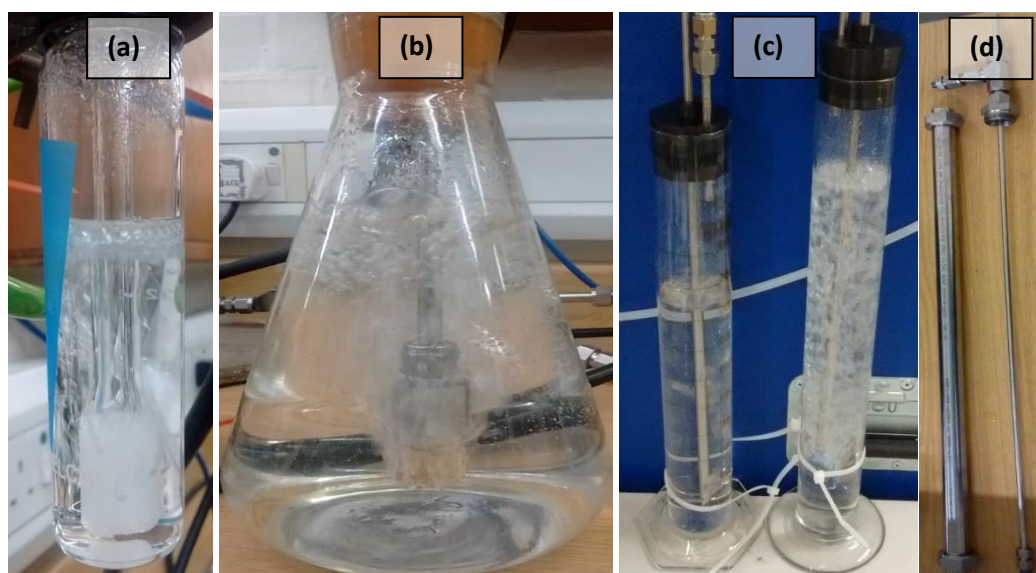


Figure 4-33: Photographs of the various bubblers used to capture nanoparticles in a liquid including a midget impinger (a), a conical flask (b), glass cylinder bubblers (c) and a stainless-steel bubbler in parts (d)

Initially, a midget impinger with a fritted nozzle and a maximal capacity of 20 ml (**Figure 4-33(a)**) was used at the exhaust of an APU engine (section 3.4) with various solvents (water, saline, isopropanol and ethanol) and surfactant (triton-X). However, the small transfer efficiency of the impinger combined with the short sampling times of about five minutes during the test campaign meant that insufficient particles were transferred to be characterised in the liquid or re-dispersed. A much larger conical flask with a volume capacity of 1L (**Figure 4-33(b)**) was investigated over longer sampling durations in the exhaust of a combustion rig. Transferred particles were detected in the liquid using Malvern instrumentation (section 3.1.4) but the very large volume of the conical flask and low liquid height meant that only a small fraction of soot was captured. To increase liquid height while maintaining a similar volume, glass measuring cylinders with an internal diameter of 50 mm and a capacity of 500 mL (**Figure 4-33(c)**) were also investigated. A 3D-printed bung with two holes for inlet and outlet gas flows was used to insulate the top of the glass cylinder. The glass cylinder bubblers displayed better performance than the conical flask at capturing combustion exhaust nanoparticles and allowed visual observation of the bubbling process, but they were fragile and required liquid extraction from the top. Hence a taller, narrower and more robust bubbler was constructed from stainless steel (**Figure 4-33(c)**) to maximise liquid height whilst keeping the total volume to a minimum. This design also facilitated extraction of the liquid from the bottom of the bubbler.

4.3.1.1 Characterisation of particle transfer efficiency

To validate particle transfer efficiency theory discussed in the previous section and to help with the design of an efficient bubbler to capture nanoparticles from gas to liquid, experiments were undertaken characterising different nozzles, liquid height and the use of beads. A glass cylinder bubbler filled with distilled water was used with graphite, soot-like, particles generated from a PALAS graphite generator (section 3.2.2). Penetration efficiencies were estimated using a DMS-500 (section 3.1.3) by successively measuring the aerosol size distribution on entry to and exit from the bubbler at a flowrate of 3 Lpm. A schematic representation of the experimental set-up is offered in **Figure 4-34**. It is noted that the PALAS graphite generator was observed to output unsteady concentrations and sizes with time, hence each condition was repeated four times with individual measurements of 30 seconds shown to have a standard deviation < 3%.

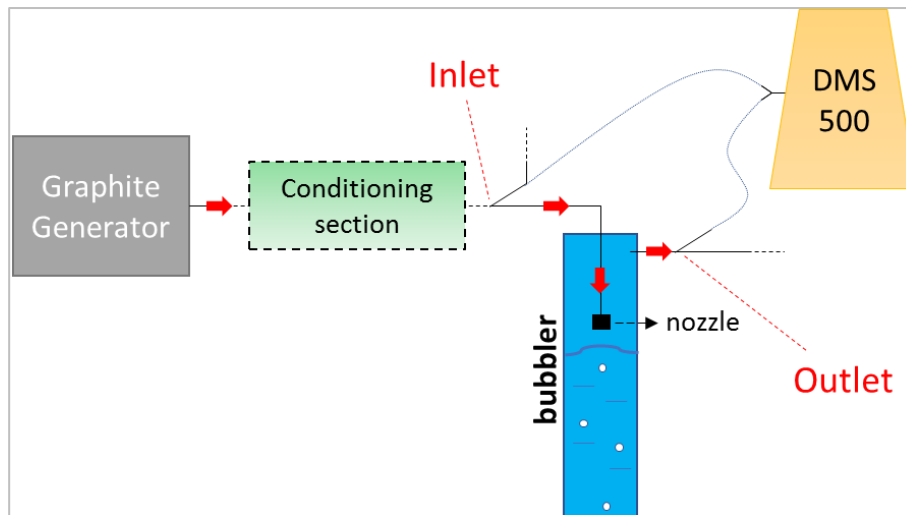


Figure 4-34: diagram of the experimental set-up of the nozzle's characterisation experiment

Whilst smaller bubbles aid the transfer of particles from bubble to liquids, additional diffusional loss may occur if the nozzle used is too small. The transmission efficiency of a sintered brass nozzle (smallest porosity – Nozzle 1), a sintered steel nozzle (larger porosity – Nozzle 2), and a single hole $\frac{1}{4}$ " stainless-steel pipe was assessed as presented using the set-up highlighted in **Figure 4-34**. To prevent agglomeration caused by the long residence time in the bubbler and the high concentration of particles produced by the PALAS generator (10^6 - 10^7 particles/cm³), the bubbler was almost completely filled with water with the nozzle positioned 30 mm above the waterline, as shown in **Figure 4-34**.

The penetration efficiency and GMD variation of the three investigated nozzles measured at two graphite generator settings are presented in **Figure 4-35**. The sintered brass nozzle displayed the largest nozzle deposition efficiency due to the smaller pore sizes, which was highest for the more diffusive smaller particles (42%). It is noted that due to higher diffusion losses of smaller particles there is also an observable increase in the measured GMD at the outlet of the bubbler for both fritted nozzles (**Figure 4-35(b)**). Losses in the $\frac{1}{4}$ " plain orifice were $\sim 25\%$ at both investigated sizes, suggesting that deposition wasn't dominated by diffusion in this case.

Theoretical losses (excluding nozzles) were estimated at 4% and 8% for the small and large graphite generator settings using the UTRC particle transport model (section **2.4.1**). Additional coagulation losses were estimated at 2% at the 23 nm setting ($\sim 2 \times 10^6$ particles/cm³) and 4% at the 45 nm setting ($\sim 8 \times 10^6$ particles/cm³). If no losses were occurring in the nozzle, 8% and 10% deposition efficiency would have been expected respectively.

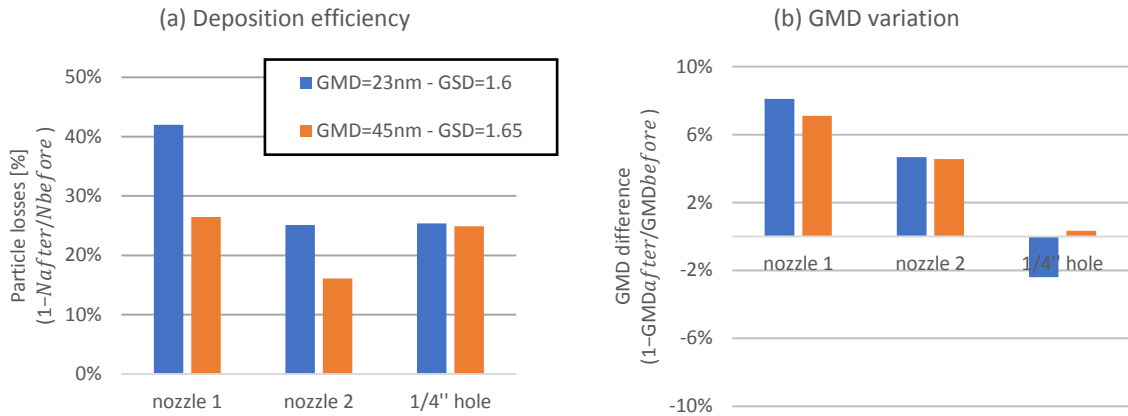


Figure 4-35: Graphite nanoparticles loss (a) and GMD variation (b) inside different nozzles measured by a DMS-500

With the 1/4" plain orifice the 25% loss was higher than expected, it was hypothesised that due to the short distance between the nozzle outlet and the water surface with the aerosol flow directed towards the water, additional inertial losses occurred at the water surface, this theory is supported by the witnessed decrease in GMD seen in **Figure 4-35(b)** which indicates a preferential loss of larger particles. As for the two fritted nozzles, additional inertial loss to the waterline should not occur given the aerosol flow was exiting the nozzles in all directions. Hence, deducting theoretical loss from the measured deposition efficiency, it was estimated that 18-32% of particles were trapped in the sintered brass nozzle and 8-15% of particles were lost in sintered steel nozzle. Similarly, Miljevic et al. [165] witnessed significant losses of nanoparticles in fritted nozzle.

Having a higher penetration efficiency than the sintered brass nozzle (nozzle 1) whilst generating smaller bubbles than the 1/4" plain orifice, the sintered steel nozzle (nozzle 2) was chosen as the most suitable nozzle from the three investigated.

The effect of liquid height and packing beads on the particle's transfer efficiency was experimentally investigated for PALAS generated particles using the sintered steel nozzle by varying the liquid volume from 200 ml to 450 ml (i.e. 100 – 225 mm height) and trialling glass beads of diameters ranging from 1 to 4 mm, as represented in **Figure 4-37**. It is noted that when using the 1 and 2mm beads, preferential gas flow paths were observed. Also, it was significantly more difficult to recover the liquid from the 1 and 2mm beads due to their smaller size. Hence, the 4 mm glass beads were chosen for further investigation.

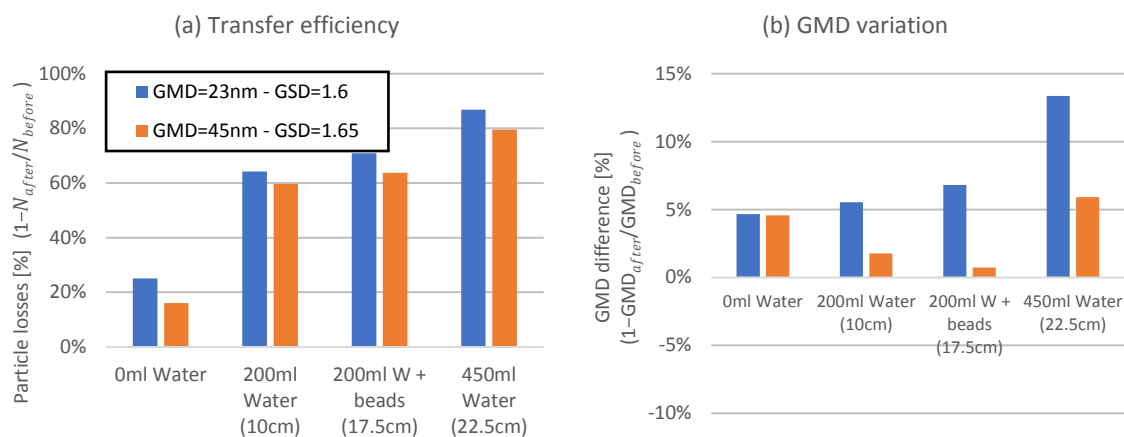


Figure 4-36: Transfer efficiency from gas to liquid (a) and GMD variation (b) of soot-like nanoparticles in a bubbler containing different volumes of water and measured by a DMS-500

The transfer efficiency and GMD variation at different liquid heights for the two PALAS graphite generator settings are presented in **Figure 4-36**. It is observed that when comparing with losses solely occurring in the nozzle (i.e. '0 ml Water'), significantly higher deposition efficiencies are measured with water, hence particles are successfully being transfer from the aerosol to the liquid (**Figure 4-36(a)**). The highest transfer efficiency achieved was 64% (nozzle losses were deduced as particles lost in the nozzles are assumed not to have transferred in the liquid) with 450 ml of water (i.e. 225 mm height).

When increasing the liquid height by a factor 2.5 from 200 ml to 450 ml and hence the bubble residence time in the liquid, the transfer efficiency is seen to increase by approximately 20%. Furthermore, adding 4 mm glass beads in 200 ml of water moderately increased the transfer efficiency by ~5%, probably caused by the increase of 75 mm in liquid height. While not significantly increasing the transfer efficiency, smaller volumes of liquids are required when using beads to reach the same liquid height, thus increasing the captured concentration of particles in the liquid. The GMD was also seen to increase with liquid height for smaller particles (blue bars **Figure 4-36(b)**), suggesting that the dominant transfer mechanism in the bubbles is diffusion as reported in the literature [159], [161], [166].

It is noted that although glass beads were shown to increase the particles concentration per volume of liquid, they weren't used for future experiments due to the witnessed challenges and contaminations associated with extracting the suspension from the bubbler.

4.3.1.2 Bubbler design and characterisation

Using literature and experimental results discussed above, a robust stainless-steel (SS) bubbler (**Figure 4-33(d)**) was designed utilising the aforementioned sintered steel nozzle. Its tall and narrow design maximised the particle's transfer efficiency and concentration per volume of liquid.

Prior to use for capturing exhaust particles during aircraft PM measurements, the particle transfer efficiency and optimal operation of the stainless-steel bubbler was experimentally assessed by varying the bubbler flowrate from 1.5-2.5 Lpm and the water volume from 0-150 ml.

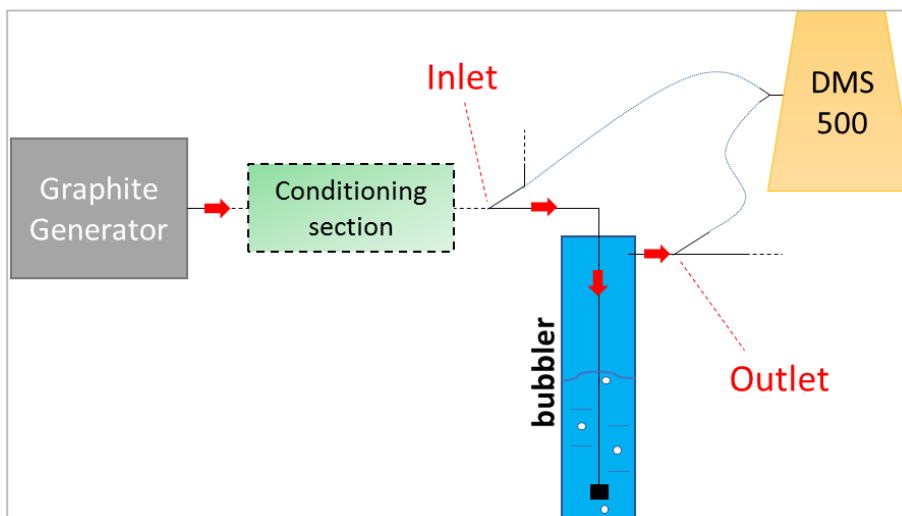


Figure 4-37: Diagram of the experimental set-up for the stainless-steel bubbler characterisation

Similarly to section 4.3.1.1, graphite soot-like nanoparticles were generated with a PALAS graphite generator and conditioned with dilution stages to prevent agglomeration (Figure 4-37). The particle size distribution was repeatedly measured at the inlet and the outlet of the bubbler with a DMS-500 at 1-minute intervals with the bubbler transfer efficiency deduced from the total number concentrations derived from the measured size distributions. It is noted that aerosol flowrates were kept constant.

The measured transfer efficiencies in the SS bubbler at different aerosol flowrates and liquid volume are presented in Figure 4-38, with each bar representing the average loss for the two size distributions (size distribution 1: GMD 30 nm and GSD 1.5 / size distribution 2: GMD 50 nm and GSD 1.7).

It can be observed that when no liquid is present in the bubbler, ~28% loss occurs in the setup from coagulation (3%), line loss (7%) and losses in the nozzle (20%), as previously discussed. It is noted that the larger reported nozzle loss than previously characterised (i.e. >15% at 3 Lpm) were caused owing to the lower volumetric flowrates.

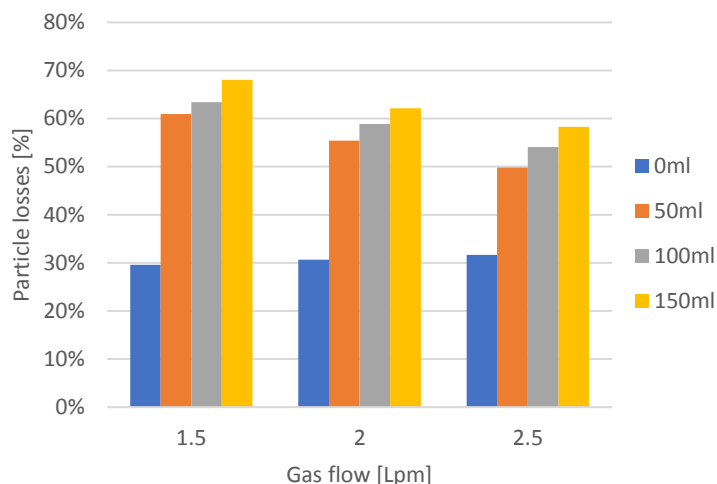


Figure 4-38: Effect of liquid height and gas flowrate on the particle transfer efficiency of a Stainless Steel bubbler with soot-like particles generated by a PALAS graphite generator and measured with a DMS-500

Again, the particle transfer efficiency from the gas to the liquid was deduced by subtracting the losses measured when no liquid was present (0 ml) with losses measured when liquid was present. As already observed, particle transfer efficiency increased with water volume (i.e. liquid height). However, as the volume and the liquid height, hence the bubbles residence time, was doubled or tripled, only a small increase of ~4% in transfer efficiency was measured. The transfer efficiency was also shown to decrease with increasing flowrate (+0.5 Lpm → -6% transfer efficiency), suggesting the increase in flowrate induced the formation of larger bubbles. In total, the particles transfer efficiency from the bubbles to the liquid with the SS bubbler varied from 18.2% with 50 ml at 2.5 Lpm to 38.5% with 150 ml at 1.5 Lpm. Although at this flowrate the overall transfer efficiency of the SS bubbler is lower than that of the glass cylinder bubbler (38.5% Vs 64%), the much lower volume of liquid required resulted in larger total concentrations of particles per volume of liquid. At sizes relevant of aircraft engine exhaust particles, some bubbler in the literature have demonstrated lower transfer efficiencies ([158], [167], [168]) but others reached transfer efficiency close to 100% when using tall bubble columns with small bubbles and dense packing beads ([159], [161]).

4.3.2 Characterisation of collected nanoparticle suspensions

Two highly concentrated nanoparticle suspensions captured in the Stainless-Steel (SS) bubbler (section 4.3.1.2) were characterised and compared to the aerosol size distributions measured in parallel using a DMS-500 during the collection period. Ultrapure water (type 1) [148] was chosen as liquid for the lower NVR contamination (section 4.1.3) and the better particle transfer efficiency as stated by Miljevic et al. [165] when compared with organic solvents.

The first sample (*sample 1*) was captured by continuously sampling PALAS graphite soot (GMD = 30 nm; GSD = 1.7; $N_{tot} = 5 \times 10^6$ particles/cm³) in the SS bubbler filled with 100 ml of ultrapure water at 2 Lpm for six hours, using the set-up presented in **Figure 4-37**. It is noted the graphite generator was set to produce particles as small as achievable (30 nm GMD) given it has been shown that particle transfer efficiency was higher for smaller particles (**Figure 4-36** blue Vs. orange).

The second sample (*sample 2*) consisted of soot from the combustion of blends of jet-A and alternative fuel in the GTRC combustion rig captured in 160 ml of ultrapure water at 1 Lpm with the SS bubbler over several days. The sampled particle size distribution, which fluctuated depending on the fuel burnt and combustion rig settings, averaged at a GMD of 31 nm, GSD of 1.81 and total number concentration of 5.3×10^5 particles/cm³.

It is noted that minimal liquid was lost with both samples from the recovery process and from liquid evaporating at the surface during the bubbling as discussed by Hogan et al. [167]

4.3.2.1 Particle measurement in the gas

The aerosol size measurements made in parallel and the previously estimated SS bubbler transfer efficiency permitted an estimation of the number concentration and size of soot in the water samples. Particle number concentrations per volume of water were estimated using equation (4.5) with the variables listed in **Table 4-5**. Total concentrations of 5.6×10^9 particles/ml and 2×10^9 particles/ml were predicted for sample 1 and 2, respectively.

$$\text{Particle concentration} \left[\frac{\#}{\text{ml}} \right] = \frac{N_{\text{gas}} \left[\frac{\#}{\text{cm}^3} \right] \times Q_{\text{gas}} \left[\frac{\text{cm}^3}{\text{s}} \right] \times \text{bubbling time}[\text{s}] \times \text{transfer efficiency} [\%]}{\text{Volume of solvent} [\text{ml}]} \quad (4.5)$$

Table 4-5: Estimated particle number concentration in water captured with the Stainless-steel bubbler

	Sample 1 (Graphite generator)	Sample 2 (combustion Rig)
Bubbling time	5h23min	13h50min
Total number concentration	$3.1 \times 10^6 \#/\text{cm}^3$	$5.3 \times 10^5 \#/\text{cm}^3$
GMD (d_m) and GSD	GMD = 33 nm GSD = 1.65	GMD = 31 nm GSD = 1.82
Volume of liquid	100 ml	160 ml
Bubbler sample flowrate	2 Lpm	1 Lpm
Bubbler transfer efficiency	~28%	~45%
Estimated concentration in liquid	$5.6 \times 10^9 \#/\text{ml}$	$1.2 \times 10^9 \#/\text{ml}$

It is noted that the transfer efficiency for sample 2 (1 Lpm and 160 ml) was deduced from the SS characterisation results (section 4.3.1.2) assuming linear trends between the transfer efficiency,

the sample flow (-6% per added 0.5 Lpm) and the liquid volume (+4% per added 50 ml = +0.8% per added 10 ml).

4.3.2.2 Particle measurement in the liquid phase

The size distribution of particles transferred from gas to liquid were measured in the water recovered from sample 1 and 2 using a Malvern Zetasizer and a Malvern Nanosight as introduced in section 3.1.4. Examples of particles detected with the Nanosight camera in sample 1 are presented in **Figure 4-39** with the white flare corresponding to light scattered by particles. A Malvern Mastersizer hydro EV was also briefly trialled but given it utilises Mie scattering theory it was found not suitable for particles below 100 nm.

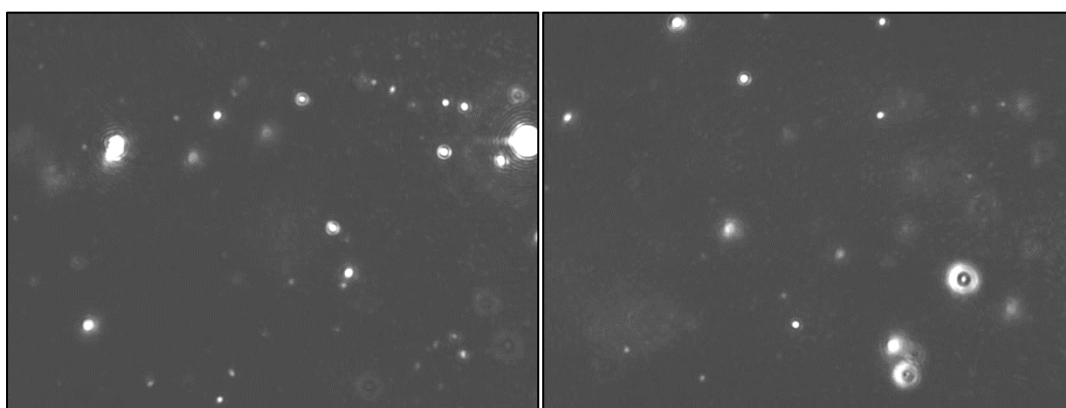


Figure 4-39: Screenshots of sample 1 containing particles captured by the Nanosight LM10 camera

It is noted that the data exported from the Zetasizer represents an average of fifteen 30-seconds runs and the data exported from the Nanosight corresponds to the average of five 20-seconds captures. Zero checks with ultrapure water (type 1) were also performed with the Malvern instruments to confirm that the solvent was particle-free.

An example size distribution measured by the Zetasizer for sample 1 with different weighing (intensity, volume and number) is presented in **Figure 4-40**. The intensity distribution is the most accurate as it only requires the solvent's refractive index and viscosity. The Volume and Number size distribution are derived from the intensity using additional particle property assumptions as listed in **Figure 4-40**. Because $I \propto d_p^6$, the smaller peak at 120 nm in the intensity distribution becomes the main peak in the number weighted distribution. Similarly, secondary peaks at 600 nm and 6 μm visible in the intensity distribution are not visible when converted to number.

The main results from the measurement of sample 1 and 2 by the Malvern instruments are presented in **Table 4-6**. As the Zetasizer doesn't provide a direct number concentration estimate, it was compared using the 'derived count rate' proportional to the scattering intensities, hence the number of particles present in the suspension.

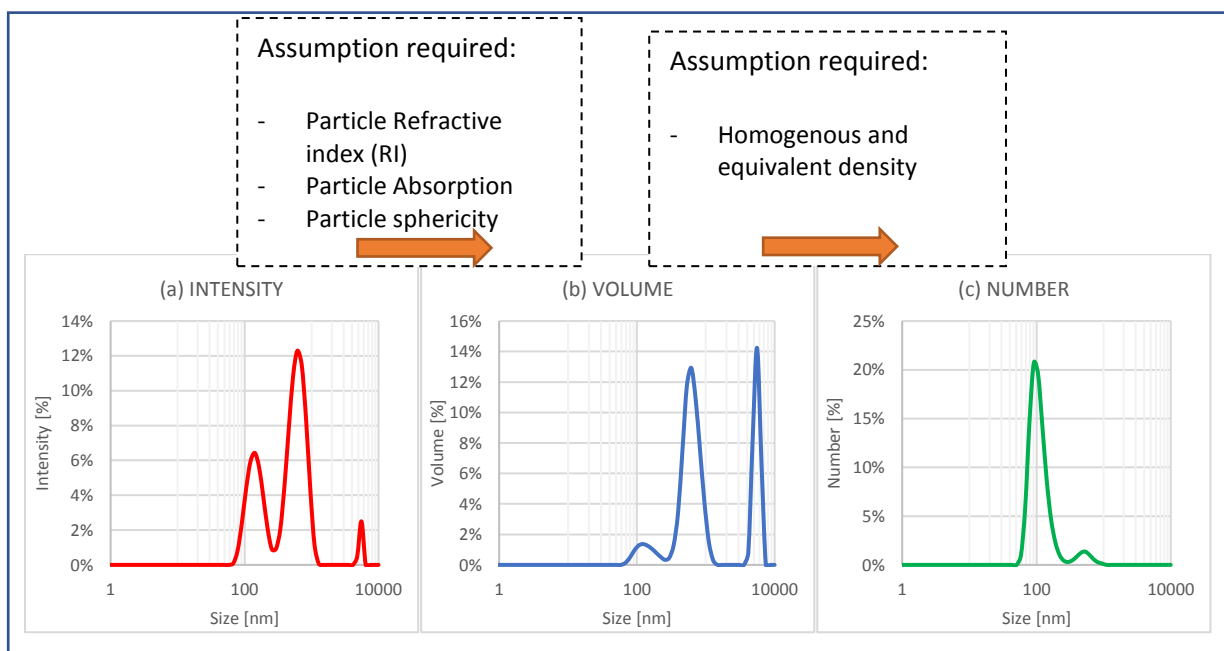


Figure 4-40: Size distribution of sample 1 measured by a Malvern Zetasizer and plotted against intensity (a), volume (b) and number (c)

It can be seen that the Zetasizer generally predicts a smaller GMD than that from the Nanosight by ~30%. Differences between the instruments may be attributed to the difference in technology and uncertainty associated with the suspension's stability from the low zeta potential as discussed in more details in section 4.3.2.3.

Table 4-6: Summary of Zetasizer and Nanosight measurements on sample 1 and 2

	Sample 1 Zetasizer	Sample 1 Nanosight	Sample 2 Zetasizer	Sample 2 Nanosight
GMD (d_h)	88 nm	131 nm	109 nm	152 nm
Concentration	~300 kcps	~ 3×10^8 #/cm ³	~1000 kcps	~ 6.3×10^8 #/cm ³
Zeta potential	-20 mV	-	-15mV	-

4.3.2.3 Comparison between liquid and gaseous measurements

Size distributions of particles in the liquid measured with Malvern instruments (section 3.1.4) were compared to gaseous size measurements of a DMS-500 made in parallel to the bubbler (section 4.3.2.1) to assess if soot particles size distribution was conserved when captured in the liquid and to evaluate size measurement capabilities in liquids of typical combustion exhaust.

Generally, the GMD measured in the liquid ($d_h > 100$ nm) was much larger than that measured in the gas ($d_m < 33$ nm), as can be seen in **Figure 4-41** presenting the individually normalised number-weighted size distribution of sample 1 and 2 measured in the gas (DMS-500) and the liquid (Zetasizer and Nanosight). It was also observed that the number concentration in the liquid derived by the

Nanosight was underpredicting that estimated from gaseous measurement by a factor 5-20. Measurements in the liquid predicted a higher concentration in sample 2 while gaseous measurement predicted a higher concentration in sample 1.

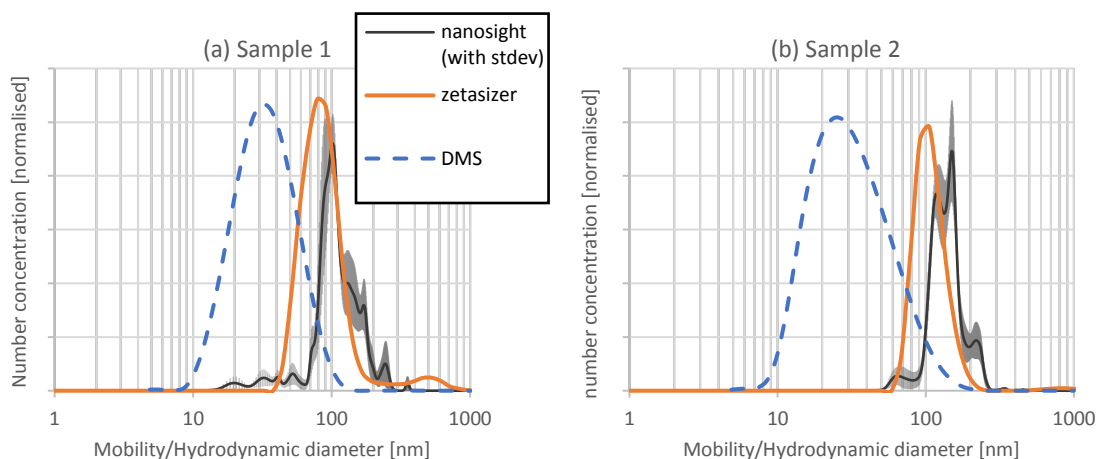


Figure 4-41: Individually normalised particle size distributions measured in the gas (DMS-500) and in the liquid (Zetasizer and Nanosight) of sample 1 (a) and sample 2 (b)

The difference in GMD and number concentration between measurements performed in the gas and in the liquid may be caused by several factors, namely:

- Different equivalent diameters: The DMS-500 measures particle's electrical mobility diameter (d_m) while the diameter measured in the liquid is the hydrodynamic diameter (d_h) (section 2.1.1). If assuming d_h equivalent to the aerodynamic diameter (d_a), then d_h should appear larger than d_m if the density of the particle in the liquid is larger than unit density (equation (2.1)). Indeed, it is expected that the density of soot in the liquid is $>1 \text{ g/cm}^3$ as primary particles have a density around 2 g/cm^3 [69] and internal voids are filled with water which have a density of 1 g/cm^3 . Anderlohr and Schaber [118] similarly observed a difference of $\sim 100 \text{ nm}$ with silica nanoparticles suspended in water when comparing the mobility diameter measured with a SMPS ($d_m=60 \text{ nm}$) in the gas with the hydrodynamic diameter measured with a Zetasizer ($d_h=160 \text{ nm}$). Furthermore, when re-atomising the liquid, they measured again a diameter of 60 nm with the SMPS, suggesting that the transfer of particles from gas to liquid didn't cause any agglomeration and that the larger mean diameter measured by the Zetasizer was solely because of the different measurement techniques.
- Larger apparent diameter in the liquid: The Zetasizer and Nanosight may have both measured a larger apparent diameter because the low ionic concentration of ultrapure water and the surface structure of the particles. Indeed, if the ionic concentration is low, an extended double layer of ions is produced around the particle, reducing the diffusion speed and resulting in a larger apparent hydrodynamic diameter with DLS [116]. Also, an absorbed polymer layer at

the surface of particles projecting out into the liquid can reduce the diffusion speed and thus increase the apparent size by several nanometres [116].

- Agglomeration in unstable suspension (Zeta potential): The measured zeta potential of -20mV and -15mV (**Table 4-5**) of both samples implies that the suspensions may be unstable causing particles to agglomerate over time as discussed in section **3.1.4.2**. To assess if agglomerates in the captured samples could be separated, ultrasonication was used for ten minutes and suspensions were re-evaluated. After sonication, the number concentration of the peak located in the 100-150 nm region increased while the larger peaks at 500-1000 nm and 6 μm seen on the Zetasizer intensity distribution decreased (peaks seen in **Figure 4-40**), suggesting that ultrasonication broke the larger agglomerate down to sizes around 100-150 nm as proposed by Kassab and al. [118], [160]. The lower concentration measured within sample 1 may also indicate that soot from the graphite generator is more hydrophobic than the combustion generated particles. Indeed, Zuberi et al. [162] discussed that soot is in nature hydrophobic but becomes hydrophilic with ageing when in contact with oxidising gaseous species modifying the surface of particles.
- Polydispersity and low resolution in liquid: The Zetasizer measured a polydispersity index ≥ 0.7 in both samples, indicating a very broad distribution of particles sizes which may not be suitable for measurement by DLS. Furthermore, the Nanosight's results were highly fluctuating, as seen with the multiple peaks (black line) and large standard deviation (grey highlight) of the size distribution as seen in **Figure 4-41**. Similarly, Fissan et al. [117] stated that the Zetasizer wasn't efficient at measuring the size distribution of mixtures below < 100 nm and generally displayed a low resolution when compared with gaseous measurements with a SMPS. Dudkiewicz et al. [169] and Jeon et al. [132] also both reported that the Nanosight (NTA) was not efficient at detecting particles below ~ 60 nm and likely overestimated the width of the distribution when compared with other techniques.

4.4 Chapter summary

In this chapter, nebulisation of suspensions and solutions was investigated to produce nanoparticles for laboratory particle loss experiments. It was witnessed that Non-Volatile-Residue (NVR) dissolved in liquid could interfere with the generation of nanoparticles < 100 nm when nebulising suspensions and were relatively difficult to remove. It was shown using the ATM-226 generating droplets ≤ 200 nm that impurities < 0.1 ppm still produced significant NVR peaks (10-20 nm GMD, $\sim 10^4$ particles/cm³). In-house ultrapure water type 1 was the most suitable solvent for nanoparticle dispersions as its low level of impurities resulted in the smallest residual contamination and NVR peak.

NVR was found to mostly originate from the manufacturing process transferring residuals in the suspensions. Heating, centrifugation, diffusion screens and aerodynamic classifications were all attempted to separate NVR from the suspended particles once in the aerosol. Evaporating NVR was difficult with its composition found to be dependent on the suspended nanoparticle. Centrifugation was effective at removing NVR for nanoparticles with large GMDs and high densities relative to unity (180 nm SiO₂) but required a lengthy procedure to avoid contamination between the sedimented particles and the solvent. Diffusion screens removed the smaller NVR peak via diffusional loss although for the three screens tested, low flows (0.5 Lpm) were required showed promise but resulted in increased uncertainty which may be reduced by increasing the number of screens used. It was shown in the experiments that the Aerodynamic Aerosol Classifier (AAC) was the best method tested at removing NVR for all investigated suspensions. In future work, NVR contamination could be reduced further using a purer grade of water and/or generating smaller droplets as discussed in the literature [117], [132].

Spark-generated graphite particles and nebulised silica and salt nanoparticles were successfully conditioned at GMDs ranging from 30-140 nm using an AAC, demonstrating the capabilities of this relatively new instrument to classify nanoparticles. The produced size distributions were characterised for laboratory line loss experiments discussed in chapter 5.

The transfer and capture of aircraft exhaust nanoparticles in a liquid was investigated for use in health studies. It was also assessed to see if captured particles remained stable for potential use as calibration sources. Bubblers and parameters affecting particle transfer efficiency from gas to liquid were experimentally investigated. The designed stainless-steel bubbler used for aerosol capture demonstrated transfer efficiencies $\leq 50\%$ but it is suggested that this could be further improved utilising metal beads, increasing the liquid height, and using a better nozzle producing smaller droplets [159], [161].

Nanoparticles captured in the suspensions were characterised using a Malvern Zetasizer and Nanosight. Measurements in the liquid using Dynamic Light Scattering (DLS) theory were compared with gaseous measurements. It was observed that the hydrodynamic diameter (d_h) was larger than the mobility diameter (d_m) which would be expected for particles with a density larger than 1 g/cm³ in the liquid. For future studies, it is proposed that the captured nvPM suspensions could be re-atomised to validate that particle size distribution does not vary in the liquid, as previously discussed [118]. Understanding particle surface properties is essential for nvPM characterisation in liquid suspensions as they can affect the reported hydrodynamic diameter and the suspension's stability. Titration and Fourier Transform analysis could be performed to better understand the bonds at the surface of particles in the liquid. Other methods could be used for measuring captured particles in a suspension. Field Flow Fractionation (FFF) is a technique shown to be capable of separating and characterising a broad range of colloidal particles in a liquid from a few nm to 1 μm [157], [170].

5 Particle Loss Experimentation and Quantification

Due to the harsh environment at the exhaust of an aircraft engine, the sampling protocols for the regulation of non-volatile Particulate Matter (nvPM) emissions specify a largely standardised sampling system of up to 35 m line length, which coupled with the small GMD of nvPM witnessed from gas turbines (20-50 nm [51]) result in significant particle loss before measurement at the instruments. Across the typical GMD range of civil aviation gas turbines, losses have been anticipated to be as high as 90% for number and 50% for mass [14], [57]. An understanding of particle loss in the sampling system is therefore critical for the reliable determination of concentrations exiting the aircraft engines.

The latest ICAO regulation (appendix 8 [14]) describes the recommended procedure to determine sampling system loss correction factors, with the system penetration efficiency estimated using the UTRC particle transport model (section 2.4) which as discussed accounts for thermophoretic, diffusional, inertial, electrostatic and bend transport loss mechanisms using expressions derived from the literature. Potential issues were highlighted in a SAMPLE report [50] concerning treatment of particle loss in the UTRC model which utilises a constant diameter base for the estimation of different loss mechanisms. Furthermore, the theory used in the UTRC model has generally only been validated at conditions not specifically representative of aircraft nvPM sampling and using spherical particles whereas aircraft nvPM is typically composed of fractal aggregates [20]. The accurate estimation of specific loss mechanisms require detailed knowledge of particle size, and their relevant equivalent diameters should be used [60, p. 154], [62] (e.g. diffused diameter for diffusion, aerodynamic diameter for inertia and bends). In addition to the UTRC modelled losses, thermophoretic loss in the collection section, where aerosol temperatures of 700°C can be reached [52], are corrected-for using the factor k_{thermo} (section 1.5.1.3) experimentally derived from experiments < 160°C using spherical particles [86]. To the author's knowledge, little thermophoretic loss validation work has been performed at > 450°C, and only for spherical particles.

This chapter aimed at experimentally validating theoretical expressions currently used in the UTRC model to estimate thermophoretic, diffusional and bend loss at conditions and segments representative of ICAO compliant aircraft nvPM sampling to assess the accuracy of the currently prescribed sampling system particle loss correction [14]. Three laboratory experiments were performed (thermophoretic, 25m line, VPR) using classified silica, salt and graphite nanoparticles (chapter 4) at sizes representative of aircraft nvPM. The use of different particle types also permitted to experimentally assess the impact of particle morphology and density on the investigated loss mechanisms.

5.1 Thermophoretic experiment

Aircraft PM is generated from the combustion of fuel at extremely hot temperatures. In an ICAO compliant sampling system [14], aerosols sampled at the exhaust of a gas turbine can reach temperatures of up to 700°C depending on the engine technology and power setting [51], [53]. The characterisation of representative turbine engine nvPM requires the exhaust aerosol to be cooled to 60°C (to prevent condensation) before being measured by the analysers. Hence, a significant temperature drop occurs in the sampling system transporting the aerosol inducing thermophoretic losses as defined in section 2.3.1.4. The majority of particle loss by thermophoresis occur in the collection section where the aerosol is cooled from exhaust temperatures to 160°C. These losses are corrected-for using a power law relationship referred as the thermophoretic correction factor k_{thermo} (equation (1.5)). The expression k_{thermo} is derived from the experimental results of Romay et al. [86] whom characterised thermophoretic deposition at temperatures of 300-425 K (<150°C) using NaCl and PSL particles. The UTRC particle transport model (section 2.4) also uses equations presented by Romay et al. [86] for thermophoretic loss estimations and assumes a particle thermal conductivity and a thermophoretic coefficient.

As presented in **Table 5-1**, many studies have investigated nanoparticles thermophoretic deposition however to the author's knowledge, little validation work has been performed at temperatures and flows representative of gas turbine exhaust using fractal soot-like particle. Messerer et al. [83] investigated thermophoretic losses using soot-like particles at 110°C. Also high temperature characterisation using a quoted furnace temperature of 900°C using spherical particles [125], [126].

Hence, this work was undertaken to validate the accuracy of k_{thermo} , and the theory currently used in the UTRC model for thermophoretic losses at gas turbine relevant conditions. Thermophoretic losses were experimentally determined using various nanoparticles types (fractal graphite, spherical silica, cubical salt) at varying flows and temperature gradients ($\Delta T \leq 880^\circ\text{C}$). It is also noted that aircraft engine manufacturers develop combustion system in combustion rigs where the probe inlet can reach temperatures of up to 1850°C with the probe water-cooled to quench the sampled aerosol [Private conversation Mark Johnson Rolls-Royce 01/19]. Understanding thermophoretic loss at high temperatures will hence aid engine manufacturer to better understand nvPM formation from combustors.

Table 5-1: Summary of nanoparticle thermophoretic experiments available in the literature

Reference	Test section dimensions	Carrier Gas	Gas Flow regime	ΔT & T_{\max} (°C)	Aerosol used	Thermophoretic deposition efficiency (%)	Measurement technique	Expression of thermophoretic penetration efficiency
<i>Nishio et al. (1974)</i>	Glass pipe ID = 5 mm L = 100 cm	Air	Laminar & Turbulent Re \approx 407 – 10300	0 – 140	Na ₂ O 300nm – 3 μ m	0-11 (number)	AAS, thermal precipitator & electron microscopy	$\eta_{th-turb} = \exp\left(\frac{\rho \cdot C_p \cdot K_{th} \cdot v(T_g - T_w)}{k_g * T_{bulk}} \left(1 - \exp\left(\frac{-4 \cdot h \cdot L}{\mu_m \cdot \rho \cdot C_p \cdot D_t}\right)\right)\right)$
<i>Montassier et al. (1991)</i>	Copper tube ID = 20 mm L = 58.6 cm	Air	Laminar Re \approx 575	0 – 90	Uranin 50nm – 8 μ m	1.5-8.5 (mass)	DMA + Photometer	$n_{th-lam} = 3.2 * \frac{Pr * K}{1 + \theta^*} * \left(1 + \frac{1 - Pr * K}{1 + \theta^*}\right) * \left(\frac{z}{R * Pe}\right)^{\left(\frac{2}{3}\right)}$ with $\theta^* = \frac{T_w}{T_{gas} - T_{wall}}$
<i>Shimada et al. (1993) (1994)</i>	ID = 13 mm L = 55 cm	Air, H ₂ , Ar, N ₂	Laminar Re \approx 35 – 230	T _{furnace} \leq 900	Ag, NaCl & TiO ₂ 7 – 40nm	0-50 (number)	DMA + CPC	
<i>Stratmann et al. (1994)</i>	ID = 12.6 mm L = 50 cm	Air	Laminar Re \approx 35	0-80	NaCl 30 – 100nm	5-9 (number)	DMA + CPC	$n_{th-lam} = \exp\left(-0.845 * \left(\frac{(Pr \cdot K_{th} + 0.025)}{T_w / (T_g - T_w) + 0.28}\right)^{0.932}\right)$
<i>Romay et al. (1998)</i>	ID = 4.3mm L=96.5cm	Air	Laminar & Turbulent Re \approx 1379 – 9656	0 - 150	NaCl, PSL 100 – 700nm	0-18 (number)	DMA + CPC	$\eta_{th-turb} = \left(\frac{T_w + (T_{gas} - T_w) \exp\left(\frac{-\pi \cdot D_{tube} \cdot h \cdot L}{\rho_p \cdot Q \cdot C_p}\right)}{T_{gas}}\right)^{Pr \cdot K_{th}}$
<i>Messerer et al. (2003)</i>	H _{plate} = 0.45 -1.45 mm L = 45 cm	Air	Laminar Re \approx 247 – 490	0-110	Soot (graphite) 34 – 300nm	0-55 (number)	DMA+CPC	$\eta_{th-lam-plate} = K_{th} * \frac{(L \cdot \mu_g \cdot \Delta T)}{\rho_g \cdot v_x \cdot H^2 \cdot T}$
<i>Tsai et al. (2004)</i>	ID = 4.3 mm L = 118 cm	Air	Laminar & Turbulent Re \approx 1340- 10200	0-100	NaCl 40 – 500nm	0-10 (number)	DMA + CPC	$\eta_{th-lam} = 78.3 \left(Pr \cdot K_{th} \cdot \frac{T_g - T_w}{T_w}\right)^{0.94}$
<i>Muñoz-Bueno et al. (2005)</i>	ID = 27.3 mm L = 40 cm	Air	Laminar Re \approx 500	0-410	NiO ₂ 20 – 200nm	35-41 (number & mass)	DMA + CPC And gravimetric (filter)	

5.1.1 Experimental setup

The experimental set-up for the thermophoretic experiment consisted of a particle generation section, a test section, and a measurement section as depicted in **Figure 5-1**. Conditioned Silica, Salt and graphite particles (section 4.2) were employed to quantify losses in a test section using a Cambustion DMS-500 (section 3.1.3) and an AVL APC (section 3.1.1.1). Size distributions measurements permitted the monitoring of any morphology change during the test (e.g. particle collapsing, evaporation).

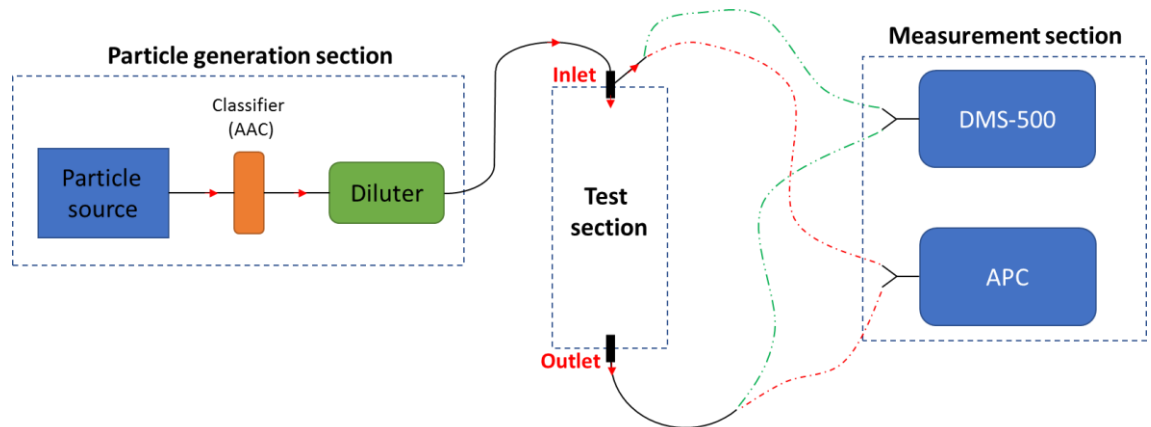


Figure 5-1: Simplified diagram of the experimental setup for thermophoretic, sample line and bends loss laboratory experiments

As is seen in **Figure 5-1**, an ejector diluter (Palas VKL 10E) was used to ensure mixing, control particle concentration, maintain a low aerosol humidity (section 4.1.1.2), maintain a near ambient pressure in the test section and facilitate sampling at various flows without affecting particle generation. The tubing length between the diluter outlet and the test section inlet was sufficiently long to ensure the sample flow was fully developed limiting any impact of entrance effects (section 5.1.2).

The test section for measuring thermophoretic losses was 3.30 m long with an ‘ambient segment’ of 0.60 m, a ‘heating segment’ of 1 m and a ‘cooling segment’ of 1.70 m as depicted in **Figure 5-2** and discussed below. Photographs of the setup are also displayed in **Figure 5-3**.

- The ‘heating section’ consisted in a 1 m x 50 mm OD Stainless Steel (SS) tube with an 8mm ID, pre-heated with six Watlow clamp heaters affording temperatures < 600°C. The tube was further heated in a 0.55 m tube furnace < 1000°C. Thermocouples were fitted at along the section to control and monitor the tube wall temperature.
- The ‘cooling section’ composed of a counterflow tube in tube Water Heat eXchanger (WHX2 in **Figure 5-2**) to cool the hot aerosol and force thermophoretic deposition.

- The ‘ambient section’ consisted of a small WHX (WHX1) to prevent heat from the ‘heating section’ conducting ‘backward’ towards the particle generation section which was fitted to limit heating prior to the inlet measurement.

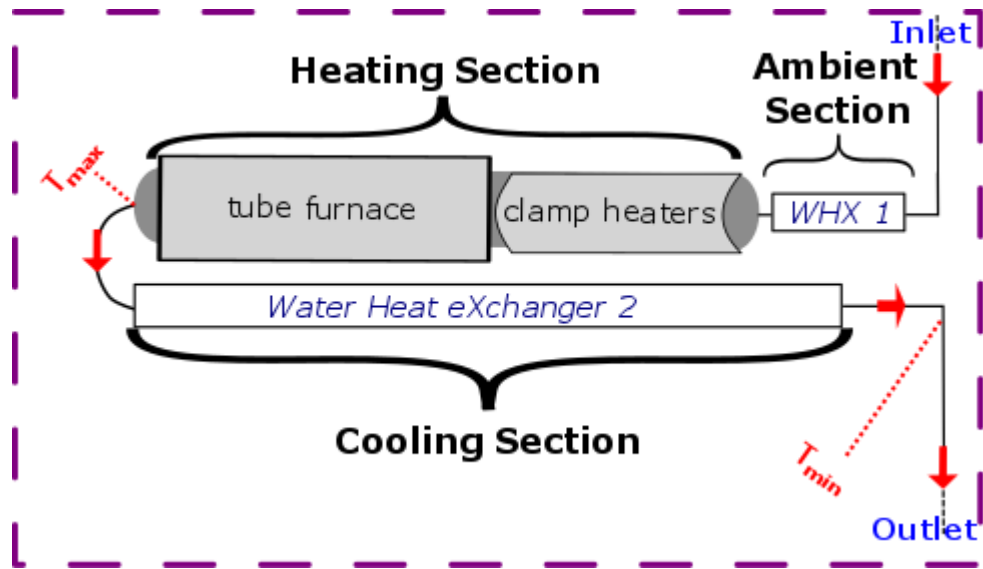


Figure 5-2: Diagram of the thermophoretic experiment test section

The cooling and heating lengths were designed using theoretical predictions (section 5.1.3) to ensure gas temperatures were reached with the measurement section kept as short and straight as possible to minimise non-thermophoretic losses. As seen in **Figure 5-3(c)**, a 180° bend was used between the heated and cooling sections to minimise/standardise the sample line length required between the inlet and outlet of the test section and the analysers. The bend was designed (curvature ratio ~ 21 [equation (2.18)] and pipe length ~ 0.55 m) in line with good engineering practice [14] ensuring negligible bend loss’ as confirmed during experimentation (section 5.2).

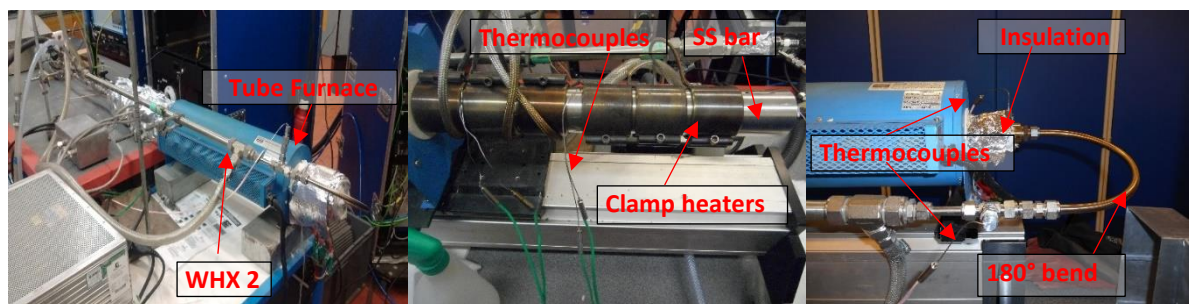


Figure 5-3: Photographs of thermophoretic experiment set-up

Two SS bars of different grades were used during this experiment. Firstly, an affordable Grade 316 SS bar was used to its maximum service temperature of 750-925°C to prove the thermophoretic experiment concept with data limited to a maximum furnace temperature of 800°C before oxidation was observed. Secondly a higher Grade RA330 SS bar was used affording higher temperatures of up to 1148°C. To minimise oxidation on the inner wall, at the highest temperatures, Nitrogen (N_2) was

triated instead of dry air as the carrier gas. It is noted that prior to testing, both bars were heated and maintained at the maximum experiment temperature for several hours to burn-off any oil and manufacturing traces from the drilling that may have impacted the results.

5.1.2 Calculation of penetration efficiency

Penetration efficiencies were estimated by dividing the total number concentration at the outlet of the test section by those at the inlet of the test section. Given particle measurements could not be performed simultaneously at the inlet and outlet of the test sections with the same instrument, carbon loaded tubing was used to transport aerosols to the analysers measuring successively at the inlet and outlet of the test section (green and red dashed lines in **Figure 5-1**) by actuating two-way valves. The dimensions and flowrate of these segments were identical ensuring losses occurring were consistent meaning they could be neglected when calculating the penetration efficiency.

Some uncertainties associated with the measurement of particle losses could not be fully eradicated. A list of these uncertainties is given below:

- Fluctuating pressure at the inlet of the analysers when measuring at the inlet and outlet, caused by pressure loss in the test section, resulting in subtly different volumetric sample flowrates.
- Unsteady particle generation processes which drift over time.

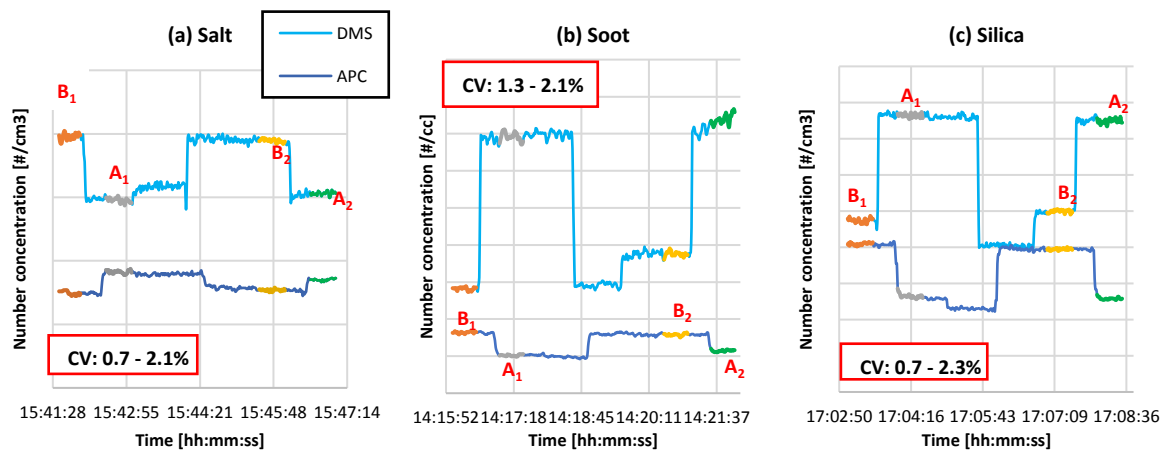


Figure 5-4: Example of measured number concentrations over time at different test points with salt (a), graphite (b) and silica (c) nanoparticles using an AVL APC a Combustion DMS-500

Particle measurements generally corresponded to a 30-second average at a stable condition with the analysers recording at 1 Hertz as depicted by the orange, grey, yellow and green highlights in **Figure 5-4**. Conditions were deemed stable when CV<3% (i.e. Coefficient of Variation) as in the author's experience, any nanoparticle generation process fluctuate. It is noted that the time between

measurements at the inlet and outlet of the test section was kept short (30 seconds - 2 minutes) to minimise the uncertainty associated with particle generation fluctuation and drift.

Classification with the AAC didn't produce truly monomodal and monodisperse aerosols (section 4.2) the GMD, GSD and total number concentration, hence DMS-500 derived data used only the aerosol mode/main particle peak as previously discussed (section 4.2). The DMS-500 monomodal inversion matrix was selected for SiO₂ and salt and the monomodal aggregate inversion matrix was used for graphite (section 3.1.3).

Other actions were taken to minimise the uncertainty associated with penetration efficiency estimations, namely:

- Zero checks were regularly performed to check for leaks and contamination.
- Analysers were within their certificated calibration period (see example calibration files in the appendix 10.1).
- Flow meters were manually calibrated to a common mass flow controller to ensure accurate flow measurements.
- Sample flow separation in splitters was kept as equal as possible to prevent additional loss in splitters (section 6.2.5).
- Grounded conductive tubing was used in the test section (stainless-steel or carbon-loaded PTFE) to minimise electrostatic loss [74], [78], [123].

5.1.3 Heating/Cooling length estimation

Considering the equipment used (tube furnace, clamp heaters) and assuming a 'worst-case' scenario, heating and cooling lengths were theoretically estimated [62], [171] to validate the design of the thermophoretic experiment. Thermal entrance lengths affecting the temperature profile were also investigated [172].

The 'worst-case scenario' corresponded to the highest investigated sample flow (24 Lpm), hottest furnace temperature (1000°C), expected gas temperature (900°C), and a cooled gas temperature of 30°C with heat exchanger wall temperature at 20°C. For simplicity, it was assumed that heat was only transferred by forced convection (radiation effects neglected) and the wall surface temperature was steady state.

The results of this study are presented in **Table 5-2**. When including thermal entrance effects, the resultant heating and cooling lengths were estimated at 1.01 m and 1.76 m respectively. Hence, the total 'heating section' length of 1.55 m and total 'cooling section; length of 1.85 m as (**Figure 5-2**) were theoretically validated.

Table 5-2: Estimations of heating and cooling length of a 8 mm ID tube at a furnace temperature of 1000°C and a cold heat exchanger temperature of 25°C

	Thermal entrance length	Heating length	Total heating length	Cooling length	Total cooling length
$T_{gas\ hot} = 900^{\circ}\text{C}$ $T_{gas\ cold} = 35^{\circ}\text{C}$	25 cm	76 cm	101 cm	151 cm	176 cm

Heating and cooling length calculation:

Heating and cooling lengths were estimated using a Nusselt number correlation, calculating the heat transfer coefficient (h), the rate of heat transfer (q), thermal conductivity (k) and a Log-Mean-Temperature-Difference (LMTD) as listed below. For the temperatures tested the majority of cases exhibited $Re < 2100$ (equation (2.11)), hence laminar flow was assumed. All gas properties were estimated at their bulk temperatures.

The heating/cooling lengths (L) were estimated using the equation for laminar heat transfer by forced convection assuming a constant wall temperature ($q = h \times A_w \times \text{LMTD}$ and $A_w = L_{\text{tube}} \times \pi \times D_{\text{tube}}$):

$$L_{\text{heating/cooling}} = \frac{q}{\pi \times D_{\text{tube}} \times h \times \text{LMTD}} \quad (5.1)$$

The heat transfer coefficient h was estimated from the Nusselt number correlation in equation (5.2). Different Nusselt numbers were considered for use: fully developed laminar circular ducts $Nu=3.66$ for a uniform surface temperature, $Nu=4.364$ for a uniform heat flux [171] and empirical fits from Sieder and Tate [173]. In this calculation, the lowest Nu value ($Nu=3.66$) representing the ‘worst-case’ scenario was used.

$$Nu = \frac{hD_{\text{tube}}}{k} \rightarrow h = Nu \times \frac{k}{D_{\text{tube}}} \quad (5.2)$$

with the thermal conductivity k in [W/(m.K)] and D_{tube} in [m].

The rate of heat transfer q was calculated as followed:

$$q = C_p \times Q \times \rho_{gas} \times (T_{gas\ out} - T_{gas\ in}) \quad (5.3)$$

with C_p the specific heat capacity [J/(kg.K)], Q the volumetric flow rate [m³/s], ρ_{gas} the gas density [kg/m³] and T the outlet and inlet gas temperatures [K].

Finally, the Log Mean Temperature Difference was calculated with:

$$\text{LMTD} = \frac{(\Delta T_{out}) - (\Delta T_{in})}{\ln\left(\frac{(\Delta T_{out})}{(\Delta T_{in})}\right)} \quad (5.4)$$

with ΔT the temperature difference between the wall and the gas at the inlet and outlet of the test section ($\Delta T_{out} = 100 \text{ K}$ when heating and $\Delta T_{out} = 10 \text{ K}$ when cooling).

Entrance effects calculation:

Entrance lengths, defined as the distance necessary for the temperature profile to be fully developed, can impact the mixing state and reduce heat transfer efficiency in a tube [171, p. 356]. In a laminar flow, the distance from the inlet at which the temperature profile reaches its fully thermally developed profile can be calculated as followed:

$$x_{\text{fully developed}} = D_{\text{tube}} \times 0.05 \times Re \times Pr \quad (5.5)$$

with D_{tube} the tube internal diameter, Re the Reynolds number and Pr the Prandtl number.

5.1.4 Theoretical sensitivity analysis

To assess thermophoretic losses, penetration efficiencies measured during the thermophoretic experiment were compared to the theory used in the UTRC model and k_{thermo} . In the UTRC model, theoretical penetration efficiencies are estimated assuming particle effective density and thermal conductivity (1 g/cm^3 [63] and 0.2 W/(m.K) for soot [83]) as recommended by the civil aviation regulation [14]. However, different particle types have different properties and hence may differently be impacted by thermophoresis. Furthermore, large temperature gradients also affect non-thermophoretic losses due to the varying carrier gas properties.

A sensitivity analysis of particle effective density and thermal conductivity for graphite, silica and salt was performed by assessing their impact on theoretical loss predictions at the investigated gas flows (8-24 Lpm), gas temperatures (20-1000°C) and size range (30-140 nm). The variation of flow and temperature was also assessed in regard to their impact on non-thermophoretic losses. This analysis was performed by the UTRC model using the dimensions of the thermophoretic experiment test section (5.1.1) with the results presented in **Table 5-3**.

Particle effective density was varied from 0.18 g/cm^3 , the lowest reported aggregated soot density [70], to 2.2 g/cm^3 representing salt material density. Similarly, particle thermal conductivity

was varied from 0.082 W/(m.K), the lower theoretical conductivity of aggregate (similar to that of air at 1000°C) [83],[85], to 7 W/(m.K) corresponding to salt’s material thermal conductivity.

Table 5-3: Effect of changing particle and gaseous variables on losses in the thermophoretic experiment setup using the UTRC model

Variable	Fixed Parameters	Effect at 30 – 140 nm	Explanation
particle effective density (at ambient conditions): 0.18 → 2.2 [kg/m ³]	$k_p = 0.2$ [W / (m.K)] $Q = 8 - 24 \text{ lpm}$ $T_{gas} = 25^\circ\text{C}$	Negligible: Larger densities increased the total deposition efficiency $\leq 0.2\%$.	Larger densities provide more inertia for particles to deviate from the gas path. As Diffusional and inertial losses are small in the current setup, changes affecting those losses are negligible.
Gas temperature (non-thermophoretic loss): 25 → 1000°C	$k_p = 0.2$ [W / (m.K)] $\rho_p = 1 \text{ kg/m}^3$ $Q = 8 - 24 \text{ lpm}$	Negligible: Increasing the temperature decreased the non-thermophoretic deposition efficiency $\leq 0.4\%$.	As the gas temperature increases, the gas velocity increases and other parameters change (diffusion coefficient, Reynolds number, etc) affecting all non-thermophoretic losses. As non-thermophoretic losses are small in the current setup, changes affecting those losses are negligible.
thermal conductivity (thermophoretic loss): 0.082 → 7 [W / (m.K)]	$\rho_p = 1 \text{ kg/m}^3$ $Q = 8 - 24 \text{ lpm}$ $T_{gas} = 1000[^\circ\text{C}]$	Negligible: Smaller particle thermal conductivity increased the deposition efficiency $\leq 0.2\%$.	In thermophoretic loss theory, the particle thermal conductivity balances with Knudsen number hence only has a significant impact when the Knudsen number is small (i.e. $d_p > 200 \text{ nm}$ with this set-up).
gas flow (at ambient): 8 → 24 lpm	$\rho_p = 1$ [kg/m ³] $k_p = 0.2$ [W / (m.K)] $T_{gas} = 25^\circ\text{C}$	Small: Lower gas flow increased the deposition efficiency $\leq 1\%$.	As the flow increases, the gas velocity increases and the particle residence time decreases, mostly reducing diffusional losses. It has an opposite effect for inertial losses, but only affects particle > 200 nm in this set-up.

In the thermophoretic test section, non-thermophoretic loss at ambient temperature are predicted to be $\leq 4\%$ between 30-140 nm at flows ranging from 8-24 Lpm, as seen in **Figure 5-5(a)**. It is noted that as the temperature increases, theoretical non-thermophoretic loss were witnessed to decrease hence non-thermophoretic loss are never expected to be >4%. Furthermore, varying the

gas temperature, particle density and gas flow induced negligible changes in non-thermophoretic losses, given the short residence time in the test section, as discussed in **Table 5-3**.

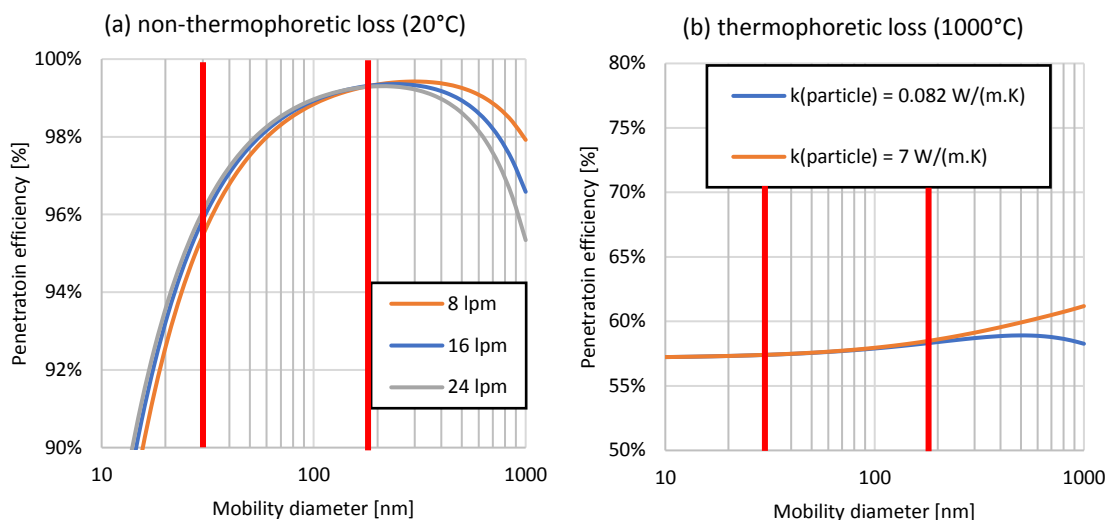


Figure 5-5: Theoretical penetration efficiencies of the thermophoretic test section at 20°C with varying sample flows (a) and at 1000°C with varying particle thermal conductivities (b)

As discussed in **Table 5-3** and witnessed in **Figure 5-5(b)**, the fluctuation of the particle thermal conductivity is expected to have a negligible impact on thermophoretic loss in the range of interest.

It is concluded from this sensitivity analysis that non-thermophoretic losses are expected to be low (<4%) and the different particles properties and flow investigated should negligibly impact all losses. Hence similar losses should be measured for all investigated particles (silica, graphite, salt) and at various flows (8-24 Lpm). As currently implemented in the UTRC model [57], a unique particle density ($1 \text{ g}/\text{cm}^3$) and thermal conductivity ($0.2 \text{ W}/(\text{m.K})$) were used to predict theoretical losses in the remaining of this chapter.

5.1.5 Gas temperature calibration

Thermophoretic losses (section **2.3.1.4**) are estimated using the maximal (i.e. hot) and minimal (i.e. cold) gas temperature. However, positioning a thermocouple in the aerosol flow may cause particles to impact on it [86], disturbing thermophoresis characterisation. Hence, only wall temperatures were recorded during the thermophoretic experiment. It is noted that positioning a thermocouple in a drilled hole at the edge of the gas flow was also investigated but ruled out as conduction of the SS bar to the thermocouple was strongly influencing temperature measurements.

To determine a precise gas/aerosol temperature measurement and accurately estimate thermophoretic losses, a post-experiment temperature calibration was performed. A suitably calibrated thermocouple (calibration certificate available in the appendix **10.2**) was alternatively

inserted in the gas flow at the outlet of the tube furnace (T_{\max}) and at the outlet of the cooling section (T_{\min}) at all investigated furnace temperatures and gas flows. To minimise wall conduction effects and facilitate access to the hottest location of the gas furnace, a 1 m long, 6 mm OD ceramic insulated thermocouple was used. The thermocouple was systematically moved through the heated pipe to ascertain the highest gas temperature.

The results of the temperature calibration experiment are presented in **Figure 5-6** with the gas temperature plotted on the y-axis and a linear fit intercepting at zero used to visualise trends ($R^2 > 98.5\%$). For the maximum temperature (**Figure 5-6(a)**), it can be observed that the gas temperatures are always below that of the furnace and the difference between the furnace temperature and T_{\max} increases with increasing flow and increasing temperatures. As the flow increases but remains in the broadly laminar regime ($Re < 2600$ from 200°C), the gas travels faster and has less time to receive heat from the wall. For the minimum temperature (**Figure 5-6(b)**), it can be seen that T_{\min} increases with furnace temperature as the gas requires more cooling. At 8 and 24 Lpm, T_{\min} generally remains below 50°C but at 16 Lpm, it rises to 120°C . A hypothesis for this is that at 8 and 16 Lpm, the flow is laminar/transitional ($Re < 2500$) and hence the cooling efficiency decreases with increasing flow but at 24 Lpm the flow becomes transitional/turbulent while cooling ($Re \sim 3800$ at 50°C) accelerating heat transfer significantly with eddy diffusion.

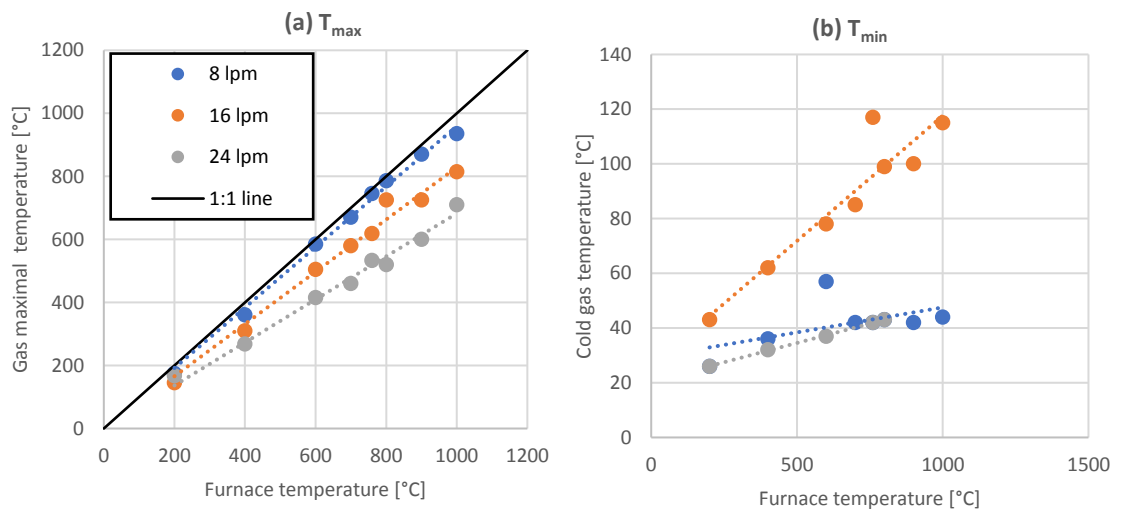


Figure 5-6: Recorded hot (a) and cold (b) temperatures at different furnace temperature in the thermophoretic set-up

It is noted that in the thermophoretic experimental set-up, additional tubing is present between the end of the test section (T_{\min}) and the analysers ($\sim 1\text{m}$ long $\frac{1}{4}$ " tubing) where the gas is further cooled. Hence, it has been approximated that the cold gas temperature was **30°C** for thermophoretic loss predictions in section 5.1.6.

In addition to the calibrated 6 mm OD thermocouple, gas measurements were performed with a thermocouple of a smaller thickness (3 mm) which could measure gas temperature nearer to the walls, as presented in **Figure 5-7**. It was witnessed that the thinner thermocouple always measured a higher T_{\min} (up to $\sim 100^{\circ}\text{C}$ at 24 Lpm) when compared with the thicker calibrated thermocouple measuring nearer the centre of the gas flow. Similarly, T_{\min} measured by the thinner thermocouple closer to the walls was always colder than that measured by the calibrated thermocouple ($\leq 25^{\circ}\text{C}$ difference). These measurements indicated that the radial temperature profile was not uniform, as discussed by Lin and Tsai [172]. It is noted that the different temperature read by the two thermocouples may also be explained in part by the thinner insulated thermocouple being more sensitive to wall conduction and/or by the thick calibrated thermocouple partially blocking the flow and hence affecting heat transfer near the thermocouple tip.

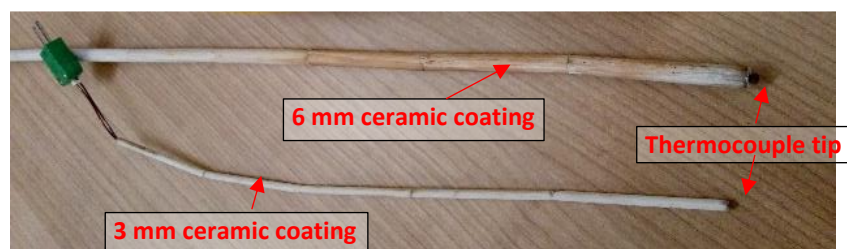


Figure 5-7: Photograph of the calibrated 6mm thick insulated thermocouple and the 3mm thick thermocouple

The gas temperature calibration experiment demonstrated that aerosol/gas temperatures were below that of the furnace. Hence, for the thermophoretic theoretical predictions, T_{\max} were estimated using the linear trendlines discussed in **Figure 5-6(a)** and a cold gas temperature of 30°C was always assumed.

5.1.6 Results

As discussed previously, a thermophoretic experiment was performed to validate the theory used in the UTRC model for thermophoresis and k_{thermo} . The effect of particle density and morphology on losses at high temperature gradients are also assessed. Penetration efficiencies in the thermophoretic test section (**Figure 5-2**) were measured for salt (NaCl), silica (SiO_2) and graphite (soot-like) particles at flows of 8-24 Lpm and furnace temperatures of 20-1000 $^{\circ}\text{C}$. These conditions were selected as being representative of aircraft nvPM sampling (25 Lpm, $T_{\text{gas}} \leq 700^{\circ}\text{C}$ [53]).

Penetration efficiencies were initially measured with the furnace off ($T_{\text{gas}} = 20^{\circ}\text{C}$) to experimentally evaluate non-thermophoretic losses in the test section. Results are presented in **Figure 5-8** with the error bars representing two standard deviations (section 2.5). It was observed that measured losses correlated well with predictions from the UTRC model (dashed lines) within the

uncertainty represented by the error bars for the large majority of the data. Non-thermophoretic penetration efficiencies including all particle types, sizes and flows averaged 97.7% when being measured with the APC and 95.4% with the DMS-500 (**Table 5-4**).

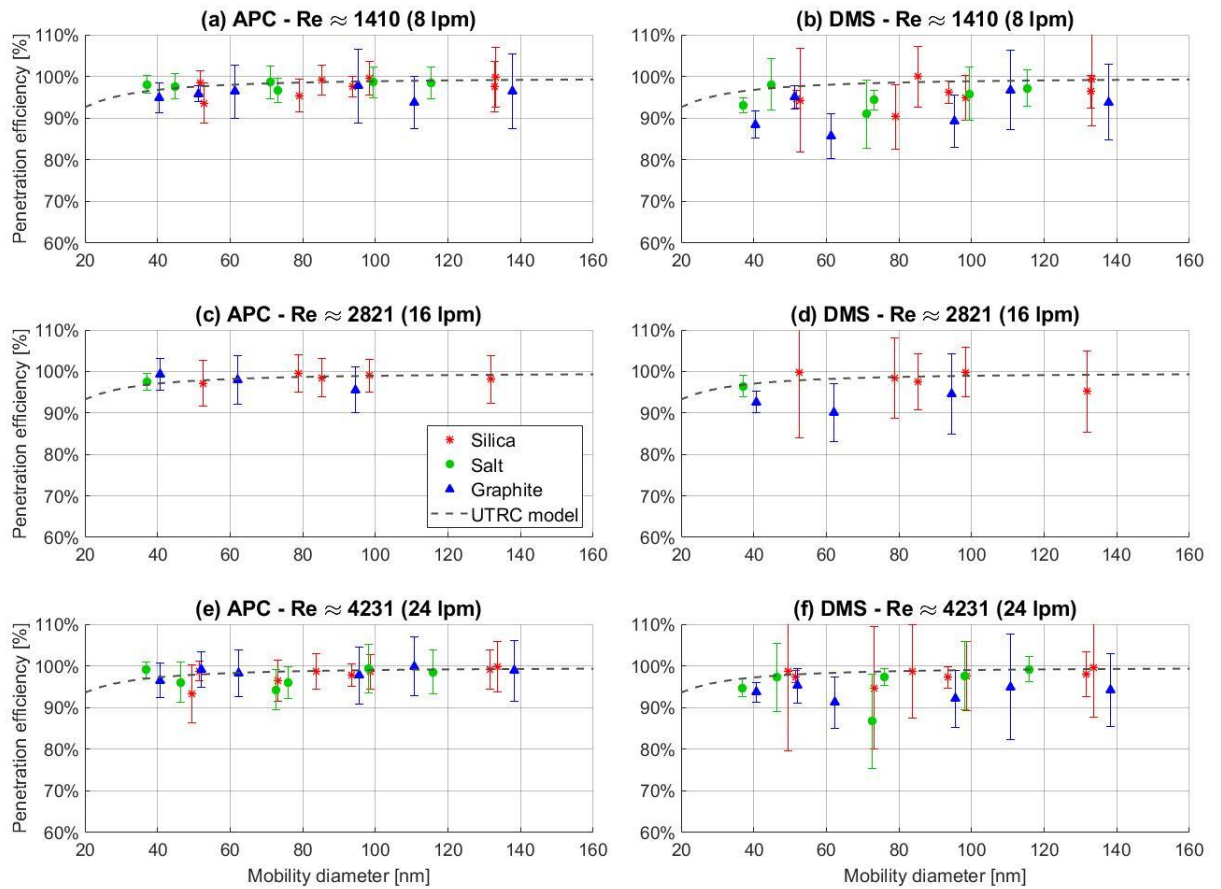


Figure 5-8: Measured (APC and DMS-500) and predicted (UTRC model) penetration efficiencies for different particle types (NaCl, SiO₂, graphite) in the thermophoretic test section at ambient temperature and flowrates of 8-24 lpm

When comparing both analysers, error bars were generally higher for the DMS-500 (**Figure 5-8 (b)(d)(f)**). This occurrence can be explained by the different nature of the measurement made by each analyser (CPC particle count Vs. number concentration derived from electrode ring currents). As it was previously established that non-thermophoretic losses theoretically decrease with increasing temperature (section 5.1.4), it can be assumed that losses occurring when the furnace on will predominantly be thermophoretic.

Table 5-4: Thermophoretic test section penetration efficiencies at ambient temperature averaged over particle type measured with an APC and a DMS-500, and predicted by the UTRC model (± 1 standard deviation)

	Average penetration efficiency APC	Average penetration efficiency DMS	Predicted (UTRC)
8 Lpm	$97.2 \pm 1.8 \%$	$94.2 \pm 3.7 \%$	97.7 %
16 Lpm	$98.1 \pm 1.3 \%$	$96.1 \pm 3.3 \%$	97.8 %
24 Lpm	$97.8 \pm 1.8 \%$	$95.8 \pm 3.2 \%$	98 %
Combined	$97.7 \pm 2.9 \%$	$95.4 \pm 5.9 \%$	97.8 %

Penetration efficiencies measured whilst heating the furnace up to 1000°C are presented in Figure 5-9 with error bars again representing two standard deviations (section 2.5).

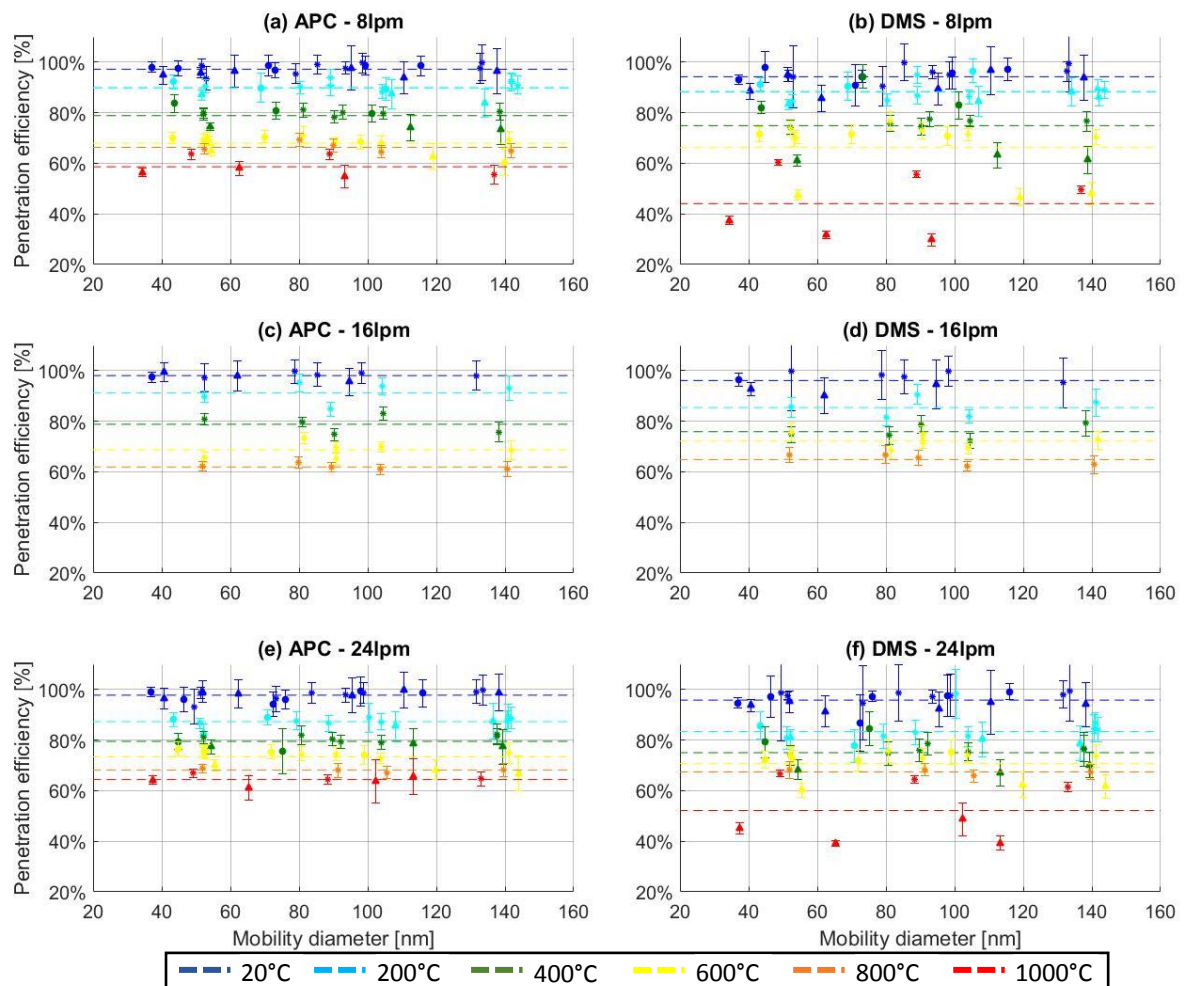


Figure 5-9: Penetration efficiencies of different nanoparticle types (graphite ‘Δ’, silica ‘*’, salt ‘o’) and sizes measured in the thermophoretic set-up with the furnace on at different temperatures, measured with the DMS-500 and the APC at 8-24 Lpm

In **Figure 5-9**, penetration efficiencies are seen to decrease with increasing furnace temperature as larger gas temperature gradients induce thermophoretic losses. At each investigated temperature, the data was fitted with a linear regression for visual aid and to confirm that thermophoretic losses were not size-dependent at the investigated size range, as has been discussed in the literature [83], [84]. It is noted that salt nanoparticles are not represented at $T_{\text{furnace}} > 600^{\circ}\text{C}$ because they were shown to evaporate as later discussed with **Figure 5-12**. It was also witnessed that graphite particles penetration efficiencies measured by the DMS-500 (triangles in **Figure 5-9(b)(d)(f)**) were generally lower than that of salt and silica, as further discussed with **Figure 5-10**.

If assuming negligible non-thermophoretic losses in this experiment, then changing the flow from 8-24 Lpm should only cause variations in the maximal gas flow temperatures. Given thermophoretic loss can also be assumed size independent between 30-140 nm (**Figure 5-9**), penetration efficiencies were hence averaged over particle size and plotted against the gas temperature gradient ($T_{\text{max}} - T_{\text{min}}$). The averaged penetration efficiencies are presented in **Figure 5-10** with the error bars representing the standard deviation of the averages.

It was observed that the penetration efficiency decreases with the increasing gas temperature gradient caused by thermophoresis, as highlighted by the power fits. Power law trends were fitted to the measured data as both k_{thermo} and theoretical thermophoretic loss (section **2.3.1.4**) are expressed with a power law relationship. When investigating particle type, silica and salt particles exhibited similar trends, in agreement with the previous reports of Shimada et al. [126] and Romay et al. [86]. However, different trends were witnessed for graphite particles with penetration efficiencies derived from the APC generally 3-4% lower (**Figure 5-10(a)**). The higher deposition of graphite particles suggests that fractal particles are more strongly affected by thermophoresis than spherical/cubical particles, potentially due to their larger thermophoretic velocity of aggregates as discussed by Brugière et al. [85].

When comparing both analysers (**Figure 5-10(a)&(b)**), it can be seen that they display similar trends for salt and silica particles. However, the DMS-500 consistently reported lower penetration efficiencies, up to 25%, for graphite. After thorough investigation of the data, no explanation was found for this occurrence. It was hypothesised that the consecutive heating and cooling of fractal graphite may have altered their state of charge which would only impact the DMS-500 measurements.

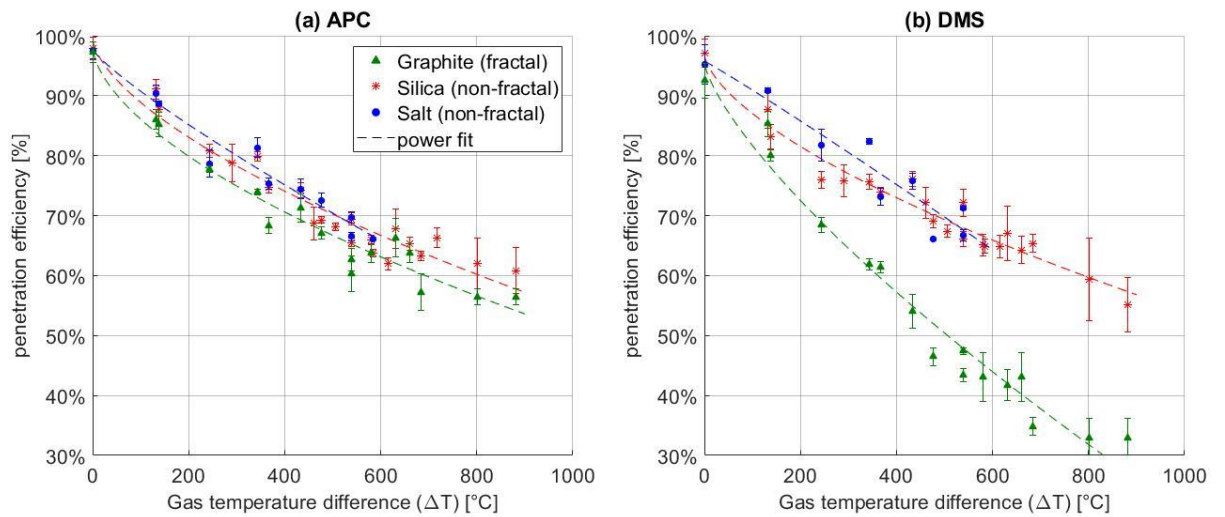


Figure 5-10: Penetration efficiencies of Graphite, silica and salt (NaCl) against gas temperature gradient averaged over size and measured with an APC (a) and a DMS-500 (b).

Given the similar trends of silica and salt (i.e. non-fractal), they were subsequently averaged and fitted with a power fit to compare with theoretical predictions and with the power fit trends of graphite (i.e. fractal), as presented in **Figure 5-11**. In **Figure 5-11**, the grey shaded area represents the total penetration efficiency estimated by the UTRC model between 30–140 nm and is slightly different to k_{thermo} exclusively representing thermophoretic losses between T_{max} ($\leq 910^{\circ}\text{C}$) and T_{min} (30°C). The red shaded area represents the temperature range at which the thermophoretic equation prescribed in the UTRC model (equation (2.24)) was experimentally validated using spherical particles only, highlighting the much larger temperature gradients investigated in this experiment. It is noted that in the heated section, thermophoretic penetration efficiency was approximated at 100% in the UTRC model.

As can be observed, theoretical predictions agree well with the averaged measured penetration efficiencies of salt and silica across the investigated temperature range ($\Delta T_{\text{gas}} \leq 880^{\circ}\text{C}$) with total losses up to 40% reported. The theoretical power law trend representing thermophoretic loss (k_{thermo}) was hence validated for silica and salt nanoparticles at gas temperatures $\leq 910^{\circ}\text{C}$, suggesting that thermophoretic loss could never exceed $\sim 60\%$.

It is again noted that graphite particles losses are 3-4% higher than salt and silica, measured using a regulatory compliant nvPM number analyser (APC - **Figure 5-11(a)**). Hence, assuming aircraft exhaust nvPM behaves similarly to graphite, this suggests thermophoretic losses of aircraft nvPM are underestimated by up to 4% in the UTRC model and by k_{thermo} .

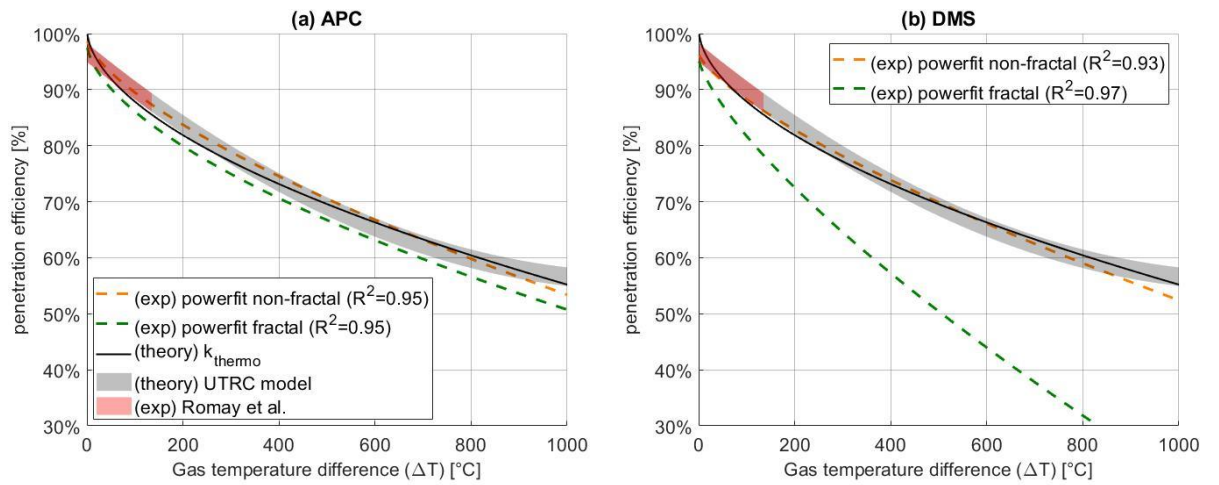


Figure 5-11: Power fit of penetration efficiencies of Graphite and silica and salt (NaCl) measured by an APC (a) and a DMS-500 (b) combined averaged over size and compared with theoretical predictions

During the thermophoretic experiment, salt shrinkage to sizes <10 nm was witnessed from aerosol temperatures (T_{max}) of 600°C , as displayed in **Figure 5-12(a)**. An observed size reduction below the melting point of NaCl material (800°C [153]) was also reported by Shimada et al. [125] and explained using the theory of evaporation in the free-molecule region.

Nitrogen gas (N_2) was also briefly investigated as the carrier gas instead of dry air. It was observed that total penetration efficiencies were on average 1.2% higher with the APC and 1.9% higher with the DMS-500 when using N_2 instead of air, as presented in **Figure 5-12(b)**. This small difference may be explained by the lower particle diffusion coefficient in N_2 reducing diffusional losses, as discussed by Shimada et al. [126].

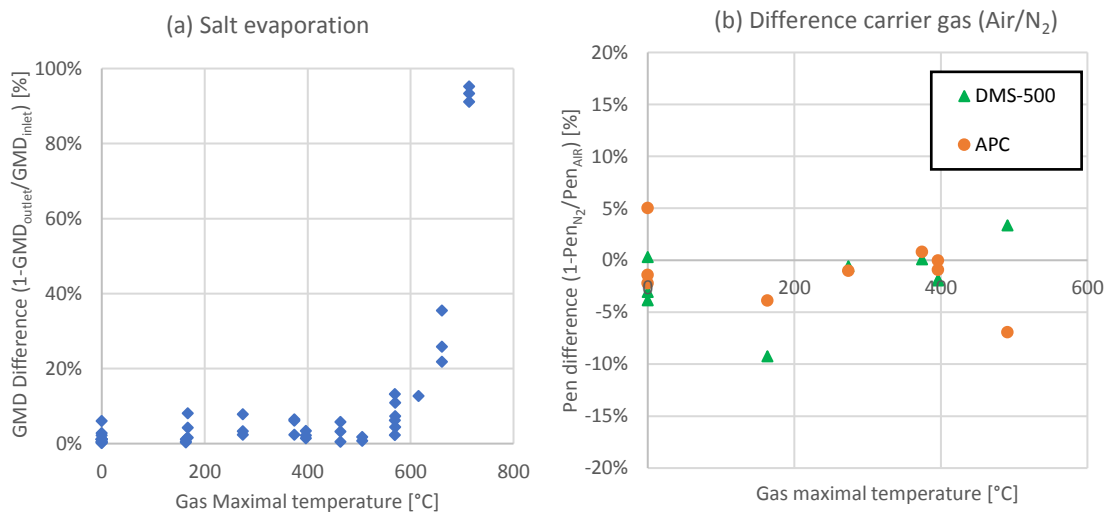


Figure 5-12: Difference in GMD measured before and after the thermophoretic test section for salt (NaCl) nanoparticles (a) and difference in the measured penetration efficiency when using air or nitrogen (N_2) as a carrier gas (b)

5.2 25 m Sample line experiment

As discussed previously, in an ICAO compliant nvPM sampling system, the exhaust aerosol must be transported through a 24.5 ± 0.5 m long heated sample line at 25 ± 2 standard Lpm and $60 \pm 15^\circ\text{C}$ [14]. The long sample line is required to have electrically conductive walls meeting the anti-static specification in ISO 8031 and hence minimising electrostatic deposition. Nevertheless, significant particle losses occur in the 25 m sample line, with aircraft PM (<100 nm [9]) typically depositing onto the wall via diffusion.

Furthermore, during the sampling of gas turbine exhaust, sample lines must sometimes be bent/coiled to reach the analysers. In a bend, particles can deviate from the gas flow and be lost to the walls [91]. To minimise additional bend losses in a sampling system, the current civil aviation regulation [14] advise the sample lines to be as straight-through as practical. When line bending is unavoidable, it is required bends have radii greater than ten times the internal diameter of the lines and that any bend in the sample line has a minimum coiled radius of 0.5 m. Losses in pipes ([76], [122], [123]) and in a compliant 25 m sample line using soot particles ([47], [48]) have been previously experimentally investigated.

In this study, the particle penetration efficiency of an ICAO compliant 25 m Winkler heated line (section 3.1.1.4) currently used in the EASA reference system was assessed using different particle types (silica, salt, graphite) and flow regimes. The sample line was coiled in agreement with the current requirements to assess the impact on losses. Results were compared to the diffusional, bend and thermophoretic theory used by the UTRC model.

5.2.1 Experimental set-up

The experimental set-up for the 25 m sample line experiment consisted of a particle generation section, a test section, and a measurement section similar to the thermophoretic experiment set-up (section 5.1.1). Conditioned Silica, Salt and graphite particles ranging between 30-140 nm (section 4.2) were employed to estimate losses in the 25 m line at aerosol flows of 8-24 Lpm using a Cambustion DMS-500 (section 3.1.3) and AVL APC (section 3.1.1.1) alternatively measuring particle number concentration at the inlet and the outlet of the test section.

The Winkler 25 metres heated sample line is constructed of 8 mm ID carbon loaded PTFE. When assessing diffusional losses, the line was kept as straight as possible given the constraints of the laboratory (bends $\approx 760^\circ$) and the curled radius kept as large as possible (**Figure 5-13(a)&(b)**). When investigating bend losses, the line was coiled eleven times with a coiled radius of ~ 0.65 m as seen in **Figure 5-13(c)**, representing the tightest and the highest number of coils the line could sustain whilst respecting ICAO regulatory requirements.

To ensure equivalent flowrates in the 25 m sample line, two cyclones with different restrictors were used at the inlet of the DMS-500 to account for the additional pressure drop in the 25 m sampling line when measuring at the inlet compared to the outlet. As discussed previously, uncertainties associated with the experimental set-up were minimised (section 5.1.2).

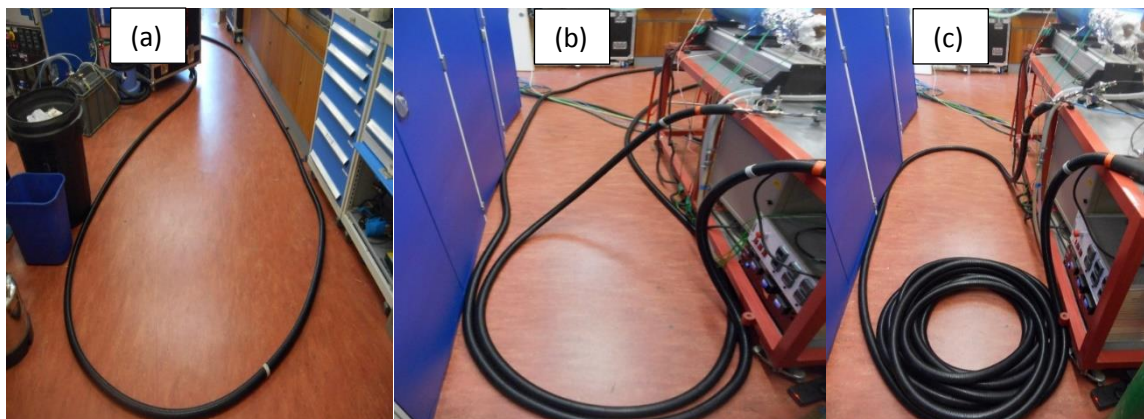


Figure 5-13: Photographs of the 25 m sample line experiment with the line 'straight' (a) & (b) and 'coiled' (c)

5.2.2 Theoretical sensitivity analysis

A sensitivity analysis of particle effective density, gas flowrate and line coiling were performed using the UTRC model prior to experimentation. Particle effective density was varied from 1 g/cm^3 , the estimated density of fractal soot particles $<100 \text{ nm}$ [63], to 2.2 g/cm^3 representing salt material density. Similarly, bends were varied between 760° (straight line) and 3960° (coiled line) with flows ranging from 8-24 Lpm.

As can be seen in **Figure 5-14(a)**, particles with larger effective densities (2.2 g/cm^3) were expected to have a lower penetration efficiency in the coiled line, although differences may be assumed negligible in the size range of interest, with differences of $<1.5\%$ at 140 nm observed the maximum difference in the $30\text{-}140 \text{ nm}$ range. Particle effective density only significantly affects inertial and bend losses for particles $>200 \text{ nm}$, as confirmed in **Figure 5-14(b)** where the coiled line is reported to have a lower penetration efficiency $<1\%$ at sizes $<140 \text{ nm}$ when compared with the straight line. Furthermore, small differences in predicted penetration efficiencies can be observed when varying the flow from 8-24 Lpm (**Figure 5-14(a)&(b)**), particularly at smaller sizes. Lower penetration $<3\%$ were reported at 30 nm and 8 Lpm when compared with 24 Lpm due to the longer residence time and hence higher diffusional losses.

It is noted that although the flow regime transitions from laminar to turbulent between 8 and 24 Lpm, diffusional losses are expected to behave similarly given it has been shown previously that turbulent diffusion theory best described losses in sample lines, even in a laminar flow regime [76].

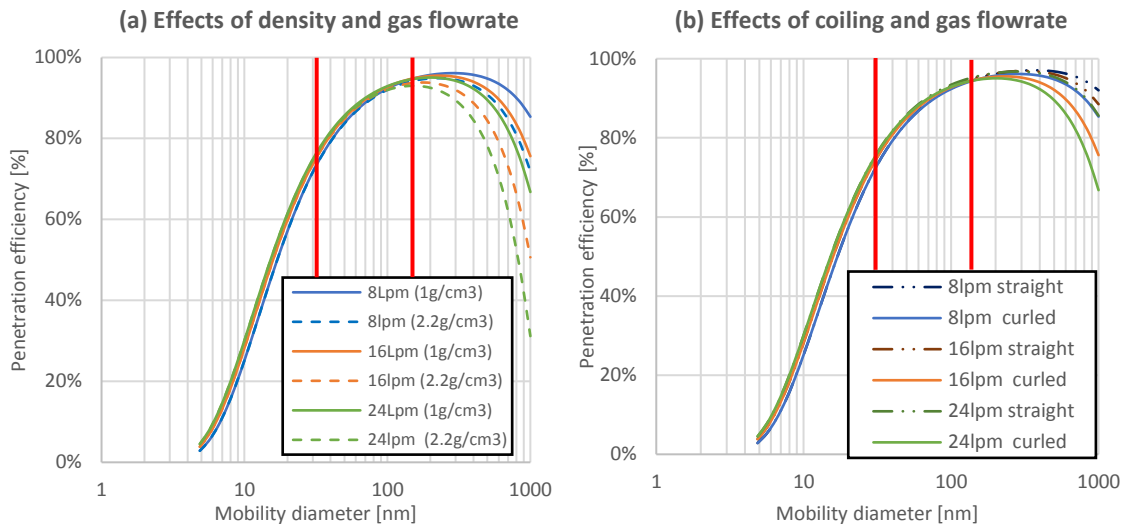


Figure 5-14: UTRC model penetration efficiency predictions in the coiled (3960°) 25 m sample line with different particles densities at 25°C (a) and difference between the coiled and straight (720°) (b) at different gas flowrates

It was concluded from this analysis that similar losses should be experienced by graphite, silica and salt nanoparticles during the 25 m sample line experiment and hence a density of 1 g/cm³ as currently prescribed by ICAO [14] was used when comparing UTRC model prediction with experimental measurements. Also, additional losses from coiling were expected to be negligible in the size range investigated.

5.2.3 Results

Losses in the 25 m sample line were investigated for three settings namely a ‘straight’ sample line (720°), a coiled sample line (3920°), and a heated sample line (60-140°C). Similarly to the thermophoretic experiment, the penetration efficiencies of aerodynamically classified graphite, salt and silica were estimated at sizes ranging from 30-140 nm and at gas flows of 8-24 lpm (Reynolds number ~1420-4240). It is noted that total nvPM number concentration was measured by the APC whilst the DMS-500 measured total number concentration, GMD & GSD derived from only the main aerosol mode (section 3.1.3).

5.2.3.1 Characterisation of diffusion loss

The measured and UTRC predicted penetration efficiencies of the 25 m ‘straight’ sample line are presented in **Figure 5-15**. The error bars represented two standard deviations from the measured penetration efficiency (section 2.5). Exponential fits to the measured data in the form ‘ $\exp(-A \times d_p(x)^{1.15})$ ’ (note: in equation (2.19), $\eta_{diffusion}(d_p) \propto \exp(-V_{diff}) \propto \exp(-Sc^{1/3} \times D) \propto \exp(-d_p(x)^{1.15})$) are represented by black dashed lines with 95% confidence bands. The fits were extrapolated from the theory of diffusional loss (section 2.3.1.3) to permit an accurate

comparison between measured and UTRC predicted diffusional losses. As can be seen in **Figure 5-15**, at 8 Lpm the coefficient of determination (R^2) is negative meaning that the exponential fit to the measured data is a worst fit than a horizontal line of the mean. This suggests that the diffusional theory used in the UTRC model (equation (2.19)) is not applicable to diffusional loss in the laminar regime (i.e. at 8 Lpm where $Re=1410$). In the turbulent regime (16 & 24 Lpm), R^2 varies between 0.4-0.92 showing that UTRC model diffusional theory is more suitable in this regime.

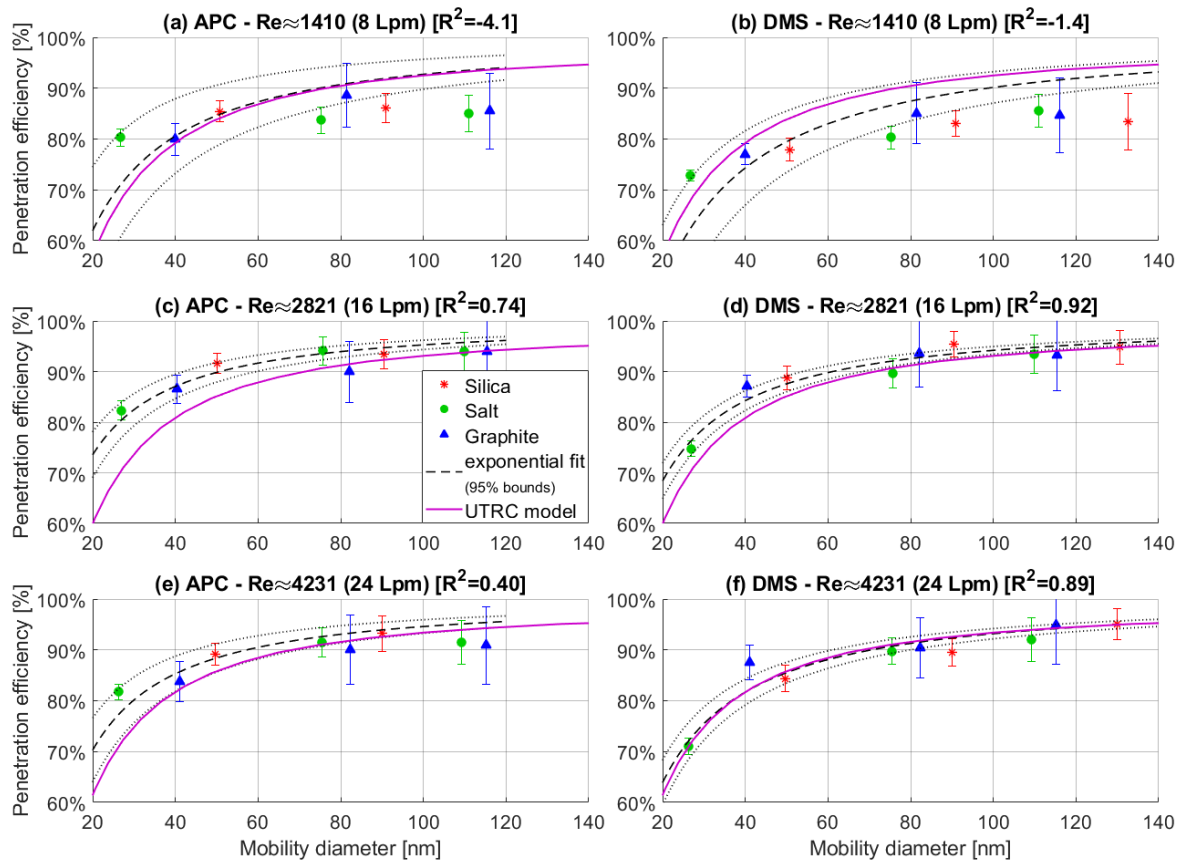


Figure 5-15: Theoretical (UTRC model) and experimental (NaCl, Graphite & SiO_2) diffusional penetration efficiencies measured with an APC and a DMS-500 in a ‘straight’ 25 m sample line at Reynolds numbers of 1410 – 2431

Also in **Figure 5-15**, it is seen that measured penetration efficiencies vary from ~70% at 30 nm and 24 Lpm up to ~90% at 140 nm at 24 Lpm. Exponential fits of both the DMS-500 and APC measured data generally display close agreement with estimations from the UTRC model (purple line) at flowrates of 16 & 24 Lpm. This is in agreement with previously reported works [47], [76], [174], [175]. It is noted that penetration efficiencies measured by the APC (**Figure 5-15 (a)(c)(e)**) for the 25 nm salt were always higher than theoretically predicted and the measured penetration efficiencies at 8 Lpm (**Figure 5-15(b)**) were generally lower than that predicted by the theory. The lower measured penetration efficiencies in the laminar regime (8 Lpm) suggest that the turbulent

penetration model used in the UTRC model underpredicts loss in laminar regime as losses are expected to be larger in this regime [62, p. 91].

When specifically investigating the flowrates, the lowest penetration efficiencies were measured at 8 Lpm, caused by the decrease in particle residence time and hence higher diffusional losses. It is noted that losses were similar at 16 and 24 Lpm. Increasing from 16 - 24 Lpm reduced the residence time and the flow regime ($Re \approx 4231$) is transitioning towards fully turbulent flow which could potentially increase the deposition rate, as discussed by Yin and Dai. [122].

It was concluded that for the investigated size range, the different densities ($1 - 2.2 \text{ g/cm}^3$) and morphologies (spherical, cubical and fractal) had a negligible impact on the reported diffusional losses, as predicted in the sensitivity analysis (section 5.2.2). However, it is conceded that more data points would be needed $< 40 \text{ nm}$ to validate or refute the observable higher measured penetration efficiencies observed by the APC.

It is observed that the penetration efficiency data point corresponding to the 180 nm SiO_2 suspension is not included in the APC results for this experiment. This is due to issues caused by an observed NVR peak ($\sim 25 \text{ nm GMD}$) still present after AAC conditioning (**Figure 4-29**) which significantly reduced the APC penetration efficiency estimations due to the inherently higher diffusional losses at these smaller sizes. However, this data point could be plotted for the DMS-500 given the penetration efficiencies are derived from the main aerosol peak only hence these particles are neglected from both the inlet and outlet measurements.

5.2.3.2 Characterisation of Bend loss

Bend loss was investigated in the 25 m sample line by coiling the line as much as possible (11 coils= 3960°) and comparing the measured penetration efficiencies when the line is coiled to those measured in the aforementioned 'straight' experiment, with the results presented in **Figure 5-16**. The measured data was again fitted ($\exp(-A \times d_p(x)^{1.15})$) as represented by the dashed line. The error bars on the measured data points represent two standard deviations from the estimated penetration efficiency (section 2.5).

At all flowrates and investigated particles in **Figure 5-16**, it was observed that the measured penetration efficiencies are generally lower for the 'coiled' data (black) compared with the 'straight' line data (orange). As predicted in the sensitivity analysis (section 5.2.2) the particle properties of the graphite, silica and salt had negligible effect on losses at sizes $< 140 \text{ nm}$.

As the flowrate increases, the difference between witnessed penetration observed for the 'coiled' and 'straight' sample line reduced. It is suggested that as the airflow increased from $8 - 24 \text{ Lpm}$, the Dean number (equation (2.18)), defined as the product of Reynold number and the square

root of the curvature ratio, increased from 223 - 669 and hence losses induced by coiling were reduced in agreement with previous works [78], [122].

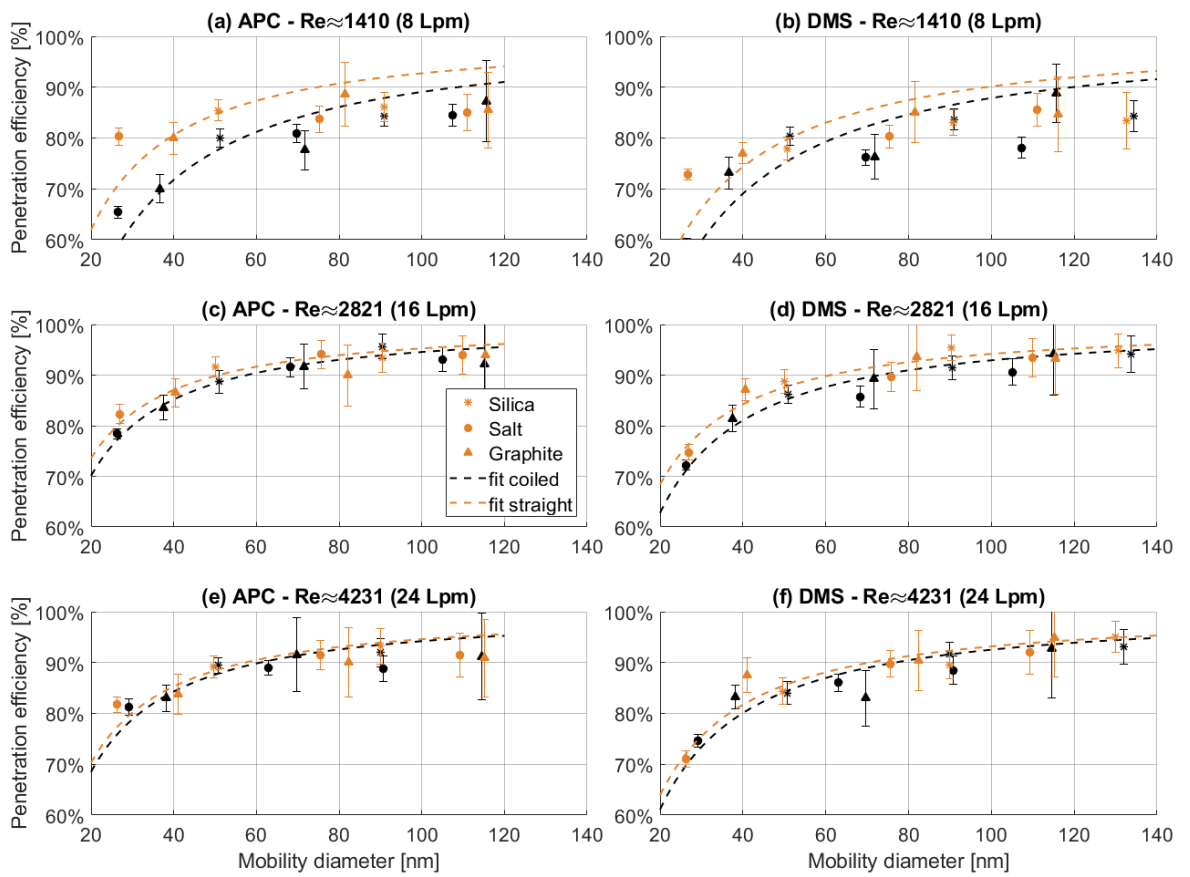


Figure 5-16: Penetration efficiencies of NaCl, SiO₂ and graphite nanoparticles in the ‘straight and ‘coiled’ 25 m sample line with their exponential fits measured by an APC and a DMS-500 at Reynolds numbers of 1410 - 4231

The GMD of classified particles fluctuated day-to-day hence bend loss couldn’t be directly deduced from subtracting the specific measured penetration efficiencies. Instead, to derive the impact of coiling (3960°) on particle losses, the difference was estimated using the ‘straight’ and ‘coiled’ line exponential fits (orange & black dashed line **Figure 5-16**). Presented in **Figure 5-17**, the estimated differences between the ‘straight’ and ‘coiled’ fits (dashed line) were compared to bend loss predictions from the UTRC model (purple line) between 30–140 nm. It is noted that the accuracy of bend loss estimations (**Figure 5-17**) are limited to the exponential fit used in this study.

As witnessed in **Figure 5-17**, the measured-derived bend losses from the fits (dashed lines) decrease with increasing size and increasing flowrate. An explanation for this trend is that coiling induces the development of secondary flows due to centrifugal force in the coil transporting particle from the central region towards regions closer to the walls as proposed by Wang et al. [91], hence enhancing diffusional losses which preferentially affect smaller particles at lower flows. The measured-derived losses induced by the eleven coils between 30-140 nm varied between 2-10% at

8 Lpm, 1-6% at 16 Lpm and 1-4% at 24 Lpm. Higher losses are observed at lower sizes suggesting that losses induced by coiling could add uncertainty to the number concentration but not the mass concentration (carried by the larger particles).

When comparing with the UTRC model (purple line), measured losses are consistently higher than the those predicted in the investigated range, with theoretical losses < 1%. It is also noted that the size dependent trend displays opposing gradients. These observations further support the hypothesis that losses in coils are induced by the additional diffusional loss impacting smaller particles rather than bend loss impacting larger particles. This finding is currently not accounted-for in the UTRC model although at conditions relevant of aircraft PM sampling (i.e. 24 Lpm), additional losses induced by coiling are low (<4%).

This analysis has demonstrated that even when in agreement the civil aviation regulation guidelines [14], additional losses up to 4% at 30 nm can occur due to coiling which is a potential uncertainty not currently accounted for in the UTRC model. Nevertheless, ICAO regulation recommends minimising coils and bends as far as practically possible and this experiment investigated the highest coiling the sample line could sustain and low additional losses were reported, hence bend losses can generally be assumed negligible in the 25m sample line if coiling is minimised.

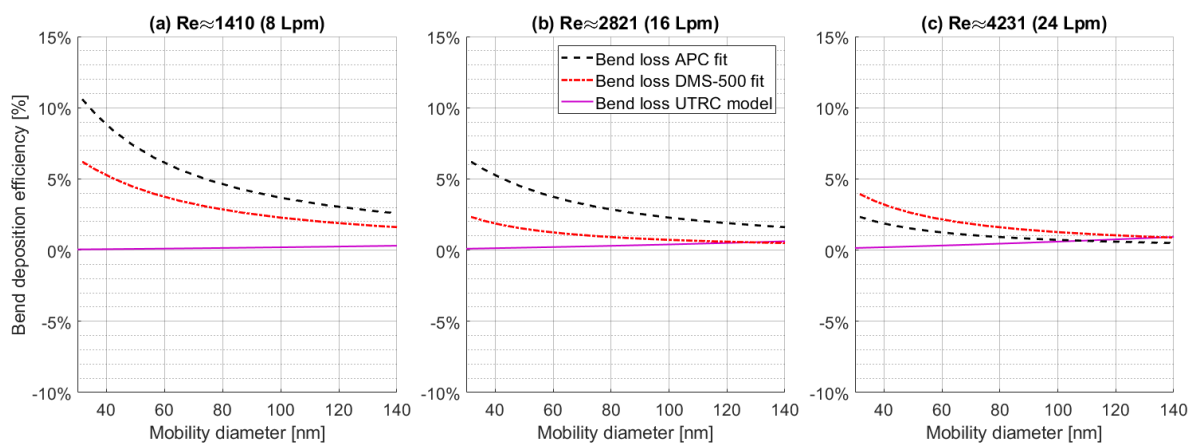


Figure 5-17: Measured (APC and DMS-500) and estimated deposition efficiency caused by coiling the 25 m sample line (i.e. difference 'straight'/'coiled') at Reynolds numbers of 1410 - 4231

5.3 VPR experiment

As discussed in section 3.1.1.1, significant particle loss can occur in an ICAO compliant VPR, mostly caused by thermophoresis in the evaporation tube and diffusion in the catalytic stripper. Accurate characterisation of losses in the VPR is necessary to predict accurate nvPM number concentration.

In this section the penetration efficiency of the EASA reference system VPR (AVL APC) was experimentally determined using different particles and compared to the calibrated values provided by AVL from the annual calibration performed with thermally pre-treated mini-CAST soot.

5.3.1 Experimental set-up

The VPR experiment was performed using salt, silica and graphite particles as presented in **Figure 5-18**. Unlike the previous thermophoretic and sample line experiments, particles in this experiment were classified between 10-50 nm using a TSI DMA 3081 and a TSI 3077 radioactive neutralizer from Manchester University rather than the Cambustion AAC. A diffusion drier was used with nebulised particles to maintain a low relative humidity in the sampled aerosol as difference in the relative humidity between the sample flow and the sheath flow in the DMA can induce size change (section 4.1.1.2).

The VPR penetration efficiency was estimated by simultaneously measuring particle number concentration at the inlet and the outlet of the VPR. Two butanol-based CPCs were used for this purpose:

- **CPC₁**: a TSI 3750 CPC with $d_{50}=7$ nm and $d_{90}=10$ nm from Manchester university.
- **CPC₂**: a TSI 3790E CPC with $d_{50}=10$ nm and $d_{90}=15$ nm from the EASA reference system (APC CPC).

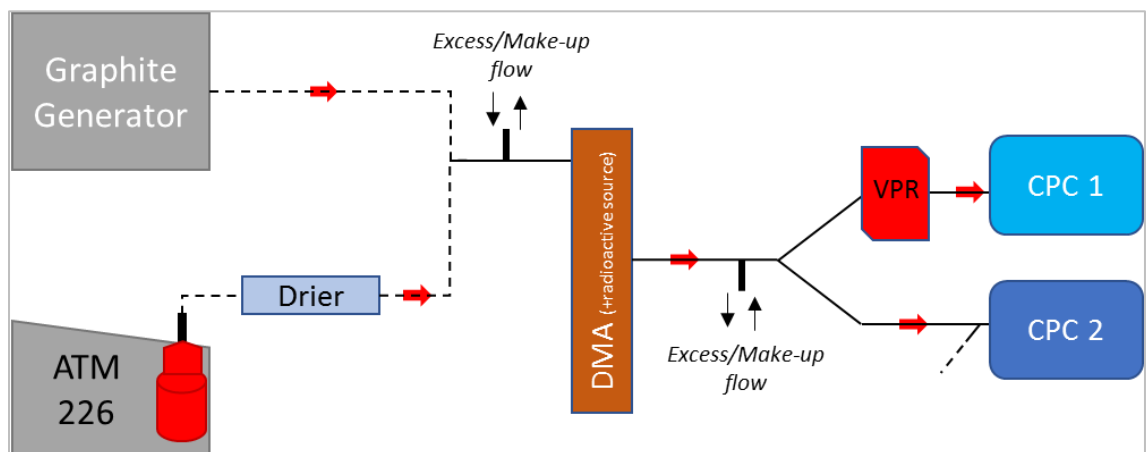


Figure 5-18: Diagram of the VPR characterisation experiment

To ensure equivalent losses between the CPCs, carbon loaded PTFE tubing of equal dimensions were used with flowrates kept consistent. It is noted that the sample lines between the DMA and CPC₁ and CPC₂ were swapped and the inlet flowrate of each CPC was calibrated with a Gilian Gilibrator-2 calibrator to ensure flows and hence losses were similar.

5.3.2 Results

Given the two CPCs used to measure the VPR penetration efficiency had different cut-off efficiencies, they were initially cross-calibrated using NaCl particles to enable correction for any observed differences between the CPCs, this methodology is similar to that employed by Yoon et al. [176]. As presented in **Figure 5-19**, CPC₁ measured progressively higher concentrations than CPC₂ ≤ 20 nm at lower classified particle sizes as expected due to its smaller d_{50} . A power fit ($R^2 > 0.99$) given in equation (5.6) was derived from the ratio of the two CPCs (red dashed line) and used to correct the CPC concentrations.

$$fit_{CPC_2/CPC_1} = -6174 \times d_p^{-3.88} + 1.038 \quad (5.6)$$

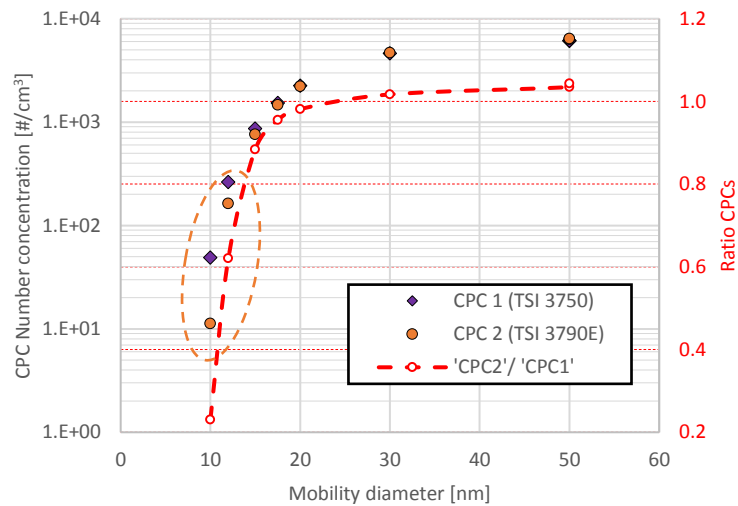


Figure 5-19: Particle number concentration of salt (NaCl) nebulised with an ATM-226 and classified with a DMA between 10-50 nm measured by two CPCs

The VPR penetration efficiencies (measured and CPC-corrected) using different particle types are presented in **Figure 5-20**, along with the four AVL calibration points and the VPR penetration function derived from the AVL calibration (black dashed line) following ICAO recommendations (Appendix 8) [14]. As can be seen in the CPC corrected graph (**Figure 5-20(b)**), all measured penetration efficiencies are above that from the AVL calibration (mini-CAST soot). Giechaskiel et al. [94] reported differences <5% between NaCl, graphite and CAST soot. However, it is noted that in this study the AVL calibration was performed 6 months before the laboratory loss experiment, using a different set-up which may partly explain the larger differences (< 10%) observed in this work.

The difference between graphite and mini-CAST soot (AVL calibration) generally remained <3% for particles >20 nm, in agreement with results from Giechaskiel et al. [94] who reported graphite penetration efficiencies on average 2% higher than that of soot produced by a mini-CAST.

The unusual graphite penetrations penetration efficiencies <20 nm (highlighted by the orange dashed circle) are thought to be due to the CPC cross-calibration as the trend in the uncorrected data is similar. It is noted that the correction may have been more accurate for graphite had it not been performed with salt which may classify differently in the DMA at the smaller sizes. ICAO compliant CPC and VPR calibration uncertainty are discussed in more detail in section 6.2.1.

When comparing the three particles investigated in this study, it is observed that graphite consistently displays lower penetration efficiencies (~5% up to 10%) than salt and silica. This result could be caused by the different morphology of graphite (fractal) which displays larger thermophoretic losses as previously observed for graphite (section 5.1.6).

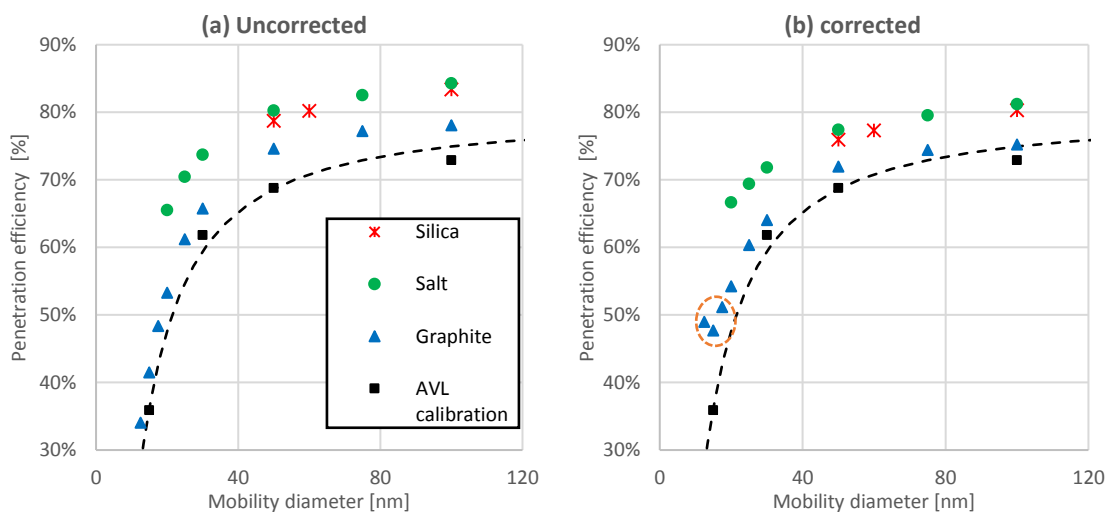


Figure 5-20: VPR penetration efficiency of Silica, salt (NaCl) and graphite measured (a) and CPC cross-calibration corrected (b) compared with mini-CAST from AVL calibration

5.4 Chapter summary

In this chapter, three laboratory experiments investigating the loss of nanoparticles of different density and morphology (NaCl, SiO₂, graphite) at sizes ranging from 30-140 nm are presented, namely:

- **A high temperature thermophoretic loss experiment:**

For the first time, thermophoretic losses were successfully measured at large temperature gradient ($\leq 880^{\circ}\text{C}$) and flowrates relevant to aircraft exhaust sampling (8-24 Lpm). In agreement with previous studies, it was found that thermophoretic losses weren't size dependent. The measured thermophoretic penetration efficiencies correlated well with theoretical predictions from Romay et al. [86] used in the UTRC model and with k_{thermo} for spherical/cubical particles (NaCl, SiO₂). However higher losses in the order of 3-4% were reported for fractal particles (graphite).

- **A diffusion and bend loss experiment in the EASA reference system 25 m line:**

During the experimental analysis of particle loss in the 25 m sample line, in agreement with previous studies [47], [175], penetration efficiencies between 70-95% were measured for nanoparticles ranging between 30–140 nm at conditions relevant of aircraft PM sampling with good correlation to the UTRC model theory. Additional data points < 40 nm would better define the higher diffusional losses witnessed at lower sizes. It was found that coiling the sample line eleven times induced additional diffusional loss' of up to 4% (30 nm) at 24 Lpm which may be attributed to additional centrifugal force leading to increased diffusional losses [78]. This finding is not predicted by the UTRC model which only considers bend loss in coils. However, coiling is minimised during aircraft exhaust sampling and bend losses can generally be assumed negligible.

- **An experiment characterising loss in the EASA reference system VPR:**

The VPR experiment highlighted that particle losses through a VPR depend on the particle morphology, with spherical/cubical penetration efficiencies (SiO₂, NaCl) up to 10% higher than that of fractal graphite/soot. The measured penetration efficiencies were always larger than the calibrated values from AVL used for system loss corrections, suggesting losses may be overestimated in the VPR. It is noted that NPL performed a VPR calibration with gold nanoparticles at 15 nm (discussed in section 6.2.1.1) and measured a larger penetration efficiency than that of soot (51% Vs. 32%) at 15 nm which supports the findings of this study.

To conclude, findings in this chapter support that the UTRC model prescribed by ICAO for sampling system loss correction performs well at predicting the two main loss mechanisms (i.e. diffusion and thermophoresis) for non-fractal particles at conditions relevant of aircraft nvPM sampling. However, higher losses were observed with fractal particles in the thermophoretic and VPR experiments, suggesting the UTRC model and k_{thermo} may underestimate losses for aircraft nvPM fractal aggregates.

6 Large-Scale Civil Aviation Engine PM measurements

The EASA reference system nvPM instruments (section 3.1.1) were used in conjunction with a Rolls-Royce sampling system and additional DMS-500 to undertake ICAO Annex 16 Volume 2 [14] compliant nvPM emission certification measurements on seven large scale (rate thrust > 26.7 kN) specific engines of four engine types representative of the current Rolls-Royce fleet (section 0). Concentrations of nvPM mass, number, and gaseous CO₂ were measured in addition to size distributions at various thrust settings. Because of the specified sampling system which is nominally > 30 metres in length with multiple dilution stages, measured data is not representative of the concentrations at the engine exit plane which are the concentrations required for accurate predictions of impact on local air quality and health.

The main objective of this chapter was to derive trends from nvPM emissions measured with an ICAO compliant sampling system across different large-scale engines to develop correlations between the reported nvPM number and mass with data derived from additional size measurements (i.e. GMD, GSD, density, lognormality). Additionally, ICAO compliant sampling system operation and nvPM instrument measurement and calibration uncertainties were investigated in view of understanding the uncertainties of deriving these concentrations and the currently reported nvPM emission indices. It was also aimed to assess the impact of ambient conditions (i.e. humidity) and fuel properties (i.e. hydrogen content) on nvPM emissions.

6.1 Measured nvPM Correlations and Properties

Due to proprietary issues, specific engine data presented in this study was normalised (plot specific), hence results are plotted against parameters such as measured GMD and N/M ratio rather than engine power or thrust as is typical in the literature [9], [20], [61], [63] (section 2.6). As discussed below, GMD generally correlates to thrust with larger particles typically witnessed at higher powers for any given engine. Similarly, the N/M ratio is a measure of size (see equation (2.6)), if density and fractal nature is assumed constant, and eliminates uncertainties associated with thermophoretic loss, CO₂ measurements, and sampling uncertainties given both number (N) and mass (M) were subject to the same sampling conditions. As discussed in section 2.4, the ratio of mass and number also acts as an input of the System loss tool.

6.1.1 Correlation of Measured nvPM to Relative Thrust

Emission Indices (EI's) are a regulatory value used to quantify nvPM number and mass emissions per mass of fuel burned (section 1.5.1.2). EI's facilitate comparison between different aircraft engines and powers only accounting for thermophoretic loss in the collection section. A

simplified measure of EI is presented in this work hence it is assumed all the fuel carbon is converted to CO₂ which is a valid approach given typical combustion efficiencies of modern engines are >95% [177].

The uncorrected nvPM EIs across the range of measured powers (7-100%) from the seven engines (four engine types) tested ranged from 2.2×10^{13} to 2.3×10^{15} particles/kg of fuel for number EIs and 0.6 to 292 mg/kg of fuel for mass EIs, corresponding to similar orders of magnitude observed in the literature [9], [20], [51], [61], [63], [92], [93]. Note that the quoted EIs were not corrected for thermophoretic loss at the collection section because engine exhaust exit plane gas temperature is commercially sensitive. As discussed later in section 7.1.1.1.2, exit plane gas exhaust temperature can reach temperatures of up to 700°C, requiring a thermophoretic correction factor k_{thermo} for losses in the collection section as high as 1.36 hence the reported EIs values are underpredictions.

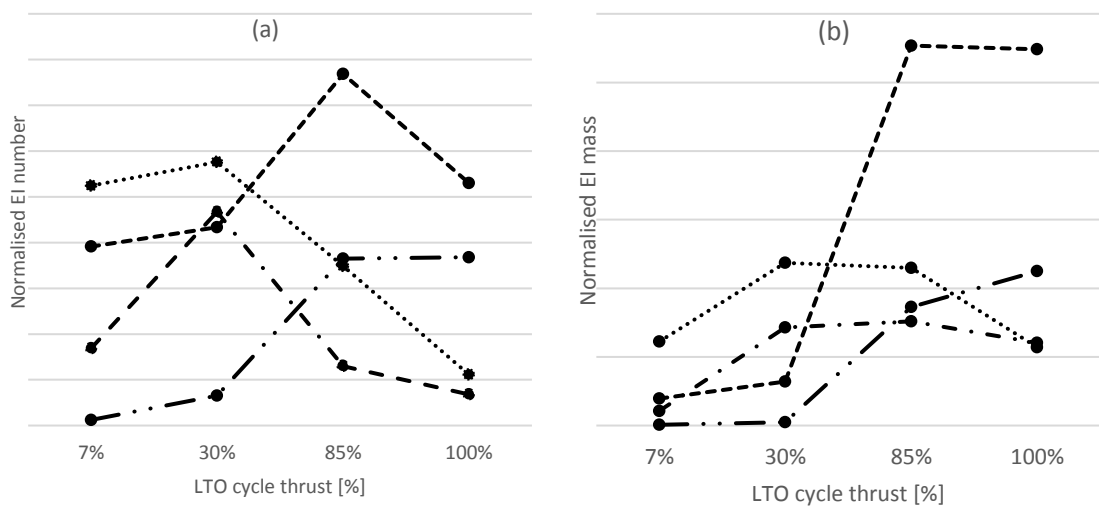


Figure 6-1: Normalised EI_{number} (a) and EI_{mass} (b) of four engine types at thrust settings corresponding to the LTO cycle

As seen in **Figure 6-1**, and in agreement with the literature discussed in section 2.6, it was observed trends between EIs and thrust appear to be dependent on engine technology hence a general correlation cannot be proposed. Similarly, to facilitate comparison of different engines/powers or predict engine exit nvPM concentrations, size-dependent particle losses in the sampling system would also need to be corrected for. This omission can result in significant errors particularly for small nvPM distributions (<20 nm) which are typically witnessed on newer engine technologies and low power conditions. Such correction methodologies are not presented in this chapter but are discussed at length in Chapter 7.

Due to confidentiality issues highlighted by Rolls-Royce, thrust specific conditions generally could not be plotted in this work hence normalised thrusts, N/M (i.e. EI_{number}/EI_{mass}) ratio as defined

by equation (6.1), and GMD correlations are presented in this chapter. The N/M ratio has several advantages: the division of EI_{number} of equation (1.3) with EI_{mass} of equation (1.4) eliminates the uncertainty related to the particle source (i.e. fuel type, CO₂ emissions) and the sampling system (i.e. thermophoretic losses in the collection section) given both nvPM number and mass are measured at the same time and location. Importantly, the N/M ratio is directly linked to emission performance and guided understanding and improvement of the System Loss correction methodology discussed in the next chapter.

$$\frac{EI_{number} \left[\frac{\#}{\text{kg}_{\text{fuel}}} \right]}{EI_{mass} \left[\frac{\text{mg}}{\text{kg}_{\text{fuel}}} \right]} = \frac{nvPM_{num} \times DF_2 \left[\frac{\#}{\text{cm}^3} \right]}{nvPM_{mass} \left[\frac{\mu\text{g}}{\text{m}^3} \right]} \times 10^9 = \frac{N_{APC}}{M_{(MSS \text{ or } LIJ)}} \times 10^9 \left[\frac{\#}{\text{mg}} \right] \quad (6.1)$$

To allow comparison of this commercially sensitive data with the literature, the trends of N/M ratio, GMD and GSD for the four engine types tested are plotted against normalised thrust in **Figure 6-2**. It is witnessed in **Figure 6-2 (a)** that for all engine types, the N/M ratio decreased with increasing thrust. It was found that the best fit was achieved using an exponential fit resulting in R² values >95%, however it is observed that the four engines have different exponents again highlighting that nvPM trends appear to be technology specific as shown in **Figure 6-1**.

As seen in **Figure 6-2 (b&c)** respectively GMD and GSD increase with increasing thrust with secondary order polynomial best fitting the data (R²>0.96). By analysing **Figure 6-2 (a-c)** together, it is apparent that as thrust increases, particles become larger with wider size distributions hence given the decreasing N/M ratio this implies that the particles are generally containing relatively more mass per particle rather than becoming more numerous as engine power increases.

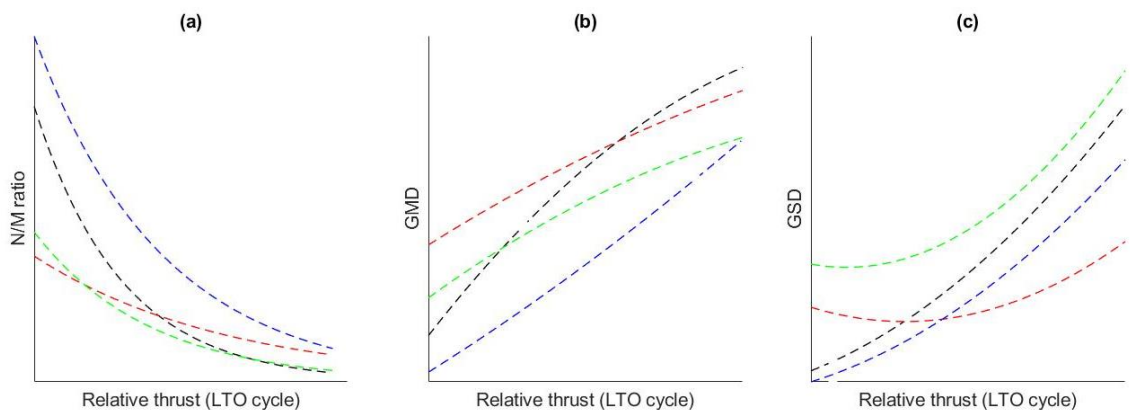


Figure 6-2: Relationship between relative thrust and N/M ratio (a), GMD (b) and GSD (c) over an LTO cycle (7%, 30%, 85% and 100% F_{00}) for four aircraft engines during certification tests

The increasing trends observed in **Figure 6-2 (b)&(c)** indicate that smaller particles are emitted at lower thrust in agreement with previous observations [9], [9], [20], [61], [63], [92]. A hypothesis suggested by Durdina et al. [63], and discussed by Liati et al.[178] and Delhaye et al. [61]

cites that as thrust increases the global AFR decreases with reduced residence time resulting in larger primary particle sizes and reduced oxidation of the agglomerated soot.

6.1.2 nvPM Size Measurements

In addition to the regulatory prescribed measurement of nvPM number and mass, a size measurement was conducted using a DMS-500 (described in section 3.1.3) near the nvPM instruments to aid with understanding sampling system loss and health impact.

Size parameters such as distribution shape (lognormality), GMD, and GSD are investigated with correlations derived to understand engine specific trends. Analysis of volume-weighted size distributions were undertaken to aid with determination of particle density and lognormal assumption as discussed later in Sections 6.1.3.

6.1.2.1 Measured Size distributions

Typical particle size distributions (PSD) measured using a DMS-500 with the monomodal aggregate inversion matrix (section 3.1.3) are presented in **Figure 6-3** for the four engine types, with the size is presented in logarithmic space. The plotted distributions were normalised to individual engine maximum concentrations, for proprietary reasons, hence relative concentrations cannot be compared across engine types. It is observed that the highest number concentration wasn't necessarily observed at the highest thrust which as discussed previously is engine technology dependent (section 6.1.1). For all engines, the highest power condition displays the largest GMD for reasons discussed previously with **Figure 6-2**.

Numerous references [9], [21], [61], [63] conclude that size distributions measured from aircraft engines are lognormal and generally, this is generally observed in **Figure 6-3**. However, on closer investigation it is apparent that some of the distributions appear to display potential bimodality and deviation from lognormality at both tails. In this dataset it appears the distributions are most symmetrical on the log scale (i.e. lognormal) at the highest measured number concentrations observed at medium power, with the PSDs appearing wider and flatter at higher powers, which may be symptomatic of a secondary peak which is too close to the primary peak to be resolved by the DMS-500. At the lowest GMDs (and power conditions), the observed PSDs become more asymmetrical with the left tail skewing horizontally and the right tail skewing vertically (see skewing definition with **Figure 6-7**). This trend may be explained by the size dependent system losses discussed in section 2.3, which result in higher particle losses at smaller sizes, rendering the PSD more asymmetrical the further through the sampling system the nvPM travels.

Although the data presented in **Figure 6-3** is normalised, the reported GMDs ranged from 19-53 nm with associated GSD ranging from 1.64-2.08. This concurs with findings from the literature

with reported GMDs varying from 7-60 nm and GSD varying from 1.3 to 2.3 reported by Kinsey et al. [92], Durdina et al. [63], Lobo et al. [51][9], Boies et al. [20], and Delhaye et al. [61]. The wider range of GMD and GSD found in the literature can be explained by the variation of aircraft engines type, sizing instruments and sampling systems.

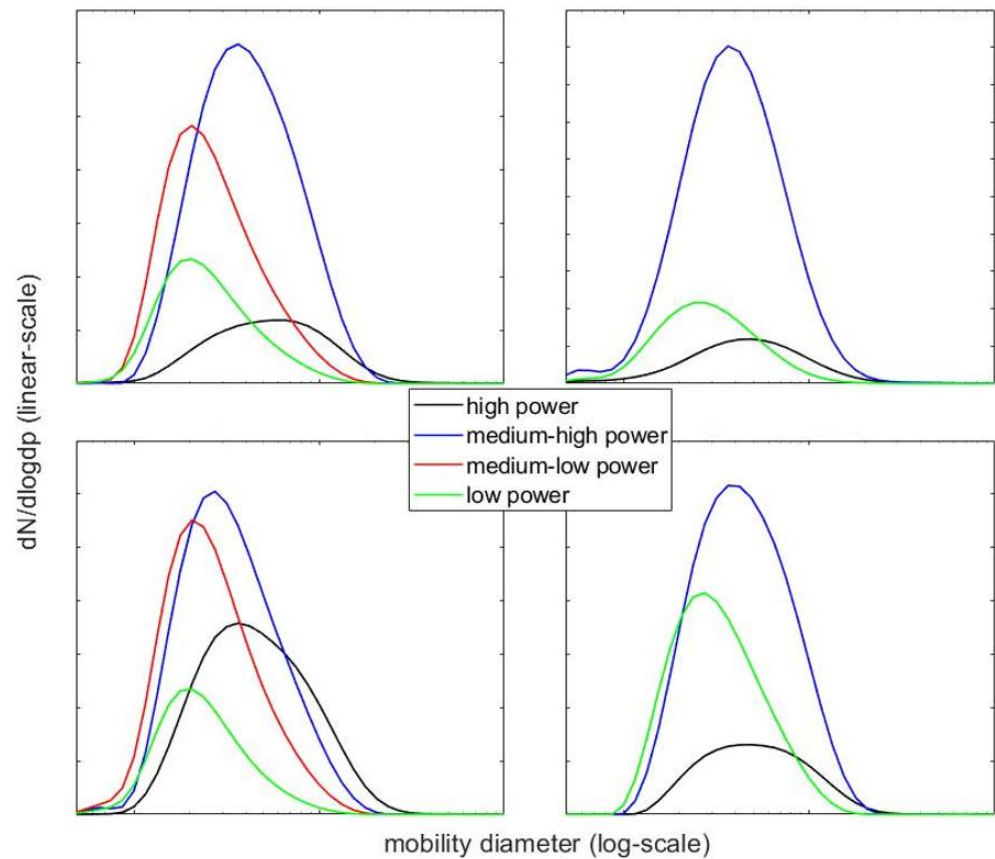


Figure 6-3: Normalised Log-Linear Particle Size Distributions of four engines types at various engine power conditions

6.1.2.2 Engine GMD and GSD nvPM Correlations

To facilitate an understanding of correlation between the regulatory prescribed number and mass and measured size, GMD (Geometric Mean Diameter) and GSD (Geometric Standard Deviation) are presented against N/M ratio in **Figure 6-4**. It is clearly observed that for the four engine types, both GMD and GSD decrease with the N/M ratio. This is as expected in agreement with **Figure 6-2** given the N/M ratio generally decreases with increasing thrust.

As seen in **Figure 6-4 (a)**, the GSD appears to correlate well with N/M ratio independent of engine type, and the scatter around an average power law trendline derived from all data is <5% (average scatter 1.3%). It is observed that at higher N/M ratios the measured GSD are typically between 1.7 and 1.9 however at lower N/M ratios (higher power conditions) this can rise to over 2.08. **Figure 6-4 (b)**, similarly displays a decreasing GMD power law trend with increasing N/M ratio. For a given N/M ratio, it is observed that the GMD can vary by up to 17.8% (average scatter 5.7%)

from the average value for the different engine types. The larger scatter from the trendline which is specific to individual engine types may be attributed to distinct particle effective density produced by different engine technologies (section 2.2) as the N/M ratio relates to size via density (equation (2.6)).

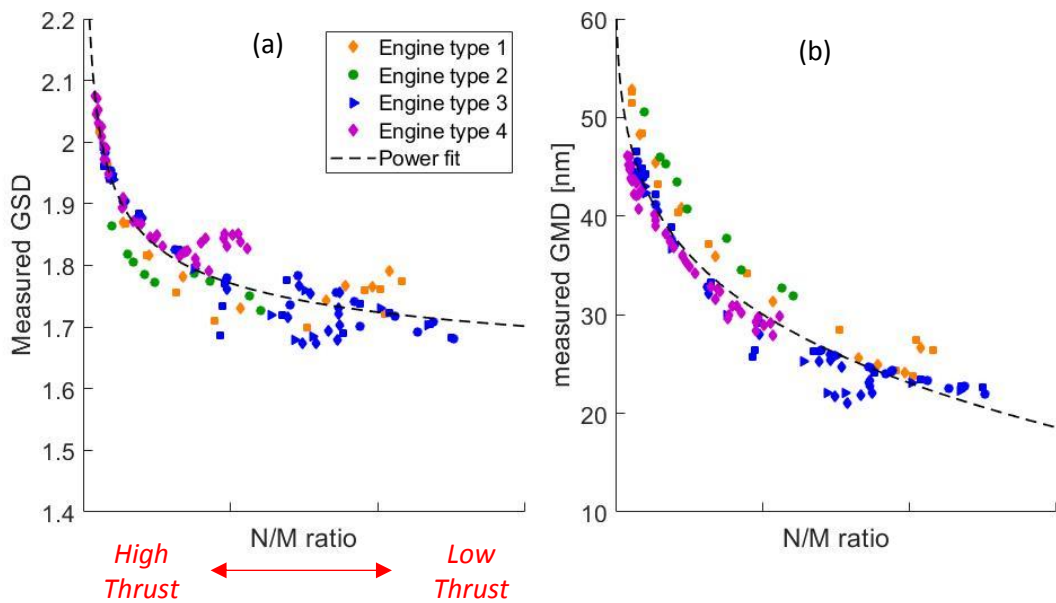


Figure 6-4: GSD (a) and GMD (b) measured by a DMS 500 on various engine types against N/M ratio with power fit

It should be noted that engine type 4 data is further scrutinised later in section 6.2.1.2, with regards to potential volatile PM presence, as such the data presented for Engine type 4 in Figure 6-4 may over predict the GSD and underpredict the GMD, which if were corrected would potentially improve the correlation.

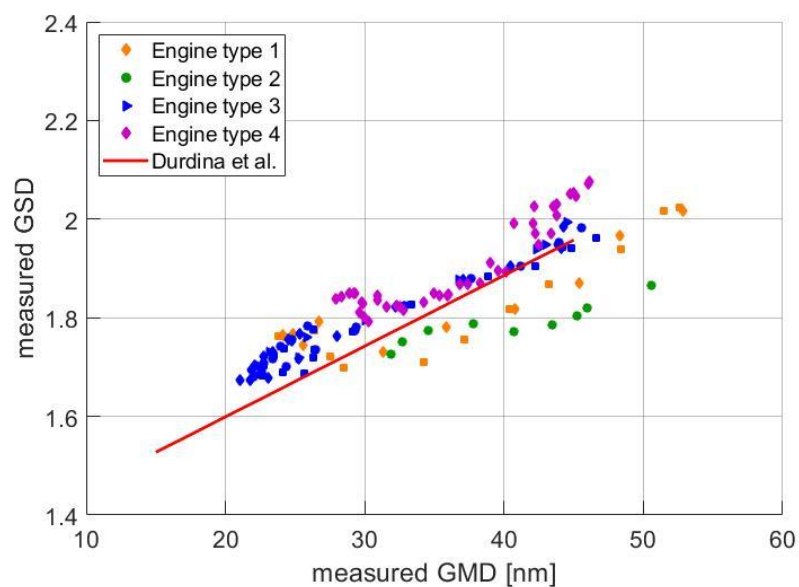


Figure 6-5: measured GMD against measured GSD on various engine types

For comparison to the limited published literature of large scale engines using ICAO certified sampling and measurement techniques, GMD was plotted against GSD and compared with the work of Durdina et al. [63]. As can be observed in **Figure 6-5** there is general agreement in correlation between GMD and GSD for the four Rolls-Royce engines and the fit proposed from a commercial turbofan engine CFM56-7B26/3. Both datasets display increased GSD at increasing GMD.

6.1.2.3 Bimodality of volume distributions

Generally, aerosol size distributions are measured and represented as number weighted. However, to derive mass and density and to assess lognormality as discussed later in sections **6.1.2.4**, **6.1.3** and **7.2**, it is necessary to represent them in terms of volume. Significant portions of the mass are held in the largest size bins of the distribution, hence small increases in number in these bins can lead to significant increases in derived volume. To assess this impact the y-axis ($dN/d\log d_p$) of number weighted, size distributions measured by the DMS-500 during engine testing were plotted in logarithmic space. As can be seen in representing the distribution as a log-log plot a small secondary peak is sometimes witnessed at $d_m > 200$ nm near the instrument's limit of detection as shown in an example given by **Figure 6-6**. It is presumed that the secondary peak is not a product of combustion and must be disregarded when estimating aircraft nvPM properties.

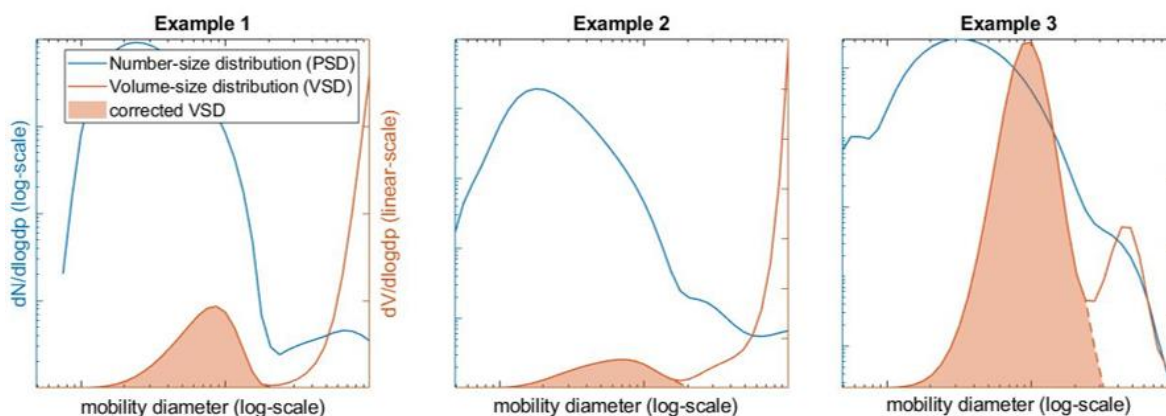


Figure 6-6: Examples of PSDs displaying a secondary peak measured by a DMS-500 and converted VSDs with and without the tail-cutting method

While the secondary peak is orders of magnitude smaller than the main nvPM peak, it negligibly impacts the GMD and GSD of number-weighted distributions. However, it can significantly distort the derived volume-size distributions because volume is proportional to d_p^3 , as displayed by the orange distributions in **Figure 6-6**.

To obtain a volume representative of aircraft nvPM emissions from the number-weighted distribution measured by the DMS-500, it was necessary to develop a method which will subsequently be referred to as ‘tail-cutting’. Tail-cutting consists in finding the locations of the

primary peak and the minima (to the right-hand side of the peak) of the nvPM volume-weighted distribution, calculating the slope between them, and re-building the right tail of the nvPM distribution. This technique cuts-out artefacts at the largest size of the spectrum while preserving the shape of the main peak as demonstrated most clearly by the dashed line in **Figure 6-6 (Example 3)**. This methodology was chosen as it permitted both lognormal and non-lognormal distributions to be assumed after the secondary tail was cut.

6.1.2.4 Lognormality of Measured Size Distribution

Aircraft engine and other combustion exhaust PM size distributions are generally assumed lognormal based on various observations and because of its mathematical advantages [60]. Kinsey et al. [92], Lobo et al. [51] and Delhaye et al. [61] all observed engine exhaust PM distribution typically monomodal and lognormal, as was the case for many of the distributions measured in this study (**Figure 6-3**). However, as discussed previously deviations from lognormality were observed at particular thrusts on different engine types.

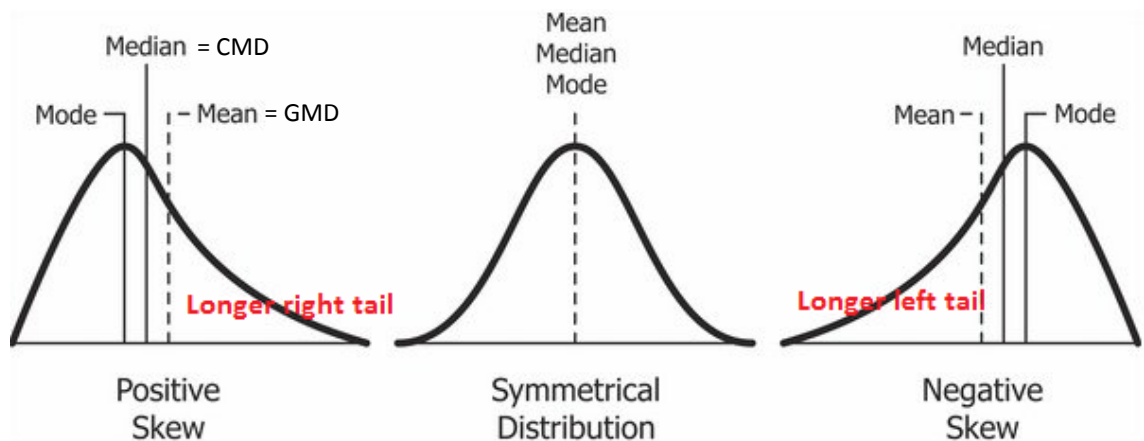


Figure 6-7: Mode, Mean and Median in lognormal and skewed distributions [60]

Lognormality can be assessed by comparing a size distribution's GMD (i.e. mean) and CMD (i.e. median) which are identical when a distribution is lognormal as previously defined in section 2.1 but differ when a distribution is skewed, as illustrated in **Figure 6-7**. If a near-log-normal distribution has a longer right tail or a shorter left tail, $CMD < GMD$. Oppositely, $CMD > GMD$ is observed if a distribution has a longer left tail or shorter right tail.

Deviation from lognormality can also be assessed by comparing the GSD of the number-size distribution (i.e. PSD) and the GSD of volume-size distribution (i.e. VSD) which are equal in lognormal distributions [60]. Since VSDs are proportional to d_p^3 , the difference between the GSD of the PSD and the GSD of the VSD will mostly indicate how the right section of the distribution behaves. If $GSD_{VSD} > GSD_{PSD}$, the distribution has a longer right tail and if $GSD_{VSD} < GSD_{PSD}$, the distribution

has a shorter right tail. **Table 6-1** summarises how differences between CMD, GMD and GSDs can modify near-lognormal distributions.

Table 6-1: Summary of the potential combinations to assess lognormality

Difference in GSDs	Distribution skew	Difference in diameters	Distribution skew	Comments on distribution skew
(1) $GSD_{VSD} > GSD_{PSD}$	Right + (or Left ---)	$GMD > CMD$	Right + or Left -	Longer right tail (and/or shorter left tail)
(2) $GSD_{VSD} > GSD_{PSD}$	Right + (or Left ---)	$GMD < CMD$	Right - or Left +	Longer right and left tails (and/or shorter left and right tails)
(3) $GSD_{VSD} < GSD_{PSD}$	Right - (or Left +++)	$GMD < CMD$	Right - or Left +	Shorter right tail (and/or longer left tail)
(4) $GSD_{VSD} < GSD_{PSD}$	Right - (or Left +++)	$GMD > CMD$	Right + or Left -	shorter right and left tails (and/or larger left and right tails)

The lognormality of PSDs from the four aircraft engine types discussed in this chapter was investigated by comparing the CMD with the GMD and the volume-size distribution GSD with the number-size distribution GSD as described above. Given the bimodality of VSDs, the size distributions were corrected with the tail-cutting method as discussed in section 6.1.2.3 with results of the lognormality assessment displayed in **Figure 6-8**.

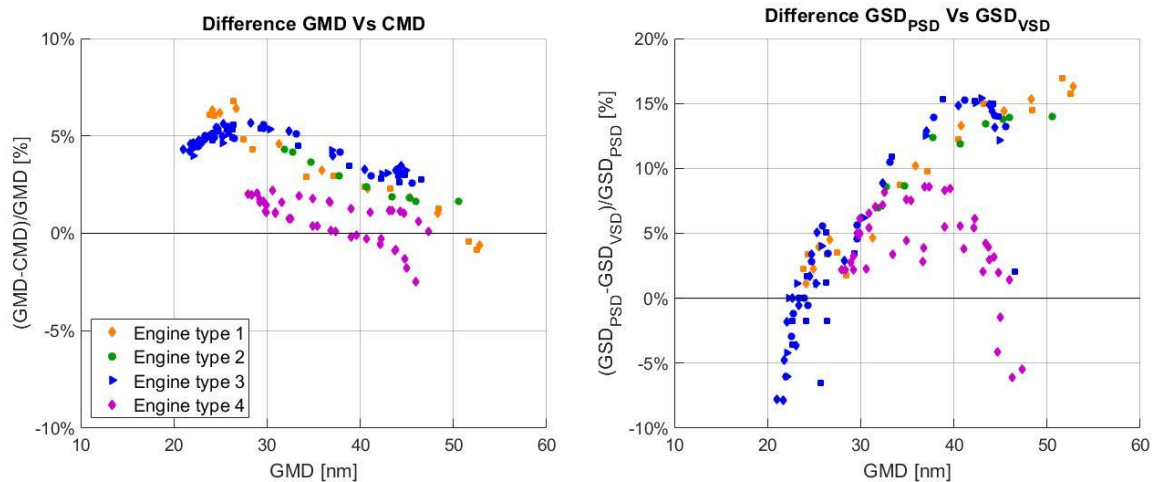


Figure 6-8: Lognormality assessment at instrument by means of comparing GMD and CMD (a) and GSD_{PSD} and GSD_{VSD} (b)

It is observed most of the number weighted size distributions are not lognormal as $GMD \neq CMD$ and $GSD_{VSD} \neq GSD_{PSD}$. In **Figure 6-8 (a)**, the GMD is generally larger than the CMD by up to 6% and the difference decreases with increasing GMD for all engine types. In **Figure 6-8 (b)**, GSD_{PSD} is generally larger than GSD_{VSD} except when the GMD is <25 nm, with deviation from lognormality typically increasing with GMD except for the case of engine type 4. The different behaviour displayed by engine type 4 at $GMD > 30$ nm is a result of the tail-cutting method used to correct the VSD which

in this case enlarged the width of the distribution as shown in **Figure 6-9**, which is symptomatic of the primary and secondary peaks being too close.

When discussing trends from **Figure 6-8 (a)&(b)** together, it is observed that small GMDs, which as discussed are typically witnessed at low engine powers, correspond to scenario (1) of **Table 6-1**. Scenario (1) indicate that size distributions have a smaller left tail, which could be explained by loss preferentially affecting the smaller particles in a compliant sampling system. At larger GMDs hence high engine powers, results are better represented by scenario (4) of **Table 6-1** showing that size distributions have a shorter right tail at high power conditions, which could originate from the highly fractal nature of soot at larger sizes.

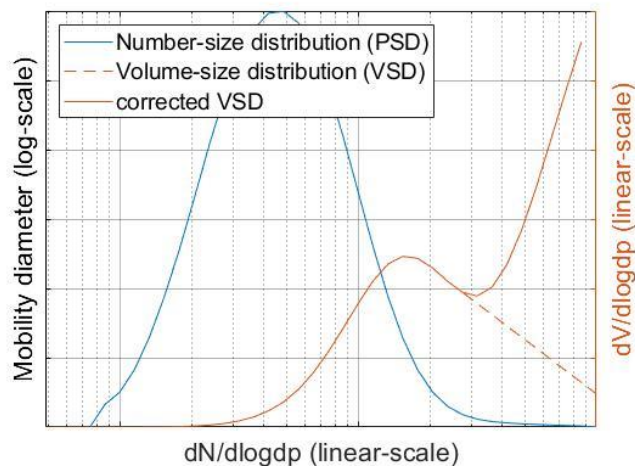


Figure 6-9: Example of the conversion from a PSD to a VSD with the tail-cutting method and its limits

6.1.3 Average particle effective density

Particle effective density is an important property giving insights to particle morphology and composition and allows mass predictions from size distributions. Particle effective density has many definitions and can be measured and calculated in various ways as previously discussed in section **2.2**. The singular effective density that could be derived from nvPM measurements on the four engines types discussed here is the average particle effective density ρ_{eff}^1 . It uses the mass concentration measured by the MSS and total volume derived from the measured DMS size distribution. It should be noted that particle effective densities were estimated from corrected mass and size data at the 1st common point of the sampling system as discussed later in section **6.1.3**. to account for differing PM loss. Average effective densities were calculated then plotted against N/M ratio and GMD facilitating comparison to the literature.

6.1.3.1 Effective density calculation methods

Because of the bimodality of volume distribution discussed above in section 6.1.2.3, three methodologies illustrated in Figure 6-10 were investigated to calculate an average effective density ρ_{eff}^1 namely:

- $\rho_{eff(1)}^1 = \frac{M_{MSS}}{V_{DMS}}$ where volume is derived from the original PSD at the 1st common point (section 6.1.3).
- $\rho_{eff(2)}^1 = \frac{M_{MSS}}{V_{DMS_{tail-cutting}}}$ where volume V_{DMS} is corrected using tail-cutting (section 6.1.2.3).
- $\rho_{eff(3)}^1 = \frac{M_{MSS}}{V_{DMS_{log(tail-cutting)}}$ where volume is corrected applying lognormal fit to ‘tail-cutting’ corrected V_{DMS} .

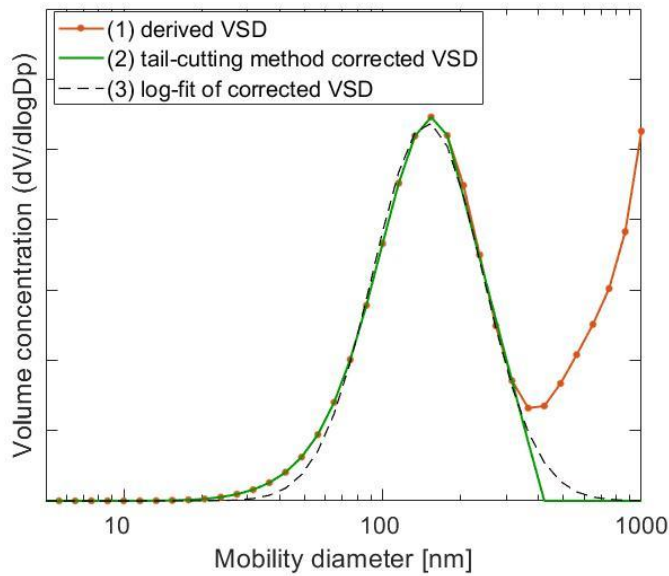


Figure 6-10: Example of a derived Volume Size Distribution (VSD) corrected with method (1), (2) and (3)

Out of the three method, the average effective density $\rho_{eff(3)}^1$ was considered the most adequate for effective density calculation and was used for the rest of this study. Although it was previously shown that deviations from lognormality occurred for the number-weighted distributions (Figure 6-8), method (3) was chosen as it removes the interfering secondary peaks and uses a lognormal fit which best fitted the data in this specific study and is mathematically more advantageous to evaluate [60].

The difference between $\rho_{eff(1)}^1$, $\rho_{eff(2)}^1$ and $\rho_{eff(3)}^1$ is featured in Figure 6-11. Difference of up to 75% are seen between method (1) and (3) as seen in Figure 6-11 (a), highlighting the importance of correcting VSDs with the tail-cutting method. The largest difference occurs at low volumes

corresponding to mass concentrations below the Limit Of Quantification (LOQ) as defined in section 6.2.2.2 highlighted by unfilled data points in **Figure 6-11**. Durdina et al. [63] similarly found that secondary peaks measured by sizing instruments significantly impacted the average effective density, stating this to be 50% at low mass conditions. Overall, the largest difference is observed with engine type 4 can be explained by wider measured size distributions (i.e. larger GSD) as seen in **Figure 6-4** coupled with higher concentrations witnessed in the secondary peak (i.e. $\sim 1 \times 10^4$ vs. $\sim 1 - 5 \times 10^3$ particles/cm³ for engines 1-3).

As shown in **Figure 6-11 (b)**, method (2) could also have been used and the difference between the effective density calculated from method (2) and (3) was always <3%. In the rest of this study, $\rho_{\text{eff}(3)}^1$ is simply referred as the measurement derived effective density ρ_{eff}^1 .

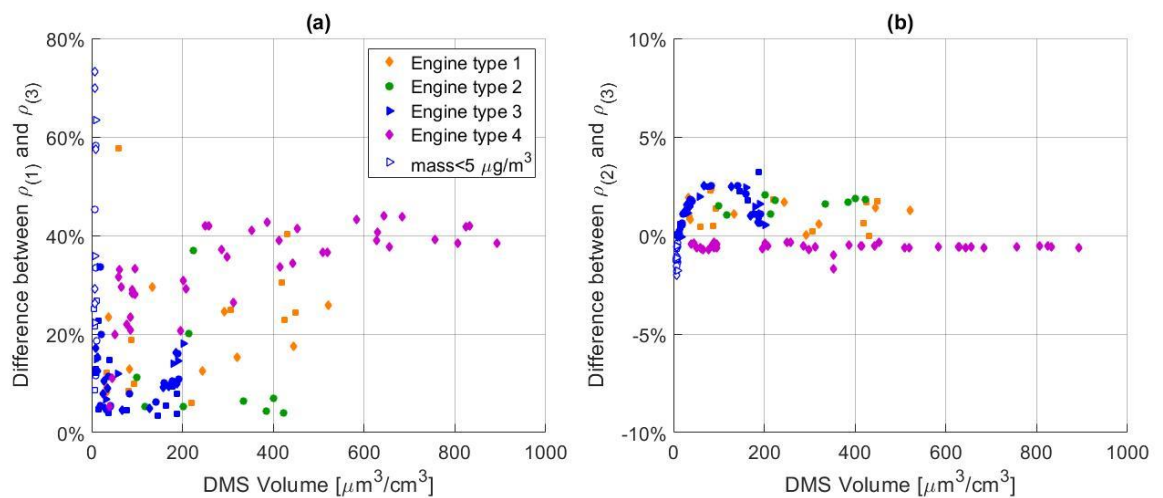


Figure 6-11: Difference between effective densities calculated with method (1) and (3) (a) and method (2) and (3) (b) for different engine types plotted against the volume derived from the DMS size distribution at the 1st common

Given that mass concentrations and size distributions were measured by different instruments sampling at different flows at slightly different locations, both measurements were first corrected to the 1st common point of the sampling system. This was achieved using the methods listed below:

- **Loss correction to the 1st common point:** Size distributions were corrected to the 1st common point by applying loss functions between the DMS-500 and the 1st common point using the UTRC particle transport model. The MSS mass was corrected by estimating the mass correction factor $k_{SL_{\text{mass}}}$ using the System Loss Tool (SLT) using the corrected DMS GMD and GSD as inputs. Because of the short sampling length between the mass instrument and the 1st common point, losses were small and mostly diffusional, impacting the smaller particles only (where little of the mass resides). Indeed, the $k_{SL_{\text{mass}}}$ varied between 1.006 and 1.022 (i.e. 0.6% to 2.2% correction) for the entire data set.

- **Converging solution for effective density calculation:** Both the UTRC model and the SLT used for loss correction to the 1st common point require a particle effective density input which is generally assumed at 1 g/cm³ for aircraft PM [14], [63]. It was found that varying the effective density input from 0.4 g/cm³ to 1.6 g/cm³ changed the estimated average density presented in this section by up to 9%. This variation was attributed to small changes in the penetration efficiencies calculated by the UTRC model at larger sizes which caused the corrected VSD to fluctuate. To minimise the effect of assumed density in the calculation of the average effective density, initial calculations were performed with the assumption $\rho_p=1$ g/cm³ and the calculations were repeated with the newly estimated average particle effective density until the input and predicted densities converged.
- **Number concentration (DMS Vs APC):** The average effective densities were estimated using the size distribution from the DMS-500 which measured total PM as later discussed in section 6.2.1. It is possible to use the nvPM APC number concentration instead to predict the average density. A comparison between effective densities predicted by the DMS and the APC was made by applying a correction factor N_{APC}/N_{DMS} to every size bins of the size distribution. It was found that the average nvPM effective density using the APC number compared with the total PM DMS-500 density agreed within the uncertainty of the DMS number measurement of 20% [113], except for engine type 4 where the nvPM density was significantly higher than the total PM density caused by the potential volatile contamination discussed in section 6.2.1 increasing the estimated volume, hence reducing the density.

Assuming that the total volume uncertainty is equivalent to the total number uncertainty of $\pm 20\%$ for the DMS [113] and that the mass measurement uncertainty is $\pm 19.5\%$ as discussed in section 3.1.1.2, the propagated uncertainty for the average effective density was estimated at 27.9% ($\sqrt{19.5\%^2 + 20\%^2}$).

6.1.3.2 Result average effective density

The particle average effective density $\rho_{\text{eff}}^1(\text{avg})$ as defined in section 2.2 is presented in **Figure 6-12** for the four engine types against the N/M ratio and the GMD. As discussed above, $\rho_{\text{eff}}^1(\text{avg})$ densities were calculated from the MSS mass concentration and the corrected DMS total volume. The calculated average particle effective density varied from $\sim 0.3\text{-}0.8$ g/cm³ for the entire dataset, except for data points with a measured mass concentration below the LOQ (i.e. $< 5\mu\text{g}/\text{m}^3$ as discussed in section 6.2.2) represented by unfilled data points, where the estimated density reached values up to 1.05 g/cm³. When disregarding the low mass concentration data, the average effective density is 0.56 ± 0.11 g/cm³. Timko et al. [21] quoted comparable average effective densities from a

PW308 engine between 0.4 and 0.82 g/cm³ for a range of fuels, using a MAAP to measure mass and an SMPS to measure the total volume.

It can be seen in **Figure 6-12** that the average effective densities decrease with increasing N/M ratio and increase with increasing GMD for all engine types. This behaviour may be explained by larger primary particle diameters at higher engine power, hence lower N/M ratios and larger GMDs (**Figure 6-2**), causing the effective particle density to increase towards the density of solid carbon, as discussed by Durdina et al. [63], Liati et al. [178] and Delhaye et al. [61]. In contrast, Durdina et al. [63] also observed slightly decreasing average effective densities with increasing engine power and GMD due to lower size-dependent effective densities at larger mobility diameters (**Figure 2-4**).

The scatter observed between different engine types in **Figure 6-12** and observations from the literature (presented in detail in section 2.2) indicate that particle effective density is dependent on engine technology, engine power and fuel type. Indeed, Beyersdorf et al. [68] measured higher average effective densities from a CFM56 engine ranging between 0.9 and 1.6 g/cm³, and averaging at 1.1 g/cm³. Durdina et al. [63], Lobo et al. [51] and Boies et al. [20] represented average effective density defined as $\rho_{\text{eff}}^2(\text{avg})$ comparable to ρ_{eff}^1 and discussed in section 2.2. They respectively measured average effective densities from CFM56 engines of 0.9 and 1.1 g/cm³, 0.85 g/cm³ and 0.72 and 0.9 g/cm³.

Again it should be noted that engine type 4 data is further scrutinised later in section 6.2.1.2, with regards to potential volatile PM presence, as such the data presented for Engine type 4 in **Figure 6-12** may under predict the average effective density. For engine 4, the density increased 0.15 g/cm³ on average when deriving the volume from the volatile stripped APC Number concentration instead of the DMS total PM which was not observed for engines 1-3.

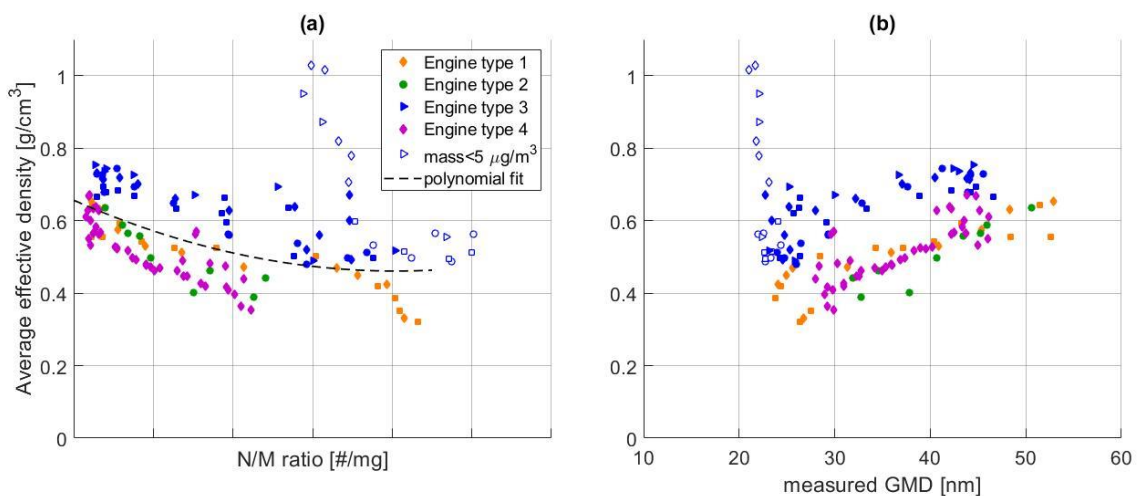


Figure 6-12: Average effective density ($\rho_{\text{eff}}^1(\text{avg})$) calculated for various engine types plotted against N/M ratio (a) and GMD (b)

6.2 Uncertainties associated with nvPM sampling & measurement

For aircraft engine nvPM certification level emission measurements, the acquisition, transport and analysis of exhaust by the sampling and measurement system must comply to specific requirements defined in Appendix 7 of ICAO Annex 16 Volume II [14]. While ICAO guidelines were designed to minimise and standardise loss, significant uncertainties are still witnessed from nvPM sampling and measurement. Lobo et al. [51] estimated the measurement uncertainty of nvPM number- and mass-based emissions indices to be ~25%, considering systematic and random errors of 10% for the number and mass instruments along with uncertainties associated with temperature, pressure, CO₂ concentration, and dilution factor measurements. In this section, uncertainties associated with nvPM sampling and measurement of the EASA nvPM reference system are analysed and discussed.

6.2.1 Number measurement uncertainty

The AVL Particle Counter (APC) as introduced and described in section 3.1.1.1, consists of a VPR to condition the aerosol (cool, dilute, removes volatiles) and a CPC to measure the concentration of resultant nvPM. As such in this section, the uncertainty associated with both the CPC and VPR calibration and drift are analysed, with concentrations compared to that derived from the Combustion DMS-500 size instrument. It is noted that other variants of compliant number nvPM measurement units such as the DEKATI DEED combined with a CPC can be used producing different uncertainties than the APC discussed below.

6.2.1.1 Regulatory nvPM number calibration uncertainty

To improve the understanding of uncertainties associated with nvPM number measurement, the counting efficiencies of the number measuring instrument of both the European (EASA) and Swiss (EMPA) nvPM Reference systems, which both utilise an AVL APC compliant nvPM number counters, were assessed. Data from the annually prescribed ‘traceable’ calibrations performed by AVL in compliance with ICAO regulation (section 3.1.1.1), national laboratories and in-house measurements performed between 2012 and 2018 are analysed.

CPC uncertainties:

The counting efficiencies of both EASA’s and EMPA’s CPCs which each have similar d_{50} and D_{90} cut-offs at 10 nm and 15 nm respectively are presented below in **Figure 6-13 (a)**. As can be seen generally both units meet the minimum penetration fraction as prescribed by ICAO [14] listed in **Table 3-1** and represented by dashed red lines. However, it is observed that there can be significant scatter year to year. At 10 nm, the combined twelve data points have a standard deviation of 8.2%,

however the standard deviation of the EASA CPC was only 2.8%. At 15 nm, the standard deviation of the combined data was 2.3%. The different scatter for each instrument represented by standard deviations and the d_{50} and d_{90} yearly variation indicate that nvPM number uncertainty may be instrument and calibration specific. Nevertheless, the variation from yearly calibration and from different CPC units remains below the specified $\pm 10\%$ counting accuracy required by both the civil aviation [14] and vehicle PMP [106] regulation. It is observed that one EASA CPC calibration point performed at the National Physical Laboratory (NPL), represented by unfilled data points, didn't meet the minimum required counting efficiency of 90%. However, on investigation NPL stated a measurement uncertainty of 7% for the 88% counting efficiency measurement hence they determined the unit passed the compliance check.

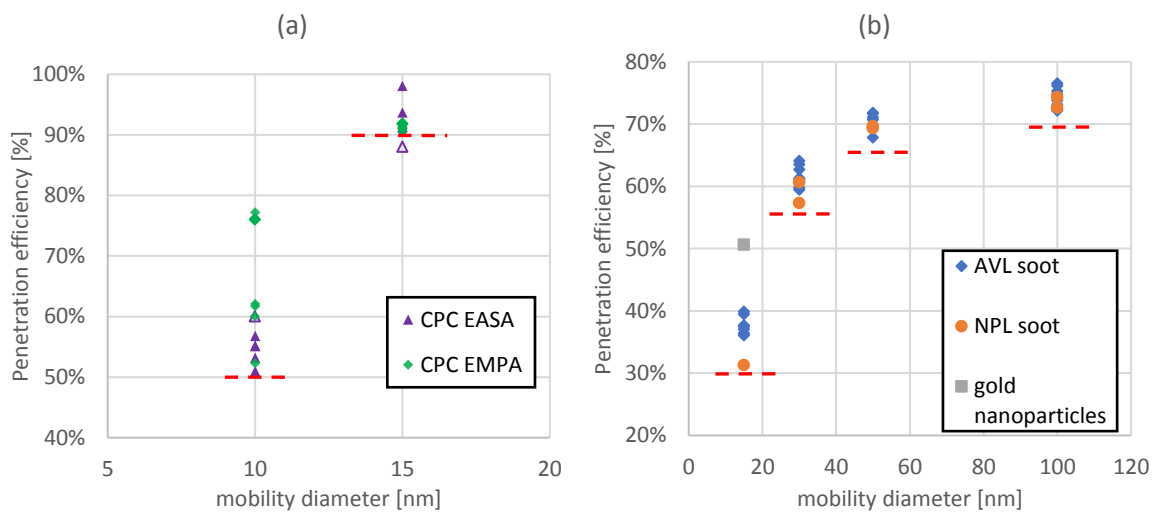


Figure 6-13: Penetration efficiencies of CPC (a) and VPR (b) from yearly calibration and laboratory experiments with dashed red line representing minimum regulatory requirements

Detailed studies have disclosed that CPCs can be calibrated to levels much more precise than the $\pm 10\%$ estimate [106]. For example, Owen et al. [179] reported the relative expanded uncertainty of a CPC to be 2.8% over the range of about 1 to 10^4 particles/cm³ with emery oil, and Mamakos et al. [101] reproduced the manufacturer's certified values of a CPC to within 4%. Nonetheless, it was also proven in many studies that CPC counting efficiency can vary significantly with the chemical composition [101], [106], [180], [181] and morphology [99], [101] of the aerosol particles measured. Indeed, lower CPC counting efficiencies were observed by Giechaskiel et al. [106] and Mamakos et al. [101] when measuring flame generated soot compared with similar concentrations of emery oil, highlighting that particle representativeness for calibration is essential for accurate measurement using a CPC. This suggests that the uncertainty of CPCs used for aircraft nvPM number measurement could be improved if they are calibrated using a soot source representative of the engine exhaust aerosol rather than the current specification (section 3.1.1.1). The issues associated with aircraft nvPM representative aerosol generational is discussed further in chapter 4 however it has been

shown chemical properties and morphology can vary with combustion technology, fuel type, thrust setting, and sampling location [9], [10].

VPR uncertainties:

The results from VPR calibrations of the EASA and EMPA APCs are similarly presented above in **Figure 6-13 (b)** with each data point representing the calibrated VPR penetration efficiencies at different mobility diameter (15-30-50-100 nm) averaged over the three only dilution settings (PCRF 100-250-500) used during certification testing for the APC. It is observed again that generally all calibration data met the minimum penetration efficiency requirements listed in **Table 3-1** and represented by dashed red lines. As no difference was observed between the EASA and EMPA VPR, the data in **Figure 6-13 (b)** was differentiated by the soot source used. VPR calibration was generally performed by AVL who used their own soot generator (propane diffusion - AVL soot). In contrast NPL calibrations were performed using both a Jing mini-CAST (NPL soot) similar to AVL soot, and nebulised gold nanoparticles. At the four calibrated mobility diameters, the standard deviation from each particle source is <2% at every calibrated mobility diameters, indicating that losses in the VPR remain fairly constant over time and that they can be well characterised for a particular particle material/morphology. Giechaskiel et al. [94] measured a calibration repeatability of $\pm 6\%$ for an AVL APC in agreement with this analysis. PMP (Particle Measurement Programme) compliant VPR calibrations which do not include penetration calibration at 15 nm were shown to have differences of $\pm 15\%$ [182].

When comparing different particle materials used for calibration, the variation in penetration efficiency at 15 nm is the largest, with the gold particle penetration efficiency almost double that witnessed with mini-CAST soot. A higher penetration efficiency was also observed during in-house measurements for both NaCl and SiO₂ nebulised nanoparticles when comparing with PALAS graphite during the EASA VPR loss experiment in this thesis, as seen previously in **Figure 5-20**.

Another compliance check prescribed by ICAO is volatile removal efficiency. Giechaskiel et al. [95], Mamakos et al. [101] and Crayford et al. [47] tested the efficiency of VPRs at removing the volatile phase and showed that both evaporation tube and catalytic stripper based VPRs were incapable of removing all coated volatiles, suggesting a thin volatile coating remained post VPR however it was discussed that VPRs generally shrink particles to sizes smaller than the prescribed measured d_{50} . The volatile removal efficiency can be increased with the VPR temperature but this would lead to higher thermophoretic losses affecting all particles [50]. Hence, it can be concluded that VPRs induce large uncertainties for nvPM number measurement through high diffusional and thermophoretic losses, particle dependent calibration, and to a lesser extent unverified efficiency volatile removal.

Total Uncertainty associated with nvPM number measurement:

As discussed in section 3.1.1.1, current ICAO regulation only requires during annual calibration the VPR and CPC to meet a certain penetration efficiency threshold at different mobility diameters and particle loss in compliant nvPM number instruments are not accounted-for in EI estimations (section 1.5.1.2). It was shown that calibrated penetration efficiencies of VPRs and CPCs could be well above the compliance set-point and could be an added uncertainty to number EIs estimation. To quantify this uncertainty, the difference in calibrated particle losses occurring in an APC were estimated at different sizes using the largest and smallest penetration efficiencies from soot calibration for the VPR (NPL and AVL combined) and from CPC calibration of the EMPA and EASA APC between 2012 and 2018 as listed in **Table 6-2**. It is noted that to estimate CPC/VPR penetration efficiencies at non-calibrated sizes, a function determined from the calibration factors was used as defined in ICAO Annex 16 (section 3.1.1.1).

Table 6-2: Minimum and maximum penetration efficiency reported during the calibration of the EASA and EMPA APCs between 2012 and 2018, and resulting difference in total number concentration at 10, 20 and 40 nm

	10 nm	20 nm	40 nm
Minimum penetration efficiency (combined)	CPC: 51% VPR: 12.7% (6.5%)	CPC: 97.1% VPR: 43.7% (42.4%)	CPC: 100% VPR: 63.2% (63.2%)
Maximum penetration efficiency (combined)	CPC: 77.2% VPR: 20.8% (16.1%)	CPC: 99.8% VPR: 51.4% (51.3%)	CPC: 100% VPR: 68.4% (68.4%)
Difference between Min and Max penetration efficiency [%]	$\left(1 - \frac{6.5\%}{16.1\%}\right) =$ 59.7%	$\left(1 - \frac{42.4\%}{51.3\%}\right) =$ 17.3%	$\left(1 - \frac{63.2\%}{68.4\%}\right) =$ 7.6%

Results from this uncertainty analysis presented in **Table 6-2** show that a compliant nvPM number instrument like the AVL APC could record different number concentrations of up to 60% at 10 nm, 17% at 20 nm and 8% at 40 nm on the same gas turbine exhaust aerosol from the different calibration factors used. This indicates typical VPR and CPC variation from yearly calibration may result in significant added uncertainty of number EIs, as currently reported (not corrected for loss other than thermophoresis in the collection section) and discussed in section 1.5.1.2. Also, the uncertainty associated with the particle type used for calibration is not currently standardised by ICAO and would need to be further assessed, especially in the case of the VPR where gold nanoparticles were shown to have almost double the penetration efficiency of soot at 15 nm. To conclude, the current total nvPM number measurement uncertainty is probably well above the

original 14.1% estimated from regulation guidelines (section **3.1.1.1**). However, as the uncertainty associated with two systems measuring the same source may be estimated as $\sqrt{14.1^2 + 14.1^2} = 19.9\%$, the uncertainty estimated during the SAMPLE III SC03 campaign [49] which measured a reproducibility for three compliant systems for nvPM number measurement to be between 18% and 22% was in agreement with the uncertainty derived from the current guidelines. Similarly, intra-laboratory number concentration measurement comparison using compliant PMP (Particle Measurement Programme) VPR and CPCs showed difference representing two standard deviations within $\pm 30\%$ [182].

It is noted that CPC and VPR calibrated penetration efficiencies are used in the determination of nvPM sampling and measurement system loss correction factors as later discussed in chapter 7, and the current regulation requires the reporting of number and mass measurement and sampling uncertainties which include CPC and VPR calibration correction.

6.2.1.2 Comparison of size derived and prescribed number measurements

While not being part of the regulatory EASA nvPM measurement system, the DMS-500 described in section **3.1.3** was used in multiple test campaigns to measure particle size distribution and number concentration.

DMS number measurement has a manufacturer quoted minimum uncertainty of 20% [113], hence is theoretically less accurate than a CPC. In this section an assessment of its applicability to precisely estimate engine exhaust particle number concentration is made. Petzold et al. [12] discussed good correlation between a DMS-500 and a CPC with an overall slope of the linear regression line of 0.93 when measuring particles produced with a gas turbine engine simulator. Boies et al. [20] also found good agreement between number measurements by a DMS-500 and a CPC of similar specifications to those in the EASA system. In this section, the number concentration measured by the DMS and APC are analysed for four engine types. Comparison of the number concentration measured with the APC and the DMS was undertaken, however it is acknowledged that the DMS was not sampling behind a VPR hence was a measure of total PM. Also, as discussed previously the DMS measures from mobility diameters ~ 5 nm compared to the APC d_{50} of 10 nm.

Significantly different losses occur prior to measurement by the APC and DMS, hence the directly measured concentrations can't be compared without correction. Lobo et al. [51] compared aircraft nvPM number measured with a DMS-500 and an APC and found that the DMS-500 measured on average $\sim 45\%$ higher total PM number concentration due to VPR losses inside the APC. To provide a comparison, it was necessary to correct both the DMS and APC measured concentrations at a point in the sampling systems common to both aerosol sampling paths. This was achieved by using the UTRC particle transport model (section **2.4.1**). It is noted that to accurately correct the APC total

number concentration for size-dependent losses, the DMS corrected size distribution was used along with the VPR and CPC penetration functions derived from calibration (section 3.1.1.1).

An example of a measured size distribution and corrected size distribution at the 1st common point in the sampling system for the DMS and CPC is shown in **Figure 6-14**. Also, size-dependent penetration efficiency functions for both the DMS and APC are presented. It is witnessed that the penetration efficiency is significantly lower for the APC because of the significant losses occurring in the VPR and the CPC with values similar to those discussed earlier by Lobo et al. [51] seen at the smaller sizes. Losses for the DMS mostly occur in the 5m heated dilution line, which was employed during engine testing.

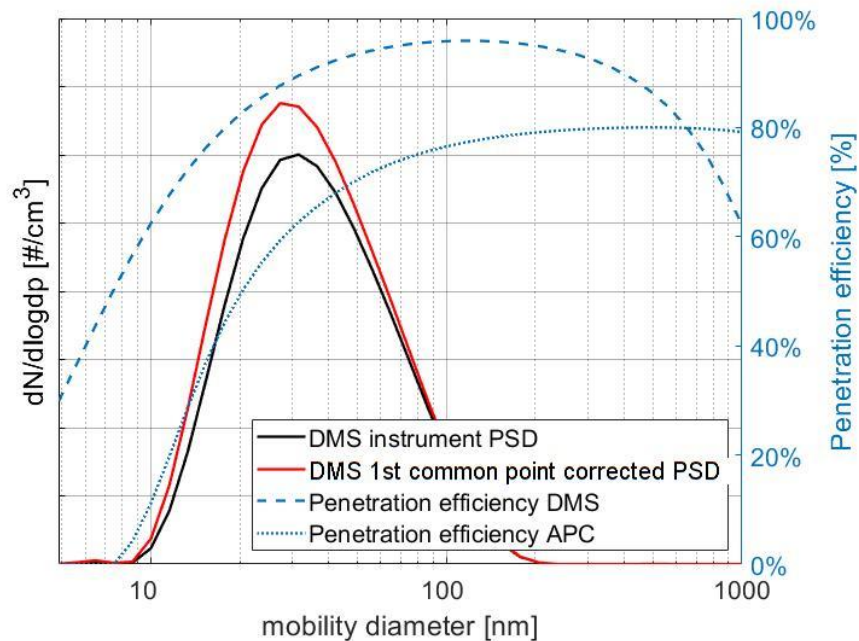


Figure 6-14: Example of a measured and corrected particle size distribution (left axis) and the associated penetration efficiencies for APC and DMS (right axis) to the 1st common point

The comparison between the total number concentration derived from the DMS size distribution (total PM) and the APC measurements (nvPM) for aerosols measured from large scale engines are presented in **Figure 6-15**. Expected uncertainty bands of 24.5% are added around the 1:1 correlation which represent a propagated uncertainty of 14.1% as calculated from ICAO instrument specifications coupled to the DMS quoted number measurement uncertainty of 20% [113] ($\sqrt{14.1\%^2 + 20\%^2} = 24.5\%$). The results show that the corrected total PM (DMS) and nvPM (APC) agree within the defined uncertainty for engines 1-3, with the APC generally predicting a slightly higher number concentration than the DMS highlighted by the points being above the 1:1 correlation.

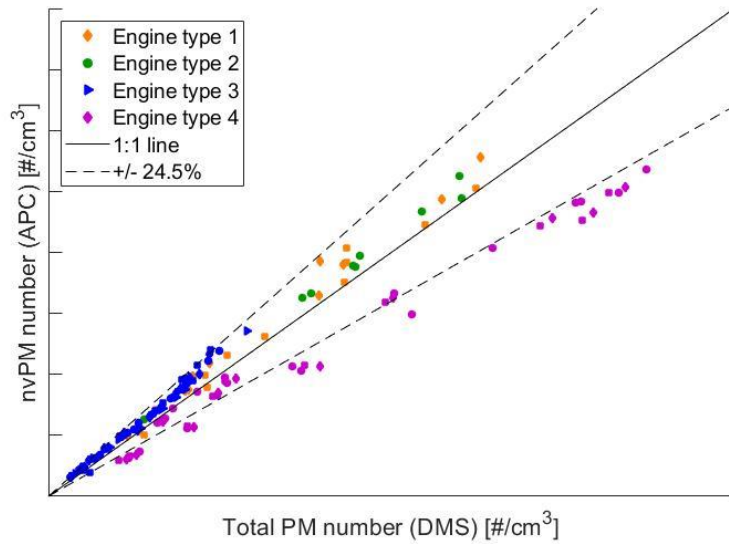


Figure 6-15: Total DMS PM concentration Vs APC nvPM concentration measured with the EASA kit for different aircraft engines corrected to 1st common point with 1 to 1 line and $\pm 24.5\%$ uncertainty lines

In the case of Engine type 4, the DMS is seen to measure a higher number concentration outside of the expected 24.5% uncertainty threshold. To further assess the correlation between DMS and APC derived number concentration the correlation between the two analysers was plotted against GMD as shown in **Figure 6-16**.

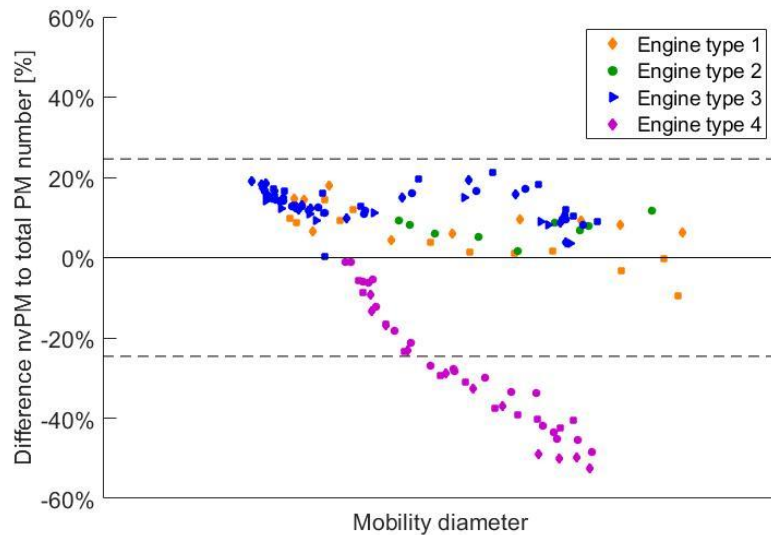


Figure 6-16: Difference between DMS Total PM concentration and APC nvPM concentration for different aircraft engines corrected to 1st common point with 1 to 1 line and $\pm 24.5\%$ uncertainty

$$\text{lines} - \left(\frac{N_{APC} - N_{DMS}}{N_{APC}} \right) \text{ Vs GMD}$$

As can be seen in representing the data in this format it is evident that in the case of engines 1-3 the correlation appears consistent across all aerosol GMDs (and by proxy engine thrusts). However, it is clearly observed for engine type 4 that the absolute difference between nvPM (APC) and total PM (DMS) increase with GMD hence engine thrust.

An explanation for the differing trend of Engine type 4 witnessed in **Figure 6-16** compared to the other engines, which is also supported by the generally larger GSD measured and discussed earlier (see **Figure 6-4**) is that volatile material is potentially being emitted within the exhaust stream of this engine technology with higher loadings witnessed at higher engine thrust settings (larger aerosol GMDs). Although there is no evidence of nucleation mode, in such a case emitted volatile matter may coat the solid soot particles in addition to spontaneously nucleating as small volatile particles overlaid by the main nvPM peak, resulting in the observed increased GSD and total number concentration measured by the DMS-500. In such a case, only the DMS would measure these volatile particles as the VPR in the APC should destroy a significant portion before measurement by the CPC.

6.2.2 Mass measurement uncertainty

To the authors knowledge, the ARTIUM LII-300 and AVL MSS both described in section **3.1.1.2** are the only two commercially available mass instruments meeting the regulatory requirements of ICAO for nvPM mass measurement, and are both used in the EASA nvPM reference system. In this section the uncertainty associated with both the LII and the MSS calibration and measurement are analysed, with mass concentrations measured on a number of soot sources compared.

6.2.2.1 Regulatory nvPM mass calibration uncertainty

As discussed previously, nvPM mass calibration consists in comparing gravimetrically measured particle mass loaded on a filter to the equivalent mass corrected by a direct measurement of the aerosol (section **3.1.1.2**). A linear calibration factor is derived from the filter correlation and applied to the specific nvPM mass instrument. Significant uncertainties surround nvPM mass instruments calibration as there is no universally agreed and scientifically precise definition of nvPM (section **1.2**) and no known method that can deliver a precise sample of nvPM for use as a reference material [53]. Mass instruments were historically calibrated with propane diffusion burner soot (e.g. mini-CAST), however subsequent issues discussed in this work have resulted in recent calibrations having to be performed on a Gas Turbine engine in the case of the LII-300.

It is currently thought that similar absorption properties are required in the calibration source as observed from the aircraft engine nvPM. Mamakos et al. [101] reported highly fluctuating mass readings with the MSS (up to 60% discrepancy with thermo-optically determined EC) when changing mini-CAST operating conditions. Marhaba et al. [183] showed that some mini-CAST operating

conditions enable generation of soot particles with morphology, internal structure and chemical structure close to those of aircraft soot, hence AVL during calibration of the MSS in compliance with ICAO use a proven setting known to be representative of both Diesel and aviation soot [private communication Michael Arndt AVL 15/05/19].

Between 2014 and 2018, annual calibration of both the European (EASA) and Swiss (EMPA) MSS were performed by AVL on mini-CAST soot. During this period, the EMPA MSS calibration factors varied by up to 10% (0.554 to 0.61) while the EASA MSS calibration factor varied by up to 8% (0.582 to 0.631). As no mini-cast set-point has to date been found for the LII which performs well on Gas Turbine aerosol, calibrations since 2016 have been performed in partnership with Rolls-Royce UK Derby using their GNOME helicopter engine test facility (section 3.4). Indeed, calibration factors of the EMPA LII varied by up to 23% (0.618 to 0.801) when calibrated on inverted flame burner and GNOME, highlighting the impact of different soot sources used for calibration.

6.2.2.2 Limit of Quantification of nvPM mass instruments

A Limit of Detection (LOD) of $1 \mu\text{g}/\text{m}^3$ is specified by the regulation for nvPM mass instruments [14]. However, it was consistently observed by the author during aircraft nvPM measurements that the Limit of Quantification (LOQ), from which one can reasonably differentiate exhaust emitted nvPM from noise, was higher than the LOD.

To determine a meaningful LOQ the Coefficient of Variation (CV defined in equation (6.2) below) derived from 30 seconds averages taken during certification test of four aircraft engine types was assessed to find the lower concentration limit at which the CV of the mass instruments typically rose above 20% corresponding to nvPM mass uncertainty from the ICAO mass instrument (section 3.1.1.2). The CV data for both the MSS and LII are plotted against MSS derived Mass and GMD and is presented in **Figure 6-17** below. As can be seen by the vertical line added to **Figure 6-17 (a)** $5 \mu\text{g}/\text{m}^3$ is the concentration at which both analysers consistently witness a CV >20% hence in the scope of this thesis, a LOQ of $5 \mu\text{g}/\text{m}^3$ was chosen.

$$CV_{\text{mass}}[\%] = \frac{\text{mass}}{\text{stdev}_{30\text{sec}}} \quad (6.2)$$

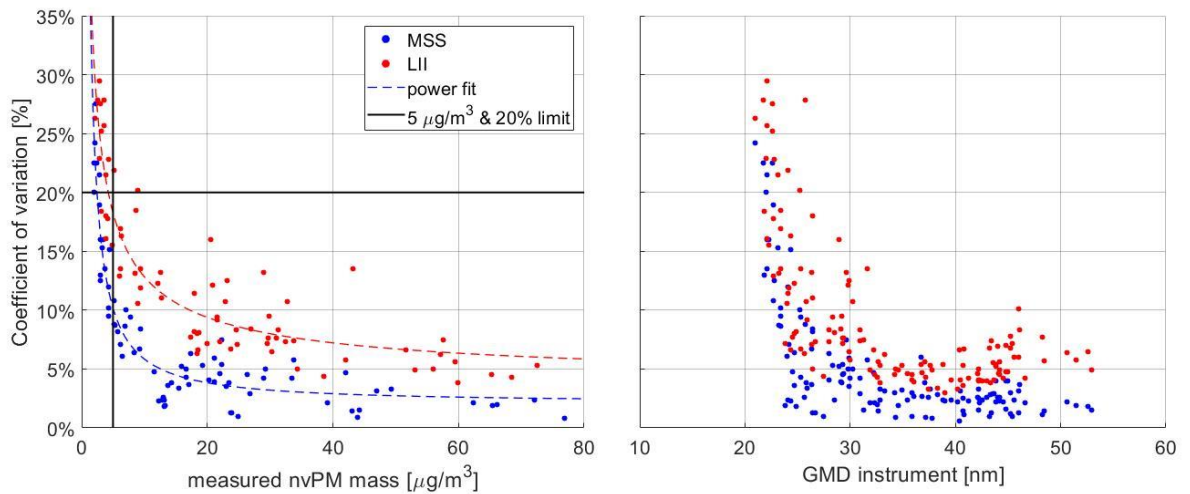


Figure 6-17: Coefficient of Variation (i.e. standard deviation/average) of MSS and LII nvPM mass measurements obtained on four aircraft engine types against mass (a) and GMD (b)

It is thought that below the $5 \mu\text{g}/\text{m}^3$ threshold, mass measured from system line shedding can't be reasonably discerned from exhaust emitted nvPM which due to its random appearance impacts the measured CV, as discussed later in section 6.2.4. However, to determine if the CV maybe a function of a different parameter other than low mass, the data is plotted against GMD as observed in **Figure 6-17 (b)**. Similarly, a $\text{CV} > 20\%$ is witnessed for both mass instruments at GMDs below ~ 25 nm, however in this data-set small sizes are symptomatic of low engine powers and hence low mass, hence unfortunately the two variables cannot be decoupled in this work, and in this study mass concentration is used to determine the LOQ with size not further considered in terms of mass uncertainty.

It is also noted that the LII generally has a larger coefficient of variation than the MSS although comparing the signal processing of the two instruments is complicated. Indeed, the LII signal is digital (occasional signal when the laser measures light) when the MSS outputs an analogue signal (constant signal from microphone) with the demodulation algorithm of the MSS containing some fast (Bessel) filtering [Private communication Michael Arndt – AVL 15/05/19].

6.2.2.3 Comparison of mass measurements

NvPM mass concentrations measured during certification level emission testing on five engine types using four LII-300 and two MSS calibrated as prescribed by ICAO regulation (section 3.1.1.2) were compared to one and other to determine any bias between the measurement techniques (this data was provided by Rolls-Royce). MSS/LII correlations are presented in **Figure 6-18** with uncertainty bands representing 27.6% which is the anticipated propagated nvPM mass uncertainty from the ICAO mass instrument specifications as discussed previously in section 3.1.1.2 (i.e. $\sqrt{19.5\%^2 + 19.5\%^2} = 27.6\%$).

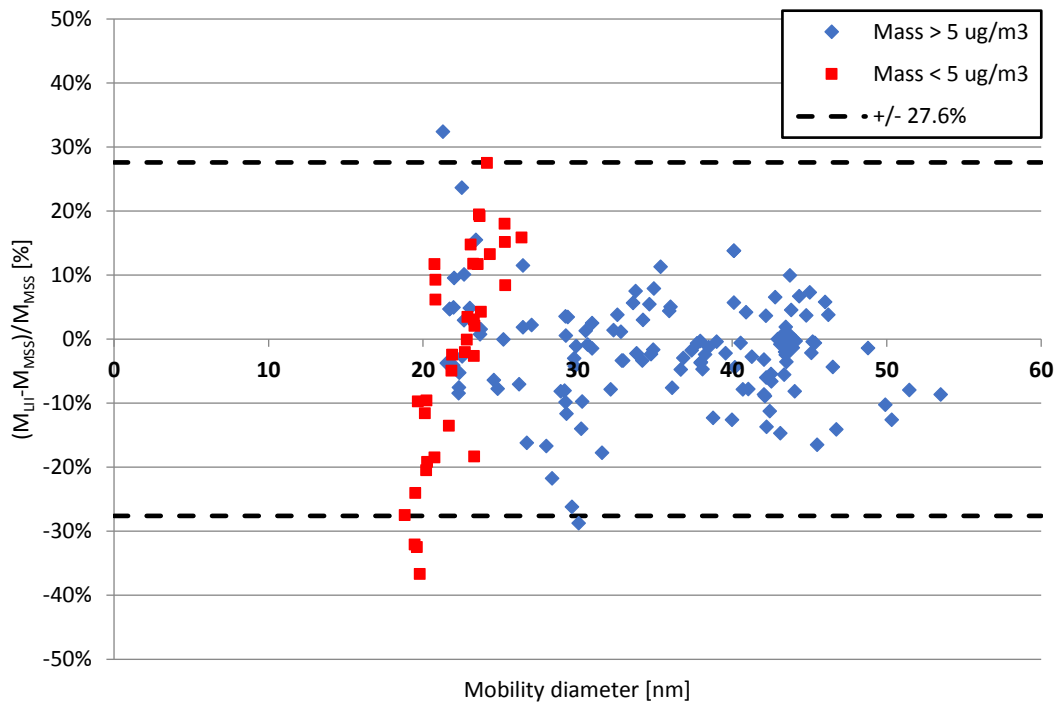


Figure 6-18: Comparison of measured MSS and LII-300 nvPM mass concentrations on various engine types

It can be seen that generally the two mass instruments agree within the defined uncertainty of 27.6% with most of the data correlating within $\pm 15\%$. At low mass (i.e. $< 5 \mu\text{g}/\text{m}^3$) hence small GMD, the difference appears generally larger due to the high uncertainty associated with the measurement (potential line shedding – section 6.2.4.4). The difference between the two analysers could be induced by different particle effective densities as it has been reported that it impacts the signal decay from LII measurements, resulting in longer decay times for particle of greater effective density [20]. On average, the LII recorded an nvPM mass $1.9 \pm 8.4\%$ lower than the MSS.

Comparable to the author’s findings, the agreement found in the literature between LII and MSS is generally within individual instrument uncertainty and the MSS tends to measure higher masses than the LII. Durdina et al. [63] reported aircraft engine nvPM mass measurements 28% lower using a LII when comparing with a MSS when both instruments were originally calibrated on the same inverted flame source. However, both instruments agreed within one standard deviation of the averaged data. Boies et al. [20] compared mass measurements from three LII located on different sampling lines. They found that the difference amongst instruments was smaller than the individual instruments variation at each thrust setting. Lobo et al. [51] compared mass measurements of two MSS and a LII using a mini-CAST burner and found that the MSS concentrations were approximately 15% higher than those reported by the LII. For masses below $200 \mu\text{g}/\text{m}^3$ which is typical of aircraft nvPM emissions, the instruments were in better agreement with a difference $< 2\%$. SAMPLE III SC.05 [50] showed that MSS and LII data from engine test campaigns agreed well with a 7% bias towards the MSS.

6.2.3 Particle size distribution measurement uncertainty

Size measurement is not currently prescribed for aircraft engine nvPM emission certification due to the absence of traceable nanoparticles in the nvPM size range witnessed from gas turbines (20-50nm GMD [9]) and the non-sphericity of combustion soot particles. However, particle size information is crucial in understanding aviation impact on local air quality and quantifying size-dependent loss in a compliant nvPM sampling system.

The DMS-500 and SMPS have been widely used for combustion PM measurement and characterisation [61], [184]. Both instruments use a similar technology consisting in charging particles to a known state of charge and then classifying them using an electric field to measure the particle electrical mobility diameter as introduced in section 3.1.3. Although both the SMPS and DMS operate on the same principle of electrical mobility, there are numerous technical differences related to the measurement technique, specifically aerosol charging, classification column and particle detection, making it crucial to compare the performance of the DMS and SMPS for the characterisation of aircraft PM [185].

In this section, size measurements performed by a TSI SMPS and a Cambustion DMS-500 (described in section 3.1.3) on aircraft engine exhaust are presented, along with a discussion on size calibration and traceability.

6.2.3.1 DMS & SMPS measurement principles and calibration

Although both SMPS and DMS measure electrical mobility diameter there are differences in the measurement principle and operation which have the potential for observed differences in measured aerosol distribution. A brief overview of these differences is discussed below:

Operation & Calibration: The SMPS classifies particles with a DMA and measures individual size bins with a CPC with both the DMA and CPC traceably calibrated. On the other hand, the DMS generates a distribution from simultaneously measuring electrometers (rings) currents representing different particle sizes and requires an inversion matrix generated from calibration. The use of an adequate inversion matrix is crucial for DMS accuracy. Indeed, Delhaye et al. [61] recorded a CMD difference of 25% between a DMS and a SMPS when measuring fractal nvPM soot using a spherical inversion matrix.

Performance: The DMS measures particles from 5 to 1000 nm with a resolution of 38 channels (16 channels per decade), at a sampling rate of up to 10 Hz allowing real-time measurements. The DMS utilises a relatively higher flowrate (~8 Lpm) and low pressure (250 mbar) resulting in low diffusion losses within the instrument and has optional dilution stages to facilitate fast measurements of combustion exhaust nanoparticles across a range of concentrations up to

$\sim 10^9$ particles/cm³. However, it can only accurately measure particle number concentrations at a minimum concentration of $\sim 10^4$ particles/cm³. On the other hand, the SMPS requires a longer scanning time of usually one minute or more, sampling at a lower flowrate, has a better resolution of up to 167 channels and can measure particle number concentrations of $\sim 10^7$ particles/cm³ [186]. It is however noted that there are many models of SMPS and new fast scan SMPS are capable of measuring at a shorter scanning time. The size range of the SMPS depends on the DMA column used.

Particle charging: The DMS uses a corona discharge to achieve unipolar charging (i.e. particles are positively charged to a predictable level). Unipolar aerosol chargers can achieve higher charging efficiency than bipolar chargers, but electrostatic and space charge effects can lead to high particle loss if not addressed. Larger nano-particles are subject to multiple charging and can become as electrically mobile as small particles (i.e. mobility inversion) [187]. This issue is minimised by running the DMS at low pressure (250 mbar). Awasthi et al. [88] showed that with unipolar charging, agglomerates carried a higher mean charge than that of spheres due to the larger relative surface area of agglomerates, resulting in overestimation of the electrical mobility and underestimation of the mobility diameter although they discussed that the mean charge per particle of agglomerates was only being overestimated for mobility size range below 80 nm. Hence size instruments using unipolar chargers like the DMS must be calibrated with agglomerates at sizes below 80 nm to correct for this phenomenon. For soot like particles with the DMS, an empirical calibration performed with a propane fuelled CAST and a DMA is performed during its calibration. The SMPS uses a bipolar diffusion charger consisting of a radioactive neutraliser to bring the aerosol to a defined, steady-state charge distribution. Bipolar diffusion charging brings the aerosol to a known charge equilibrium but has a low charging efficiency and is only effective at low flowrates and small number concentrations [188], [189].

As discussed previously when measuring spherical particles, DMS and SMPS can be calibrated using NIST traceable nano-spheres such as PSL spheres which are typically characterised using electron microscopy. However, PSL spheres require surfactant to remain stable in suspensions which induces a Non-Volatile-Residue peak in the 10-100 nm region (section 4.1), hence PSL spheres are generally used for calibration at diameters larger than 100 nm. For calibration in the 10-100 nm range, spherical nanoparticles can be produced by atomising sulphuric acid, DEHS, emery oil or sodium chloride solutions and classified with a DMA. A size uncertainty of $\pm 10\%$ from calibration is quoted by manufacturers (see DMS-500 calibration certificate in appendix 10.1) and was used by Johnson et al. [190] and Boies et al. [20] for a DMS.

6.2.3.2 Comparison of sizing analysers for aircraft engine nvPM measurement

Comparisons of DMS and an SMPS (operated by University of Manchester) were performed on two soot sources namely; a GNOME engine burning jet-A fuel and an RQL combustor rig burning numerous blends of jet-A and alternative fuels, a DMS and an SMPS composed of a CPC 3776 and a 3085 DMA (offering size range of 4.6-145.9 nm) were used to simultaneously measure particle size distributions in parallel from a common split point. As individual size instruments recorded data at a different rate, the DMS data was averaged over the same three-minute-long scans taken by the SMPS at stable conditions. Examples of the size distributions from each of the DMS and the SMPS are presented in **Figure 6-19**, where the shape of the distributions from both instruments closely relate, however as noted by the requirement of different concentration axis the uncorrected number concentrations were offset by approximately 10 to 60% as discussed below. It is noted that the small secondary peak seen on the left plot with the SMPS is assumed to be an artefact, commonly witnessed in SMPS measurements towards the upper range of size measurement [Private communication Paul Williams Manchester University 12/18].

To precisely compare both instruments, a method was designed to estimate the GMD, GSD and total number concentrations for any size distribution by numerically integrating the distributions and using equations (2.2), (2.3) and (2.4) in MATLAB (trapezoidal numerical integration). The inversion matrix chosen for the DMS was the monomodal aggregate as soot nanoparticles were being measured. The comparison between the DMS 500 and the SMPS was performed over a wide range of GMDs (30 - 90 nm), GSDs (1.4 - 1.8) and varying total number concentrations (10^5 - 2.5×10^6).

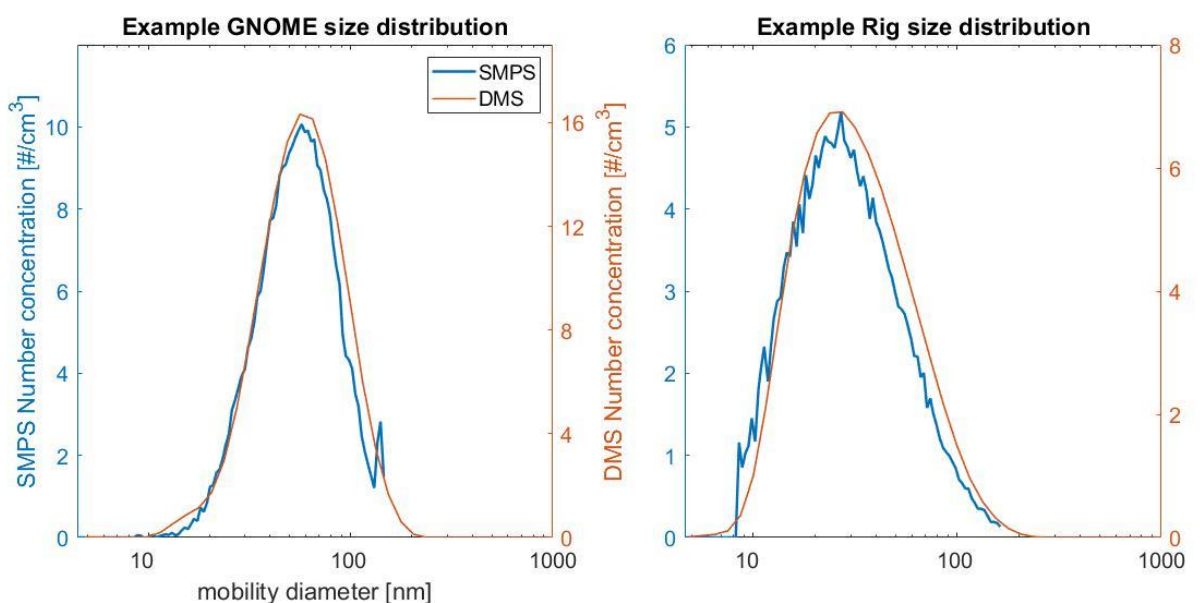


Figure 6-19: Example particle size distributions measured by a DMS and a SMPS at the exhaust of a GNOME engine (a) and RQL burner (b)

Results comparing the measured GMD from the DMS and SMPS are shown in **Figure 6-20**, twenty test points from the GNOME engine where soot size and morphology were varied and sixty-five test points from the RQL combustor rig where blends of Jet-A and alternative fuels were burnt producing aerosols with varying morphology and volatile content. Based on the DMS size uncertainty discussed above in section **6.2.3.1**, a 10% uncertainty was chosen for each instrument, resulting in 14.1% uncertainty bands ($\sqrt{10\%^2 + 10\%^2} = 14.1\%$) applied to the 1:1 correlation. As can be seen in **Figure 6-20 (a)**, the GMDs measured by both instruments generally agree within the uncertainty, with the DMS GMD typically larger than the SMPS GMD by 3.3 ± 1.7 nm (i.e. $9.6 \pm 4\%$) on average. The GSD from the DMS is also larger than the SMPS by 0.04 ± 0.03 . The slightly larger and wider size distributions observed with the DMS could originate from the calibration uncertainties (i.e. DMS inversion matrix), unaccounted-for diffusional losses in the 5 m heated dilution line of the DMS and the higher resolution of the SMPS, but also may be explained by the SMPS not measuring the full aerosol distribution at sizes >145.9 nm as seen clearly in **Figure 6-19 (a)** particularly at larger GMDs due to the relative size of the DMA.

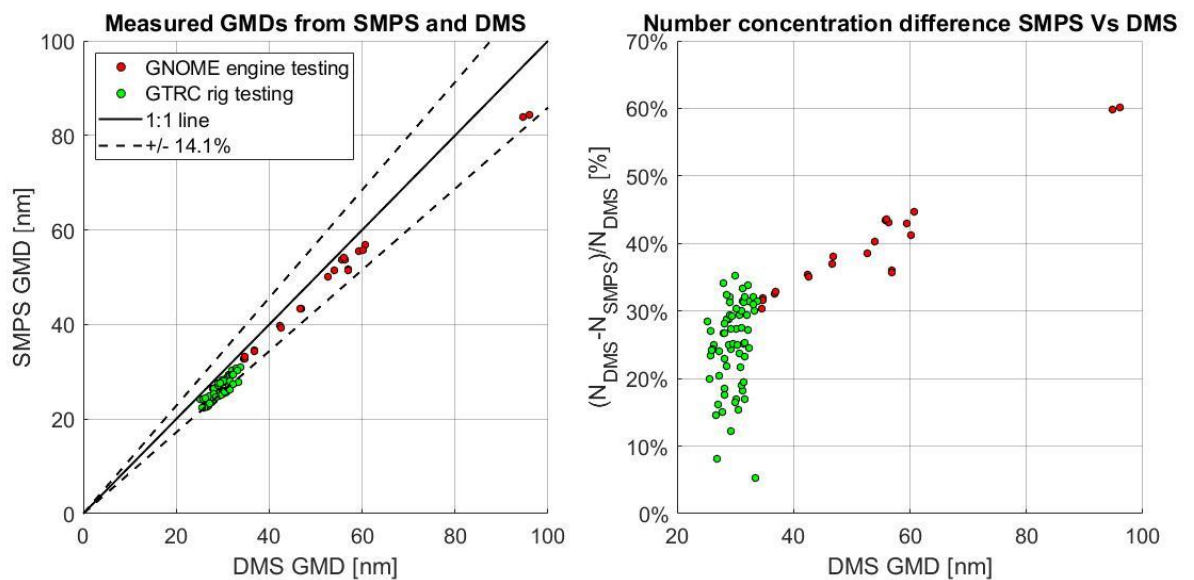


Figure 6-20: Comparison of size (a) and Number (b) measurements performed by a DMS-500 and SMPS on aircraft exhaust aerosols

Figure 6-20 (b), which displays the difference in the total number concentration from the DMS and the SMPS, shows that the DMS number concentration is always higher to the SMPS by $28.5 \pm 9.2\%$ on average, this observation could in part be related to the different sampling temperature at the instrument as the DMS sampled exhaust PM at 60°C whereas the SMPS sampled at ambient temperatures hence had slightly higher thermophoretic losses. Assuming the SMPS has the same total number uncertainty as the DMS (20% [113]), then the average difference between the DMS and SMPS is just above the propagated uncertainty of 28.3% ($\sqrt{20\%^2 + 20\%^2} = 28.3\%$). In addition to the calibration uncertainty, instrument drift over time may also contribute to these

observed differences, since DMS as found calibration checks have shown drifts of up to 34% over a fourteen-month period. The difference in number concentration between DMS and SMPS also seems to increase with increasing GMD for the GNOME engine data points. However as discussed as the GMD gets larger, the right tail of SMPS distribution is underpredicted given the upper size limit of the SMPS used (145.9 nm).

Similarly, Hagen et al. [185] compared a DMS and a SMPS during aircraft emission measurements and recorded average differences of 10% for sizing data and 30% for concentration measurements. They provided potential reasons for the observed deviations such as elevated diffusional losses in the instruments, Non-spherical shape of aircraft emission particles and pressure fluctuations. SAMPLE III SC.05 [50] also compared SMPS and DMS on a lean burn engine and found GMDs within 4% average variance.

To address the disparity between SMPS and DMS shown in **Figure 6-19 & Figure 6-20** the data were re-analysed using a lognormal fit (equation (2.5)) instead of the directly applied measured distributions. After this analysis it was observed that the differences in GMD and number concentration were negligible (<1%) when compared with the results presented here, highlighting differences are more likely an artefact of the different sampling and measurement principles rather than data clipping in the SMPS.

6.2.4 Sampling system uncertainties

In addition to uncertainty associated with measurement analysers and their calibration, further uncertainties can originate from the sampling system itself. In this section the uncertainties associated with the operation of an ICAO compliant system are estimated by varying factors such sample flow, gas and wall temperature, line length, etc as permitted by the current legislation in ICAO Annex 16 [14]. Issues associated with particle shedding are also individually assessed.

6.2.4.1 25 m sample line (section 3):

The 25 m sample line transports aerosols from the outlet of the primary diluter to the cyclone near the analysers. A significant fraction of smaller particles can be lost in this line via diffusion. The ICAO requirements for this section of the sampling system are listed below:

- Line length 24.5 ± 0.5 m
- Internal Diameter 7.59-8.15 mm
- Line walls temperature $60 \pm 15^\circ\text{C}$
- Sample flow 25 ± 2 standard Lpm

In addition to these requirements, the primary diluter body and diluent must have temperatures of $60\pm 15^\circ\text{C}$, indicating that the aerosol at the inlet of the long sample line can have a temperature of $60\pm 15^\circ\text{C}$.

Using the parameters listed above in the UTRC particle transport model, best- and worst-case penetration efficiency functions were determined as illustrated in **Figure 6-21**. The loss difference between best and worst case was estimated at $\sim 5\%$ for particles sizes of 10-100 nm and $\sim 4\%$ for sizes of 50-200 nm. As typically, for aircraft PM, the majority of the number concentration reside in the 10 – 100 nm range, the uncertainty associated with losses in the long sampling line for number EI was estimated at 5%. Similarly, the mass weighted distribution of gas turbine exhaust nvPM was found to have a GMD in the 80-120 nm region with most of the mass concentration in the 50-200 nm size range. Hence, the uncertainty associated with losses in the long sample line for EI mass was estimate at 4%. It is noted that typical aircraft PM mass distributions were deducted assuming lognormality, a particle effective density of 1 g/cm^3 , a GSD of 1.7-1.9 and using equation (2.6) to convert from number weighting to mass weighting.

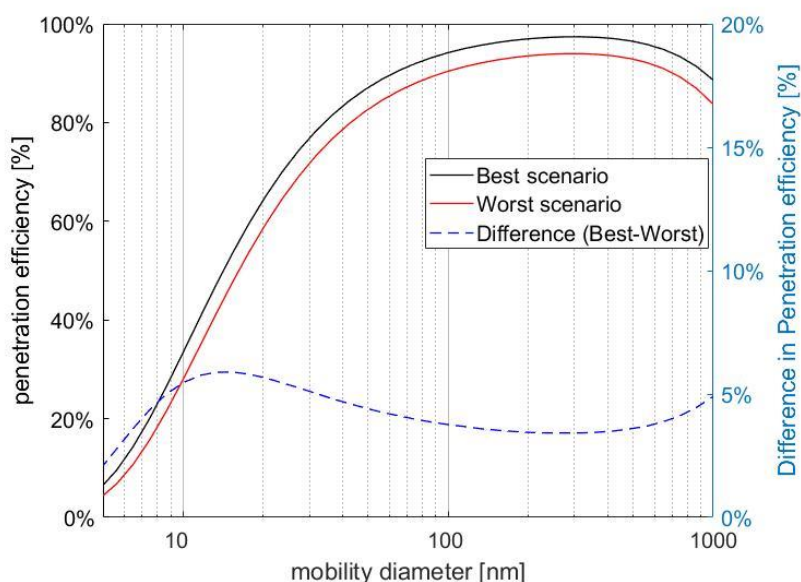


Figure 6-21: Best and Worst penetration efficiencies of an ICAO compliant long sample line (left-axis) with their difference (right-axis)

6.2.4.2 Primary diluter (section 2):

Due to the relatively large nanoparticle concentrations, high temperature and potential volatile components in the exhaust of an aircraft gas turbine engine [74], rapid dilution within 8 m is prescribed by ICAO appendix 7 [14]. Dilution prevents coagulation and condensation from occurring and reduces thermophoretic losses by cooling the gas with diluent instead of via the walls in sample lines [48].

Current ICAO regulation requires the primary dilution system to dilute the exhaust aerosol at 8-14 using an ejector diluter which meets the performance specification listed in **Table 3-2**. Ejector diluters are advantageous because the sample flow enters the mixing chamber through a small orifice at very high speed, ensuring rapid entrainment and mixing with the diluent [107]. Particle loss in an ICAO primary diluter are currently assumed negligible and a penetration efficiency of 100% is prescribed when correcting for losses. The uncertainty associated with the primary dilution and possible nvPM morphology changes were assessed in this section.

ICAO primary diluter uncertainty:

Two uncertainties can arise from a compliant primary diluter in a sampling system namely particle loss in the diluter and prediction of the dilution factor from CO₂ measurements.

In regard to the minimum particle penetration fractions tolerated for a compliant diluter as listed in **Table 3-2**, up to 20% of particles can be lost at 15 nm and 10% from 30 nm. Hence, associated uncertainties of 20% for EI number and 10 % for EI mass (because the mass is carried by the larger particles) can originate from losses in the diluter.

Regarding CO₂ measurements, gas analysers must be calibrated to calibration gas with a $\pm 2\%$ accuracy, must maintain a stability better than $\pm 2\%$ of Full-Scale (FS) range, a repeatability better than $\pm 1\%$ FS, zero drift better than $\pm 1\%$ FS, a noise lower than $\pm 1\%$ FS and a resolution better than $\pm 0.5\%$ FS. As appendix 3 of ICAO annex 16 [14] doesn't currently state a minimum range for CO₂ readings, the lowest 'CO₂ measurement to FS range' ratio was chosen from the data presented in this chapter (engine type 1-4) and was found to be 25%. This ratio coupled with the above listed CO₂ uncertainties proportional to FS ranges were propagated providing a final CO₂ measurement uncertainty of 11% for the worst-case scenario ($\sqrt{2\%^2 + 8\%^2 + 4\%^2 + 4\%^2 + 4\%^2 + 2\%^2}$). Hence, diluted CO₂ measurements can induce an additional uncertainty of 11% as they are required in the calculation of number and mass EIs.

In total, a compliant primary diluter has uncertainties associated with particle loss and CO₂ measurements which can lead to a propagated uncertainty of 22.8% for EI number ($\sqrt{20\%^2 + 11\%^2}$) and 14.9% for EI mass ($\sqrt{10\%^2 + 11\%^2}$).

CO₂ measurement uncertainty is generally lower than the estimated 11% because most CO₂ readings are closer to the FS range and analysers uncertainties are lower than the ones quoted by the current regulation.

Experimental investigation of nvPM morphology change in primary diluter:

Potential morphology changes in the Dekati DI-1000 ejector diluter (similar model to that used in the EASA reference system) were investigated by comparing measured size distributions at

the inlet and outlet of the diluter heated (diluter walls + diluent) at temperatures of 20-150°C. As dilution factors weren't measured, penetration efficiencies could not be estimated, however GMD and GSD changes could be monitored assessing if size-dependent losses or morphology change occurred in the diluter.

Experimental set-up:

The ejector diluter experiment was performed at Rolls-Royce Derby facilities in collaboration with Rolls-Royce and Manchester university who provided a TSI nano-SMPS (DMA 3085 + CPC 3776). The experimental set-up consisted of a particle generation section, a test section and a measurement section as depicted in **Figure 6-22**. Polydisperse monomodal nanoparticles were generated from a Gnome helicopter engine (section 3.4) and volatiles were removed from the aerosol using a Catalytic Stripper. The size and morphology of exhaust soot was varied from 30-80 nm (GSD 1.5-1.8) by controlling the residence time in the particle generation section using additional dilution and different sample paths as shown in the particle generation section in **Figure 6-22**. This changed the particle agglomeration rate and hence the measured aerosol size. To replicate typical operation during aircraft exhaust sampling and to assess the effect of heating/cooling in the ejector diluter, its walls and the diluent (dry air) were heated at 20-150°C.

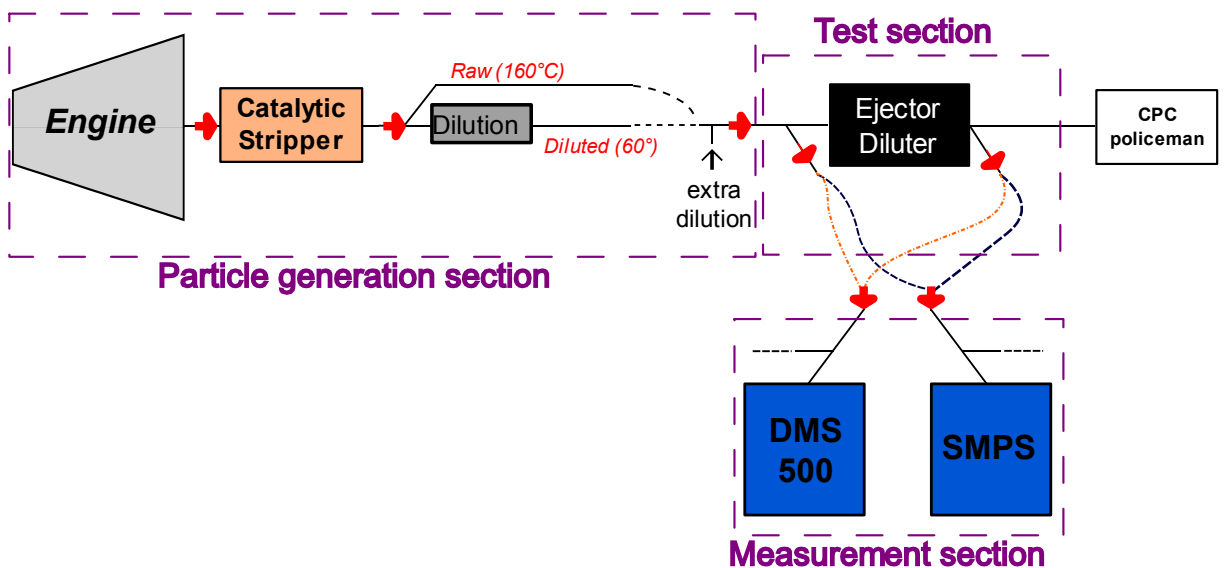


Figure 6-22: Diagram of the ejector diluter experimental set-up

Particle size distributions were measured alternatively at the inlet and the outlet of the investigated ejector diluter using the nano-SMPS and DMS-500 by actuating two-way valves. Hypothetical particle fluctuations within the diluter were estimated by comparing the inlet and outlet size distributions. Given the SMPS required longer sampling times (3 minutes), a 'policeman' CPC was used to monitor particle stability during measurement.

It is noted that to minimise uncertainties and to provide direct comparison between the two analysers, tubing dimensions and gas flowrates were kept identical between the test section and each analyser.

Results:

Generally, the measured size distributions at the inlet and outlet of the diluter, using unheated dilution (20°C), had a similar shape (i.e. GSD and GMD). This is highlighted in **Figure 6-23** where outlet size distributions were multiplied by a particle number derived dilution factor (PNDF) and are seen to match the inlet size distributions. As seen in **Figure 6-24(blue)**, measured GSDs and GMDs remained generally constant through the diluter, hence it was concluded that the unheated ejector diluter did not lead to morphology change. These findings are in agreement with Cheng and al. [108] whom measured no discernible difference in the GMD and GSD for polydisperse NaCl passing through an ejector diluter. Yoon et al. [176] also reported that loss in an ejector diluter were negligible (<5%) and were not size dependent for particles in the 3-20 nm region using nichrome.

It is noted that when comparing the two analysers, the particle number dilution factor ($N_{\text{outlet}}/N_{\text{inlet}}$) was generally different. It is assumed that this was caused by the large uncertainty (>20%) associated with total number concentration derived from size distribution measurements, as discussed in section **6.2.3.2**.

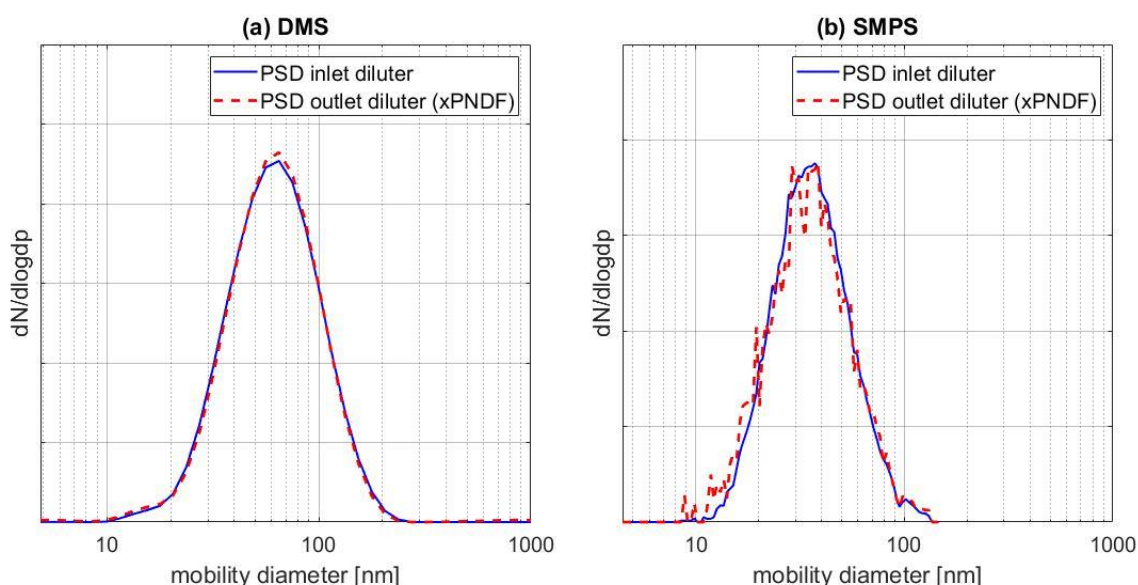


Figure 6-23: Example particle size distributions of soot measured at the inlet and outlet (Particle Number Dilution Factor corrected) of an ejector diluter using a DMS-500 (a) and an SMPS (b)

Particle size distributions were also measured at the inlet and outlet of the diluter at increasingly hotter diluent and diluter wall temperatures (20-150°C), with the induced GMD and GSD differences presented in **Figure 6-24**. As can be seen, the higher diluter/dilution temperatures did not significantly impact the GMD (**Figure 6-24(a)**) nor the GSD (**Figure 6-24(b)**) with fluctuations

consistently <10%. The generally larger GSD observed at the outlet of the diluter (**Figure 6-24(b)**), particularly with the SMPS, may be explained by the lower number concentrations (order of magnitude) at the outlet of the diluter and increasing the measurement uncertainty. It was again concluded that the ejector diluter did not induce size-dependent loss or morphology change even when heated at temperatures of up to 150°C. These results are in agreement with Giechaskiel et al. [105], [106] who reported nvPM losses <5% in the 15-100nm size range in an ejector diluter heated at 150°C.

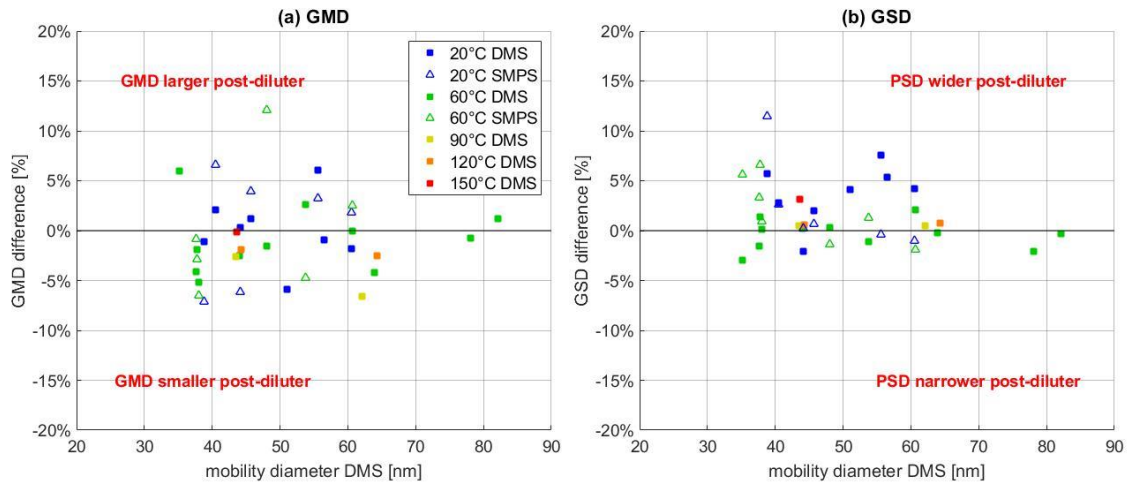


Figure 6-24: Difference in soot GMD (a) and GSD (b) when passing through an ejector diluter heated at different temperatures measured using a DMS-500 and an SMPS

It is noted that as soot GMD was varied by changing engine power settings and sampling paths (**Figure 6-22**), the pressure at the inlet of the ejector diluter, hence the dilution ratio, was changing during the experiment. Given no significant variation in GMD and GSD were observed, it was concluded the operation pressure of the ejector diluter has non-measurable effect on the distribution shape, again in agreement with Giechaskiel et al. [105].

6.2.4.3 Collection section (section 1):

A regulatory compliant collection section is made of a sampling probe and sampling path up to 8 m in length. Sampling probe design is commercially sensitive information and specific geometries are typically not shared by OEM's hence losses in a 'hypothetical' sampling probe are conjectured in this section. Transport efficiency in the collection section can be hard to predict as it depends on the engine thrust setting and combustion technology given exhaust gas temperature and dynamic pressure vary with these two parameters. In this section, the uncertainty associated with non-thermophoretic loss in a regulatory compliant collection section were investigated with best- and worst-case scenarios derived from ICAO Annex 16 and the literature, as listed in **Table 6-3**. It is noted that thermophoretic losses in the collection section were not considered as they are separately

corrected using the thermophoretic correction factor k_{thermo} and are already included in EIs as discussed in section **1.5.1.2**.

The exhaust gas temperature at the probe is commercially sensitive, hence the highest gas temperature at the inlet of the collection section was conjectured from the literature. ARP 6320 [53] and the AIR 6241 [52] refer to aircraft engine combustion exhaust gas temperatures ranging from 273 to 973K (i.e. 0-700°C). The exhaust gas temperature recorded by Lobo et al. [51] for various turbofan engines ranged from 327 to 577°C, at minimum and maximum engine power conditions respectively. The highest exhaust gas temperature derived from the literature and used for the ‘worst-case’ scenario study is 700°C.

Similarly, the sample flowrate within the collection was conjectured as it is not measured during certification level testing. AIR6241 [52] states that for particle losses to be minimised in the collection section, the residence time should be equal to or lower than 3 seconds. Using the maximum line length of 8 metres and the smallest compliant internal diameter 4 mm, a minimum flowrate was estimated at 2 Lpm using equation **(6.3)**. However, at most engine power setting, the conditions at the engine exhaust produce much larger flows in the collection section which also must deliver a minimum of 9 Lpm for gaseous measurement (annex 16 appendix 5 [14])ⁱ. Durdina et al. [63] numerically investigated varying the sample flow in the collection section between 20-80 Lpm and found that the total penetration efficiency varied in average by 0.5%.

$$t_{\text{res}} = \frac{L_{\text{tube}}}{Q/A} = L_{\text{tube}} * \pi * \left(\frac{D_{\text{tube}}}{2}\right)^2 / Q \quad (6.3)$$

with t_{res} is the residence time in seconds, D_{tube} is the sampling line diameter in meters and Q is the flowrate rate in m³/s.

ⁱ ICAO Annex 16 Appendix 5 states that the transport time for gaseous measurements must be less than 10 seconds. Using a typical line length of 8+25=33m and a typical ID of 7.747mm and using equation **(6.3)**, the minimum flowrate is ~9 Lpm

Table 6-3: Typical dimensions and gas properties encountered in the collection section of a compliant sampling system

Input	Collection section (Worst / Best)
$T_{gas}[K]$	$418^W - 973^B$
$T_{wall}[K]$	$418^{(W-B)} - 448$
$P_{gas}[atm]$	1
flowrate Q [slpm]	$2^W - 100^B$
$D_{tube}[cm]$	$0.4^W - 0.85^B$
$L_{tube}[cm]$	$200^B - 800^W$

Best- and worst-case scenario penetration efficiencies in the collection section were both investigated using the UTRC model and the listed properties in **Table 6-3** (superscripts B and W stand for Best and Worst) with an assumed particle effective density of 1 g/cm³. It is noted that for the best-case scenario, a line length of 2 m and a mean gas temperature of 422.5°C (700°C probe to 145°C line walls) were assumed. The resulting penetration efficiencies are presented in **Figure 6-25** with their difference (dashed blue line) representing the uncertainty associated with particle loss in the collection section. Given the difference is size-dependent, an average was made between 10-100 nm for EI number and between 50-200 nm for EI mass assumed to be representative of aircraft nvPM (section **6.2.4.1**). The resultant associated uncertainty with loss in the collection section corresponding to the difference in the corresponding size range is 7.3% ($\pm 5.4\%$) for EI number and 1.6% ($\pm 0.7\%$) for EI mass.

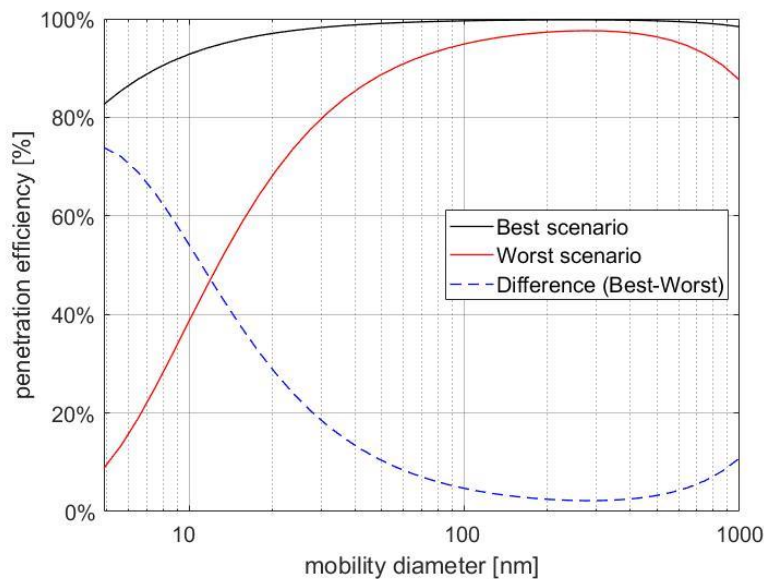


Figure 6-25: Best and Worst penetration efficiencies of an ICAO compliant collection section with their difference

6.2.4.4 Line shedding & Cleanliness and background checks

The added uncertainty of particle shedding in the sampling system (section 2.3.1.8) was investigated by analysing PM measurements during cleanliness and background checks (section 3.1.2). Due to the relatively low number concentration of particles measured during cleanliness checks when comparing with sampled PM, the potential impact of particle shedding is assumed negligible on number concentration and GMD measurements. However, because of the relatively large size of shed particles when compared with aircraft nvPM, mass measurements can be distorted by particle shedding at low mass concentrations.

During cleanliness checks (see section 3.1.2) conducted within the certification tests of four Rolls-Royce engine types, neither the MSS nor the LI300 generally detected shed particles. However, because of the relatively small sample cell dimensions and the use of a laser only focusing on a fraction of the sampled aerosol, it is possible the LI300 and MSS miss the occasional shed particles. On the other hand, the DMS-500 which charges all large particles passing through the analyser measured clear signals above its detection limits during cleanliness checks as illustrated in **Figure 6-26 (a)** displaying log-log scale size distributions with the DMS-500 sensitivity coloured in red [191]. While the DMS-500 could not effectively resolve the peaks at number concentrations this low, the signal is clearly above noise levels and could be equivalent to a non-negligible PM mass. A secondary peak in the 200-600 nm region was also observed by Williams et al. [10] and Durdina et al. [63] with a DMS-500 during aircraft PM measurement, whom disregarded it when calculating volume or mass from size distributions. It is noted that the potential shedding signal observed by the DMS-500 during cleanliness check could, if real, be stronger when sampling aircraft exhaust as sampled nvPM would be continuously hitting and adhering to the inner walls of the sampling system, enhancing shedding events.

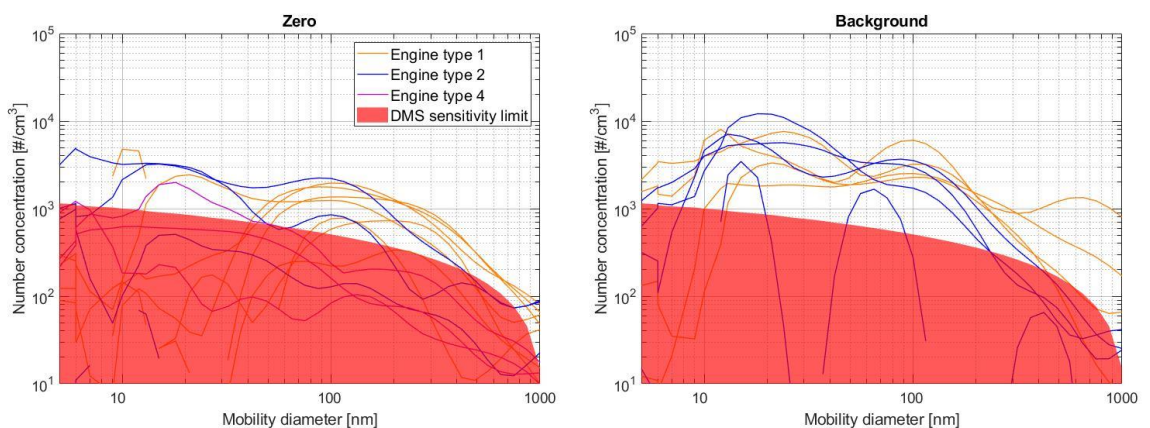


Figure 6-26: Typical Zero/Cleanliness (a) and Background/Ambient (b) checks measured by a DMS-500 prior and after three engine types emission test

Size measurements performed during background checks (**Figure 6-26 (b)**) show that the measured size distribution is higher than that measured during zero checks, with an apparent peak in the 10-50 nm region in the order of 10^4 particles/cm³ corresponding to atmospheric particles.

DMS-500 mass estimation – particle-shedding:

It was investigated whether the data recorded by the DMS-500 during cleanliness check was meaningful, originated from particle shedding and whether the mass derived from size distribution measurements corresponded to a concentration below $1 \mu\text{g}/\text{m}^3$ as required by ICAO regulation. To estimate the mass from the DMS-500 during cleanliness checks, a ‘maximum zero Number-weighted size distribution’ was generated using the highest concentrations of each size bin observed in **Figure 6-26 (a)**. The ‘maximum’ size distribution was then converted into a Mass-size distribution using equation (2.6) for each size bin and assuming a constant effective density. Both Number- and Mass-size distribution for the “maximum zero signal” are shown in **Figure 6-27** where it can be seen that most of the mass is carried by particles larger than 300 nm. To the author knowledge, shed particles properties (effective density, morphology) have never been measured, hence the DMS “zero” mass concentrations were derived from the Mass-size distribution using potentially representative effective densities taken from the literature as listed in **Table 6-4**.

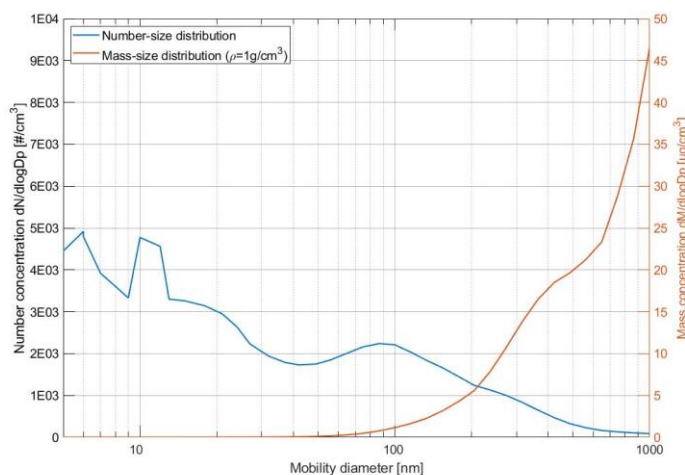


Figure 6-27: Maximum Number & Mass size distribution measured by the DMS-500 during

Assuming the lowest aircraft PM size-dependent effective density reported in the literature ($0.4 - 0.1 \text{ g}/\text{cm}^3$ estimated for particles 100-1000 nm [72]) documented in section 2.2, the mass derived from the DMS ‘maximum zero signal’ was $2.5 \mu\text{g}/\text{m}^3$. It increased to $15.8 \mu\text{g}/\text{m}^3$ when using the highest density (i.e. soot material/bulk density [69]). Results in **Table 6-4** highlight the high dependency of mass concentrations derived from size distributions to particle effective density.

Table 6-4: Total mass measured by the DMS-500 during cleanliness checks assuming different effective densities

Effective density (<i>VSD</i> → <i>MSD</i>)	Total mass DMS [$\mu\text{g}/\text{m}^3$]
Aircraft nvPM assumption ($\rho_{eff}(avg) = 1 \text{ g}/\text{cm}^3$)	15
$\rho(d_p)_{engine-min}$ literature ($\rho_{100-1000[\text{nm}]} \sim 0.4 \rightarrow 0.1 \text{ g}/\text{cm}^3$)	2.5
$\rho(d_p)_{engine-max}$ literature ($\rho_{material} \sim 2 \text{ g}/\text{cm}^3$)	15.8

It is noted that the signal recorded by the DMS-500 could originate from shedding occurring in the 5 metres heated dilution line, as similar secondary peaks were detected when a HEPA filter was placed at the inlet of the 5 metres line but not present when performing an autozero which uses a HEPA filter at the inlet of the main unit. Nevertheless, if shedding of particles in the 200-1000 nm region occurs in the DMS-500 5 m line where the flow is laminar and the pressure is 0.25 bar, then shedding is also likely to occur in the longer sample lines of the sampling system. It is also possible that shed particles measured by the DMS-500 mostly contain volatile material, hence are not detected by nvPM instruments. Other authors have suggested secondary peaks as artefacts from sulfuric acid particles generated in the high electric field near the corona discharge if enough SO_2 and H_2O are present in the carrier gas [185], which in this case should be disregarded as during zero checks there are insignificant levels of these gases.

6.2.5 Total uncertainty from nvPM sampling & measurement

An uncertainty of 66.3% for EI_{number} and 24.9% for EI_{mass} was estimated for the currently reported nvPM emission indices as presented in fishbone diagrams in **Figure 6-28** and **Figure 6-29**.

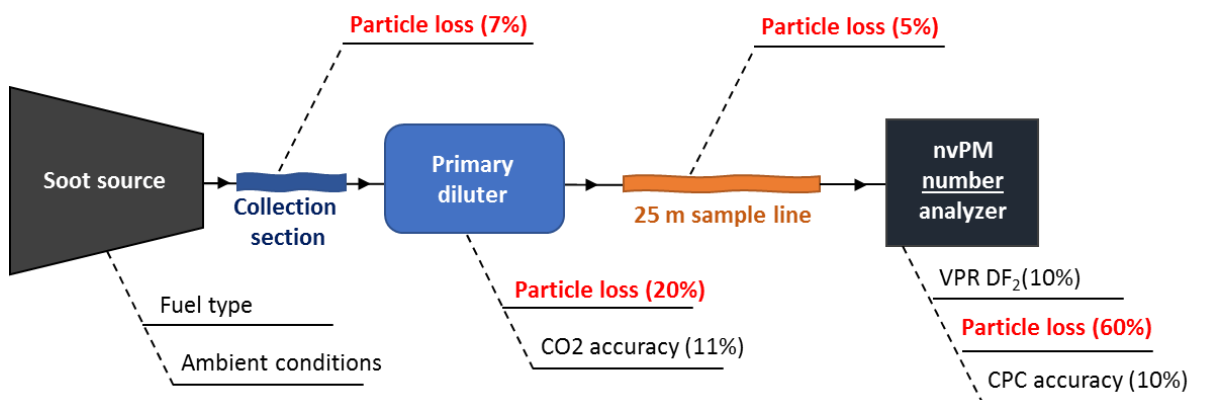


Figure 6-28: Diagram of the uncertainties associated with ICAO compliant nvPM number concentration measurement

They combined uncertainties associated with number measurement, mass measurement and transport in the sampling system as discussed above. However, they do not include other known uncertainties such as line shedding, humidity effects and fuel properties. It can be seen that a significant portion of the estimated uncertainty was attributed to particle loss in the sampling system and analysers (bold red in **Figure 6-28** and **Figure 6-29**). By accounting for particle loss (sampling system, VPR, CPC, etc), number and mass emission indices uncertainty could be reduced to 17.9% and 22.4% respectively.

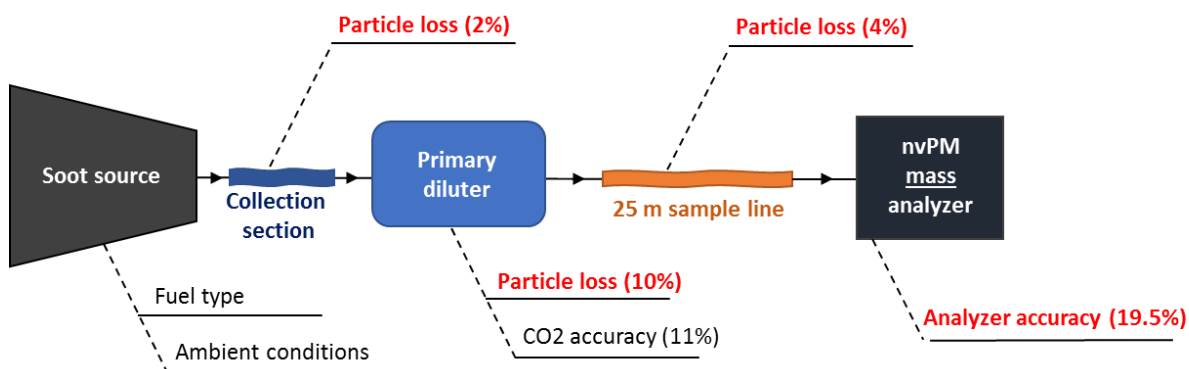


Figure 6-29: Diagram of the uncertainties associated with ICAO compliant nvPM mass concentration measurement

It is noted that other uncertainties associated with sampling system components and correction methodologies not discussed in this study are listed below:

- **Unequal flow 1st splitter:** In the 1st splitter of a compliant sampling system (**Figure 3-1**), highly unbalanced flows can occur that are thrust, probe and system control dependent. Inertial separation from unequal flows in splitters may result in significant mass variability as larger particles carrying most of the mass are most affected. Currently, the regulation doesn't standardise the uncertainty associated with unequal flows in the 1st splitter. However, it has been suggested that using a larger pipe diameter in the spill leg, hence reducing Stokes number to equalise flow velocities in the 1st splitter could minimise potential losses.
- **Sampling probe:** Sampling probe design is commercially sensitive information and specific geometries are typically not shared by OEM's. However, two different probes meeting ICAO standards were used during engine certification testing presented in this chapter and no noticeable difference in nvPM emissions were detected.
- **Instrument drift:** NvPM number and mass analyser may drift in between yearly calibration, increasing the measurement uncertainty. A 5% drift was reported after 6 months for a ICAO compliant CPC in a SAMPLE report [47]. A solution to minimise this uncertainty would be to perform calibration checks prior to any testing.

6.3 Uncertainty associated with soot source

6.3.1 Effect of humidity on nvPM emissions

The influence of ambient environmental conditions, particularly water vapour, on nvPM emissions produced from a gas turbine engine has received little attention and is currently poorly understood [51]. The effect of ambient air humidity on nvPM production in a diffusion flame was investigated during a test campaign at the GTRC facilities (section 3.4) on a generic swirl burner by sequentially injecting more vaporised water to the primary air used in the primary combustion zone from the dry base case. In order to ensure that the quantities of water injected were representative of relative humidity encountered at test cells around the world, vaporised water was mixed with the primary air from loadings representative of ICAO STP humidity of $0.0064 \text{ kg}_{\text{water}} / \text{kg}_{\text{air}}$ [14] to loadings of up to 800 mg/s corresponding to $0.05 \text{ kg}_{\text{water}} / \text{kg}_{\text{air}}$ which is equivalent to 100% humidity at 40°C and hence would cover all likely water loading scenarios for aircraft engine emission testing. To ensure change in rig conditions caused by water addition hadn't affected nvPM production, repeats of the dry case were done after injecting water in the primary combustion zone. Exhaust emissions were collected and measured by the EASA nvPM reference system and an additional DMS-500 and the EI's were derived from APC and MSS measurements.

The impact of elevated humidity on measured EI number is presented in **Figure 6-30**, for a range of fuel blends. Increased water loadings resulted in reductions in observed number and mass emission indices (as defined in section 1.5.1.2), and particle size. When looking at the exponential fit for the Jet A experiments, it is observed that there are ~40% and ~65% reductions in EI number and mass respectively over the tested water loading range. Similarly, a corresponding reduction in measured GMD from ~65 – 45 nm was observed, suggesting the water was either suppressing soot formation in the flame front, reducing soot concentrations in the post flame boundary or causing the larger soot aggregates to restructure to a more compact form. Exposition to high humidity of freshly formed soot aggregates can induce a reduction in mobility diameter, via restructuring to a more compact structure [192], [193]. De Risi et al. [194] also discussed that a change in absolute humidity in the burned zone gas causes change in specific heat, thus affecting soot formation. It is apparent that the nvPM reduction is chemically achieved rather than through dilution as the added water mass contributes to only 0.05% of the total mass of reactants.

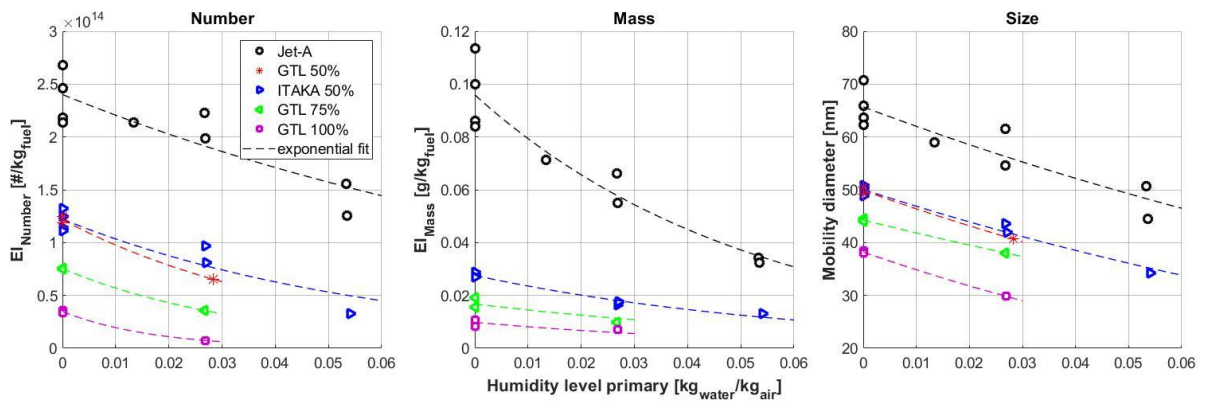


Figure 6-30: Reduction of Number (a), Mass (b) and Size (c) when injecting steam in the primary air for multiple fuels at primary diffusion flame Air-Fuel-Ratios of 6.2

Experimental investigations of humidity on nvPM reduction have demonstrated that increased volumes of water introduced within the primary combustion zones have correlated to nvPM reductions. Nevertheless, this phenomenon probably associated with reductions in primary soot formation may be offset by reduced soot burnout likely experienced in the cooler quench zone when high humidity is also present in the secondary combustion zone. Hence, it is difficult to interpret whether the reductions in measured nvPM observed in this study are witnessed in high pressure RQL combustors typical of large-scale engines experiencing humidity fluctuations. Large-scale engine testing performed over numerous days as part of the SAMPLE programme [49] on two engines variants namely Single Annular Combustor (SAC) and Dual Annular Combustor (DAC) provided limited data linking nvPM to relative ambient humidity.

6.3.2 Effect of fuel properties on nvPM emissions

The potential to produce nvPM emissions is highly influenced by the underlying properties of the fuel, especially the fuel aromatic content, which varies globally by several percent for conventional jet-A (15-23% (v/v)) [195]. Alternative fuels could also be used as replacements for conventional fuel to mitigate rising costs and security of supply of jet-A fuel. Alternative fuels have an additional benefit in that they have been shown to reduce non-volatile PM emissions via larger hydrogen content and lower aromatic content [93] which could potentially improve local air quality around airports [196] and mitigate contrail formation and hence the climate impact of aviation [39]. Brem et al. [195] showed that the comparison of two ICAO LTO cycles with jet-A fuels of different aromatic contents would result in up to 22% and 15% different nvPM mass and number emissions. Lobo et al. [71] reported that for a blend which would meet current ASTM International specifications, the average reduction in nvPM number number-based emissions was ~35%, while that for mass-based emissions was ~60%.

In the results presented below, nvPM emissions were generally plotted against the Hydrogen to Carbon (H/C) ratio as it correlated better with sooting tendencies of fuels than fuel aromatics and

was strongly interdependent with fuel total aromatic [195]. Also, nvPM emission indices (section 1.5.1.2) were corrected for fuel energy to allow better comparison between the fuel blends.

In this section, results from two distinct test campaigns are presented: firstly on a combustor rig at the GTRC facilities at atmospheric pressure using blends of Jet-A , Gas-To-Liquid (GTL) and Towards SustAinable Kerosene for Aviation (ITAKA) fuel (HEFA & Camelina derived) at numerous primary diffusion flame AFR's; Secondly, fourteen blends of alternative (HEFA & Camelina derived) and conventional (jet A) fuel were also tested on a Honeywell Garrett APU (section 3.4), as used in Boeing 737 aircraft, at three power settings. Exhaust emissions were collected and measured by the EASA nvPM reference system and EI_{number} were derived from nvPM number concentrations measured by an APC.

Data from the GTRC rig test is displayed in **Figure 6-31**, showing that the effect of fuel composition on nvPM formation is pronounced with increased concentrations of GLT or ITAKA (HEFA) fuel resulting in an observed decrease in measured EI number concentration at all power conditions (i.e. AFR). It is seen in **Figure 6-31 (a)** that increased hydrogen content in the fuel associated with a 100% GTL derived aviation kerosene with low aromatic content (0.05%) reduced nvPM number concentrations by up to an order of magnitude compared to a baseline Jet-A fuel with representative aromatic content (24.24%), with reductions also observed in nvPM mass and size. **Figure 6-31 (b)** presents the fuel effect data as a function of H/C ratio, showing good exponential correlation with increasing Hydrogen content, which is symptomatic of reducing aromatic concentrations witnessed in increasing alternative fuels content fuels. It is noted for EI number, an order of magnitude reduction is experienced with pure alternative fuel with a H/C ratio of 2.196 ($H_2 = 13.43\%$) compared to the base Jet-A fuel which had a H/C ratio of 1.861 ($H_2 = 15.47\%$), with progressively lower nvPM emissions noted for increasing volumes of alternative fuel, independent of fuel processing method.

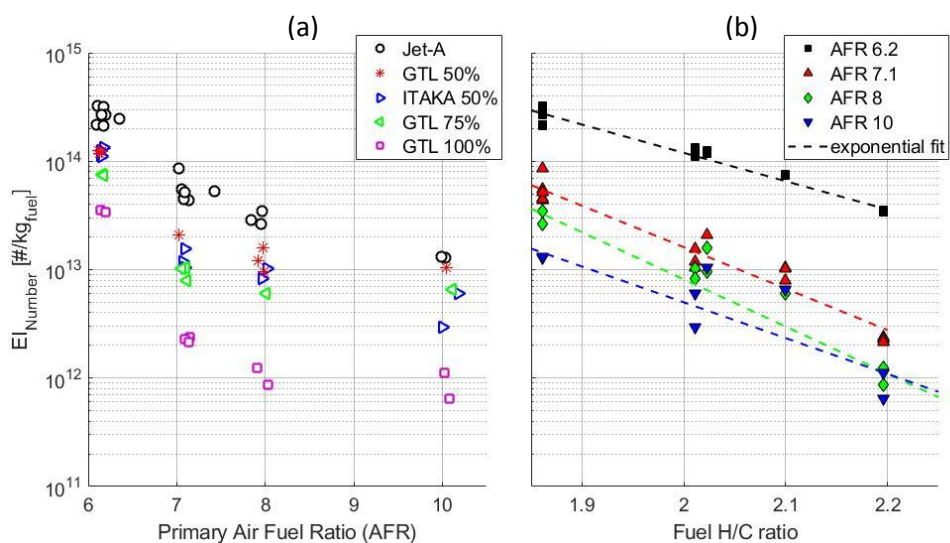


Figure 6-31: Effect of blends of alternative and conventional fuel on EI_{number} plotted against primary ARF (a) and Hydrogen/Carbon ratio (b)

During the APU testing, nvPM data was collected using the EASA reference system with additional size measurements taken by a DMS-500 which were subsequently analysed and used to investigate fuel effects on nvPM production. As seen in **Figure 6-32**, EI_{number} , EI_{mass} and GMD all decrease with increasing H/C ratio at all power settings, with a H/C ratio of 1.92 ($H_2 = 15.25\%$) representing the base jet A fuel and a H/C ratio of 2.144 ($H_2 = 13.88\%$) representing 100% ITAKA fuel.

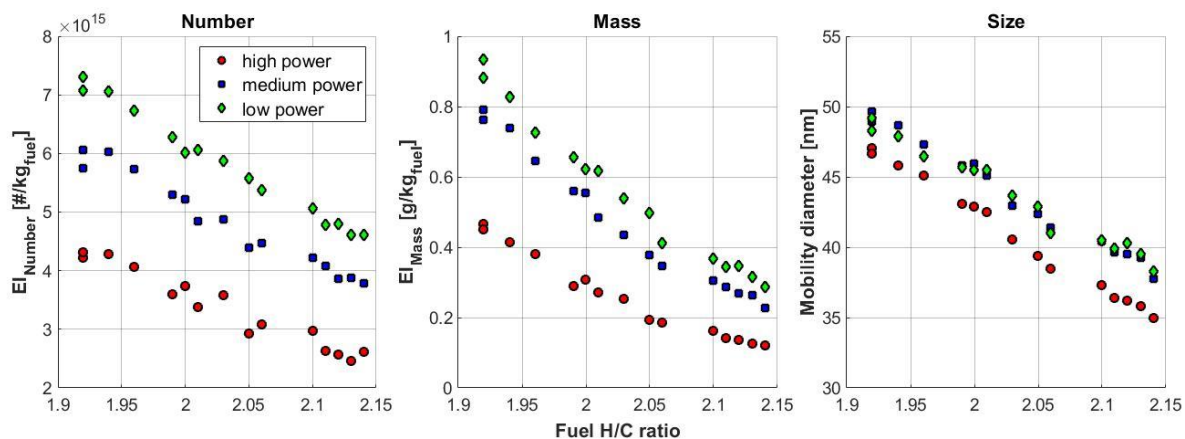


Figure 6-32: Effect of blends of alternative and conventional fuel on EI_{number} (a), EI_{mass} (b) and GMD (c) at three power conditions plotted against hydrogen/carbon ratio

The results from both test campaigns presented in **Figure 6-31** & **Figure 6-32** are in agreement with previous studies investigating the effect of alternative fuels on nvPM emissions from gas turbines [10], [21], [71], [93], [195]–[197] which also reported reductions in nvPM number, mass number and particle size with increasing H/C ratio in the fuel, indicative of lower aromatic content. This dependence has been explained as follows [195]: PAHs may be formed by condensed parent aromatic molecules present in conventional fuel acting as additions sites for products of incomplete combustion, subsequently nucleating and carbonising to form soot. In contrast to aromatics in alternative fuels, aliphatic have to undergo a slower fragmentation and aromatic ring formation process when compared with the aromatics pathway, resulting in less soot formation. It is also noted in the literature that larger soot effective densities were measured when using alternative fuels [21], with three plausible explanations to account for it: the material density of soot is greater for alternative fuel combustion, the size of the primary particles depends on the fuel properties, and the number of primary particles is smaller for alternative fuel combustion.

6.4 Chapter summary

In this chapter, PM emissions of four large-scale Rolls-Royce engine types representative of their commercial fleet were presented and discussed in depth along with an uncertainty analysis of the currently prescribed ICAO sampling and measurement system [14].

The advantage of an additional size measurement next to the prescribed nvPM measurements was highlighted, with measured size distribution permitting the assessment of the shape of emitted PM (GMD, GSD, lognormality), the derivation of an average particle effective density and the detection of potential volatile contamination when compared with nvPM data. It was shown that GSD correlated well with the N/M ratio independently of engine type and that measured size distributions were monomodal and appeared lognormal although deviation from lognormality was observed and shown to be dependent on the engine technology and power. Average particle effective densities derived from total volume (size measurement) and nvPM mass measurements ranged between 0.3 and 0.8 g/cm³.

Reported nvPM emission indices from large-scale engine nvPM certification testing may differ by several orders of magnitudes specific to engine power, engine technology and uncertainties within the sampling and measurement methodology. An allowed performance specification uncertainty of 66.3% for EI_{number} and 24.9% for EI_{mass} was estimated for the currently reported nvPM emission indices, not inclusive of other known uncertainties such as line shedding, humidity effects and fuel properties. These uncertainties could be reduced to 17.9% and 22.4% respectively by accounting for particle loss in the sampling and measurement system.

An investigation on nvPM morphology change in an ICAO compliant ejector diluter demonstrated that no size dependent losses occur within the diluter. It is noted that this experiment permitted the direct comparison between a TSI SMPS and a Cambustion DMS-500, which displayed similar size distribution shapes, GMD and GSD.

Additional uncertainties from humidity effects and increased hydrogen content in the fuel were also assessed. The hydrogen (aromatic content) of the fuel and humidity have been shown to affect aircraft engine nvPM generation and are an added uncertainty to aircraft nvPM reporting as both parameters are not currently accounted for in the regulation. Experimental investigations of fuel on nvPM reduction presented in this chapter support that increased Hydrogen and/or increased humidity within the diffusion combustion zone results in a reduction in nvPM number, mass and size. Increased volumes of low aromatic content fuels have been shown to reduce measured EI_{number} concentrations by up to an order of magnitude, which demonstrates the potential to improve local air quality surrounding airports now and in the future.

It was highlighted that shedding of particles from the sample line wall at sizes of 200-1000 nm could be occurring during nvPM measurement of aircraft engine exhaust and could bias the mass concentration measurements at low levels approaching the regulatory limit of detection of 1 µg/m³, which was shown to be the case for some modern engine types at low power conditions. Based on uncertainty of nvPM mass measurements near the regulatory limit of detection, a new limit of quantification of 5 µg/m³ was estimated. It has been shown to be challenging to characterise

shedding events with a fast response size instruments like the DMS-500 because of its minimum sensitivity at $\sim 10^3$ particles/cm³. Using an Optical Particle Counter (OPC) in parallel with other nvPM measurement during engine certification could be a useful addition to better characterise shedding events as it only measures particles from 300 nm and measures concentrations from 0 to 3000 particles/cm³ [98].

7 System Loss Correction of Regulatory nvPM

Measurements

As has been previously discussed, the sampling and measurement protocols for the regulation of aircraft engine non-volatile Particulate Matter (nvPM) emissions, which have been used for the majority of the measurements within this thesis, specify a standardised sample line length of up to 35 m, which coupled with the small GMD of nvPM witnessed from gas turbines result in significant particle loss before measurement at the calibrated analysers. Across the typical GMD range of civil aviation gas turbines (20-50 nm [51]), losses have been anticipated to be as high as 90% for number and 50% for mass [14], [57].

As different gas turbine generated aerosols have inherently different GMDs and hence size dependent losses, engine exit nvPM concentrations are required to facilitate inter-comparison of different engine technologies and power settings. These engine exit concentrations are also crucial for inventory purpose and understanding aviation impact on local air quality.

Historically, loss correction factors have been experimentally determined by measuring a size distribution upstream and downstream of a sampling system, as performed by Altaher et al. [175], Lobo et al. [93] and Delhaye et al. [61]. However as has been noted previously, there is no requirement for a size measurement in a compliant nvPM system, hence the necessity of a System Loss Tool (SLT) which has been proposed by the SAE E31 [57]. The SLT method uses the prescribed measured nvPM concentrations of mass and number with assumptions of particle density and Geometric Standard Deviation (GSD) to predict an engine exit size distribution which is subsequently used to estimate the number and mass correction factors $k_{SL_{num}}$ and $k_{SL_{mass}}$ using loss theory as described in sections **2.3** and **2.4**. The use of system loss correction factors significantly reduces emission indices uncertainty by accounting for losses in the sampling and measurement system. Recently, ICAO annex 16 volume II [14] was updated to prescribe the derivation of nvPM mass and number system loss corrections factors using the methodology described in Appendix 8, for reporting, inventory and modelling purposes.

Due to the recent publication of the SLT, to date, there are no appraisals of the loss correction concept in the literature. However, predictions have been made using the UTRC particle transport model on which the SLT is based together with the effective density and the measured size distribution corrected to the Engine Exit Plane (EEP), as shown by Durdina et al. [13], Brem et al. [195] and Boies et al [20].

The SLT uses default assumptions to predict a size distribution from measurements of number and mass only. Assumptions which are generally accepted as being representative of combustion nvPM [59] are further discussed in this chapter, namely:

- nvPM average effective density of 1 g/cm^3
- Particle size distribution is log-normal at the EEP
- GSD of the size distribution at the EEP is 1.8

To the author's knowledge, there is no appraisal of these assumptions for large-scale gas turbine in the public literature. Work previously presented in this thesis argues that assuming an effective density of 1 g/cm^3 (sections **2.2** & **6.1.3**) and a GSD of 1.8 (section **6.1.2.2**) could lead to unquantified uncertainties in predicted size across all engine types and powers. During the SAMPLE campaign [50], it was found that a modelled GMD from number and mass measurements was consistently smaller than the measured corrected GMD (order of two difference), resulting in differences in $k_{SL_{\text{num}}}$ of up to 100% and $k_{SL_{\text{mass}}}$ of up to 15%.

In this chapter, the assumptions of assumed particle effective density, GSD and lognormality were investigated using the SLT and data from certification nvPM measurements taken on four large-scale Roll-Royce engine types (Chapter **6**) with the aim of determining the uncertainty associated with the currently reported nvPM correction factors. To assess the accuracy of the ICAO prescribed system loss correction methodology [14], the SLT GMD predictions are compared to predictions made using an additional DMS-500 size measurement with relevant corrections to EEP. This work highlights the potential for improved loss correction methodology if an additional measure of size, not currently prescribed by regulation, is adopted.

7.1 System loss tool inputs

The System Loss Tool (SLT), as introduced in section **2.4**, estimates mass and number correction factors by first calculating a GMD at the inlet of the sampling system or section investigated. The desired outcome for nvPM aircraft emission research is to evaluate particle number and mass concentrations at the inlet of the sampling system (i.e. probe). The length and multitude of components in the sampling system result in significant particle loss. To enable size distributions measured by the DMS-500 to be compared with SLT predictions, individual loss corrections in the specific sampling system supplying each analyser were first made.

This section discusses the required inputs of the SLT (dimensions, flows, temperatures, etc), the different locations investigated in the sampling system and assesses size distribution correction and predictions.

7.1.1 Sampling system dimensions & locations

The System Loss Tool (SLT) requires inputs to facilitate correction factors calculations as listed below:

- Measured nvPM Number & Mass concentrations
- Dimensions & operation of the sampling system
- VPR penetration efficiencies at 15, 30, 50 & 100 nm
- CPC penetration efficiencies at 10 & 15 nm
- 1 μ m cyclone sharpness

For the data presented in this chapter, the nvPM mass concentration used for SLT appraisal was that measured by the AVL MSS and not the LII300 for reasons discussed previously (section 6.2.2). Otherwise the data used in the SLT is the same as discussed in Chapter 6. Similarly, for this analysis the size measurement was always conducted with a DMS-500. VPR and CPC penetration efficiencies were taken from the relevant annual calibration certificates and the cyclone sharpness was assumed as 1.25, being the maximum sharpness tolerated by ICAO regulation, because there is no prescription for individual annual calibration of the cyclone [14]. Subsequent sensitivity analysis of the cyclone sharpness has demonstrated negligible impact to SLT prediction for this dataset, hence validating this approach.

7.1.1.1 Sampling system dimensions

7.1.1.1.1 Dimensions Primary diluter to analysers

Table 7-1 lists the input dimensions of the EASA reference system (section 3.1.1) which was used as an exemplar in order to appraise the SLT. These dimensions were used to predict loss corrections required from the entrance of the primary diluter down to each measurement instrument at the end of the sampling system. Values representative of the Roll-Royce collection section are not included in **Table 7-1** for proprietary reasons as later discussed. The sampling system is divided into multiple sections, with some sections common to all measuring instruments highlighted by the header 'All' and other sections dedicated to a specific flow path highlighted by the specific instrument heading (e.g. size, mass or number), further details of measurement flow paths are described in section 3.1.1. Idealised flow conditions and system operation were assumed for all comparisons (e.g. temperatures of 160°C and 60°C pre and post-dilution, flowrate 25 Lpm, pressure 1atm, etc).

Table 7-1: Inputs used in the UTRC particle transport model to calculate typical penetration efficiencies from each instrument to the inlet of the collection section (i.e. splitter 1)

	Instruments → Primary Diluter									
	Instruments → 1 st common point									
	Heated dilution line	Size out to split3	VPR out to split3	Split3 to split2	0.8m line	0.8m out to split2	Split2 to cyclone	25 m sample line	Long line to diluter inlet	Diluter out to splitter1
Section	5	4	4	4	4	4	4	3	2	2
Analyzer	Size	Size	Number	Number & Size	Mass	Mass	All	All	All	All
T_{gas} [K]	333	333	333	333	333	333	333	333	333	433
T_{wall} [K]	333	333	333	333	333	333	333	333	333	433
P_{gas} [atm]	0.25	1	1	1	1	1	1	1	1	1
flow [Lpm]	8	8	4	13.5	3.2	3.2	25	25	25	25
D_{tube} [mm]	4.572	7.747	4.572	7.747	8	7.747	7.747	8	7.747	7.747
L_{tube} [cm]	500	30	30	5	80	65	10	2500	40	46
Bend [°]	360	270	270	0	180	240	0	720	0	0

An example of a typical penetration function derived for the parameters stated in **Table 7-1** is presented in **Figure 7-1** with different losses occurring for the three different analysers given the slightly different sampling path and losses within the instruments (e.g. VPR loss in APC). It is noted that **Figure 7-1** only represents losses from the entrance of the primary diluter (losses in the collection probe are not included).

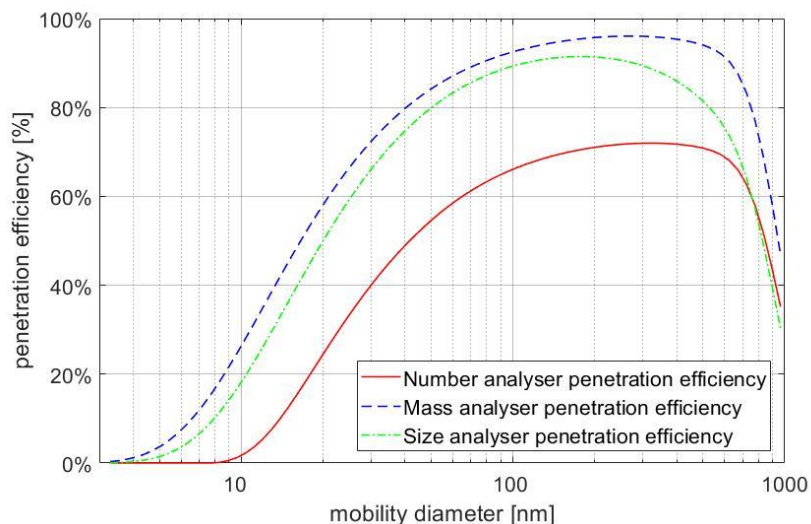


Figure 7-1: Typical Number, Mass and Size penetration efficiencies calculated using the UTRC model for a compliant aircraft engine emission sampling system (excluding collection section)

As expected from size dependant loss theory, it is observed that losses are maximal for all instruments at the smallest sizes because of higher diffusional loss, and that the penetration efficiency is highest in the 100-500 nm region. The penetration efficiency reduces from around 600 nm because of the 1 μm cyclone sharpness, bend and inertial losses. Penetration efficiency for the number instrument, particularly at the smallest sizes, are noted as the lowest due to the additional losses witnessed in the VPR and counting efficiency in the CPC ($d_{50}=10$ nm). The penetration efficiency of the size instrument is slightly lower than that of the mass instrument due to the use of the additional 5m heated dilution line.

7.1.1.1.2 Dimensions collection section

As previously discussed in section 6.2.4.3, the collection section of a regulatory compliant sampling system consists of a sampling probe and flow path up to 8 m length connecting the probe to Splitter 1 (Figure 3-1). Sampling probe design is commercially sensitive information, thus specific geometries are typically not shared by OEM's. Consequently, losses in a 'hypothetical' collection section are conjectured in this chapter. Based on personal experience and the work presented in section 6.2.4.3, dimensions of a 'typical' collection section were selected as shown in Table 7-2 and used in this analysis. It is noted that an exhaust gas temperature of 160°C was chosen, even though in reality it can reach a temperature of 700°C [53], because thermophoretic losses in the collection section are separately accounted-for by the prescribed thermophoretic correction section (k_{thermo}).

Table 7-2: Inputs used in the UTRC particle transport model to calculate typical penetration efficiencies in the collection section

Section	Collection section
Instrument	All
T_{gas} [K]	433
T_{wall} [K]	433
P_{gas} [atm]	1
flow [sLpm]	50
D_{tube} [mm]	7.747
L_{tube} [cm]	800
Bend [$^{\circ}$]	0

7.1.1.2 Sampling system locations used in loss correction analysis

Later in this chapter, the GMD derived from DMS-500 measurements is assumed as the true particle size to which System Loss Tool (SLT) predictions are compared. However, as previously

discussed the DMS-500, AVL APC and AVL MSS all have subtly different sample flow paths hence direct comparisons of their measured concentrations, given the different witnessed losses, cannot be made without first correcting their respective concentrations back to a common position in their respective sampling paths.

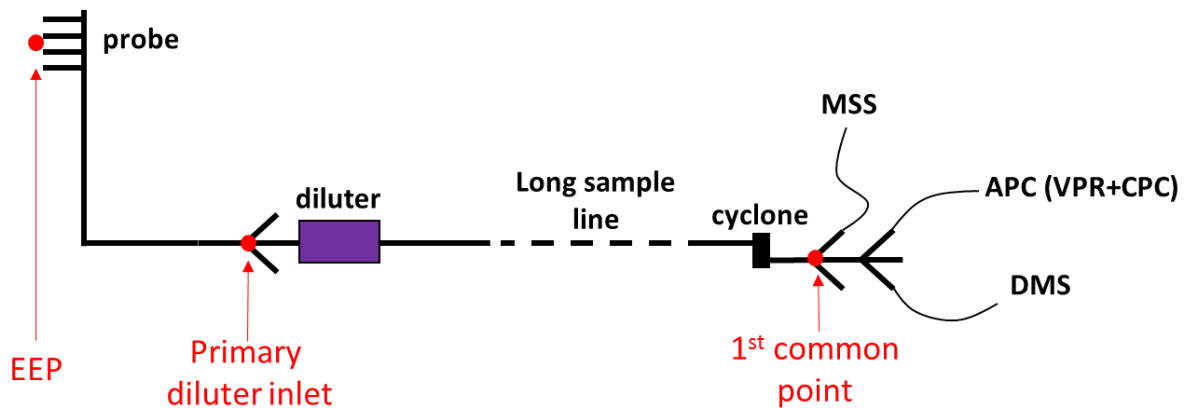


Figure 7-2: Diagram of an ICAO compliant sampling system with key locations for comparison of SLT

In this chapter, three locations of the sampling system were investigated, represented in **Figure 7-2** as:

- The 1st common point (i.e. splitter 2) – represents the final location in the sampling system flow path which is common to all measuring instruments corresponding to the splitter located on the outlet of the cyclone. Being the closest common point to the measuring instruments, this is the location where applied loss corrections are minimum.
- The Primary Diluter inlet (i.e. Dilution Box entrance) – includes all sample flow paths from the diluter inlet to the specific instruments, (splitter 1, diluter, 25 m sample line, cyclone, splitter 2, specific instrument inlets). This is the closest point to the engine exhaust from which the dimensions and operation of the sampled aerosol are standardised across compliant nvPM systems.
- The Engine Exit Plane (i.e. inlet to sample probe) – Location from where the engine exhaust enters the particle sampling system. The SLT was originally designed to correct to the EEP to quantify the true number and mass of emitted particles. As it includes the entire sampling system, it has the highest loss correction.

Example Particle Size Distributions (PSD) at the different investigated locations of the sampling system are presented in **Figure 7-3** where an assumed measured distribution at the DMS is corrected for losses back to each sampling location. As would be expected, it is seen that the measured PSD displays the lowest number concentrations and largest GMD. Getting closer to the EEP, more loss corrections are applied to the original PSD, increasing its number concentration,

preferentially for the smallest particles, hence reducing the predicted GMD due to the size-dependent nature of the losses.

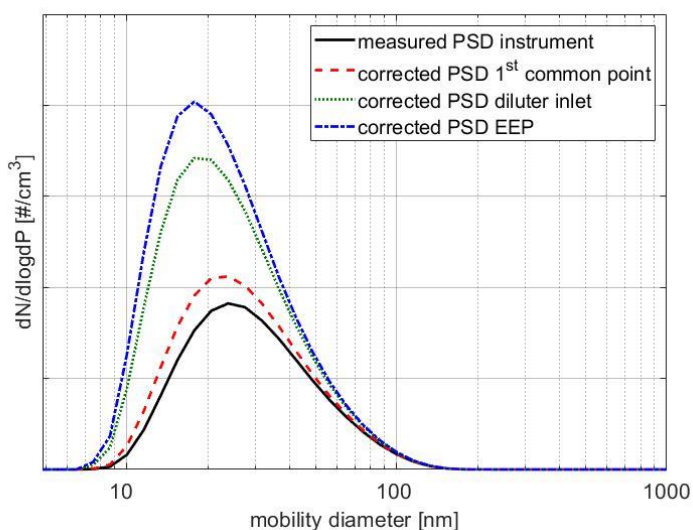


Figure 7-3: Example of a PSD measured by the DMS-500 at end of compliant sampling system, corrected for losses to various location of the sampling system

7.1.2 Prediction of GMD & GSD using measured size distribution

7.1.2.1 Removal of artefacts from size distributions

As previously shown in **Figure 7-1**, penetration efficiency in a regulatory compliant sampling system is low at sizes smaller than 20 nm. Correcting the measured Particle Size Distributions (PSD) for losses can sometimes produce an artefact (additional mode) resulting from the multiplication of the low concentrations of small particles (left-hand tail of the distribution) by relatively large correction factors derived from their poor penetration efficiencies. Such artefacts are highlighted in **Figure 7-4**, which are examples selected from the data reported in Chapter 6 from large-scale Rolls Royce Engines. If unaccounted for, the artefact can result in unrealistic estimations of GMDs and GSDs. In a SAMPLE campaign [50], large artefacts were observed when correcting measured PSD to the engine exit plane, and were deemed unrealistic. However, as the DMS is measuring total PM, these artefacts could be symptomatic of a volatile nucleation mode at engine exit but in such a case this again should not be included as a measure of nvPM.

A tail-cutting method similar to the method described to remove artefact peaks for DMS-500 derived volume size distributions at large sizes (section 6.1.2.3) was again used to remove the artefact introduced by loss correction, as highlighted by the dashed line in **Figure 7-4**. The size distribution data for all four engine types presented in this chapter were corrected using the tail-cutting methodology if an inflection was observed to the left-hand side of the distributions main nvPM peak. Similarly, artefacts to the right-hand side of the distribution, symptomatic of line

shedding, were also removed if an inflection was witnessed to the right-hand side of the distribution main nvPM peak. Because losses in the sampling system are typically negligible for larger particles (see **Figure 7-1**), the removal of the large-size artefact generally had a negligible impact.

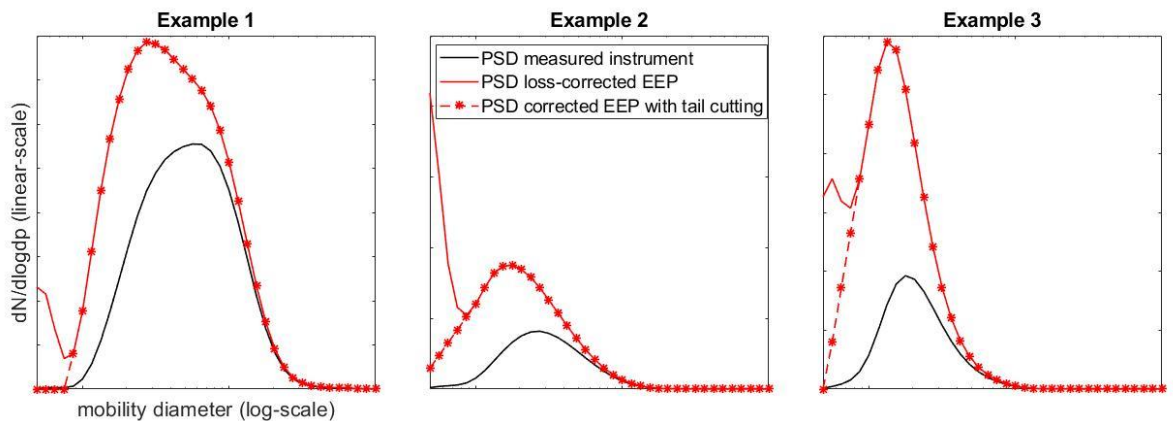


Figure 7-4: Examples of artefacts appearing when correcting some measured PSD down to the EEP

7.1.2.2 Predicted GMD and GSD

Using the penetration efficiencies estimated by the UTRC particle transport model and correcting for artefact secondary peaks as discussed in section **7.1.2.1**, the size distributions measured by the DMS-500 for four engine types were corrected to three locations in the sampling system namely: the 1st common point, the inlet of the primary diluter and the Engine Exit Plane (EEP) (section **7.1.1.2**). GMDs and GSDs were derived from the corrected size distributions at the different locations of the sampling system using equations **(2.2)** and **(2.4)**, respectively. A particle density of 1 g/cm³ was used in the UTRC model to estimate penetration efficiencies. It is noted that varying the density between 0.3-1.4 g/cm³ varied the predicted GMD by less than 0.5%, hence the impact of this assumption was considered negligible.

Using combined data of the four Rolls-Royce engine types, **Figure 7-5 (a)** displays measured and predicted GMDs plotted against the N/M ratio at different locations of the sampling system. Generally, the GMD decreases with increasing N/M ratio (i.e. decreasing engine power) and the scatter observed at each sampling location may be attributed to engine type specific particle effective density as previously discussed (**Figure 6-4**). It is noted that the light blue data (instrument) in **Figure 7-5** corresponds to the combined data previously presented in **Figure 7-4**. Power fits were observed to best fit the data (based on R²) at each sampling location and are presented in **Figure 7-5 (b)**. It can be seen that predicted GMDs are generally smaller than measured GMDs, with the smallest GMDs being at the EEP due to smaller particles to being preferentially lost during transport. This trend was also reported in the supplementary information by Boies et al. [20]. The GMD predicted at the 1st common point is on average 1.6 ± 0.4 nm larger than the GMD measured at the instrument. Similarly, GMDs predicted at the primary diluter inlet are larger by 6.4 ± 1.6 nm, and GMDs predicted

at the EPP larger still by 7.7 ± 2.2 nm when compared with measured GMDs. The highest GMD increase occurs between the 1st common point and the primary diluter inlet because the majority of particle loss occur in the standardised 25 m long sample line. It is also noted that the scatter around the power law fit increases from instrument, to 1st common point, to diluter inlet and EEP resulting in a reduction of $R^2=0.92$ to 0.81 resulting from larger corrections applied to the distributions.

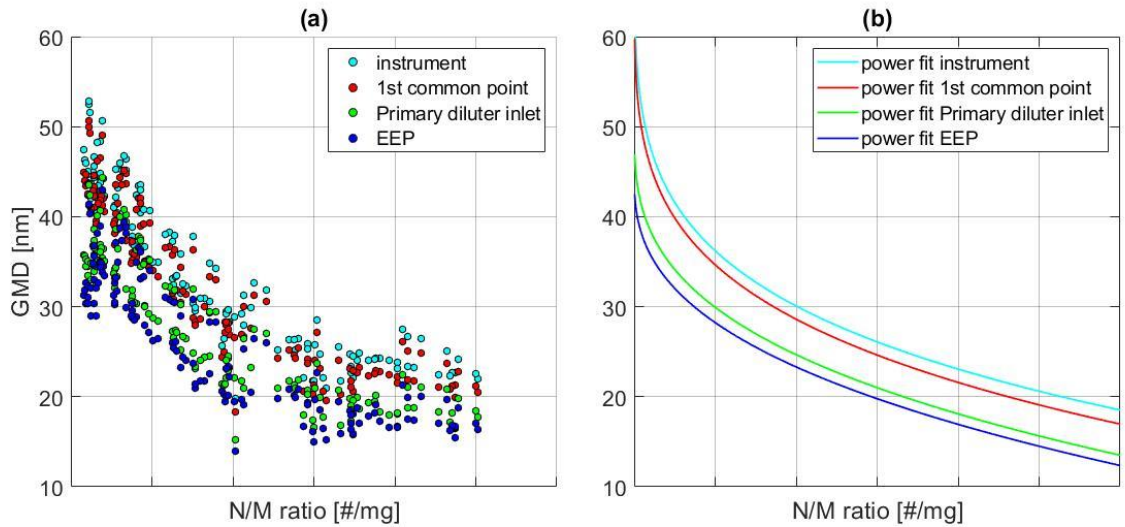


Figure 7-5: GMD Vs N/M ratio at multiple locations of the sampling system with power fits

Figure 7-6 shows the measured and predicted GSDs against the N/M ratio at different locations of the sampling system. As previously discussed with **Figure 6-4**, the GSD generally decreases with increasing N/M ratio. Exponential fits were shown to best fit the data as presented in **Figure 7-6 (b)** with R^2 values ≥ 0.83 , and it noted that the GSD doesn't significantly change with the location, except at lower N/M ratios where the GSD is slightly larger at the EEP.

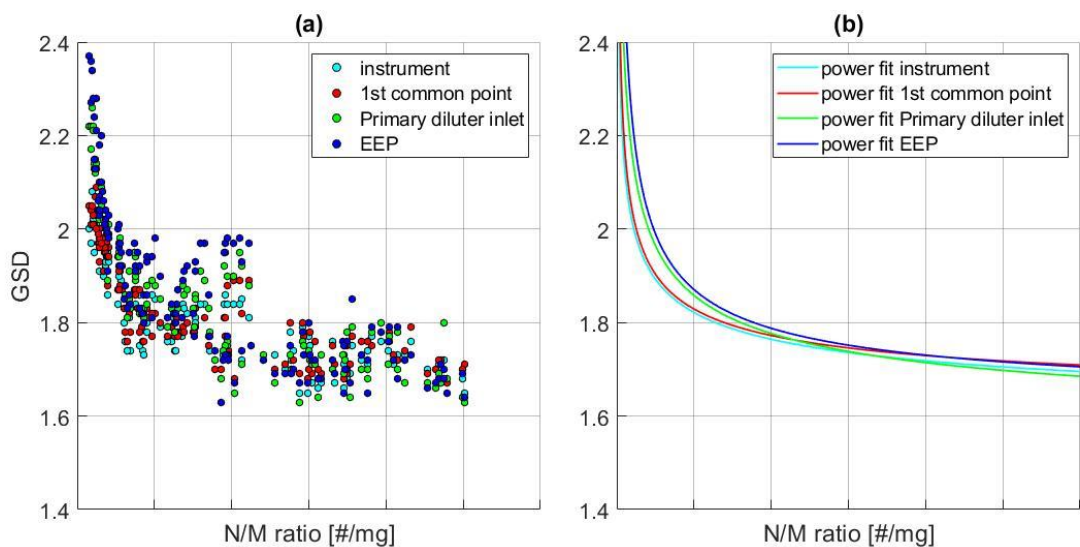


Figure 7-6: GSD Vs N/M ratio at multiple locations of the sampling system (a) with power fits (b)

To determine if predicted GSD and GMD correlate, the EEP GMD and GSD were plotted against one and other **Figure 7-7**, and compared to a polynomial fit from Lobo et al. [9] which was derived from PM measurements from several in-service commercial aircraft engines. It is observed that GSD typically increases with GMD at the EEP for all engine types as previously shown at the measurement location (**Figure 6-5**). The scatter between different engine types may originate from the added uncertainty of correcting measured size distributions to the EEP. The difference between the data from engine type 1-4 and Lobo et al. [9] may arise from the different sampling system used. Indeed, Lobo et al. [9] experimentally characterised their sampling system penetration efficiency which was significantly lower than a typical compliant sampling system as represented by **Figure 7-1**. It is noted that the larger GSDs observed with engine type 4 may be a result of the higher number concentrations recorded by the DMS in the small 4.5-20 nm size bins resulting from volatile inclusions discussed in section **6.2.1.2**.

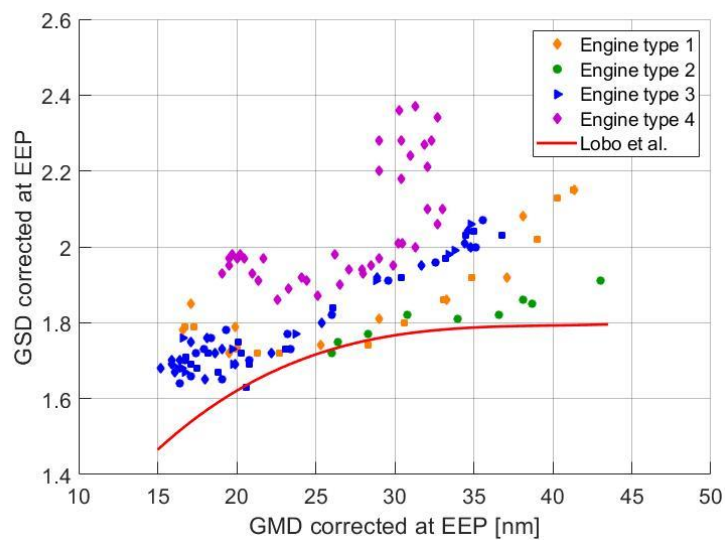


Figure 7-7: Engine Exit Plane (EEP) corrected GMD against EEP GSD on various engine types

As previously discussed, the current System Loss Tool assumes a GMD of 1.8 at the EEP which corresponds to the asymptote of the Lobo et al. [9] fit shown in **Figure 7-7**. However, in the case of the four Rolls-Royce engine types tested in this work, this assumed GSD generally under-predicts the EEP derived GSD.

To assess the equivalence between measured and predicted GMDs, the measured GMD was plotted against the GMD predicted at the EEP as presented in **Figure 7-8**. It can be seen that the predicted GMD increases linearly with the measured GMD as previously observed by Boies et al. [20] for a gas turbine with a double annular combustor. The different slope determined by Boies et al. can be explained by the different correction methodology used as Boies et al. [20] only corrected for losses in a 25 metres long line at a temperature of 160°C with the UTRC particle transport model, hence applied lower correction factors to their measured size distributions.

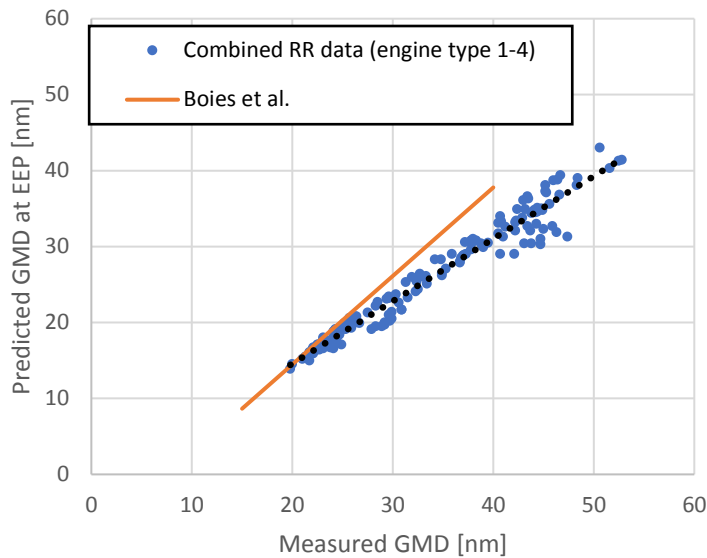


Figure 7-8: Measured GMD of four combined engine types against GMD predicted at the Engine Exit Plane (EEP) with linear trends

7.2 SLT lognormality assumption at Engine Exit Plane

As discussed previously and introduced in this chapter, the System Loss Tool (SLT) assumes a lognormal Particle Size Distribution (PSD) at the Engine Exit Plane (EEP) coupled with the predicted GMD and assumed GSD to estimate correction factors from measured number and mass concentrations. Deviations from lognormality may increase errors/uncertainties of the number and mass correction factors estimated by the SLT.

In this section, the lognormal assumption at the EEP is interrogated using the predicted size distributions at EEP by comparing GMD/CMD and GSD_{PSD}/GSD_{VSD} using similar methodologies discussed in section 6.1.2.4. The impact of assumed lognormality on number and mass correction factors is also assessed.

7.2.1 Assessment of lognormality using assumed lognormal distribution at exit plane

If a lognormal PSD is assumed at EEP, then logically the measured size distribution should become less lognormal along the sample path length as losses are size-dependent. **Figure 7-9** highlights this using a mathematically generated EEP lognormal aerosol of 25 nm GMD and 1.8 GSD (black distribution). Applying typical sampling system losses (dashed blue line) to the EEP distribution, a slightly skewed distribution is observed at the instrument (red distribution). It is noted that dilution correction was not applied to this analysis as the relative concentrations of each size bin

were not being investigated, rather the size and shape of the distribution in order to assess lognormality.

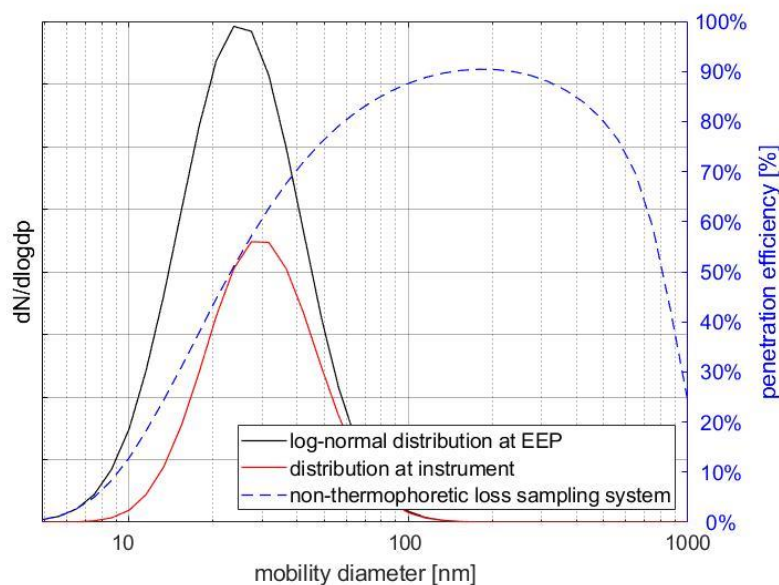


Figure 7-9: Lognormal distribution at the Engine Exit Plan and the estimated distribution at the instrument after applying typical non-thermophoretic size-dependent sampling system loss (Dilution omitted)

To determine the non-lognormality of the distribution as measured at the instrument whilst the EEP distribution is assumed lognormal, three example lognormal size distributions at EEP with different GMDs and GSDs representative of aircraft PM were assessed. Loss correction to these example distributions yielded predicted distributions at the instrument, as displayed in **Table 7-3**, to assess the level of lognormality.

It is observed from the results in **Table 7-3** that the CMD is generally smaller than the GMD at the instrument by up to 1.1% ($GMD > CMD$). Also, GSDs of the volume- and number-size distributions vary by 1.7-5.3% with GSD_{VSD} generally larger ($GSD_{VSD} > GSD_{PSD}$). This indicates that if nvPM size distributions were lognormal at the EEP, they by definition become skewed, exhibiting a longer right-hand tail and/or a slightly shorter left-hand tail when measured after the sampling system (scenario (1) of **Table 6-1**).

As expected for larger sized aerosols the deviation from lognormality is reduced compared to the smaller aerosols as the penetration efficiency is more consistent across the distribution. When comparing with the previously discussed lognormality assessment at the instrument (i.e. measured size distributions) shown in **Figure 6-8**, it is seen that size distributions meeting the criteria listed above are only observed with engine type 4 when the GMD is below 25 nm (low power conditions). Generally, the measured differences between GMDs, CMDs and GSDs discussed with **Figure 6-8** are

higher than the expected differences listed in **Table 7-3**, suggesting that the size distributions of the four engine types are not perfectly lognormal at the EEP.

Table 7-3 : Examples of the predicted GMD, CMD and GSDs from PSD and VSD at the instrument when assuming a lognormal distribution at the EEP and accounting for losses in the sampling system

	GMD	CMD	GSD _{PSD} (number)	GSD _{VSD} (volume)	$\frac{\text{GMD} - \text{CMD}}{\text{GMD}}$	$\frac{\text{GSD}_{\text{PSD}} - \text{GSD}_{\text{VSD}}}{\text{GSD}_{\text{PSD}}}$
EEP (lognormal)	15	15	1.65	1.65		
Instrument	20.4	20.2	1.51	1.59	1%	-5.3%
EEP (lognormal)	30	30	1.8	1.8		
Instrument	36.9	36.5	1.70	1.75	1.1%	-2.9%
EEP (lognormal)	60	60	1.8	1.8		
Instrument	65.9	65.5	1.73	1.76	0.6%	-1.7%

7.2.2 Assessment of lognormality using predicted size distributions at the EEP

Size distributions measured during emission certification tests of four Rolls-Royce aircraft engine types were corrected to EEP by applying typical sampling system line losses with an assumed particle effective density of 1 g/cm³ (section 7.1.2).

The results of the lognormality assessment of the predicted size distributions at the EEP are presented in **Figure 7-10 (a)** displaying the GMD/CMD difference, and **Figure 7-10 (b)** displaying the GSD_{PSD}/GSD_{VSD} difference. It can be seen at small GMDs (low engine powers) that GMD>CMD and GSD_{PSD}<GSD_{VSD}. This is indicative that PSDs have a longer right and/or a shorter left tail. At larger GMDs (high engine powers), the difference between the CMD and GMD ranges between 0-5% depending on the engine type and GSD_{PSD} > GSD_{VSD}. Using **Table 6-1**, these results may indicate that predicted distributions at the EEP have a shorter right tail which could originate from the highly fractal nature of soot at larger sizes or that line shedding has less impact at higher powers given the larger distributions and higher concentrations.

When comparing **Figure 7-10** results with the lognormality assessment of the measured size distributions presented at the instrument (**Figure 6-8**), the predicted size distributions at the EEP

appear to be less lognormal than the size distributions at the instrument, given the GMD/CMD and GSD_{PSD}/GSD_{VSD} are approximately 2% higher on average.

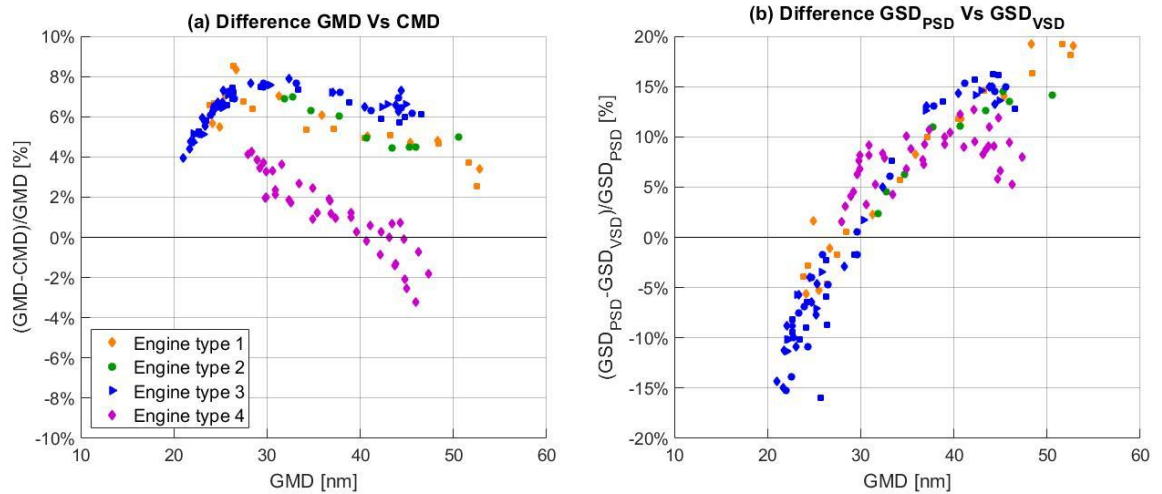


Figure 7-10: Lognormality assessment at the Engine Exit Plane by means of comparing GMD and CMD (a) and GSD_{PSD} and GSD_{VSD} (b)

7.2.3 Correction factor uncertainty associated with lognormality assumptions

As discussed previously, the SLT uses the assumptions of lognormality and GSD coupled with a predicted GMD to generate a size distribution at EEP. A penetration function is combined with the EEP size distribution to generate a distribution at the instruments to estimate the number and mass corrections factors using equation (7.1).

$$k_{SL} = \frac{\sum(N_{\text{dist}_{EEP}}(d_p \geq 10\text{nm}))}{\sum(N_{\text{dist}_{EEP}} * f_{\text{loss}})} \quad (7.1)$$

Lognormal assumptions don't affect SLT GMD predictions but can play an important role in the estimation of the number and mass correction factors. It has been shown (section 7.2.2) that predicted size distributions are generally non-lognormal at the EEP. An investigation of the correction factors ($k_{SL_{\text{num}}}$ and $k_{SL_{\text{mass}}}$) was undertaken using both the lognormal assumption (with the DMS-predicted GMD and GSD) and the generally not lognormal predicted distribution shape derived from DMS-500 measurements, with the differences presented in Figure 7-11. Using the lognormal assumption at the EEP the average $k_{SL_{\text{num}}}$ varied by $16.2 \pm 4.6\%$ (up to 24.5%) and $k_{SL_{\text{mass}}}$ by $4.6 \pm 3.6\%$ (up to 13.5%) when compared with the predicted distributions.

It is observed in Figure 7-11 (a) that the difference in $k_{SL_{\text{num}}}$ is generally overpredicted with the lognormal assumption and that the agreement becomes better with increasing GMD. This trend may be explained by the predicted PSD having a smaller left-hand tail than the lognormally generated

distribution at the EEP. The difference in predictions reduces with increasing GMD, indicating the predicted distribution is more lognormal with increasing GMD and because of the lower correction factors at larger GMDs.

It is seen in **Figure 7-11 (b)** that the difference in $k_{SL_{mass}}$ is generally overpredicted when assuming lognormality at smaller GMDs and underpredicted at larger GMDs. As the mass is generally carried in the right-hand tail of the PSD, this may imply that predicted size distributions at the EEP have a relatively larger right-hand tail at smaller GMDs and a smaller right-hand tail at larger GMDs. It can be seen with engine type 2 and 3, and to a lesser extent engine type 1, that the right-hand tail of the predicted distributions agrees with the lognormal distribution. These results are in line with the lognormality assessment at the EEP performed using predicted size distribution (section 7.2.2).

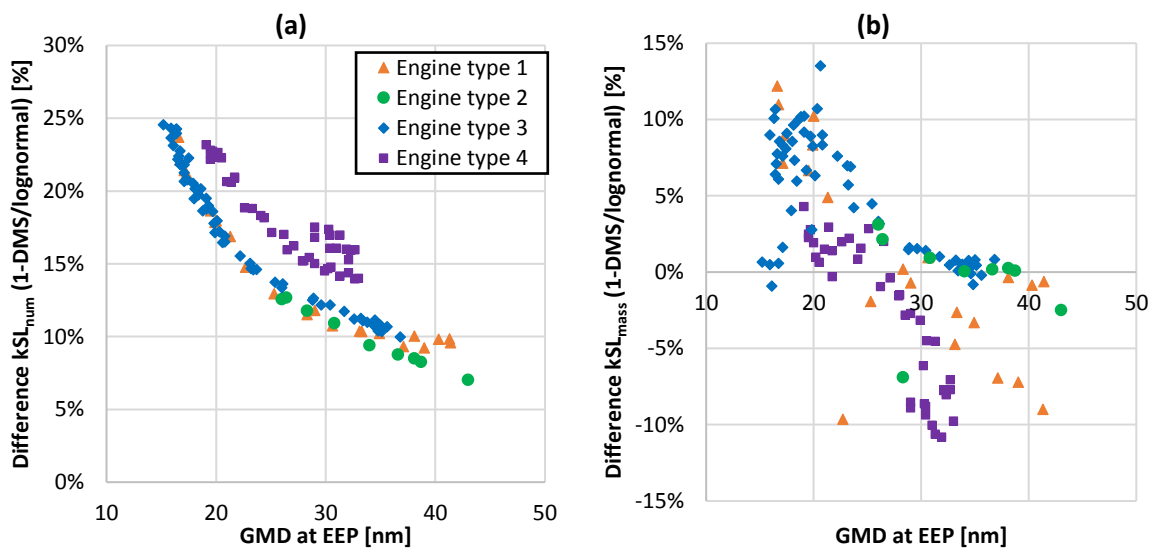


Figure 7-11: Difference in number (a) and mass (b) correction factors for four engine types estimated using the DMS-500 predicted size distributions and a lognormal distribution generated from the PSD's GMD and GSD

As such, these results highlight an additional 25% uncertainty in $k_{SL_{num}}$ and 10% uncertainty in $k_{SL_{mass}}$ is observed at $GMD < 20$ nm due to lognormal assumption.

7.3 SLT GSD and particle density assumptions

The SLT predicts a GMD at EEP using the assumption of a particle effective density (1 g/cm^3) and GSD (1.8). The predicted GMD and assumed GSD are used to generate a lognormal distribution at the EEP from which line loss correction factors are estimated. To the author's knowledge, there is no appraisal of the GMD and loss correction factors predicted by the SLT using the current assumptions in the literature. Moreover, results discussed in chapter 6 suggest that the current

assumptions of constant particle effective density and GSD may not be appropriate for the four Rolls-Royce engine types.

In this section, particle effective density and GSD assumptions are assessed by comparing the SLT size predictions to the measured-derived GMDs at different locations of the sampling system. The aim of this work was to assess the accuracy and validity of the current SLT assumptions for various engine types and to propose potential improvements.

7.3.1 Effect of assumed density and GSD on SLT predictions

It is reminded that combustion exhaust particles aren't perfectly spherical and have voids, hence are best described using an effective density term which is a function of material density and particle shape (section 2.2). The particle effective density term currently used in the SLT refers to an average effective density valid for all particle sizes. Although the proposed effective density of 1 g/cm^3 was determined from the literature [63], most research available in the literature suggests that particle effective density is size-dependent and could significantly vary with engine type, power conditions, and fuel. In this study, it was found that the average effective density calculated from measured nvPM mass concentration and total volume varied from 0.3 to 0.8 g/cm^3 (section 6.1.3).

Varying the assumed particle effective density in the SLT can have a significant impact on the predicted GMD and hence correction factors. For example, Durdina et al. [63] found $k_{SL_{mass}}$ to vary by 5-20% when changing the average effective density of 1 g/cm^3 to the size-dependent effective densities. Given the SLT uses the effective density to convert the number-size distribution to the mass-size distribution using the total black carbon mass (M_{MSS}), the total nvPM number (N_{APC}) and assuming $\text{nvPM} \approx \text{black carbon}$, it may be assumed that particle effective density in the SLT should be the average black carbon (i.e. nvPM) effective density, as calculated from the ratio of measured mass to size derived volume.

The particle effective density is used in the SLT as discussed below:

- In the UTRC particle transport model, particle density is used for the calculation of particle relaxation time and Stokes number, which are used to predict inertial and bend losses, predominantly affecting the larger particles (i.e. $d_p > 100 \text{ nm}$).
- In the mass correction factor (i.e. $k_{SL_{mass}}$) calculation, particle density is used to convert Number-size distributions (i.e. PSD) into Mass-size distributions for each size bin of the size distribution (equation (2.6)).
- In the Chi-Squared minimisation to predict the exit plane GMD, particle density is used to predict mass at the EEP.

The SLT assumed GSD (1.8) is used to set the width of the generated log-normal distribution at the EEP. As the mass and number correction factors are calculated by dividing the log-normal distribution at the EEP with the distribution at the instruments, the GSD can significantly impact both correction factors $k_{SL_{num}}$ and $k_{SL_{mass}}$.

Findings from the literature (section 6.1.2.2) highlight measured GSDs vary between 1.3 to 2.3 hence the current constant GSD assumption leads to varying inaccuracies dependant on engine type and power. In this work, predicted GSD at the EEP was shown to vary between 1.6 and 2.4 (Figure 7-6). Boies et al. [20] used an assumed constant GSD of 1.7 at the EEP to estimate correction factors using measured corrected PSD and measured density and found that the impact of varying the GSD had little impact (<10% relative error) on overall line loss correction factors for the one engine tested.

7.3.2 Comparison of GMD predicted by SLT and size measurement

In this section, measured nvPM number and mass are used as input for the SLT to predict a GMD at the different locations of the sampling system using various particle effective densities and GSDs. The GMD predicted by the SLT is compared to GMD derived from measured size distributions to assess the uncertainty associated with the density and GSD assumptions in number and mass correction factors.

7.3.2.1 Comparison using default SLT GSD and density assumptions

To assess the accuracy of the SLT with the default assumptions (GSD=1.8 and $\rho_{eff}=1 \text{ g/cm}^3$), the SLT-predicted GMD was plotted against the measured-derived GMD at the three different locations in the sampling system (section 7.1.1.2). The results are presented in Figure 7-12 with the black line again representing the 1:1 correlation and the dashed lines symbolizing $\pm 10\%$ uncertainty bands derived from the DMS size calibration uncertainty (section 6.2.3.1).

It is observed that most data points do not lie within the given uncertainty at any of the three locations, with the SLT GMD consistently underpredicting the measured-derived GMD at lower GMDs and overpredicting at large GMDs. The average difference between the modelled and measured-derived GMD was estimated to be approximately 19.5% as shown in Table 7-4. The engine specific trends and the average difference of 19.5% are indicative of GSD and effective density varying with GMD and hence engine power (sections 6.1.2.2 & 6.1.3.2). During a SAMPLE campaign [50], it was similarly observed for GMDs <40 nm that a predicted GMD was always smaller than the measured corrected GMD with differences of up to 100% stated. Assuming the GMD derived from size measurement is precise, it can be concluded that the SLT with the current GSD and density

assumption doesn't perform well over the majority of the data from the four Rolls-Royce engine types measured in this study.

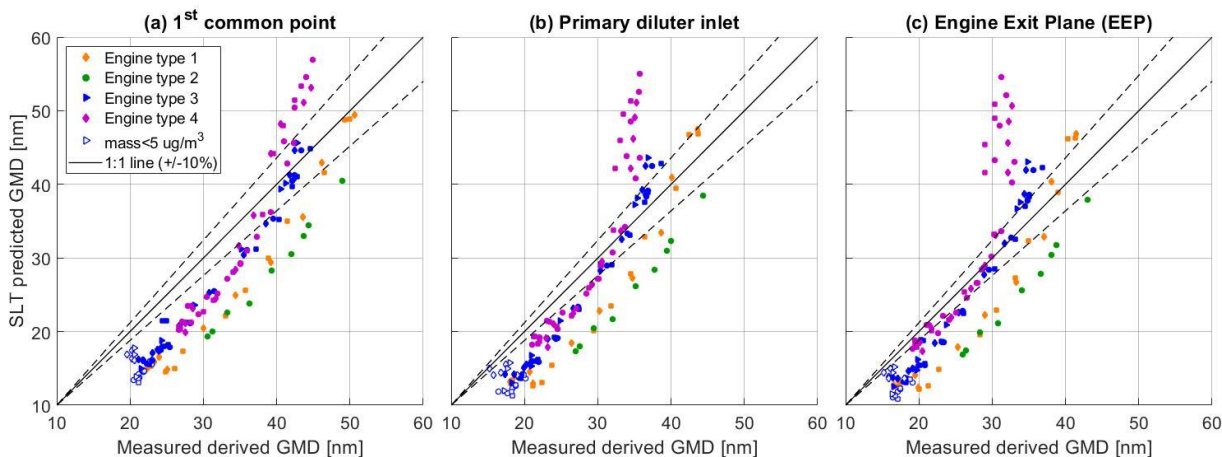


Figure 7-12: Measured-derived GMD against SLT-predicted GMD using default density and GSD assumptions for different engine types at various locations of the sampling system

An uncertainty analysis was performed on the input measured number and mass concentration to better understand the scatter observed in **Figure 7-12**. GMDs were predicted at the EEP using the default SLT and varying the input nvPM mass and nvPM with their respective measurement/calibration uncertainties (i.e. 19.5% for nvPM mass measurement and 14.1% for nvPM number measurement as defined in section 6.2). It was found that SLT GMD predictions varied by $16.1 \pm 2.2\%$ on average. Substituting these uncertainties into the SLT results in up to 13.9% and 7.4% variations in reported number and mass correction factors, respectively. Hence, the poor agreement observed in **Figure 7-12** may in part be attributed to the nvPM number and mass measurement uncertainty.

When comparing sampling system locations, it can be seen in **Table 7-4** that the average differences between SLT-predicted GMDs and measured-derived GMDs remain around 19.5% regardless of the sampling location and hence loss penetration correction. However, the scatter as defined by the standard deviation increases from the 1st common point to the EEP which may be symptomatic of the higher uncertainty introduced by larger loss corrections.

Table 7-4: Average absolute difference between predicted and measured corrected GMDs at different locations of the sampling system for four engine types combined (Mass > LOQ)

	1 st common point	Primary diluter inlet	EEP
Average GMD difference (\pm STD)	$19.7 \pm 10.1\%$	$19.3 \pm 12\%$	$19.4 \pm 15.4\%$

It should be noted that at large GMDs (i.e. high engine powers), the SLT-predicted significantly larger GMDs for engine type 4, which again may be attributed to the potential volatile contamination (section 6.2.1.2).

To analyse how correction factors fluctuate with the predicted GMD when using default density and GSD, $k_{SL_{num}}$ and $k_{SL_{mass}}$ were respectively plotted against the SLT GMD at different locations of the sampling system as presented in **Figure 7-13**.

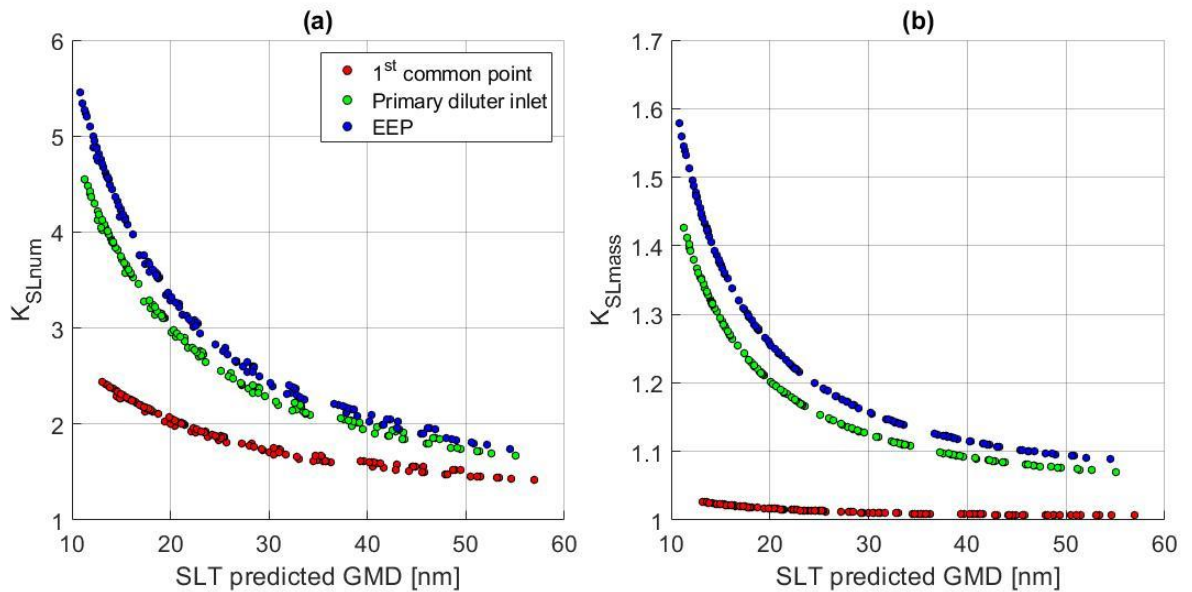


Figure 7-13: Number (a) and Mass (b) correction factors against SLT GMD using default density and GSD assumptions at different locations of the sampling system for four Rolls-Royce Engine Types

As expected, it is observed that both number and mass correction factors are higher the further from instrument the sampling location is. $k_{SL_{num}}$ and $k_{SL_{mass}}$ are seen to decrease with increasing GMD, as a result of the size-dependent nature of sampling loss. It is also noted that the trends observed in **Figure 7-13**, with the plotted data combining different engine types, are remarkably smooth due to the assumed typical sampling system dimension and operation (section 7.1.1).

At the EEP, $k_{SL_{num}}$ varied from 1.8 to 5.5 and $k_{SL_{mass}}$ ranges from 1.1 to 1.6 non-inclusive of thermophoretic loss in the collection section. Similarly, Boies et al. [20] proposed mass correction factors are smaller than number correction factors because number weighted distributions are dominated by small particles whereas mass is proportional to d_p^3 hence are dominated by larger particles with smaller loss corrections. The range of calculated $k_{SL_{num}}$ and $k_{SL_{mass}}$ displayed in **Figure 7-13** concurs with previously proposed correction factors. Using measured size distributions and effective densities, Durdina et al. [63] estimated $k_{SL_{mass}}$ from 2.8 at low thrust (i.e. smaller GMD) down to 1.5 at maximum thrust (i.e. larger GMD). Brem et al. [195] evaluated $k_{SL_{mass}}$ from 1.52 to 2.1 and $k_{SL_{num}}$ ranging between 3.8 to 9.2. Boies et al. [20] estimated $k_{SL_{num}}$ varying from 1.7 to 4.4 and $k_{SL_{mass}}$ varying from 1.5 to 2.2. Delhaye et al. [61] measured a number correction

factor of 6.25 for their sampling system. A SAMPLE campaign [50] estimated $k_{SL_{num}}$ from 3 to 9.5 and $k_{SL_{mass}}$ from 1.4 to 2.05.

7.3.2.2 Comparison using measured-derived GSD and density

In this section, instead of the default SLT assumptions ($GSD = 1.8$ & $\rho_{eff} = 1 \text{ g/cm}^3$), GSD and particle effective density derived from measured size distribution and nvPM mass were used in an attempt to improve the agreement between measured corrected and modelled GMDs. For each data point, the GSD was taken from the measured-derived size distributions (section 7.1.2), and the average particle effective density was estimated using the size derived volume distribution and nvPM mass concentrations (section 6.1.3).

To assess the SLT accuracy with the newly assumed GSD and density, the SLT-predicted GMD was plotted against the measured-derived GMD is presented in **Figure 7-14**.

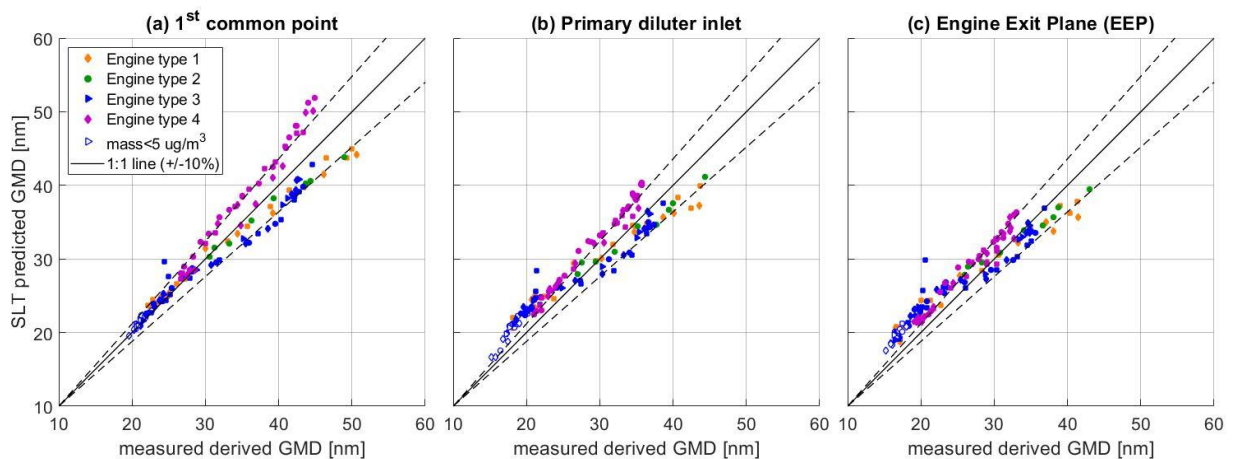


Figure 7-14: Measured-derived GMD against SLT-predicted GMD using measured-derived GSD and density assumptions for different engine types at various locations of the sampling system

It is noted that the agreement between GMDs has generally improved compared to the previous predictions using default assumptions (**Figure 7-12**). Indeed, the majority of the data points in **Figure 7-14** now agree within the 10% uncertainty bands and the average absolute difference at the EEP reduced to $9.3 \pm 6.8\%$, even with an average effective density uncertainty of 27.9% (section 6.1.3.1) and nvPM number and mass uncertainties of 14.1% and 19.5%, respectively (section 6.2). Similarly, it was observed in a SAMPLE campaign [50] that lowering the assumed density from 1 g/cm^3 to 0.55 g/cm^3 significantly improved the agreement between the predicted GMD and the GMD derived from SMPS measurements on a small Helicopter engine. It is observed at the primary diluter inlet and EEP (**Figure 7-14 (b)&(c)**) that the SLT GMD overpredicts the measured-derived GMD at small sizes ($< 25 \text{ nm}$). This may be indicative of the measured-derived average effective density being underpredicted at smaller GMDs or that the density changes in the sampling system.

When comparing the different sampling locations, the correlation between the SLT-predicted and measured-derived GMD is better at the 1st common point with an average difference of $6.4 \pm 4.3\%$. This may be explained by the fact that the assumed average effective density (mass/volume) was estimated at the 1st common point and may slightly vary with the sampling location. Using the measured-derived GSD and density it is noted that predicted SLT GMDs overpredict the measured-derived values at small GMDs (<20 nm) at locations further from the instrument. Again, it should be noted that engine type 4 seems to behave differently from engine type 1-3 because the average effective density for engine type 4 data may have been underpredicted due to potential volatile PM presence as discussed in section 6.1.3.2.

The results presented in **Figure 7-14** demonstrate that additional size distribution measurement significantly improves the agreement of the SLT GMD predictions (~factor of two) by providing a GSD and an average effective density when combined with nvPM mass measurement, hence giving more confidence in the generated number and mass correction factors.

The difference in SLT-predicted mass and number correction factors were also investigated using both the default assumptions of density and GSD and using the density and GSD derived from measured size distribution and nvPM mass concentration as discussed above. The difference $\frac{k_{SL\text{default}} - k_{SL\text{meas}}}{k_{SL\text{meas}}}$ is presented for both number and mass correction factors in **Figure 7-15**.

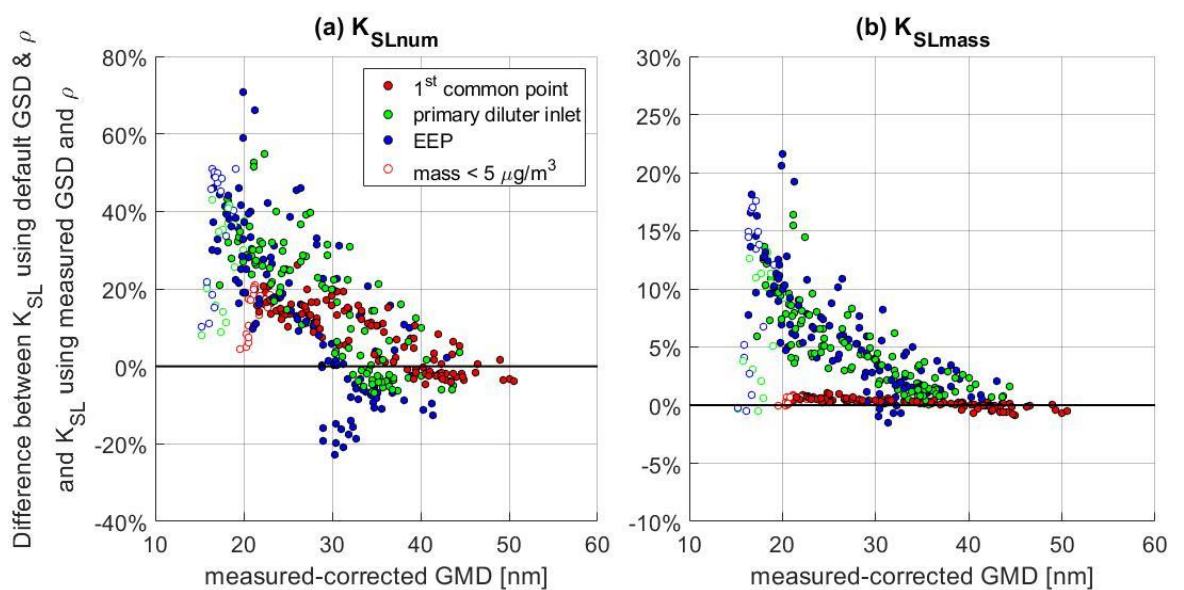


Figure 7-15: Differences in number (a) and mass (b) correction factors estimated from the System Loss Tool using the combined data of four engine types with different density and GSD assumptions

It is observed that changing the particle effective density and GSD assumptions lead to differences of up to 70.9% for number correction factors and 21.6% for mass correction factors at the EEP, as listed in **Table 7-5**. This again highlights the importance of the GSD and density assumptions in SLT predictions. The difference in **Figure 7-15 (a)&(b)** tend to reduce with increasing

GMD, indicating that the default assumptions ($GSD = 1.8$ & $\rho_{eff} = 1 \text{ g/cm}^3$) may be more accurate at larger GMDs with the investigated data-set.

When comparing the sampling system locations, the difference in $k_{SL_{num}}$ and $k_{SL_{mass}}$ is largest at the EEP due to higher loss corrections, hence larger differences with varying GSD and density assumptions. It is noted that the small group of EEP data points (blue) with negative $k_{SL_{num}}$ correspond to engine type 4 data at large GMDs which was previously shown to deviate (**Figure 7-12**) due to a potential volatile contamination (**6.2.1.2**) modifying the particle effective density and GSD. Differences in correction factors when changing the density and/or GSD assumptions were also witnessed in a SAMPLE report [50] and by Durdina et al. [63] who stated that $k_{SL_{mass}}$ varied by 5 to 20% when changing the effective density from 1 g/cm^3 to their measured size-dependent effective density (ranging between 0.6 & 1.6 g/cm^3).

Table 7-5: Maximum difference of SLT number and mass correction factors using different density and GSD assumptions at multiple locations of the sampling system using combined data of four engine types

	1 st common point	Primary diluter	EEP
Max Difference $k_{sl_{num}}$	26.3%	54.9%	70.9%
Max Difference $k_{sl_{mass}}$	1.1%	16.4%	21.6%

7.3.2.3 Comparison using empirically derived GSD and density correlations

It was previously demonstrated that using particle effective densities and GSD derived from an additional size distribution measurement improved the correlation between the SLT GMD predictions and the measured-derived GMD (**Figure 7-14**). However, given the current regulation doesn't prescribe a size measurement, it may not be possible to derive effective densities and GSDs during engine certification testing. In an attempt to improve the SLT predictions without the requirement of a specific size measurement, it was assessed if empirically derived correlations for GSD and average particle effective density could improve SLT predictions. Given nvPM number and mass concentrations are inputs in the SLT, correlations from the four Rolls-Royce engines were made to the N/M ratio as defined in equation (**6.1**). It is noted that in this section, correlations are only presented at the EEP.

Proposed GSD fit:

As previously discussed with **Figure 6-4** and **Figure 7-6**, it was observed that the GSD decreases with a power law for increasing N/M ratio at both the instrument and EEP, with good agreement noted for the four engine types. Hence, the default SLT GSD assumption of 1.8 was

replaced by a correlation fit at the EEP. This correlation derived from the data presented in **Figure 7-6** is given in equation (7.2). It is noted that data with mass below the LOQ ($5 \mu\text{g}/\text{m}^3$) was disregarded for the fit presented below.

$$\text{GSD}_{\text{EEP}} = 2.1503 \times 10^6 \times \left(\frac{N_{\text{meas}}}{M_{\text{meas}}} \times 10^9 \right)^{-0.5310} + 1.6014 \quad (7.2)$$

Proposed average particle effective density:

As previously discussed with **Figure 6-12**, it was shown that the measured-derived average effective density of the four engine types typically varied between 0.3 and 0.8 g/cm^3 . Hence, densities estimated for different Rolls-Royces engines did not agree with the default density assumption of 1 g/cm^3 valid for a commercial turbofan engine CFM56-7B26/3 [63].

Similarly to the GSD, the default density assumption was replaced by a correlation fit empirically derived from data presented in **Figure 6-12** and given in equation (7.3). Data with mass below the LOQ ($5 \mu\text{g}/\text{m}^3$) were again disregarded for the fit presented below. It is noted that the density fit poorly explains the data with a R^2 of 0.34, due to particle effective density being engine specific as discuss previously (section 6.1.3). however, it was anticipated that it would still improve agreement between SLT-predicted and measured-derived GMDs.

$$\rho_{\text{eff}^{\text{fit}}} = 1.19 \times 10^{-28} \times \left(\frac{N_{\text{meas}}}{M_{\text{meas}}} \times 10^9 \right)^2 - 9.66 \times 10^{-15} \times \left(\frac{N_{\text{meas}}}{M_{\text{meas}}} \times 10^9 \right) + 0.656 \quad (7.3)$$

GMDs were predicted at the EEP using the SLT with the newly proposed GSD and density fits (equations (7.2) & (7.3)) and compared with measured-derived GMD, as presented in **Figure 7-16**.

The GMD difference using the GSD fit and default density ($1 \text{ g}/\text{cm}^3$) in the SLT (**Figure 7-16(a)**) is shown to slightly reduce ($18.2\% \pm 8.3\%$) when compared with the default GSD and density assumptions ($19.4 \pm 15.4\%$). When using the GSD fit only, it can be seen that the SLT GMD is underpredicting the measured-derived GMD, especially at larger GMDs where the GSD is supposedly larger. On the other hand, the GMD difference was increased to $25.8 \pm 22.5\%$ when using the default GSD (1.8) and the density fit in the SLT (**Figure 7-16(b)**), with an observed SLT GMD overprediction, particularly at larger GMDs where the density is smaller.

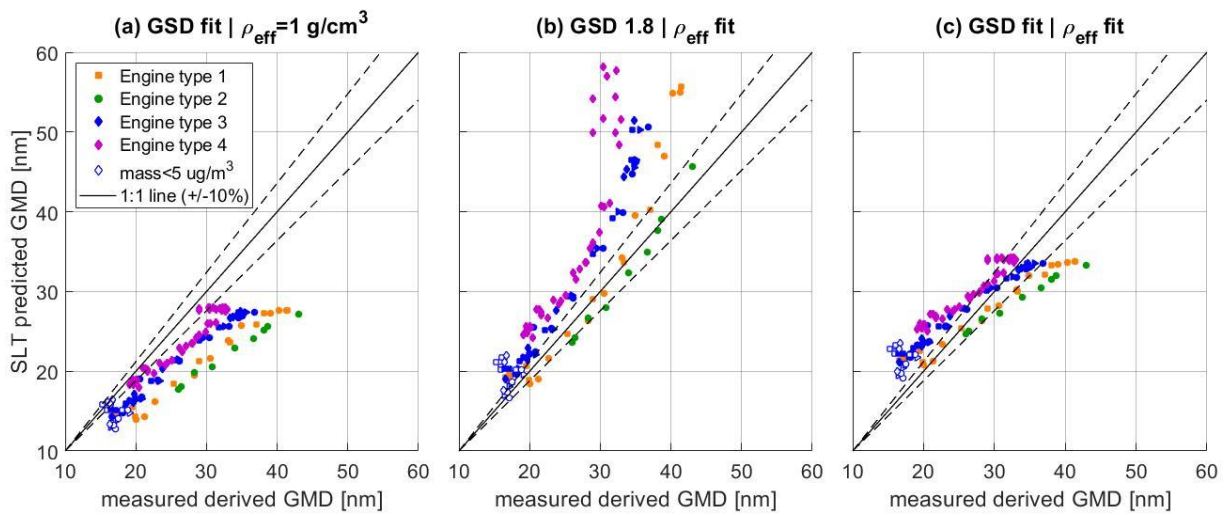


Figure 7-16: Measured-derived GMD against SLT-predicted GMD using empirically derived GSD and density assumptions for different engine types at the EEP

When using both the empirically derived GSD and density (**Figure 7-16(c)**), significant improvement in the agreement between the SLT-predicted GMD and measured-derived GMD is observed with an average difference of $13.2 \pm 8.9\%$. It can be concluded that both the density and GSD assumptions are important for accurate SLT predictions and that replacing the default GSD and density assumptions by empirical fits improved the correlation between SLT and measured-derived GMDs for the four engine types, however the correlation wasn't generally as good as with the measured-derived assumptions ($9.3 \pm 6.8\%$).

Because the density fit poorly explained the measured density for the investigated data, SLT performances were also examined using an 'optimal' constant average particle effective density. Using the GSD fit (equation **(7.2)**) and forcing the SLT GMD to agree with the measured-derived GMD at the EEP, it was found that the 'optimal' particle average effective density for this data was $0.62 \pm 0.12 \text{ g/cm}^3$.

The SLT-predicted GMD using the GSD fit and a density of 0.62 was plotted against the measured-derived GMD as presented in **Figure 7-17**. With those assumptions, the average difference between the GMDs was reduced to $9.2 \pm 5.8\%$ corresponding to the best GMD agreement obtained so far for the combined four engine types.

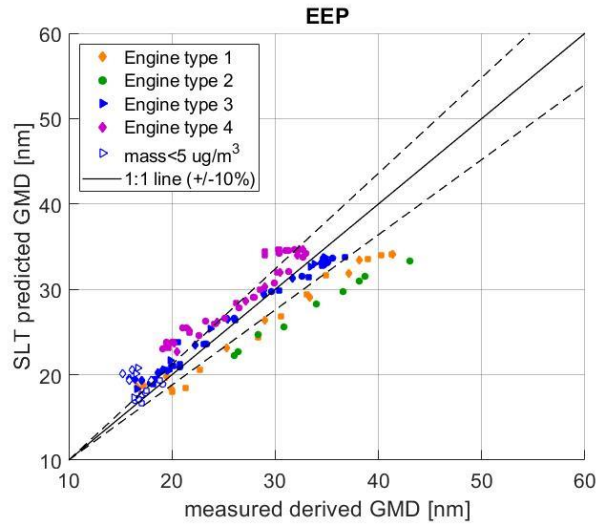


Figure 7-17: Measured-derived GMD against SLT-predicted GMD using a GSD fit and $\rho_{\text{eff}} = 0.62 \text{ g/cm}^3$ assumptions for different engine types at the Engine Exit Plane (EEP)

7.3.2.4 Comparison using historical size-dependent effective density

As previously discussed (section 2.2), aircraft PM effective density is size-dependent and can vary with engine type, engine power, fuel and sampling conditioning (i.e. volatile remover). As suggested in a SAMPLE report [50], using a size-dependent density instead of the current average effective density in the SLT may improve its accuracy. However, because of the observed dependency of size-dependent particle effective density to mobility diameter and engine power (Figure 2-4) both differently related to the N/M ratio (Figure 6-2), it was expected that using a size-dependent effective density may actually not improve the correlations. In contrast, average particle effective density does not appear dependent on engine power [63].

In this section, the default average effective density assumption of 1 g/cm^3 was replaced by a size-dependent effective density derived from the literature to investigate if it would improve agreement between SLT-predicted and measured-derived GMDs. It is noted that small modifications in the STL code were necessary to use a size-dependent density.

Given aircraft PM size-dependent effective density data from the literature is very scattered (Table 2-1), a fit was derived from reported size-dependent densities measured using a compliant sampling system on gas turbines representative of modern engines at medium to high power settings [51], [69], [72], [127]. The size-dependent effective density derived from the literature is given below:

$$\rho_{\text{eff}}(d_p) = 3.11 \times (d_p[\text{nm}])^{2.664-3} \quad (7.4)$$

Using the size-dependent effective density from equation (7.4) with the default GSD assumption (i.e. 1.8) or the empirical GSD fit (equation (7.2)), SLT GMD predictions were compared with the measured-derived GMD and the EEP as presented in **Figure 7-18**.

When comparing the size-dependent effective density (**Figure 7-18(a)**) with the default density (**Figure 7-12(c)**) using a GSD of 1.8, it was witnessed that the GMD correlation did not improve with an average difference of $25.1 \pm 24.6\%$ (Vs. 19.4% with $\rho_{\text{eff}} = 1 \text{ g/cm}^3$).

As previously demonstrated, it was shown in **Figure 7-18(b)** that using an empirical GSD fit instead of 1.8 (**Figure 7-18(a)**) significantly improved the GMD agreement, with an average difference reduced to $10.2 \pm 7.9\%$ in this case. When comparing the literature derived size-dependent effective density assumption with the measured-derived average effective density (**Figure 7-14 (c)**), the GMD correlation is slightly better with the latter ($9.3 \pm 6.8\%$).

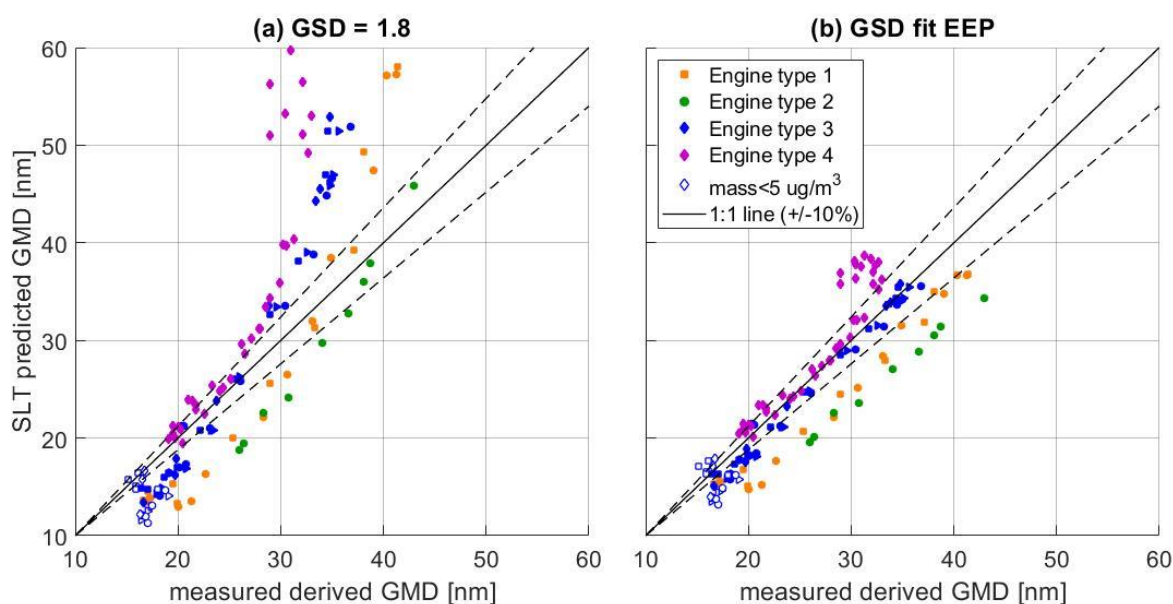


Figure 7-18: Measured-derived GMD against SLT-predicted GMD using GSD=1.8 (a) or GSD from fit at the EEP (b) and a size-dependent effective density derived from the literature for different engine types at the EEP

It is noted that the size-dependent effective density derived from the literature (equation (7.4)) averaged to $0.99 \pm 0.08 \text{ g/cm}^3$ although the ‘optimal’ density was previously found to be 0.62 g/cm^3 (section 7.3.2.3) for the four investigated engine types. Consequently, SLT predictions were also assessed using a generated size-dependent density which averaged toⁱⁱ 0.62 g/cm^3 to examine if GMD correlations could be further improved. However, this new size-dependent effective density

ⁱⁱ size-dependent effective density averaging at 0.62 was estimated using $\rho_{\text{eff}}(d_p) = C * d_p^{D_m-3}$ with $C = 3.45$ and $D_m = 2.42$. It is noted that multiple other combinations of C and D_m would also result in an average of 0.62 for the investigated data.

combined with the GSD from the empirical fit worsened the difference between the SLT-predicted GMD and measured-derived GMD to an average of $43.1 \pm 23.2\%$, showing that using a size-dependent density averaging at 0.99 g/cm^3 was a better assumption for GMD correlation.

7.3.2.5 Comparison using DMS-500 number concentration

In this section, the total PM number concentration derived from the additional size measurement (DMS-500) was used as a SLT input replacing the usual nvPM number concentration (APC). One advantage of using the total number concentration derived from a size instrument is the absence of additional VPR and CPC loss, lowering the number loss correction factor, hence reducing the uncertainty.

To assess how the SLT correlated with the new number concentration input, the SLT-predicted GMD was again compared to the measured-derived GMD at the EEP as presented in **Figure 7-19** and **Figure 7-20**. It is noted that extra losses in the DMS-500 heated dilution line needed to be accounted for the number sample path.

With the default density and GSD assumptions, it is witnessed that using the number concentration from size measurement (**Figure 7-19(b)**) instead of the regulatory compliant nvPM number (**Figure 7-19(a)**) in the SLT improved the GMD agreement by approximately 4%, from 19.4% (section 7.3.2.1) down to 15.7%. Better correlations were anticipated as the SLT GMD predicted using the number concentration from the size instrument is compared to the GMD from that same instrument.

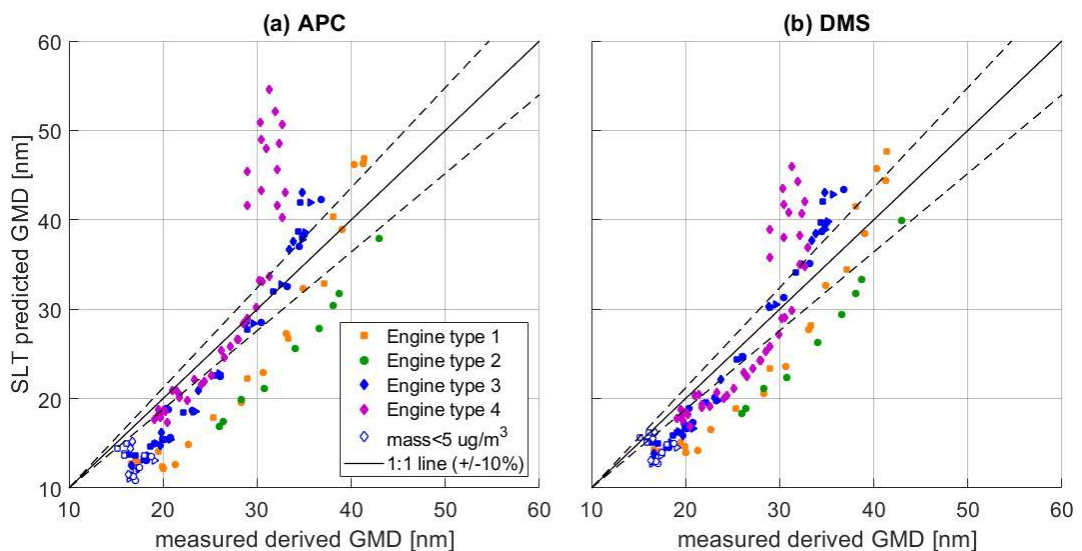


Figure 7-19: Measured-derived GMD against SLT-predicted GMD using default assumptions and the input APC nvPM number (a) or the DMS-500 total number (b) for different engine types at the EEP

With the measured-derived density and GSD assumptions, it was again observed that the GMD correlation improved when using the total PM number measurement as seen in **Figure 7-20**, with the average GMD difference decreasing from 9.2% (**Figure 7-20(a)**) previously reported in section 7.3.2.2) to 8.4% (**Figure 7-20(b)**).

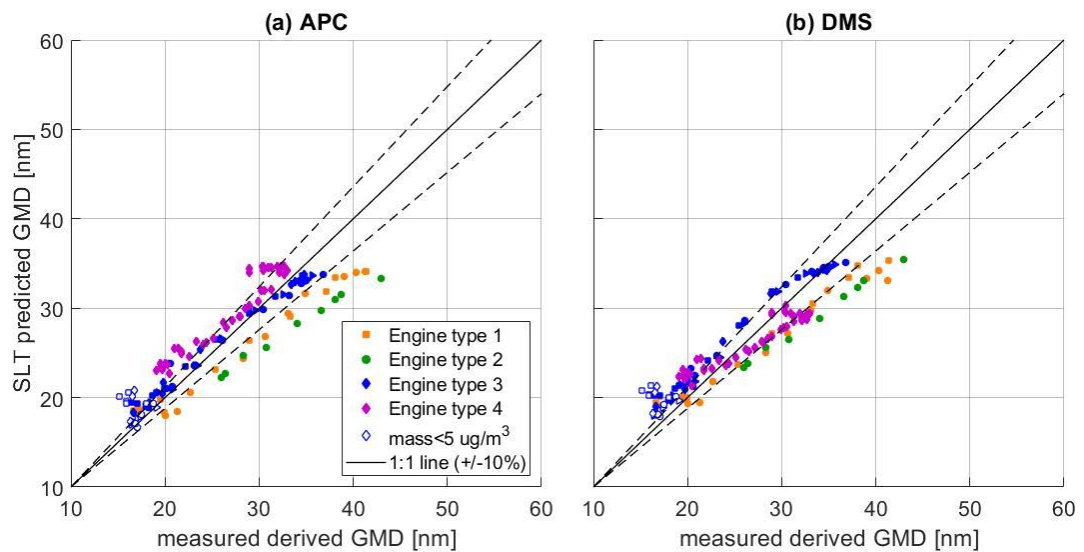


Figure 7-20: Measured-derived GMD against SLT-predicted GMD using measured-derived assumptions and the input APC nvPM number (a) or the DMS-500 total number (b) for different engine types at the EEP

It was again observed that engine type 4 behaved differently when comparing SLT predictions using the nvPM or total PM number concentration, indicative of a potential volatile contamination (section 6.2.1.2). Indeed, it was previously observed for engine type 4 that the total PM number concentration increased relatively to the nvPM number (**Figure 6-16**). Hence, for a given nvPM mass, the SLT GMD predictions using the total PM number were logically smaller when compared with nvPM number as the N/M ratio increases, as highlighted in **Figure 7-20 (b)**.

7.4 Chapter Summary

A System Loss Tool (SLT) has recently been proposed by the SAE E-31 committee [57] to correct for size-dependent particles losses occurring in an ICAO compliant sampling system [14] when measuring nvPM emission from certification testing of aircraft engines. The correction methodology aims to reduce the uncertainty associated with particle loss when reporting emission indices as discussed in chapter 6.

In this chapter, uncertainties associated with the required assumptions used by the SLT, namely lognormality at the Engine Exit Plane (EEP), particle effective density and GSD were assessed at different locations of the sampling system. Their impact on the calculated system loss correction factors ($k_{SL_{num}}$ and $k_{SL_{mass}}$) were estimated using PM data from four Rolls-Royce engine types

presented in chapter 6. It was demonstrated that the lognormal, GSD and density assumptions strongly impacted GMD and hence correction factors predictions from the SLT. As expected from chapter 6, the default density (1 g/cm³) and GSD (1.8) assumptions currently recommended did not provide good correlations between measured-derived and SLT-predicted GMD for all engine types due to GSD varying with N/M ratio and density being engine type and power specific. It was also shown that the predicted particle size distributions at the EEP were generally not perfectly lognormal. The worst-case scenario propagated uncertainty witnessed at the smallest GMD totalled to:

- 76.3% for $k_{SL_{num}} \sqrt{24.5\%^2(\text{lognormal}) + 13.9\%^2(N/M_{meas}) + 70.9\%(GSD, \rho_{eff})^2}$
- 26.5% for $k_{SL_{mass}} \sqrt{13.5\%^2(\text{lognormal}) + 7.4\%^2(N/M_{meas}) + 21.6\%(GSD, \rho_{eff})^2}$

These uncertainties are directly proportional to number and mass emission indices as currently reported.

Table 7-6: Summary of the average difference between SLT-predicted GMD and measured-derived GMD at the EEP using different GSD and density assumptions

SLT GSD and density assumptions	GSD	Density	Average GMD difference
Default GSD + empirically derived density	1.8	Fit	25.8 ± 22.5%
Default GSD + size-dependent density from the literature	1.8	Size-dependent	25.1 ± 24.6%
Default GSD & density	1.8	1 g/cm ³	19.4 ± 15.4%
Empirically derived GSD + default density	Fit	1 g/cm ³	18.2 ± 8.3%
Empirically derived GSD & density	Fit	Fit	13.2 ± 8.9%
Empirically derived GSD + size-dependent density	Fit	Size-dependent	10.2 ± 7.9%
Measured-derived GSD & density	Measured	Measured	9.3 ± 6.8%
Measured-derived GSD & density with N input from size measurement	Measured	Measured	8.4 ± 5.1%

It was demonstrated that using different assumptions in the SLT (i.e. GSD, density, lognormality) could significantly improve the correlation between SLT-predicted and measured-derived GMD and hence reduce loss correction factor uncertainty. A summary of the results presented in this chapter is found in **Table 7-6**, highlighting that an additional size measurement significantly improved SLT predictions by providing specific measured density and GSD. It was also discussed that empirical fits from historical data could be derived and correlated to measured N/M

ratio, improving GSD and density estimates compared to the default SLT assumptions, without the requirement for an additional size measurement. Particle effective density has been shown to be dependent on engine type, limiting the applicability of a single density fit. The GSD generally displayed similar trends with the N/M ratio regardless of the engine type and hence could be directly implemented in the SLT to replace the current value of 1.8. However, more data from different engine types and manufacturers would be required to further validate this finding.

It was also shown that using a size-dependent effective density, either derived from the literature or with an average matching the 'optimal' GMD did not necessarily further improve correlations between measured-derived GMD and SLT predicted GMD when compared with the use of average effective density. This confirms that an average effective density is currently the most appropriate assumption for the SLT.

Lastly, total PM number measurement derived from a size instrument were shown to be successfully used as the input measured number concentration in the SLT. The SLT predicted GMD using this number measurement logically correlated better with the GMD derived from the same size instrument. However, as only nvPM is currently regulated, a VPR would need to be placed at the inlet of the size instrument if it were to be used for certification purpose, which may mitigate the GMD correlation improvements witnessed in this chapter.

It is noted that given the results combine four engine types with measurements taken over a period of two years, subtle variations in the sampling system dimensions and operation (flowrate, temperature, pressure, shedding etc.) and calibration uncertainty may have also impacted the SLT predictions.

8 Conclusions

The aim of this thesis is to quantify uncertainties and identify potential improvements to the prescribed methodology for sampling and measuring aircraft nvPM for the accurate reporting of concentrations at the engine exit plane. This chapter presents the main conclusions from this thesis and proposes future research to help reduce the uncertainty associated with currently reported aircraft nvPM and to allow better assessment of its impact on human health and the environment.

8.1 Aerosol Generation and Characterisation

Nanoparticle generation was investigated with the aim of producing well characterised aerosols representative of aircraft PM in a laboratory setup, suitable for investigating the effect of particle morphology and density on different loss mechanisms in a regulatory compliant sampling system. Nebulisation of suspensions and solutions with a collision nebuliser was assessed. Non-Volatile-Residue (NVR) contamination, originating from impurities present in the nebulised liquid, was found to interfere with the generation of particles <100 nm and shown to be difficult to suppress. Centrifugation, diffusion screens, furnace heating and aerodynamic classification were successfully used to minimise NVR interference of the nebulised aerosols, resulting in monodisperse, monomodal aerosols. Salt (NaCl), Silica (SiO₂) and graphite particles with GMD's ranging from 30-140 nm and GSD's varying from 1.3–1.9 were produced when classified with a Combustion Aerodynamic Aerosol Classifier (AAC).

Combustion exhaust particles were captured into a liquid at an efficiency of ≈50%, with ultrapure water found to be the most suitable suspension fluid. Particles transferred from the aerosol to liquid were characterised with gaseous mobility diameters which were smaller than the hydrodynamic diameters measured in the liquid.

8.2 Particle Loss Characterisation

Particle loss occurring when transporting aircraft nvPM in a regulatory compliant sampling and measurement system is currently estimated using the UTRC particle transport model which predicts diffusional, thermophoretic, inertial, bend and electrostatic deposition mechanisms.

To the author's knowledge, thermophoresis theory has not been validated for soot-like fractal particles at temperatures typical of aircraft exhaust sampling ($\leq 700^{\circ}\text{C}$). In this work, thermophoretic losses for spherical, cubical and fractal nanoparticles (30-140 nm) were measured at temperatures of up to 910°C (temperature gradient $\leq 880^{\circ}\text{C}$) and compared with theoretical predictions. It was found that both the UTRC model and k_{thermo} correlate well with measured

thermophoretic loss for spherical and cubical particles, however higher losses in the order of 3-4% were reported for fractal particles, suggesting the currently prescribed system loss correction methodology for aircraft nvPM underestimates thermophoretic loss.

Diffusional and 'bend' loss were experimentally characterised in the EASA nvPM reference system's 25 m sample line using generated particles. Good agreement was found between the measured losses and those estimated by the UTRC model at typical aircraft nvPM sampling flowrates (~25 Lpm). The effect of sample line coiling was assessed, and it was found that it induced additional diffusional losses which are not accounted for in the UTRC model. These losses were relatively low (<4% at 24 Lpm) and can be assumed negligible if minimising line coiling as recommended in ICAO regulation.

The penetration efficiency through the EASA nvPM reference system Volatile Particle Remover (VPR) was quantified using generated particles. Losses in the VPR were morphology dependent with higher losses of up to 10% measured for fractal particles when compared with spherical particles. Penetration efficiencies were generally higher than that quoted in the annual calibration certification, highlighting additional uncertainties associated with calibration and loss correction in the VPR.

8.3 Large-scale Engine PM Emission Measurements

NvPM emissions and additional particle size measurements performed on four large-scale Rolls-Royces engine types representative of their current commercial fleet were presented and discussed in depth along with an allowed performance specification uncertainty analysis of the currently prescribed ICAO sampling and measurement system.

It was demonstrated that particle size distribution measurements permitted a better characterisation of the sampled aerosol by assessing the particle distribution shape (GMD, GSD, lognormality) and by permitting the calculation of an average particle effective density when combined with nvPM mass concentration. It was shown that GSD correlated well with the nvPM N/M ratio independently of engine type. The measured size distributions were generally monomodal and appeared lognormal, although deviations from lognormality were observed for some engine technologies and power settings. Derived particle average effective densities ranged between 0.3 and 0.8 g/cm³.

An uncertainty of 66.3% and 24.9% for currently reported nvPM number (EI_{number}) and mass (EI_{mass}) emission indices (excluding line shedding, fuel properties and humidity effects) was determined using the regulatory performance specifications. The largest uncertainty originated from high variation in particle loss in the sampling system at the smaller sizes (10 nm) which is largely accounted for with size-dependent diffusion loss.

Increased hydrogen content in the fuel characteristic of alternative fuels and increased humidity in the diffusion combustion zone were both shown to reduce nvPM number, mass and size. These findings highlighted that additional uncertainties not accounted-for in current regulation originate from the fuel type and ambient conditions and demonstrated the potential of alternative fuels with higher hydrogen content to improve local air quality surrounding airports.

8.4 System Loss Correction Methodology for Regulatory nvPM Measurements

To predict nvPM emissions at the engine exit plane concentrations, ICAO regulation has recently prescribed a methodology to estimate system loss correction factors (k_{SL}). Given the size dependent nature of some nanoparticle loss and the lack of size measurement in the current regulation, the System Loss Tool (SLT) predicts a size distribution at the Engine Exit Plane (EEP) from the N/M ratio using multiple assumptions.

The impact of particle density, GSD and lognormality assumptions were assessed by comparing the GMD predicted by the SLT to that derived from additional particle size distribution measurements. A propagated uncertainty of 76.3% and 26.5% was estimated for the number and mass system loss correction factors using the currently prescribed assumptions on nvPM data from four Rolls-Royce engine types.

It was demonstrated that replacing the current density and GSD assumptions with those derived from the particle size measurements led to significantly better correlations and hence more accurate system loss correction factors. It was also assessed that if no particle size instrument was available, the GSD and density assumptions derived from empirical fits improved SLT correlations but to a lower extent. Trends between the GSD and the nvPM N/M ratio appeared independent of engine type and hence could be implemented in the SLT to replace the current fixed value of 1.8. The GSD trend should be validated on other engine types from different manufacturers to ensure it is representative of the entire fleet. Particle average effective density appeared engine type dependent and hence general trends poorly correlated to individual engine types.

The SLT was shown to be a promising tool permitting the prediction of nvPM concentrations at the engine exit, however the large uncertainty originating from the currently prescribed fixed assumptions can be improved with an additional particle size measurement or with derived assumptions from trends. If particle size measurement is implemented, alternative system loss correction methodologies could be used by comparing measured and exit plane corrected particle size distributions.

8.5 Future Work

A discussion on potential future research to improve the sampling and measurement methodology and further reduce the uncertainty associated with the current practice for aircraft engine exhaust nvPM sampling, measurement and reporting is made below.

Given modern aircraft gas turbine engines tend to produce smaller nvPM particles with lower mass concentrations and that engine exit plane concentrations are of interest, the uncertainty associated with system loss correction factor and low mass measurements needs to be further assessed. For nvPM mass concentration measurements $< 5 \mu\text{g}/\text{m}^3$, the effect of line shedding needs to be investigated in more detail as it can strongly influence the reported mass. Alternatively, nvPM mass concentration measurements could be performed on the undiluted line.

While additional particle size measurements were proven to be beneficial, their typically high cost and the lack of traceable particle representative of fractal soot particles can make their implementation challenging in future regulation. Particle size information could be derived more simply by combining two CPCs with different penetration functions, or alternatively by using diffusion screens or different analysers. These alternative methods to predict exhaust particle size could be experimentally investigated to assess their potential.

The work presented in this thesis only included nvPM data from four Rolls-Royce engine types, thus all analysis presented in chapter 6 and 7 should be repeated on different engine types from other aircraft engine manufacturers to validate the findings of this thesis and to improve the understanding of aircraft nvPM emissions.

Significant uncertainties are associated with the calibration of nvPM number (VPR and CPC) and mass instruments. Improved calibration practices to better represent typical aircraft nvPM and hence reduce the uncertainty could be investigated.

Lastly, as only nvPM is currently regulated, there is need for more research on total PM emitted by gas turbine engines and their formation during transportation in the sampling system to help with the implementation of new regulation implementing total PM.

9 References

- [1] Advisory Council for Aviation Research and Innovation in Europe (ACARE), 'Strategic Research & Innovation Agenda - 2017 Update Volume 1', 2017.
- [2] ACI, 'Annual World Airport Traffic Report (WATR)', 2018.
- [3] World Wildlife Fund (WWF), 'New global agreement will help curb pollution from aviation', 10-Oct-2016. [Online]. Available: <https://www.worldwildlife.org/stories/new-global-agreement-will-help-curb-pollution-from-aviation>. [Accessed: 09-Jun-2019].
- [4] European Commission, 'Reducing emissions from aviation', 23-Nov-2016. [Online]. Available: https://ec.europa.eu/clima/policies/transport/aviation_en. [Accessed: 09-Jun-2019].
- [5] European Commission, 'Flightpath 2050 Europe's vision for aviation: maintaining global leadership and serving society's needs', Jul. 2011.
- [6] Z. Yu *et al.*, 'Identification of Lubrication Oil in the Particulate Matter Emissions from Engine Exhaust of In-Service Commercial Aircraft', *Environ. Sci. Technol.*, vol. 46, no. 17, pp. 9630–9637, Sep. 2012.
- [7] M. Masiol and R. M. Harrison, 'Aircraft engine exhaust emissions and other airport-related contributions to ambient air pollution: A review', *Atmos. Environ.*, vol. 95, pp. 409–455, Oct. 2014.
- [8] D. M. Walters, 'Characterisation of Particulate Matter Emitted from Aviation Gas Turbines and Spray-Guided Direct Injection Gasoline Engines', Cardiff University, 2014.
- [9] P. Lobo, D. E. Hagen, P. D. Whitefield, and D. Raper, 'PM emissions measurements of in-service commercial aircraft engines during the Delta-Atlanta Hartsfield Study', *Atmos. Environ.*, vol. 104, pp. 237–245, Mar. 2015.
- [10] P. I. Williams *et al.*, 'Impact of Alternative Fuels on Emissions Characteristics of a Gas Turbine Engine – Part 2: Volatile and Semivolatile Particulate Matter Emissions', *Environ. Sci. Technol.*, vol. 46, no. 19, pp. 10812–10819, Oct. 2012.
- [11] A. Petzold *et al.*, 'Recommendations for the interpretation of "black carbon" measurements', *Atmos Chem Phys Discuss*, vol. 13, no. 4, pp. 9485–9517, Apr. 2013.
- [12] A. Petzold *et al.*, 'Evaluation of Methods for Measuring Particulate Matter Emissions from Gas Turbines', *Environ. Sci. Technol.*, vol. 45, no. 8, pp. 3562–3568, Apr. 2011.
- [13] P. R. Buseck, K. Adachi, A. Gelencsér, É. Tompa, and M. Pósfai, 'Are black carbon and soot the same?', *Atmos Chem Phys Discuss*, vol. 12, no. 9, pp. 24821–24846, Sep. 2012.
- [14] ICAO, 'Annex 16 - Environmental Protection Volume 2 - Aircraft Engine Emissions', Jul. 2017.
- [15] A. Fushimi, K. Saitoh, Y. Fujitani, and N. Takegawa, 'Identification of jet lubrication oil as a major component of aircraft exhaust nanoparticles', *Atmospheric Chem. Phys.*, vol. 19, no. 9, pp. 6389–6399, May 2019.
- [16] H. Wang, 'Formation of nascent soot and other condensed-phase materials in flames', *Proc. Combust. Inst.*, vol. 33, no. 1, pp. 41–67, 2011.
- [17] D. Kittelson and M. Kraft, 'Particle Formation and Models in Internal Combustion Engines', *Camb. Cent. Comput. Chem. Eng.*, Jan. 2014.
- [18] A. H. Lefebvre and D. R. Ballal, *Gas Turbine Combustion: Alternative Fuels and Emissions, Third Edition*. Taylor & Francis, 2010.
- [19] Y. Sevcenco, 'Measurement Techniques and Characterisation of Combustion Species at Operating Conditions Relevant to Gas Turbines', Cardiff University, 2010.
- [20] A. M. Boies *et al.*, 'Particle Emission Characteristics of a Gas Turbine with a Double Annular Combustor', *Aerosol Sci. Technol.*, vol. 49, no. 9, pp. 842–855, Sep. 2015.
- [21] M. T. Timko *et al.*, 'Particulate Emissions of Gas Turbine Engine Combustion of a Fischer–Tropsch Synthetic Fuel', *Energy Fuels*, vol. 24, no. 11, pp. 5883–5896, Nov. 2010.
- [22] A. Nemmar *et al.*, 'Passage of Inhaled Particles Into the Blood Circulation in Humans', *Circulation*, vol. 105, no. 4, pp. 411–414, Jan. 2002.
- [23] V. Stone, H. Johnston, and M. J. D. Clift, 'Air Pollution, Ultrafine and Nanoparticle Toxicology: Cellular and Molecular Interactions', *IEEE Trans. NanoBioscience*, vol. 6, no. 4, pp. 331–340, Dec. 2007.

- [24] M. Hussain, P. Madl, and A. Khan, 'Lung deposition predictions of airborne particles and the emergence of contemporary diseases Part-I', *Health (N. Y.)*, vol. 2, no. 2, pp. 51–59, May 2011.
- [25] G. Oberdörster, E. Oberdörster, and J. Oberdörster, 'Nanotoxicology: An Emerging Discipline Evolving from Studies of Ultrafine Particles', *Environ. Health Perspect.*, vol. 113, no. 7, pp. 823–839, Jul. 2005.
- [26] S. H. L. Yim *et al.*, 'Global, regional and local health impacts of civil aviation emissions', *Environ. Res. Lett.*, vol. 10, no. 3, p. 034001, Feb. 2015.
- [27] World Health Organisation (WHO), 'Health effects of particulate matter Policy implications for countries in eastern Europe, Caucasus and central Asia'.
- [28] M. Shiraiwa *et al.*, 'Aerosol Health Effects from Molecular to Global Scales', *Environ. Sci. Technol.*, vol. 51, no. 23, pp. 13545–13567, Dec. 2017.
- [29] C. A. Pope, D. W. Dockery, and J. Schwartz, 'Review of Epidemiological Evidence of Health Effects of Particulate Air Pollution', *Inhal. Toxicol.*, vol. 7, no. 1, pp. 1–18, Jan. 1995.
- [30] World Health Organisation (WHO), 'Ambient (outdoor) air quality and health', 02-May-2018. [Online]. Available: [https://www.who.int/news-room/fact-sheets/detail/ambient-\(outdoor\)-air-quality-and-health](https://www.who.int/news-room/fact-sheets/detail/ambient-(outdoor)-air-quality-and-health). [Accessed: 12-Apr-2019].
- [31] H. R. Jonsdottir *et al.*, 'Non-volatile particle emissions from aircraft turbine engines at ground-idle induce oxidative stress in bronchial cells', *Commun. Biol.*, vol. 2, no. 1, p. 90, Mar. 2019.
- [32] O. J. Puckering, 'Blood clot microstructures: The role of engineered and combustion derived carbon nanoparticles in thrombus formation', Swansea University, 2009.
- [33] A. S. Wolberg and R. A. Campbell, 'Thrombin Generation, Fibrin Clot Formation and Hemostasis', *Transfus. Apher. Sci. Off. J. World Apher. Assoc. Off. J. Eur. Soc. Haemapheresis*, vol. 38, no. 1, pp. 15–23, Feb. 2008.
- [34] P. Bhattacharjee and D. Bhattacharyya, 'An Insight into the Abnormal Fibrin Clots — Its Pathophysiological Roles', *Fibrinolysis Thrombolysis*, May 2014.
- [35] C.-E. Boström *et al.*, 'Cancer risk assessment, indicators, and guidelines for polycyclic aromatic hydrocarbons in the ambient air.', *Environ. Health Perspect.*, vol. 110, no. Suppl 3, pp. 451–488, Jun. 2002.
- [36] European Commission, 'Air Quality Standards'. [Online]. Available: <http://ec.europa.eu/environment/air/quality/standards.htm>. [Accessed: 10-Jun-2019].
- [37] IPCC, 'Climate Change 2013: The Physical Science Basis. Chapter 7: Clouds and Aerosols', 2013.
- [38] O. Dessens, M. O. Köhler, H. L. Rogers, R. L. Jones, and J. A. Pyle, 'Aviation and climate change', *Transp. Policy*, vol. 34, pp. 14–20, Jul. 2014.
- [39] U. Burkhardt, L. Bock, and A. Bier, 'Mitigating the contrail cirrus climate impact by reducing aircraft soot number emissions', *Npj Clim. Atmospheric Sci.*, vol. 1, no. 1, p. 37, Oct. 2018.
- [40] B. Kärcher, 'The importance of contrail ice formation for mitigating the climate impact of aviation', *J. Geophys. Res. Atmospheres*, vol. 121, no. 7, pp. 3497–3505, Apr. 2016.
- [41] G. P. Brasseur *et al.*, 'Impact of Aviation on Climate: FAA's Aviation Climate Change Research Initiative (ACCRI) Phase II', *Bull. Am. Meteorol. Soc.*, vol. 97, no. 4, pp. 561–583, Jul. 2015.
- [42] B. Miljevic, N. C. Surawski, T. Bostrom, and Z. D. Ristovski, 'Restructuring of carbonaceous particles upon exposure to organic and water vapours', *J. Aerosol Sci.*, vol. 47, pp. 48–57, May 2012.
- [43] D. S. Lee *et al.*, 'Aviation and global climate change in the 21st century', *Atmos. Environ.*, vol. 43, no. 22, pp. 3520–3537, Jul. 2009.
- [44] ICAO, 'About ICAO'. [Online]. Available: <https://www.icao.int/about-icao/Pages/default.aspx>. [Accessed: 19-Apr-2019].
- [45] A. Petzold and R. Marsh, 'SAMPLE I-Studying, sAmpling and Measuring of Particulate Matter', EASA, OP13, 2009.
- [46] R. Marsh, A. Crayford, A. Petzold, and M. Johnson, 'SAMPLE II-Studying, sAmpling and Measuring of Particulate Matter II', EASA, OP18, 2011.
- [47] A. Crayford and M. Johnson, 'SAMPLE III SC.01- Studying, sAmpling and Measuring of aircraft Particulate Emission', EASA, SC01, 2011.

- [48] A. Crayford and M. Johnson, 'SAMPLE III SC.02 - Studying, sAmpling and Measuring of aircraft ParticuLate Emission', EASA, SC02, 2012.
- [49] A. Crayford and M. Johnson, 'SAMPLE III SC.03- Studying, sAmpling and Measuring of aircraft ParticuLate Emission', EASA, SC03, 2013.
- [50] A. Crayford, M. Johnson, Y. Sevcenco, and P. Williams, 'SAMPLE III SC.05 - Studying, sAmpling and Measuring of aircraft ParticuLate Emission', EASA, SC05, 2014.
- [51] P. Lobo *et al.*, 'Measurement of Aircraft Engine Non-Volatile PM Emissions: Results of the Aviation-Particle Regulatory Instrumentation Demonstration Experiment (A-PRIDE) 4 Campaign', *Aerosol Sci. Technol.*, vol. 49, no. 7, pp. 472–484, Jul. 2015.
- [52] SAE international, 'AIR 6241-Procedure for the Continuous Sampling and Measurement of Non-Volatile Particle Emissions from Aircraft Turbine Engines', 2013.
- [53] SAE international, 'ARP 6320 - Procedure for the Continuous Sampling and Measurement of Non-Volatile Particulate Matter Emissions from Aircraft Turbine Engines', Jan. 2018.
- [54] SAE international, 'ARP 1179D - Aircraft Gas Turbine Engine Exhaust Smoke Measurement', SAE International, 2011.
- [55] R. L. Wayson, G. G. Fleming, and R. Iovinelli, 'Methodology to Estimate Particulate Matter Emissions from Certified Commercial Aircraft Engines', *J. Air Waste Manag. Assoc.*, vol. 59, no. 1, pp. 91–100, Jan. 2009.
- [56] 'New standards | European Aviation Environmental Report'. [Online]. Available: <https://www.easa.europa.eu/eaer/topics/technology-and-design/new-standards>. [Accessed: 19-Apr-2019].
- [57] SAE international, 'ARP 6481- Procedure for the Calculation of Sampling Line Penetration Functions and Line Loss Correction Factors', SAE International, Feb. 2019.
- [58] C. M. Sorensen, 'The Mobility of Fractal Aggregates: A Review', *Aerosol Sci. Technol.*, vol. 45, no. 7, pp. 765–779, Jul. 2011.
- [59] SAE international, 'AIR 6504 - Procedure for the Calculation of Sampling System Penetration Functions and System Loss Correction Factors', Nov. 2014.
- [60] W. C. Hinds, *Aerosol Technology: Properties Behavior, and measurement of airborne particles*. Wiley-Interscience, 1998.
- [61] D. Delhaye *et al.*, 'The MERMOSE project: Characterization of particulate matter emissions of a commercial aircraft engine', *J. Aerosol Sci.*, vol. 105, pp. 48–63, Mar. 2017.
- [62] P. Baron, K. Willeke, and P. Kulkarni, *Aerosol Measurement, Principles, Techniques, and applications*, Third edition. John Wiley & Sons, Inc, 2011.
- [63] L. Durdina *et al.*, 'Determination of PM mass emissions from an aircraft turbine engine using particle effective density', *Atmos. Environ.*, vol. 99, pp. 500–507, Dec. 2014.
- [64] P. F. DeCarlo, J. G. Slowik, D. R. Worsnop, P. Davidovits, and J. L. Jimenez, 'Particle Morphology and Density Characterization by Combined Mobility and Aerodynamic Diameter Measurements. Part 1: Theory', *Aerosol Sci. Technol.*, vol. 38, no. 12, pp. 1185–1205, Jan. 2004.
- [65] M. Abegglen *et al.*, 'Effective density and mass–mobility exponents of particulate matter in aircraft turbine exhaust: Dependence on engine thrust and particle size', *J. Aerosol Sci.*, vol. 88, pp. 135–147, Oct. 2015.
- [66] J. Ristimäki, A. Virtanen, M. Marjamäki, A. Rostedt, and J. Keskinen, 'On-line measurement of size distribution and effective density of submicron aerosol particles', *J. Aerosol Sci.*, vol. 33, no. 11, pp. 1541–1557, Nov. 2002.
- [67] K. Park, F. Cao, D. B. Kittelson, and P. H. McMurry, 'Relationship between Particle Mass and Mobility for Diesel Exhaust Particles', *Environ. Sci. Technol.*, vol. 37, no. 3, pp. 577–583, Feb. 2003.
- [68] A. J. Beyersdorf *et al.*, 'Reductions in aircraft particulate emissions due to the use of Fischer-Tropsch fuels', *Atmospheric Chem. Phys.*, vol. 14, no. 1, pp. 11–23, Jan. 2014.
- [69] T. J. Johnson *et al.*, 'Effective Density and Mass-Mobility Exponent of Aircraft Turbine Particulate Matter', *J. Propuls. Power*, vol. 31, no. 2, pp. 573–582, 2015.
- [70] F. Tavakoli and J. S. Olfert, 'Determination of particle mass, effective density, mass–mobility exponent, and dynamic shape factor using an aerodynamic aerosol classifier and a differential mobility analyzer in tandem', *J. Aerosol Sci.*, vol. 75, pp. 35–42, Sep. 2014.

- [71] P. Lobo, S. Christie, B. Khandelwal, S. Blakey, and D. Raper, 'Evaluation of Non-Volatile PM Emissions Characteristics of an Aircraft Auxiliary Power Unit with Varying Alternative Jet Fuel Blend Ratios', *Energy Fuels*, vol. 29, p. 151016011415009, Oct. 2015.
- [72] J. S. Olfert *et al.*, 'Effective density and volatility of particles sampled from a helicopter gas turbine engine', *Aerosol Sci. Technol.*, vol. 0, no. 0, pp. 1–11, Feb. 2017.
- [73] E. A. Ubogu, J. Cronly, B. Khandelwal, and S. Roy, 'Determination of the effective density and fractal dimension of PM emissions from an aircraft auxiliary power unit', *J. Environ. Sci.*, 2018.
- [74] B. Giechaskiel, 'Sampling of Non-Volatile Vehicle Exhaust Particles: A Simplified Guide', 2012.
- [75] Jung Hyeun Kim, George W. Mulholland, Scott R. Kukuck, and David Y. H. Pui, 'Slip Correction Measurements of Certified PSL Nanoparticles Using a Nanometer Differential Mobility Analyzer (Nano-DMA) for Knudsen Number From 0.5 to 83', *Journal of Research of the National Institute of Standards and Technology*, vol. 110, Feb. 2005.
- [76] P. Kumar, P. Fennell, J. Symonds, and R. Britter, 'Treatment of losses of ultrafine aerosol particles in long sampling tubes during ambient measurements', *Atmos. Environ.*, vol. 42, no. 38, pp. 8819–8826, Dec. 2008.
- [77] Cambustion Ltd, 'Aerodynamic Aerosol Classifier - User manual (V1.12)'. 2016.
- [78] S.-J. Yook and D. Y. H. Pui, 'Experimental Study of Nanoparticle Penetration Efficiency Through Coils of Circular Cross-Sections', *Aerosol Sci. Technol.*, vol. 40, no. 6, pp. 456–462, Jul. 2006.
- [79] UTRC, 'User Manual for UTRC Particle Transport Spreadsheet Tool'. Nov-2009.
- [80] H. W. Chiang, S. R. Mulpuru, and C. J. Berkis, 'Analysis of models for turbulent deposition of aerosols', *J. Aerosol Sci.*, vol. 27, Supplement 1, pp. S455–S456, Sep. 1996.
- [81] F. Zheng, 'Thermophoresis of spherical and non-spherical particles: a review of theories and experiments', *Adv. Colloid Interface Sci.*, vol. 97, no. 1, pp. 255–278, Mar. 2002.
- [82] L. Talbot, R. K. Cheng, R. W. Schefer, and D. R. Willis, 'Thermophoresis of particles in a heated boundary layer', *J. Fluid Mech.*, vol. 101, no. 04, pp. 737–758, Dec. 1980.
- [83] A. Messerer, R. Niessner, and U. Pöschl, 'Thermophoretic deposition of soot aerosol particles under experimental conditions relevant for modern diesel engine exhaust gas systems', *J. Aerosol Sci.*, vol. 34, no. 8, pp. 1009–1021, Aug. 2003.
- [84] R. Muñoz-Bueno, E. Hontañón, and M. I. Rucandio, 'Deposition of fine aerosols in laminar tube flow at high temperature with large gas-to-wall temperature gradients', *J. Aerosol Sci.*, vol. 36, no. 4, pp. 495–520, Apr. 2005.
- [85] E. Brugière, F. Gensdarmes, F. X. Ouf, J. Yon, and A. Coppalle, 'Increase in thermophoretic velocity of carbon aggregates as a function of particle size', *J. Aerosol Sci.*, vol. 76, pp. 87–97, Oct. 2014.
- [86] F. J. Romay, S. S. Takagaki, D. Y. H. Pui, and B. Y. H. Liu, 'Thermophoretic deposition of aerosol particles in turbulent pipe flow', *J. Aerosol Sci.*, vol. 29, no. 8, pp. 943–959, Sep. 1998.
- [87] B. Y. H. Liu, D. Y. H. Pui, K. L. Rubow, and W. W. Szymanski, 'Electrostatic Effects in Aerosol Sampling and Filtration', *Ann. Occup. Hyg.*, vol. 29, no. 2, pp. 251–269, Jan. 1985.
- [88] A. Awasthi, B.-S. Wu, C.-N. Liu, C.-W. Chen, S.-N. Uang, and C.-J. Tsai, 'The Effect of Nanoparticle Morphology on the Measurement Accuracy of Mobility Particle Sizers', *MAPAN*, vol. 28, no. 3, pp. 205–215, Sep. 2013.
- [89] R. I. Crane and R. L. Evans, 'Inertial deposition of particles in a bent pipe', *J. Aerosol Sci.*, vol. 8, no. 3, pp. 161–170, Jun. 1977.
- [90] D. Y. H. Pui, F. Romay-Novas, and B. Y. H. Liu, 'Experimental Study of Particle Deposition in Bends of Circular Cross Section', *Aerosol Sci. Technol.*, vol. 7, no. 3, pp. 301–315, Jan. 1987.
- [91] J. Wang, R. C. Flagan, and J. H. Seinfeld, 'Diffusional losses in particle sampling systems containing bends and elbows', *J. Aerosol Sci.*, vol. 33, no. 6, pp. 843–857, Jun. 2002.
- [92] J. S. Kinsey, Y. Dong, D. C. Williams, and R. Logan, 'Physical characterization of the fine particle emissions from commercial aircraft engines during the Aircraft Particle Emissions eXperiment (APEX) 1–3', *Atmos. Environ.*, vol. 44, no. 17, pp. 2147–2156, Jun. 2010.

- [93] P. Lobo, D. E. Hagen, and P. D. Whitefield, 'Comparison of PM Emissions from a Commercial Jet Engine Burning Conventional, Biomass, and Fischer–Tropsch Fuels', *Environ. Sci. Technol.*, vol. 45, no. 24, pp. 10744–10749, Dec. 2011.
- [94] B. Giechaskiel, M. Cresnoverh, H. Jörgl, and A. Bergmann, 'Calibration and accuracy of a particle number measurement system', *Meas. Sci. Technol.*, vol. 21, no. 4, p. 045102, Apr. 2010.
- [95] B. Giechaskiel *et al.*, 'Evaluation of the particle measurement programme (PMP) protocol to remove the vehicles' exhaust aerosol volatile phase', *Sci. Total Environ.*, vol. 408, no. 21, pp. 5106–5116, Oct. 2010.
- [96] Z. Zheng *et al.*, 'Investigation of solid particle number measurement: Existence and nature of sub-23 nm particles under PMP methodology', *J. Aerosol Sci.*, vol. 42, no. 12, pp. 883–897, Dec. 2011.
- [97] S. Amanatidis, L. Ntziachristos, B. Giechaskiel, D. Katsaounis, Z. Samaras, and A. Bergmann, 'Evaluation of an oxidation catalyst ("catalytic stripper") in eliminating volatile material from combustion aerosol', *J. Aerosol Sci.*, vol. 57, pp. 144–155, Mar. 2013.
- [98] 'Optical Particle Sizer 3330', *TSI.com*. [Online]. Available: <https://tsi.com//Products/Particle-Sizers/Particle-Size-Spectrometers/Optical-Particle-Sizer-3330>. [Accessed: 12-Apr-2019].
- [99] T. Tuch *et al.*, 'Dependence of CPC cut-off diameter on particle morphology and other factors', *Aerosol Sci. Technol.*, vol. 50, no. 4, pp. 331–338, Apr. 2016.
- [100] National Institute of Occupational Safety and Health, 'Diesel particulate matter (as elemental carbon). Method 5040: Issue 3', 2003.
- [101] A. Mamakos, I. Khalek, R. Giannelli, and M. Spears, 'Characterization of Combustion Aerosol Produced by a Mini-CAST and Treated in a Catalytic Stripper', *Aerosol Sci. Technol.*, vol. 47, no. 8, pp. 927–936, Aug. 2013.
- [102] W. Schindler, M. Arndt, A. Painsi, and B. Giechalskiel, 'AVL Micro Soot Sensor Applications', presented at the AVL Tech Days 2012, 21-Mar-2012.
- [103] H. A. Michelsen, C. Schulz, G. J. Smallwood, and S. Will, 'Laser-induced incandescence: Particulate diagnostics for combustion, atmospheric, and industrial applications', *Prog. Energy Combust. Sci.*, vol. 51, pp. 2–48, Dec. 2015.
- [104] Artium, 'LII theory of operation'. [Online]. Available: <https://www.artium.com/lii>. [Accessed: 16-Jun-2019].
- [105] B. Giechaskiel, L. Ntziachristos, and Z. Samaras, 'Effect of ejector dilutors on measurements of automotive exhaust gas aerosol size distributions', *Meas. Sci. Technol.*, vol. 20, no. 4, p. 045703, 2009.
- [106] B. Giechaskiel, M. Carriero, G. Martini, A. Krasenbrink, and D. Scheder, 'Calibration and Validation of Various Commercial Particle Number Measurement Systems', *SAE Int. J. Fuels Lubr.*, vol. 2, no. 1, pp. 512–530, Apr. 2009.
- [107] J. Lyyränen, J. Jokiniemi, E. I. Kauppinen, U. Backman, and H. Vesala, 'Comparison of Different Dilution Methods for Measuring Diesel Particle Emissions', *Aerosol Sci. Technol.*, vol. 38, no. 1, pp. 12–23, Jan. 2004.
- [108] M.-D. Cheng, J. M. Storey, T. Wainman, and T. Dam, 'Impacts of venturi turbulent mixing on the size distributions of sodium chloride and dioctyl-phthalate aerosols', *J. Aerosol Sci.*, vol. 33, no. 3, pp. 491–502, Mar. 2002.
- [109] Winkler, 'Heating solutions for exhaust measurement technology', Nov-2011.
- [110] Cambustion, 'Fast response aerosol size measurements with the DMS500 | Cambustion (Aerosol Science applications brochure)'. [Online]. Available: <https://www.cambustion.com/products/dms500/aerosol>. [Accessed: 16-Apr-2019].
- [111] Cambustion, 'Calibration of DMS Series Fast Particle Spectrometers'. 2008-2007.
- [112] Cambustion Ltd, 'DMS-500 User Manual (V3.5)'. 2011.
- [113] J. P. R. Symonds and K. St. J. Reavell, 'Calibration of Fast Response Differential Mobility Spectrometers'. European Aerosol Conference, Salzburg, 2007.
- [114] Malvern Panalytical, 'Zetasizer Nano ZS for protein size, zeta potential, protein mobility and microrheology'. [Online]. Available: <https://www.malvernpanalytical.com/en/products/product-range/zetasizer-range/zetasizer-nano-range/zetasizer-nano-zs>. [Accessed: 29-Jan-2019].

- [115] Malvern Panalytical, 'Nanoparticle Tracking Analysis NTA'. [Online]. Available: <https://www.malvernpanalytical.com/en/products/technology/nanoparticle-tracking-analysis>. [Accessed: 29-Jan-2019].
- [116] Malvern Panalytical, 'Dynamic Light Scattering: An Introduction in 30 Minutes'. [Online]. Available: <https://www.malvernpanalytical.com/en/learn/knowledge-center/technical-notes/TN101104DynamicLightScatteringIntroduction>. [Accessed: 29-Jan-2019].
- [117] H. Fissan, S. Ristig, H. Kaminski, C. Asbach, and M. Eppe, 'Comparison of different characterization methods for nanoparticle dispersions before and after aerosolization', *Anal. Methods*, vol. 6, no. 18, pp. 7324–7334, 2014.
- [118] C. Anderlohr and K. Schaber, 'Direct Transfer of Gas-Borne Nanoparticles into Liquid Suspensions by Means of a Wet Electrostatic Precipitator', *Aerosol Sci. Technol.*, vol. 49, no. 12, pp. 1281–1290, Dec. 2015.
- [119] C.-J. Tsai, J.-S. Lin, S. G. Aggarwal, and D.-R. Chen, 'Thermophoretic Deposition of Particles in Laminar and Turbulent Tube Flows', *Aerosol Sci. Technol.*, vol. 38, no. 2, pp. 131–139, Feb. 2004.
- [120] J. Lin, Z. Yin, F. Gan, and M. Yu, 'Penetration efficiency and distribution of aerosol particles in turbulent pipe flow undergoing coagulation and breakage', *Int. J. Multiph. Flow*, vol. 61, no. Supplement C, pp. 28–36, May 2014.
- [121] Z. Yin, J. Lin, and M. Lou, 'Penetration efficiency of nanoparticles in a bend of circular cross-section', *J. Hydrodyn. Ser B*, vol. 27, no. 1, pp. 93–98, Feb. 2015.
- [122] Z. Yin and Z. Dai, 'Investigating the Nanoparticles Penetration Efficiency through Horizontal Tubes Using an Experimental Approach', *Adv. Math. Phys.*, 2015.
- [123] C. S.-J. Tsai, 'Characterization of Airborne Nanoparticle Loss in Sampling Tubing', *J. Occup. Environ. Hyg.*, vol. 12, no. 8, pp. D161–D167, Aug. 2015.
- [124] G. Nishio, S. Kitani, and K. Takahashi, 'Thermophoretic Deposition of Aerosol Particles in a Heat-Exchanger Pipe', *Ind. Eng. Chem. Process Des. Dev.*, vol. 13, no. 4, pp. 408–415, Oct. 1974.
- [125] M. Shimada, T. Seto, and K. Okuyama, 'Thermophoretic and evaporational losses of ultrafine particles in heated flow', *AIChE J.*, vol. 39, no. 11, pp. 1859–1869, Nov. 1993.
- [126] M. Shimada, T. Seto, and K. Okuyama, 'Wall Deposition of Ultrafine Aerosol Particles by Thermophoresis in Nonisothermal Laminar Pipe Flow of Different Carrier Gas', *Jpn. J. Appl. Phys.*, vol. 33, no. 2R, p. 1174, Feb. 1994.
- [127] L. Durdina *et al.*, 'Response of real-time black carbon mass instruments to mini-CAST soot', *Aerosol Sci. Technol.*, vol. 50, no. 9, pp. 906–918, Sep. 2016.
- [128] L. A. Dailey *et al.*, 'Nebulization of biodegradable nanoparticles: impact of nebulizer technology and nanoparticle characteristics on aerosol features', *J. Controlled Release*, vol. 86, no. 1, pp. 131–144, Jan. 2003.
- [129] V. Gomez, S. Irusta, F. Balas, and J. Santamaria, 'Generation of TiO₂ Aerosols from Liquid Suspensions: Influence of Colloid Characteristics', *Aerosol Sci. Technol.*, vol. 47, no. 12, pp. 1383–1392, Dec. 2013.
- [130] 'Nanostructured Materials Through Ultrasonic Spray Pyrolysis | Technical Article', *Sigma-Aldrich*. [Online]. Available: <https://www.sigmaaldrich.com/technical-documents/articles/materials-science/nanostructured-materials-through-ultrasonic-spray-pyrolysis.html>. [Accessed: 07-Mar-2018].
- [131] Y. Wu, A. Duong, L. J. Lee, and B. E. Wyslouzil, 'Electrospray Production of Nanoparticles for Drug/Nucleic Acid Delivery', *InTech*, 2012.
- [132] S. Jeon, D. R. Oberreit, G. Van Schooneveld, and C. Hogan, 'Nanomaterial Size Distribution Analysis via Liquid Nebulization Coupled with Ion Mobility Spectrometry (LN-IMS)', *The Analyst*, vol. 141, Jan. 2016.
- [133] M. J. Sheehan, T. M. Peters, L. Cena, P. T. O'Shaughnessy, and R. A. Gussman, 'Generation of Nanoparticles with a Nebulizer-Cyclone System', *Aerosol Sci. Technol.*, vol. 43, no. 11, pp. 1091–1098, Oct. 2009.
- [134] Topas GmbH, 'Atomizer Aerosol Generator ATM 226 - Instruction manual', 2015.

- [135] M. Frei, 'Centrifugation Basics', *Sigma-Aldrich*. [Online]. Available: <https://www.sigmaaldrich.com/technical-documents/articles/biofiles/centrifugation-basics.html>. [Accessed: 15-Mar-2018].
- [136] PALAS GmbH, 'Operating Manual Graphite Aerosol Generator GFG 1000'.
- [137] C. Helsper, W. Mölter, F. Löffler, C. Wadenpohl, S. Kaufmann, and G. Wenninger, 'Investigations of a new aerosol generator for the production of carbon aggregate particles', *Atmospheric Environ. Part Gen. Top.*, vol. 27, no. 8, pp. 1271–1275, Jun. 1993.
- [138] M. Wentzel, H. Gorzawski, K.-H. Naumann, H. Saathoff, and S. Weinbruch, 'Transmission electron microscopical and aerosol dynamical characterization of soot aerosols', *J. Aerosol Sci.*, vol. 34, no. 10, pp. 1347–1370, Oct. 2003.
- [139] Cambustion Ltd, 'Aerodynamic Aerosol Classifier Brochure'. [Online]. Available: <https://www.cambustion.com/sites/default/files/instruments/AAC/Cambustion%20Aerodynamic%20Aerosol%20Classifier.pdf>. [Accessed: 05-Apr-2018].
- [140] F. Tavakoli and J. S. Olfert, 'An Instrument for the Classification of Aerosols by Particle Relaxation Time: Theoretical Models of the Aerodynamic Aerosol Classifier', *Aerosol Sci. Technol.*, vol. 47, no. 8, pp. 916–926, Aug. 2013.
- [141] F. Tavakoli, J. P. R. Symonds, and J. S. Olfert, 'Generation of a Monodisperse Size-Classified Aerosol Independent of Particle Charge', *Aerosol Sci. Technol.*, vol. 48, no. 3, pp. i–iv, Mar. 2014.
- [142] T. J. Johnson, M. Irwin, J. P. R. Symonds, J. S. Olfert, and A. M. Boies, 'Measuring aerosol size distributions with the aerodynamic aerosol classifier', *Aerosol Sci. Technol.*, vol. 52, no. 6, pp. 655–665, Jun. 2018.
- [143] S. Bau and J. Nuvoli, 'Combining the Particle Size Selector and a condensation particle counter to determine the number size distribution of airborne nanoparticles', *J. Aerosol Sci.*, vol. 128, pp. 22–33, Feb. 2019.
- [144] TSI Incorporated, 'Particle Size Selector Model 376060 (User's Manual)'. 2013.
- [145] M. A. Altaher, H. Li, P. Williams, M. Johnson, and S. Blakey, 'Determination of Particle Penetration Factors in a Particle Transfer Line for Aero Gas Turbine Engine Exhaust Particle Measurement', 2014.
- [146] J. Y. Park, P. H. McMurry, and K. Park, 'Production of Residue-Free Nanoparticles by Atomization of Aqueous Solutions', *Aerosol Sci. Technol.*, vol. 46, no. 3, pp. 354–360, Mar. 2012.
- [147] Kanomax FMT, 'Nanoparticle Nebulizer Model 9110', 2016. [Online]. Available: http://www.kanomaxfmt.com/uploads/5/7/5/4/57542039/nanoparticle_nebulizer_model_9110_brochure.pdf. [Accessed: 16-Mar-2018].
- [148] Labconco, 'Infographic: The rundown-What water type should I use in my application?', 2015. [Online]. Available: <https://www.labconco.com/articles/water-type-difference>. [Accessed: 15-May-2019].
- [149] SNP, 'The spray nozzle people : Guide to spray properties'. [Online]. Available: <http://www.spray-nozzle.co.uk/resources/engineering-resources/guide-to-spray-properties/4--droplet-size>. [Accessed: 09-Mar-2018].
- [150] Planetcalc, 'Online calculator: Relative humidity to absolute humidity and vice versa calculators'. [Online]. Available: <https://planetcalc.com/2167/>. [Accessed: 25-May-2019].
- [151] 'Gold nanoparticles 100 nm', *BBI Solutions*. [Online]. Available: <https://www.bbisolutions.com/en/catalog/product/view/id/256/s/gold-nanoparticles-100nm/category/25/>. [Accessed: 02-Oct-2018].
- [152] J. P. R. Symonds, K. St. J. Reavell, J. S. Olfert, B. W. Campbell, and S. J. Swift, 'Diesel soot mass calculation in real-time with a differential mobility spectrometer', *J. Aerosol Sci.*, vol. 38, no. 1, pp. 52–68, Jan. 2007.
- [153] K. Park, J.-S. Kim, and A. L. Miller, 'A study on effects of size and structure on hygroscopicity of nanoparticles using a tandem differential mobility analyzer and TEM', *J. Nanoparticle Res.*, vol. 11, no. 1, pp. 175–183, Jan. 2009.
- [154] F. Zheng *et al.*, 'Controlled Crystallization of Sodium Chloride Nanocrystals in Microdrop-lets Produced by Electrospray from an Ultra-Dilute Solution', *Eur. J. Inorg. Chem.*, vol. 2016, no. 12, pp. 1860–1865, 2016.

- [155] B. W. LaFranchi, M. Knight, and G. A. Petrucci, 'Leaching as a source of residual particles from nebulization of deionized water', *J. Aerosol Sci.*, vol. 34, no. 11, pp. 1589–1594, Nov. 2003.
- [156] W.-S. Kim, Y. H. Park, J. Y. Shin, D. W. Lee, and S. Lee, 'Size Determination of Diesel Soot Particles Using Flow and Sedimentation Field-Flow Fractionation', *Anal. Chem.*, vol. 71, no. 15, pp. 3265–3272, Aug. 1999.
- [157] W.-S. Kim, Y. H. Park, D. W. Lee, and S. Lee, 'Sample Preparation for Size Analysis of Diesel Soot Particles Using Field-Flow Fractionation', *J. Liq. Chromatogr. Relat. Technol.*, vol. 24, no. 13, pp. 1935–1951, Aug. 2001.
- [158] A. Charvet, N. Bardin-Monnier, and D. Thomas, 'Can bubble columns be an alternative to fibrous filters for nanoparticles collection?', *J. Hazard. Mater.*, vol. 195, pp. 432–439, Nov. 2011.
- [159] M. C. Cadavid-Rodriguez, A. Charvet, D. Bemer, and D. Thomas, 'Optimization of bubble column performance for nanoparticle collection', *J. Hazard. Mater.*, vol. 271, pp. 24–32, Apr. 2014.
- [160] J. R. Kassab, R. A. Zahoransky, A. Wollmann, M. Claussen, and P. J. P. Cardot, 'Analysis of Soot Particles Emitted from a Modern Light Duty Diesel Engine Running in Different Operating Conditions using Field Flow Fractionation and Granulometric Techniques', *J. Liq. Chromatogr. Relat. Technol.*, vol. 30, no. 9–10, pp. 1525–1546, Apr. 2007.
- [161] D. Koch and A. P. Weber, 'Separation of gas-borne nanoparticles in bubble columns', *J. Aerosol Sci.*, vol. 53, pp. 61–75, Nov. 2012.
- [162] B. Zuberi, K. S. Johnson, G. K. Aleks, L. T. Molina, M. J. Molina, and A. Laskin, 'Hydrophilic properties of aged soot', *Geophys. Res. Lett.*, vol. 32, no. 1, 2005.
- [163] M. A. R. Talaia, 'Terminal Velocity Of A Bubble Rise In A Liquid Column', *World Acad. Sci. Eng. Technol.*, Apr. 2007.
- [164] A. Charvet, N. Bardin-Monnier, and D. Thomas, 'Can bubble columns be an alternative to fibrous filters for nanoparticles collection?', *J. Hazard. Mater.*, vol. 195, pp. 432–439, Nov. 2011.
- [165] B. Miljevic, R. L. Modini, S. E. Bottle, and Z. D. Ristovski, 'On the efficiency of impingers with fritted nozzle tip for collection of ultrafine particles', *Atmos. Environ.*, vol. 43, no. 6, pp. 1372–1376, Feb. 2009.
- [166] K.-P. Yu, Y.-P. Chen, J.-Y. Gong, Y.-C. Chen, and C.-C. Cheng, 'Improving the collection efficiency of the liquid impinger for ultrafine particles and viral aerosols by applying granular bed filtration', *J. Aerosol Sci.*, vol. 101, pp. 133–143, Nov. 2016.
- [167] C. J. Hogan, E. M. Kettleison, M.-H. Lee, B. Ramaswami, L. T. Angenent, and P. Biswas, 'Sampling methodologies and dosage assessment techniques for submicrometre and ultrafine virus aerosol particles', *J. Appl. Microbiol.*, vol. 99, no. 6, pp. 1422–1434, Dec. 2005.
- [168] M. Spanne, P. Grzybowski, and M. Bohgard, 'Collection Efficiency for Submicron Particles of a Commonly Used Impinger', *Am. Ind. Hyg. Assoc. J.*, vol. 60, no. 4, pp. 540–544, Jul. 1999.
- [169] A. Dudkiewicz *et al.*, 'A uniform measurement expression for cross method comparison of nanoparticle aggregate size distributions', *Analyst*, vol. 140, no. 15, pp. 5257–5267, 2015.
- [170] M. Hassellöv, B. Lyvén, C. Haraldsson, and W. Sirinawin, 'Determination of Continuous Size and Trace Element Distribution of Colloidal Material in Natural Water by On-Line Coupling of Flow Field-Flow Fractionation with ICPMS', *Anal. Chem.*, vol. 71, no. 16, pp. 3497–3502, Aug. 1999.
- [171] F. Kreith, R. M. Manglik, and M. S. Bohn, *Principles of Heat Transfer, SI Edition*. Cengage Learning, 2012.
- [172] J.-S. Lin and C.-J. Tsai, 'Thermophoretic deposition efficiency in a cylindrical tube taking into account developing flow at the entrance region', *J. Aerosol Sci.*, vol. 34, no. 5, pp. 569–583, May 2003.
- [173] E. N. Sieder and G. E. Tate, 'Heat Transfer and Pressure Drop of Liquids in Tubes', *Ind. Eng. Chem.*, vol. 28, no. 12, pp. 1429–1435, Dec. 1936.
- [174] Y. A. Sevcenco, D. Walters, A. P. Crayford, R. Marsh, P. J. Bowen, and M. P. Johnson, 'Evaluation of Transport Line Effects on PM Size Distribution for Aircraft Exhaust for Different Flow Regimes and Dilution Methodology', pp. 1125–1133, Jun. 2012.

- [175] M. A. Altaher, H. Li, P. Williams, M. Johnson, and S. Blakey, 'Determination of Particle Penetration Factors in a Particle Transfer Line for Aero Gas Turbine Engine Exhaust Particle Measurement', p. V04AT04A028, Jun. 2014.
- [176] Y. J. Yoon, S. Cheevers, S. Gerard Jennings, and C. D. O'Dowd, 'Performance of a venturi dilution chamber for sampling 3–20 nm particles', *J. Aerosol Sci.*, vol. 36, no. 4, pp. 535–540, Apr. 2005.
- [177] 'ICAO Aircraft Engine Emissions Databank', EASA. [Online]. Available: <https://www.easa.europa.eu/easa-and-you/environment/icao-aircraft-engine-emissions-databank>. [Accessed: 07-Mar-2019].
- [178] A. Liati *et al.*, 'Electron Microscopic Study of Soot Particulate Matter Emissions from Aircraft Turbine Engines', *Environ. Sci. Technol.*, vol. 48, no. 18, pp. 10975–10983, Sep. 2014.
- [179] M. Owen, G. Mulholland, and W. Guthrie, 'Condensation Particle Counter Proportionality Calibration from 1 Particle·cm⁻³ to 104 Particles·cm⁻³', *Aerosol Sci. Technol.*, vol. 46, no. 4, pp. 444–450, Apr. 2012.
- [180] B. Giechaskiel, X. Wang, D. Gilliland, and Y. Drossinos, 'The effect of particle chemical composition on the activation probability in n-butanol condensation particle counters', *J. Aerosol Sci.*, vol. 42, no. 1, pp. 20–37, Jan. 2011.
- [181] X. Wang, R. Caldow, G. J. Sem, N. Hama, and H. Sakurai, 'Evaluation of a condensation particle counter for vehicle emission measurement: Experimental procedure and effects of calibration aerosol material', *J. Aerosol Sci.*, vol. 41, no. 3, pp. 306–318, Mar. 2010.
- [182] Mamakos, Athanasios, 'Particle measurement programme : volatile particle remover calibration round robin : final report.', *EU Publ. PMP Programme*, Nov. 2012.
- [183] I. Marhaba, D. Ferry, C. Laffon, T. Z. Regier, F.-X. Ouf, and P. Parent, 'Aircraft and MiniCAST soot at the nanoscale', *Combust. Flame*, vol. 204, pp. 278–289, Jun. 2019.
- [184] J. Xue *et al.*, 'Comparison of Vehicle Exhaust Particle Size Distributions Measured by SMPS and EEPs During Steady-State Conditions', *Aerosol Sci. Technol.*, vol. 49, no. 10, pp. 984–996, Oct. 2015.
- [185] D. E. Hagen, P. Lobo, P. D. Whitefield, M. B. Trueblood, D. J. Alofs, and O. Schmid, 'Performance Evaluation of a Fast Mobility-Based Particle Spectrometer for Aircraft Exhaust', *J. Propuls. Power*, vol. 25, no. 3, pp. 628–634, 2009.
- [186] TSI Incorporated, 'Scanning mobility particle sizer spectrometer (SMPS) MODEL 3938'. 2019.
- [187] C. Qi, D.-R. Chen, and P. Greenberg, 'Performance study of a unipolar aerosol mini-charger for a personal nanoparticle sizer', *J. Aerosol Sci.*, vol. 39, no. 5, pp. 450–459, May 2008.
- [188] Y. G. Stommel and U. Riebel, 'A corona-discharge-based aerosol neutralizer designed for use with the SMPS-system', *J. Electrostat.*, vol. 63, no. 6–10, pp. 917–921, Jun. 2005.
- [189] P. Intra and N. Tippayawong, 'An Overview of Unipolar Charger Developments for Nanoparticle Charging', *Aerosol Air Qual. Res.*, vol. 11, no. 2, pp. 187–209, 2011.
- [190] T. J. Johnson, J. P. R. Symonds, and J. S. Olfert, 'Mass–Mobility Measurements Using a Centrifugal Particle Mass Analyzer and Differential Mobility Spectrometer', *Aerosol Sci. Technol.*, vol. 47, no. 11, pp. 1215–1225, Nov. 2013.
- [191] Cambustion, 'Urban ambient aerosol measurements with the DMS500 (Cambustion Application Notes DMS10)'. 2009.
- [192] X. Ma, C. D. Zangmeister, J. Gigault, G. W. Mulholland, and M. R. Zachariah, 'Soot aggregate restructuring during water processing', *J. Aerosol Sci.*, vol. 66, pp. 209–219, Dec. 2013.
- [193] K. K. Leung, E. G. Schnitzler, W. Jäger, and J. S. Olfert, 'Relative Humidity Dependence of Soot Aggregate Restructuring Induced by Secondary Organic Aerosol: Effects of Water on Coating Viscosity and Surface Tension', *Environ. Sci. Technol. Lett.*, vol. 4, no. 9, pp. 386–390, Sep. 2017.
- [194] A. de Risi, T. Donato, and D. Laforgia, 'Theoretical investigation on the influence of physical parameters on soot and NO_x engine emissions', presented at the ASME, 2001, p. 13.
- [195] B. T. Brem *et al.*, 'Effects of Fuel Aromatic Content on Nonvolatile Particulate Emissions of an In-Production Aircraft Gas Turbine', *Environ. Sci. Technol.*, vol. 49, no. 22, pp. 13149–13157, Nov. 2015.


- [196] P. Lobo *et al.*, 'Impact of Alternative Fuels on Emissions Characteristics of a Gas Turbine Engine – Part 1: Gaseous and Particulate Matter Emissions', *Environ. Sci. Technol.*, vol. 46, no. 19, pp. 10805–10811, Oct. 2012.
- [197] R. H. Moore *et al.*, 'Biofuel blending reduces particle emissions from aircraft engines at cruise conditions', *Nature*, vol. 543, pp. 411–415, Mar. 2017.

10 Appendices

10.1 Calibration certificates PM measurement

AIR 6241 Calibration Protocol Annual Calibration Micro Soot Sensor AVL 483 S/N 273

Instrument	Measuring unit complete
Serial No.	273



Aviation mode adjusted?	ok
-------------------------	----

Calibration data				
Calibration factor			Zero drift	Rise time
old f cal	f corr	new f cal	$\mu\text{g}/\text{m}^3/\text{hr}$	sec
0,582	1,084	0,631	-0,1192	0,4
Reference phase angle			Reference value span check	
old_phase		new_phase	old	new
-63		-60	3,850	4,060

MW (mg/m ³) 60 sec begin	MW (mg/m ³) 60 sec end
0,0000	-0,0001

The calibration was performed in accordance with the requirements from Annex 16, Appendix 7.


Date 30.03.2018

Signature Alfred Stampfl

Dok.Nr. D00090245
Seite / page 1 von 4
50000681 / 01

AIR 6241 Calibration Protocol Annual Calibration Micro Soot Sensor AVL 483 S/N 273

AS FOUND Measurement



Calibration factor	Reference phase angle (°)
0,582	-63

Notes:

Span Check

Reference Value Absorber (mg/m ³)	Result (mg/m ³)	Deviation (%)
3,85	3,694	-4,064

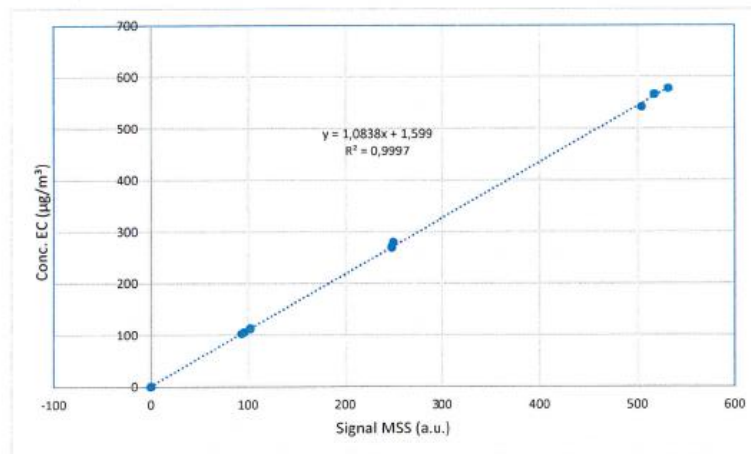
Resonance scan

ARAS: 4146 140,10 52,0 956,9

Test No	Nominal EC	EC CONC.	EC conc.	MSS soot	MSS soot
	0°C	20°C ($\mu\text{g}/\text{m}^3$)	0°C	0°C	
500_001	500	541,0	580,6	530,4	0,5304
500_002		495,1	531,4	488,1	0,4881
500_003		513,9	551,6	495,0	0,4950
			mean value	mean value	
			554,5	504,5	
		Deviation MSS to EC (EC/OC)		-9,0%	

Dok.Nr. D00090245
Seite / page 2 von 4
50000681 / 01

Test No	Nominal EC conc.	OC CONC.	EC CONC.	EC MASS	% EC	EC mass	EC conc.	Deviation from nominal	MSS soot conc.	MSS soot conc.
	0°C (µg/m³)	20°C (µg/m³)	20°C (µg/m³)	(µg)		(µg/m²)	0°C (µg/m³)	%	0°C (µg/m³)	0°C (mg/m³)
0 001	0						0,0		-0,1	-0,0001
0 002							0,0		-0,2	-0,0002
0 003							0,0		-0,2	-0,0002
100 BG	100	46,2							100,2	0,1002
100 001		46,9	105,5	17,7	99,3	13,5	113,2	13,2	102,3	0,1023
100 002		44,0	95,8	16,0	102,3	12,2	102,8	2,8	93,6	0,0936
100 003		44,5	98,0	16,4	101,7	12,5	105,2	5,2	95,9	0,0959
250 BG	250	67,9							249,5	0,2495
250 001		70,9	260,8	17,3	98,9	13,2	280,0	12,0	249,2	0,2492
250 002		69,8	252,1	16,7	99,3	12,8	270,6	8,2	247,6	0,2476
250 003		69,4	251,0	16,7	99,4	12,7	269,4	7,8	247,6	0,2476
500 BG	500	98,0							512,8	0,5128
500 001		91,2	504,5	16,6	101,4	12,6	541,5	8,3	504,5	0,5045
500 002		94,7	527,3	17,3	100,6	13,2	565,9	13,2	517,5	0,5175
500 003		93,3	537,9	17,7	100,9	13,5	577,3	15,5	531,9	0,5319



CALIBRATION REPORT

Calibration of One Mass Concentration Instrument: Cardiff University LII300 (s/n 0435)

for

Cardiff School of Engineering
Queens Buildings, the Parade
Cardiff, CF24 3AA, UK

Attention: Andrew Crayford

NRC project number: A1-008999

Measurements:

Authorized by:

Dan Clavel & Brett Smith, Technical Officers
Dan.Clavel@nrc-cnrc.gc.ca

Dr. Gregory Smallwood, Program Lead
Greg.Smallwood@nrc-cnrc.gc.ca

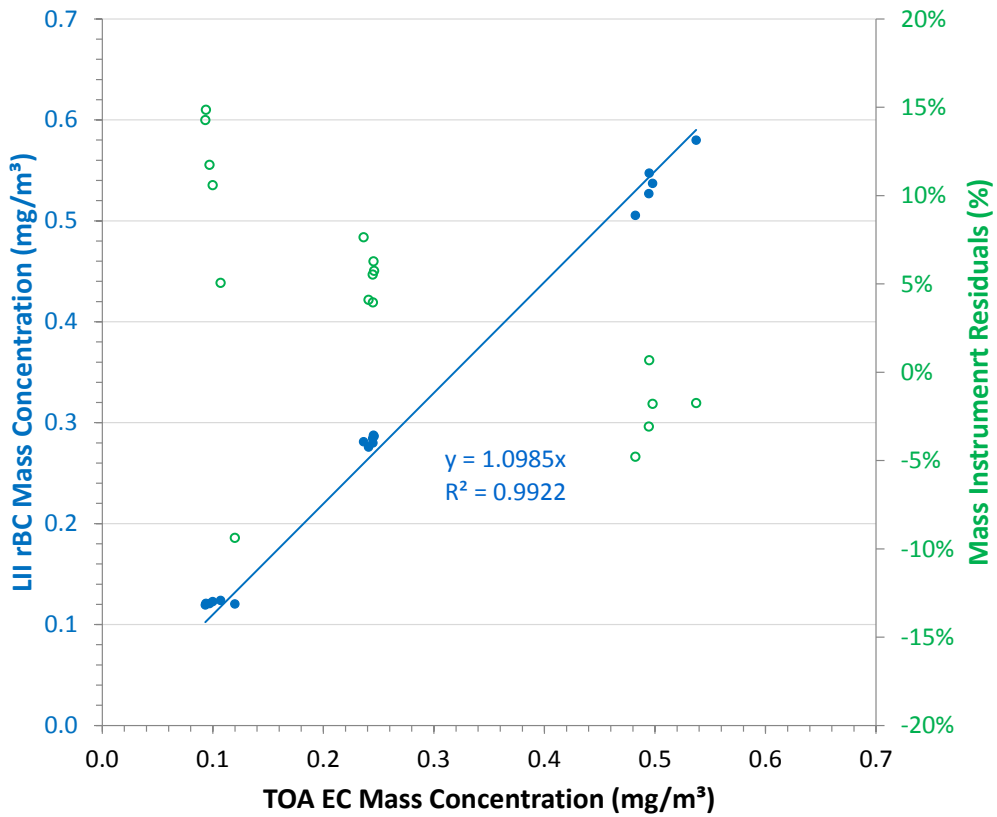


Figure 3 – Thermo-optical analysis EC versus LII300 rBC

AVL 489 Particle Counter Aviation Calibration Certificate

***Only calibrated at Stages 1-5. One of those stages MUST be used for AIR6241 compliant measurements.**

Date: 21-Jan-2016	
Device: GH0672	382C
Chopper Diluter	460

Makro	XF0339	V1.25b
-------	--------	--------



Used Instruments	Type	Serial No.
DMA	TSI 3080N	71207121
Master CPC	TSI 3772	3772121004
Mass Flow Meter	RedY GCR-B5SA-BA25	145143
Calibration aerosol: APG combustion soot		

Measured Inlet Flows of Instruments		
Device	Vol. Flow	Normalization Cond.
APC Chopper Dil. low	4475 ml/min	25°C, 1013.25mbar
Master CPC	980 ml/min	ambient conditons

Zero Concentration with HEPA-Filter		
APC	0.09 #/cm ³	at pcrf=10*10=100
Master CPC	0.000 #/cm ³	

Nr	Diluter 1 low/high	values set		set pcrf	Flows Dilution Factor	Measured Penetrations			
		Diluter 1	Diluter 2			100nm (>70%)	50nm (>65%)	30nm (>55%)	15nm (>30%)
1	low	10	10	100	67	74.7%	69.0%	60.3%	39.3%
2	low	25	10	250	173	76.5%	72.8%	60.7%	40.2%
3	low	50	10	500	352	78.4%	73.3%	62.1%	39.0%
4	low	100	10	1000	693	76.3%	70.5%	62.5%	36.9%
5	low	150	10	1500	1030	75.8%	70.9%	61.0%	36.5%

Volatile Particle Removal Efficiency for Tetracontane 15nm:	100.00%
Volatile Particle Removal Efficiency for Tetracontane 30nm:	100.00%

AVL List GmbH does hereby certify that the above described instrument conforms to the original manufacturer's specifications and has been calibrated using standards whose accuracies are traceable to national standards or have been derived from accepted values of natural physical constants or have been derived by the ration type of self calibration techniques. This report may not be reproduced, except in full, unless permission for the publication of an approved abstract is obtained in writing from the calibration organization issuing this report.

Signature 
(CELIK Caglayan)

Nr	Flows Dilution Factor	Measured particles dilution			
		100 nm	50 nm	30 nm	15 nm
1	67	90	98	112	172
2	173	226	237	285	430
3	352	451	482	570	907
4	693	911	965	1112	1884
5	1030	1364	1458	1696	2832

Calibration values set in firmware

Directly measured values for the seven fixed PCRF settings

PCRF	calib. value
100	1.14
250	1.11
500	1.09
1000	1.11
1500	1.12

Pressures during calibration

Sample Rel. Pressure	-48 mbar
Diluted. Rel. Pressure	18 mbar
Absolute Pressure	981 mbar

Demand temperatures during calibration

Catalytic Stripper Temp.	350 °C
Diluter 1 Temperature	150 °C

Specifications of the Catalytic Stripper

Oxidation efficiency: >99% for decane inlet concentration of 4%
Sulphur Storage Capacity: > 6mg

* These values are calculated by averaging the values measured at the highest and the lowest Diluter 1 setting for each Diluter 2 setting.

CAMBUSTION

DMS500 Certificate of Calibration after Service and Adjustment

Company Name: *Cardiff University*

Instrument Serial No: *M44*

Company Location: *Wales*

Calibration No (matrix): *m2cqw252*

Ship Date: *July 2016*

Date Calibrated: *30th June 2016*

The DMS500 system is certified as meeting or exceeding the Test Specifications, when tested prior to dispatch. The calibration standards used for these measurements are traceable to relevant international standards. The results refer to measurements made at the time of test and not to the instrument's ability to maintain calibration. *The reported measurement uncertainties are based upon a standard uncertainty multiplied by a coverage factor $k = 2$, which for a normal distribution provides a level of confidence of approximately 95%. The standard uncertainties are a consolidation of the uncertainty in the standard and the uncertainty in performing the measurement.*

(a) Size and Gain: against Differential Mobility Analyser Sized Aerosol, with concentration indicated with a standard aerosol electrometer

Electrometer filter flow = 10 slpm

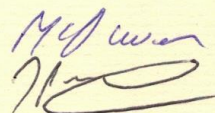
Aerosol	DMA Size (nm)	DMS Size (nm)	Electrometer Concentration (#/cc)	DMS Concentration (#/cc)
H ₂ SO ₄	15.0 ± 1.5	15.1	72900 ± 14600	72500
NaCl	50.0 ± 5.0	49.5	60200 ± 12000	59400
NaCl	100 ± 10	99.7	19400 ± 3870	19400

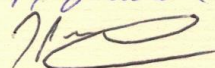
(b) Size Only: Nebulised, dried and neutralised suspension of NIST Traceable Certified NanoSpheres (PSL), Thermo Scientific

PSL Size (nm)	DMS Size (nm)	Lot No	Expiry Date
303 ± 30	316	164765	01/01/2019
600 ± 60	610	44868	01/08/2018
903 ± 90	942	44869	01/08/2018

Standards used for part (a)

Function	Mfr and Model	Serial Number	Calibrated By	Calibration Reference	Calibration Date	Calibration Due	
DMA	TSI 3082	3082001529001	TSI	3082001529001_210715	21/07/2015	20/07/2016	
Aerosol Electrometer	Electrometer	Keithley 617	425680	Keithley Instruments	1767070001	23/12/2014	14/01/2017
	Mass flow meter	Aalborg GFC171	162693-1	Aalborg	151020162693-1	20/10/2015	19/10/2016

Calibrator: 

Approved By: 

Dr J.P.R. Symonds

Director

CAMBUSTION LTD

J6 The Paddocks
347 Cherry Hinton Road
Cambridge CB1 8DH
United Kingdom

Tel: +44 1223 210250

Fax: +44 1223 210190

E-mail: cambustion@cambustion.com

Page 1 of 1 This calibration certificate shall not be reproduced except in full, without written approval of Cambustion.

CPC MODEL 3790E CERTIFICATE OF CALIBRATION

3790132002 Serial Number Test Aerosol: Emery Oil
 18 June 2014 Date

	Units	Low Limit	High Limit			
Inlet Flow						
0.99	Measured Flow (Volumetric)	L/min	0.95 1.05			
0.916	Calculated Flow (Standard)	SL/min	- -			
<i>Standard Conditions: 0° C, 101.3 kPa</i>						
Temperature and Pressure						
20.94	Room Temperature	°C	- -			
46%	Room Relative Humidity	-	- -			
100.9	Room Barometric Pressure	kPa	- -			
39	Saturator Temperature	°C	38 40			
22	Condenser Temperature	°C	20 24			
40	Optics Temperature	°C	39.8 40.2			
29.5	Cabinet Temperature	°C	20 35			
70.9	Pressure Drop Across Orifice	kPa	70 88			
0.7	Pressure Drop Across Nozzle	kPa	0.2 1			
Laser Check						
17	Laser Power (Measured)	mW	14 20			
Optics						
44	Laser Current Reading	mA	12 -			
2	Minimum Pulse Height	V	1 3.65			
600	Minimum Pulse Width	ns	230 950			
3	Maximum Pulse Height	V	2 3.65			
700	Maximum Pulse Width	ns	230 950			
Zero Count Test						
0	Concentration Average Over 12 Hours	p/cc	0 0.001			
Lower Detection & Concentration Linearity Test Results						
51.0%	10 nm Particle Counting Efficiency	-	50% -			
93.7%	15 nm Particle Counting Efficiency	-	90% -			
96.8%	Linearity Test: Slope (up to 10,000 p/cc)	-	90% 110%			
0.9992	Linearity of Regression (R ²)	-	0.97 -			
Final Voltage Measurements						
Pass	Analog Input and Output Voltages					
Linearity Response: CPC vs. Electrometer 3068B						
Nominal Conc.	UUT	Electrometer	%Difference	Units	Low Limit	High Limit
2000 p/cc	1999.44	2117.99	-5.60%	% Diff.	-10%	10%
4000 p/cc	4056.00	4275.99	-5.14%	% Diff.	-10%	10%
6000 p/cc	6195.51	6457.41	-4.06%	% Diff.	-10%	10%
8000 p/cc	8200.56	8468.02	-3.16%	% Diff.	-10%	10%
10000 p/cc	10247.25	10507.69	-2.48%	% Diff.	-10%	10%
<i>Particle Size Used in Linearity Test: 55 nm</i>						

CAMBUSTION

DMS500 Certificate of Calibration
As received without service and adjustment

Company Name: *Cardiff University*

Instrument Serial No: *M44*

Company Location: *Wales*

Calibration No (matrix): *m2cqw68*

Date Calibration Checked: *22nd June 2016*

The calibration standards used for these measurements are traceable to relevant international standards. The results refer to measurements made at the time of test as the instrument was received and not to the instrument's ability to maintain calibration, and furthermore no implication is made that the agreement of these results with the standards used are within the tolerances which Cambustion would require of a new or newly re-adjusted instrument. The reported measurement uncertainties are based upon a standard uncertainty multiplied by a coverage factor $k = 2$, which for a normal distribution provides a level of confidence of approximately 95%. The standard uncertainties are a consolidation of the uncertainty in the standard and the uncertainty in performing the measurement.

Size and Gain: against Differential Mobility Analyser Sized Aerosol, with concentration indicated with a standard aerosol electrometer
Electrometer filter flow = 8.0 slpm

Aerosol	DMA Size (nm)	DMS Size (nm)	Electrometer Concentration (#/cc)	DMS Concentration (#/cc)
NaCl	50.0 ± 5.0	45.6	75200 ± 15000	91400
NaCl	100 ± 10	87.5	16800 ± 3360	21500

Standards used above:

Function	Mfr and Model	Serial Number	Calibrated By	Calibration Reference	Calibration Date	Calibration Due	
DMA	TSI 3082	3082001529001	TSI	3082001529001_210715	21/07/2015	20/07/2016	
Aerosol Electrometer	Electrometer	Keithley 617	425680	Keithley Instruments	1767070001	23/12/2014	14/01/2017
	Mass flow meter	Aalborg GFC171	162693-1	Aalborg	151020162693-1	20/10/2015	19/10/2016

Calibrator:

Approved By:

Dr J.P.R. Symonds

Director

CAMBUSTION LTD

J6 The Paddocks
347 Cherry Hinton Road
Cambridge CB1 8DH
United Kingdom

Tel: +44 1223 210250

Fax: +44 1223 210190

E-mail: cambustion@cambustion.com

10.2 Other calibration certificates



TC Ltd for Temperature Sensing, Measurement and Control

TC Ltd
PO Box 130
Uxbridge, UB8 2YS
United Kingdom

Telephone: 01895 252222
Email: info@tc.co.uk

CERTIFICATE OF CALIBRATION

Date of Issue:	18. May 2018	Ambient Temp:	20°C +/- 2°C
Customer:	Cardiff University	Approved Signatory:	Kerry Grice
Address:	School of engineering Trevithick Building 5 The Parade Cardiff CF24 3AA	Certificate Number:	18-0778-A-001
Order Number:	ENGIN30875956	Revision_0	
Our Reference:	129859		
Date Received:	10. May 2018		
Type:	K, 1.63mm x 1000mm		
Product Code:	409-028 C/W 753-526 (S/N: 1701499) Ceramic Twin Bore Insulated Thermocouple		

Calibration Procedure:

The thermocouple and indicator were calibrated as a unit by comparison with a reference resistance thermometer and a type R reference thermocouple. The calibration took place in a Dry block and a Triple zone furnace. All measurements are traceable to recognised national standards. The thermocouple wires were referenced to 0 Degrees Celsius with the cold junction of the unit under test at ambient. All resistance / voltage outputs were measured on a precision digital multimeter. All tests were carried out in a controlled environment using devices having known and traceable values. The temperature measurements are traceable to ITS-90. The thermocouple voltages were converted using IEC60584-1:2013. The Indicator was allowed to stabilize in the laboratory for 4 hours prior to calibration. The resolution of the indicator was 0.1°C up to 20°C and 1°C above. An additional value of +/- 1 least significant digit of the indicator applies to the uncertainty.

Serial Number	Reference Temperature (°C)	UUT (µV)	Equivalent Value (°C)	Error (°C)
129859-A-001	20.00	n/a	19.65	-0.35
129859-A-001	250.00	n/a	248.07	-1.93
129859-A-001	500.00	n/a	498.27	-1.73
129859-A-001	750.00	n/a	751.31	1.31
129859-A-001	1000.00	n/a	1002.66	2.66

Uncertainty: +/-0.35°C at 20°C, +/-0.61°C up to 500°C and +/-1.80°C up to 1000°C

The depth of immersion of the UUT was a minimum of 125mm.

Calibration date: 18. May 2018

The reported expanded uncertainty is based on a standard uncertainty multiplied by a coverage factor of k = 2, providing a level of confidence of approximately 95%. The uncertainty evaluation has been carried out in accordance with UKAS requirements.

Note: It is the user's responsibility to determine the long-term drift and the uncertainty under the conditions of use

This certificate is issued in accordance with the laboratory accreditation requirements of the United Kingdom Accreditation Service. It provides traceability of measurement to the SI system of units and/or to units of measurement realised at the National Physical Laboratory or other recognised national metrology institutes. This certificate may not be reproduced other than in full, except with the prior written approval of the issuing laboratory.

ATOMIZER AEROSOL GENERATOR ATM 226

Serial no.: 226 17 04 4C8

Identification: /

Nozzle no.: 1786

Protective grounding

Functional test at 100VAC

Measured data

Pressure for opening the safety valve: 0.42 bar

Check of aerosol specification at 20SKT (250/h)	Mean particle size μm	Number concentration Particle/cm ³	Volumetric flow rate l/min
Upper limit:	1.0	$1.8 \cdot 10^7$	4.4
Measured value **)	1.0	$0.82 \cdot 10^7$	4.0
Lower limit	0.8	$0.8 \cdot 10^7$	3.9

Measurements of the aerosol concentration were made by using an aerosol monitor. The noted values are significant quality parameters. By realising the limits, the aerosol specifications which are shown at next page are guaranteed.

Following measuring instruments were used

Type	Manufacturer	Identification	last calibration	Certificate number	next calibration
Laminar flow meter FCO96 F-30L	Furness Controls	0109306 / -305	03/2016	DFCG11712	03/2018
Protective earth tester Metratester 5+	Gossen Metrawatt	M700DTL1845	05/2017	2017-3751	05/2018
Pressure indicator 0...1.0bar	WIKA				
Process aerosol monitor PAM 510	Topas	510 94 01 302	05/2017	---	05/2018

The instrument is built and tested to conform to the high quality standards of Topas GmbH. The manufacturer guarantees that the instrument fulfils the technical specification as defined in the instruction manual.

Dresden, 2017-09-27 tested by: Jens Rudolf

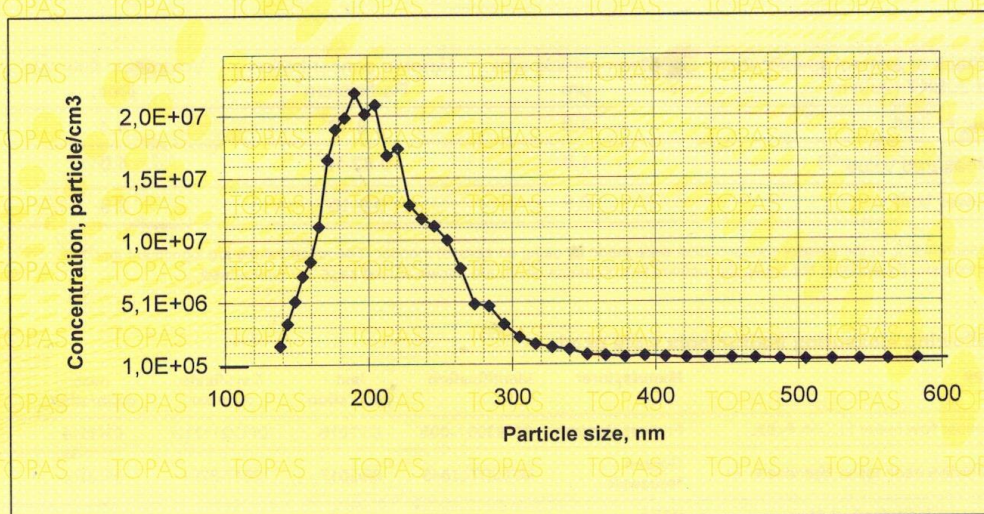



Topas GmbH
Technologie-orientierte Partikel-,
Analysen- und Sensortechnik
Oskar-Röder-Straße 12
01237 Dresden
GERMANY
Tel. + 49 (351) 21 66 43-0
Fax: + 49 (351) 21 66 43-55

Specification of the DEHS-Aerosol

Number concentration

Table	Particle/cm ³	Particle/cf
Total number concentration	>10 ⁸	2,8·10 ¹²
Number concentration (Size 0,3 up to 0,5µm):	1,5·10 ⁷	4,2·10 ¹¹
Number concentration (Size 0,5 up to 1,0µm):	8·10 ⁶	2,3·10 ¹¹



Particle size distribution of a DEHS aerosol measured by a Scanning Mobility Particle Sizer (TSI, Inc.)

Topas GmbH
 Technologie-orientierte
 Partikel-, Analysen- und Sensortechnik
 Oskar-Röder-Str. 12 · D-01237 Dresden

Telefon + 49 351 216643-0
 Telefax + 49 351 216643-55
 e-mail office@topas-gmbh.de
 Internet www.topas-gmbh.de

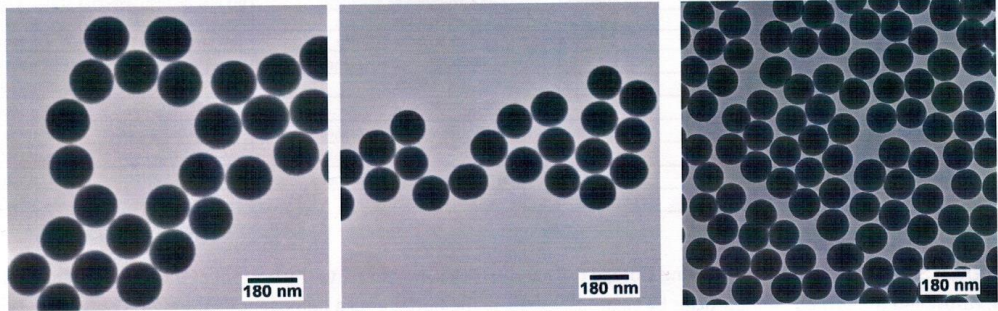
10.3 Suspension/solution certificates



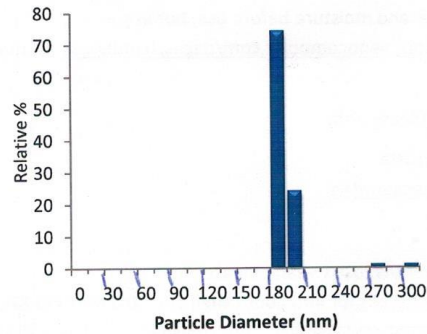
180 nm Non-Functionalized NanoXact™ Silica

Lot Number: JEA0224

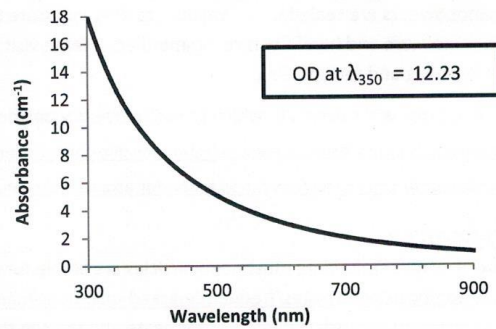
Diameter (TEM):	179 ± 16 nm	Hydrodynamic Diameter:	198 nm
Coefficient of Variation:	8.9 %	Zeta Potential:	-54 mV
Surface Area (TEM):	14.9 m ² /g	pH of Solution:	9.6
Mass Concentration (SiO₂):	10.5 mg/mL	Particle Surface:	Silanol
Particle Concentration:	1.6E+12 particles/mL	Solvent:	Milli-Q Water



Size Distribution



Optical Properties



Characterization Instrumentation

Diameter and Size Statistics:	JEOL 1010 Transmission Electron Microscope
Mass Concentration:	Gravimetric Analysis- AND HM-202
Spectral Properties:	Agilent 8453 UV-Visible Spectrometer
Hydrodynamic Diameter/Zeta Potential:	Malvern Zetasizer Nano ZS.

Shake vigorously before use. Bath sonicate if needed. Storage: 25°C. DO NOT FREEZE.

nanoComposix, Inc
4878 Ronson Ct. Suite K
San Diego, CA 92111

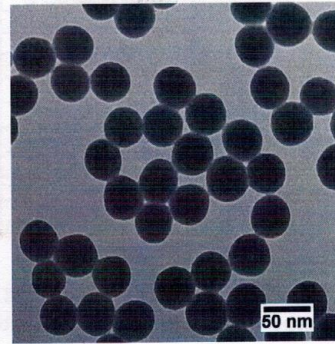
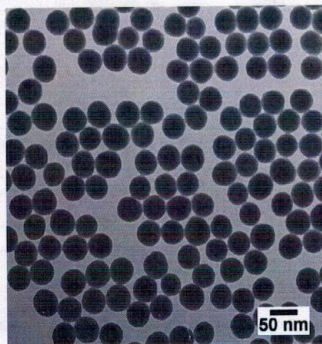
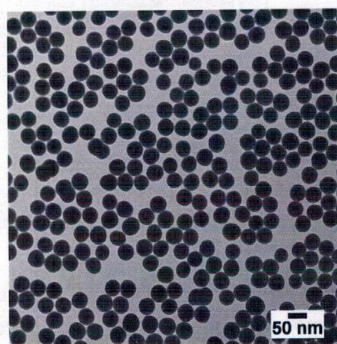
nanoComposix.com

info@nanocomposix.com
Phone: (858) 565-4227
Fax: (619) 330-2556

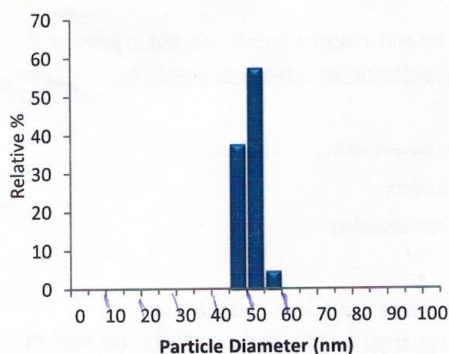
50 nm Silica Nanospheres, NanoXact™

Lot Number: MEL0053

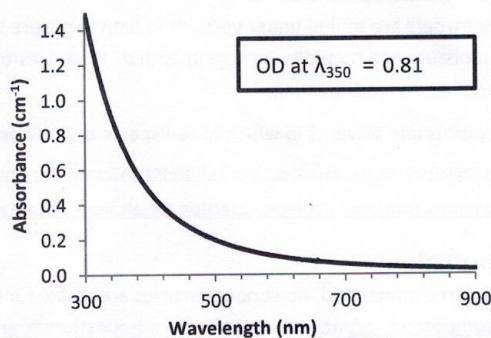
Diameter (TEM):	46 ± 2 nm	Hydrodynamic Diameter:	57 nm
Coefficient of Variation:	4.8 %	Zeta Potential:	-50 mV
Surface Area (Calc'd):	59.0 m ² /g	pH of Solution:	9.7
Mass Concentration (SiO₂):	10.4 mg/mL	Particle Surface:	Silanol
Particle Concentration (Calc'd):	9.2E+13 particles/mL	Solvent:	Milli-Q Water



Size Distribution



Optical Properties



Characterization Instrumentation

Diameter and Size Statistics:	JEOL 1010 Transmission Electron Microscope
Mass Concentration:	Gravimetric Analysis- AND HM-202
Spectral Properties:	Agilent 8453 UV-Visible Spectrometer
Hydrodynamic Diameter/Zeta Potential:	Malvern Zetasizer Nano ZS
pH:	Horiba - Laqua Twin pH Meter

Shake vigorously before use. Bath sonicate if needed. Storage: 25°C. DO NOT FREEZE.

nanoComposix, Inc
4878 Ronson Ct. Suite K
San Diego, CA 92111

nanoComposix.com

info@nanocomposix.com
Phone: (858) 565-4227
Fax: (619) 330-2556

EM Grade Data Sheet

Information	
Product	Gold colloid – 100nm
Product Code	EM. GC100
Batch Number	009717
Storage Buffer	Suspended in H ₂ O, no preservative Residual chemical left from manufacture
Storage Instructions	Store at 2-8°C – DO NOT FREEZE
Expiry Date	February 2016 (Use within one month of opening)

Technical Data	
Mean Diameter	100.6nm
Coefficient of Variation	≤8%
Gold Chloride Concentration	0.01%
No. of Particles per ml	5.60E+09
No. Moles Particle per ml	9.29924E-15
Molar Particle Concentration (No. moles per L)	9.29924E-12
Mass of gold per ml (g)	5.66E-05

USA: 1-800-423-8199 | International: +44 (0)2920 767 499 | info@bbisolutions.com | www.bbisolutions.com

Part of **BBI Group**

Registered office: c/o Berry Smith LLP, Haywood House, Dumfries Place, Cardiff, CF10 3GA.
BBI Solutions is the trading name of BBI Solutions OEM Limited. Registered in England and Wales Number 8368483

Catalog Number C37485
Product Name Carboxyl latex, 4% w/v 0.1 µm
Appearance white suspension
Medium de-ionized water
Lot Number 1048446

Negatively charged polystyrene microspheres with carboxyl functional groups on the surface.
 Surface charge is pH dependent. Stable at neutral to high pH. Surface is hydrophobic in nature.
 SONICATE WELL BEFORE USE. STORE AT 4°C, DO NOT FREEZE

	LOT DATA	SPECIFICATION
INTERFACIAL DYNAMICS		
Batch/Material Number	508,1	n.a.
Mean Diameter ¹	0.11 µm	0.09 - 0.14 µm
Standard Deviation of Diameter	0.013 µm	n.a. µm
Coefficient of Variation of Diameter	11.5 %	≤12 %
Percent Solids w/v	4.0 %	3.5 - 4.5 %
Particle Number Per Milliliter of Latex	5.4×10^{13}	n.a.
Specific Surface Area	$5.2 \times 10^5 \text{ cm}^2/\text{g}$	n.a. cm^2/g
Density of Polystyrene at 20°C	$1.055 \text{ g}/\text{cm}^3$	$1.055 \text{ g}/\text{cm}^3$
Refractive Index of Polystyrene at 590 nm, 20°C	1.591	1.591
Charge Content ²	18.5 µEq/g	n.a. µEq/g
Surface Charge Density	$3.4 \text{ µC}/\text{cm}^2$	n.a. $\text{µC}/\text{cm}^2$
Area per Carboxyl Group	465 Å^2	n.a. Å^2
Charge Groups per Particle	8.2×10^3	n.a.

1. Determined from transmission electron microscopy.
2. Measured from conductometric titration.

Betty Wood

Betty Wood, Quality Assurance Manager
 12-Oct-2011

Life Technologies Corporation, on behalf of its Invitrogen business, Molecular Probes® labeling and detection technologies, certifies on the date above that this is an accurate record of the analysis of the subject lot and that the data conform to the specifications in effect for this product at the time of analysis.

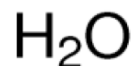
Molecular Probes, Inc.
 29851 Willow Creek Road
 Eugene, OR 97402-9132
 Phone (541) 465-8300 Fax (541) 335-0504

Printed Jan 16, 2013

Product Specification

Product Name:
Water - for UHPLC, for mass spectrometry

Product Number: **900682**
CAS Number: 7732-18-5



Formula: H₂O
Formula Weight: 18.02 g/mol

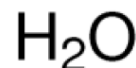
TEST	Specification
Appearance (Clarity)	Clear
Appearance (Color)	Colorless
Appearance (Form)	Liquid
UV Absorbance 230nm	≤ 0.003
UV Absorbance 210nm	≤ 0.020
Residue on Evaporation	≤ 0.0001 %
Fluorescence 254nm as Quinine	≤ 1 ppb
Fluorescence 365nm as Quinine	≤ 1 ppb
HPLC Absorbance 254 nm	≤ 0.9 mAU
HPLC Absorbance 210 nm	≤ 2 mAU
LCMS	Suitable
Suitability Confirmed	
Chloride by Ion Chromatography	≤ 0.01 ppm
Fluoride by Ion Chromatography	≤ 0.01 ppm
NO ₃ by Ion Chromatography	≤ 0.1 ppm
SO ₄ by Ion Chromatography	≤ 0.1 ppm
Trace Metal Analysis	Complete
Aluminum	≤ 20 ppb
Cadmium	≤ 20 ppb
Calcium	≤ 20 ppb
Chromium	≤ 15 ppb

Sigma-Aldrich warrants, that at the time of the quality release or subsequent retest date this product conformed to the information contained in this publication. The current Specification sheet may be available at Sigma-Aldrich.com. For further inquiries, please contact Technical Service. Purchaser must determine the suitability of the product for its particular use. See reverse side of invoice or packing slip for additional terms and conditions of sale.

Product Specification

Product Name:
Water - for UHPLC, for mass spectrometry

Product Number: **900682**
CAS Number: 7732-18-5
Formula: H₂O
Formula Weight: 18.02 g/mol



TEST	Specification
Cobalt	< 15 ppb
Copper	< 10 ppb
Iron	< 20 ppb
Magnesium	< 20 ppb
Manganese	< 20 ppb
Nickel	< 20 ppb
Potassium	< 20 ppb
Silver	< 20 ppb
Sodium	< 50 ppb
Tin	< 20 ppb
Zinc	< 20 ppb
Expiration Date Period	-----
1 Year	

Specification: PRD.1.ZQ5.10000079410

Sigma-Aldrich warrants, that at the time of the quality release or subsequent retest date this product conformed to the information contained in this publication. The current Specification sheet may be available at Sigma-Aldrich.com. For further inquiries, please contact Technical Service. Purchaser must determine the suitability of the product for its particular use. See reverse side of invoice or packing slip for additional terms and conditions of sale.